ANALYSIS AND CONTROL OF NONLINEAR PHENOMENA IN ELECTRICAL DRIVES

Nelson Chidiebere Okafor

B.Sc., M.Sc.

A thesis submitted for the degree of

Doctor of Philosophy

September 2012

School of Electrical, Electronic and

Computer Engineering

Newcastle University

United Kingdom

`

ABSTRACT

Electrical motors are key to the growth of any modern society. In order to ensure optimal utilisation of the motors, the shaft speed and armature current must be controlled. Currently, the most efficient way of achieving both speed and current control in electrical motors is through power electronic switching, thus making the system both nonlinear and time varying. The combination of electric motors and control electronics is referred to as electric drives.

Due to the inherent nonlinear nature of electrical drives, the system is prone to complex dynamical phenomena including bifurcations, chaos, co-existing attractors and fractal basin boundaries. The types of nonlinear phenomena that occur in some of the more common electrical drive systems, namely *permanent magnet dc* (PMDC) *drives, series connected dc* (SCDC) *drives* and *switched reluctance motor* (SRM) *drives*, are considered for analysis in this project.

The nominal steady state behaviour of these drives is a periodic orbit with a mean value close to the reference value. But as some system parameters are being varied, the nominal orbit of the system referred to as the period-1 orbit, may lose its stability leading to the birth of new attracting orbit that is periodic, quasi-periodic or chaotic in nature.

The most common technique for performing stability analysis of a periodic orbit is the Poincaré map approach, which has been successfully applied in DC-DC converters. This method involves reducing the continuous time dynamical system into a discrete time nonlinear iterative map and the periodic orbit into a fixed point. The stability of the periodic orbit then depends on the eigenvalue of the Jacobian matrix of the map evaluated at the fixed point. However, for some power electronic based system the nonlinear map cannot be derived in closed form due to the transcendental nature of the equation involved.

In this project, the recently introduced Monodromy matrix approach is employed for the stability analysis of the periodic orbit in electrical drives. This method is based on Filippov's method of differential inclusion and has been successfully applied in the stability analysis of periodic orbits in both low order and higher order DC-DC converters. This represents the first application of the technique in electrical drives. The Monodromy matrix approach involves computing the State Transition Matrix (STM) of the system around the nominal orbit including the STM at the switching manifold (sometimes referred to as the Saltation matrix). Also, by manipulating some of the parameters in the Saltation matrix, it is possible to control the instabilities and thus extend the system parameter range for nominal period-1 operation.

The experimental validation of the nonlinear phenomena in a proportional integral (PI) controlled PMDC drive, which is absent in literature, is presented in this thesis. The system was implemented using dsPIC30F3010 which is a low cost and high performance digital signal controller.

ACKNOWLEDGEMENTS

I will first express my deepest gratitude to my supervisors Dr. Damian Giaouris and Dr. Bashar Zahawi for their guidance and support throughout my study. They encouraged me to delve into the world of bifurcation and chaos which I found strange at the commencement of my research.

I am also deeply indebted to Professor Soumitro Banerjee of the Department of Electrical Engineering, Indian Institute of Technology, Kharagpur, for his kind advice and suggestions towards my research.

One of the greatest challenges which most PhD students have to confront is financial support. Therefore, I would like to thank the Petroleum Technology Development Fund (PTDF) of Nigeria for providing all the necessary funding I needed throughout my study. I am also grateful to the Nigerian Army and Nigerian Communication Satellite (Nigcomsat) Ltd for all the support they offered me during the research.

Several colleagues and staff offered me advice and support during the project. I would like to thank Dr. Chris Batman and Mr James Widmer for their advice during the switched reluctance machine modelling. I will also like to thank Dr. John Bennett for his advice while writing the firmware for the digital signal controller. I'm also grateful to Mr James Richardson for providing all the needed test instruments and Mr Stuart Baker for building a suitable platform for my machine. I'm also grateful to all the tutors in power electronics, drives and machine (PEDM) research group and my colleagues in the UG laboratory.

Without the support from my family, this work would have not been possible. Therefore, I would like to express my sincere gratitude to my wife and children for helping me to forget all the worries of research. They are the source of my inspiration and joy. I am also grateful to my parents for making all the sacrifice to offer me good education.

Finally, I would like to thank the almighty God who provided me with sound health and guidance throughout the period of my study.

To the memory of my mother who could not live to see me complete my research.
May her soul rest in peace.

TABLE OF CONTENTS

LIST OF FIGURES

LIST OF TABLES

LIST OF SYMBOLS AND ABBREVIATIONS

Symbols	**Description**
$\mathbf{A}$	State matrix
$\mathbf{A}_{\mathbf{ON}}$	State matrix when the power switch is closed
$\mathbf{A}_{\mathbf{OFF}}$	State matrix when the power switch is opened
$\mathbf{B}$	Input matrix
D	Diode
d	Duty cycle (fraction of time the power switch is closed in one period)
E_b	Back emf induced at the armature coil terminals (V)
$\mathbf{f}$	Vector field
$\mathbf{f}_{\mathbf{ON}}$	Smooth vector field after switching
$\mathbf{f}_{\mathbf{OFF}}$	Smooth vector field before switching
h	Switching hypersurface (also known as switching manifold)
$\mathbf{I}$	Identity matrix
$\mathbf{I}_{\mathrm{nxn}}$	Identity matrix of the same order with the system
i_L	Armature current (A)
$\mathrm{I}_{\mathrm{ref}}$	Reference current (A)
J	Moment of inertia (Nm.rad^{-1}.sec^{2}.)
K_e	Back emf constant (V. rad^{-1}.sec)
Ki	Integral gain
K_p	Proportional gain

K_t	Torque constant (Nm/A)
L	Inductance (H)
L_a	Inductance of the armature coil (H)
L_f	Inductance of the field coil (H)
N	Number of turns of a coil
$\mathbf{n}$	Normal to the hypersurface
R	Resistance (Ω)
R_a	Resistance of the armature coil (Ω)
R_f	Resistance of the field coil (Ω)
$\mathbf{S}$	Saltation matrix
T	Period of the PWM cycle (s)
T_L	Load torque (Nm)
T_e	Electrical torque (Nm)
T_{on}	The time interval when the power switch is ON (s)
T_{off}	The time interval when the power switch is OFF(s)
V_{avg}	The average voltage applied at the armature coil terminals (V)
V_{in}	The supply voltage (V)
V_{con}	Control signal (V)
V_L	Lower voltage limit of the ramp signal (V)
V_{OFF}	Product of the input matrix (**B**) and the input vector (**U**) when the switch is OFF
V_{ON}	Product of the input matrix (**B**) and the input vector (**U**) when the switch is ON
V_{ramp}	Ramp signal (V)

V_U	Upper voltage limit of the ramp signal (V)
ω	Angular velocity (shaft speed) (rad/s)
ω_{ref}	Reference speed (rad/s)
$\mathbf{X}$	State vector
$\mathbf{X}^*$	State vector at the equilibrium point
δ	The fraction of time when the switch is OFF in one period $(\delta = 1 - d)$
ϕ	Magnetic flux (Wb)
λ	Flux linkage (Wb)
θ	Angular displacement (rotor position) (rad)
∇	Gradient (del operator)
φ	Flow
Φ	State transition matrix
Σ	Switching hypersurface

Abbreviations

AC	Alternating Current
ADC	Analog to Digital Converter
AI	Artificial Intelligence
ANN	Artificial Neural Network
BDCM	Brushed DC Motor
BLDCM	Brushless DC Motor
CCM	Continuous Conduction Mode

CTS	Continuous Time System
DC	Direct Current
DCM	Discontinuous Conduction Mode
DSC	Digital Signal Controller
DTS	Discrete Time System
EP	Equilibrium Point
FEDC	Field Excited DC Motor
FP	Fixed Point
LTI	Linear Time Invariant
LTV	Linear Time Variant
MCPWM	Motor Control PWM
MM	Monodromy Matrix
MMF	Magnetomotive Force
PI	Proportional Integral
PMDC	Permanent Magnet DC Motor
PMSM	Permanent Magnet Synchronous Motor
PS	Poincaré section
PWM	Pulse Width Modulation
QEI	Quadrature Encoder Interface
SCDC	Series Connected DC Motor
SMPE	Switched Mode Power Electronic
SRM	Switched Reluctance Motor
STM	State Transition Matrix

CHAPTER 1

INTRODUCTION

1.1 Introduction

Electrical motors can be found in steel rolling mills, drilling machines, railway traction, industrial robots, and in most household items and office equipment. They convert electrical energy into mechanical energy by exploiting the 19th century discovery by Michael Faraday that a current carrying coil within a magnetic field will experience a force. Today, there are several variants of electric motors whose operation depend on this simple principle.

In order to ensure more diverse application of electric motors, there is a need for both speed and torque control. This was achieved in the past with DC motors by connecting a rheostat in series with either the armature or field winding or through the use of an external dc generator [1-3]. These old control techniques were expensive, inefficient and complex. The amount of heat dissipated in the rheostat was also a huge problem to deal with. With the recent advances in power electronics, digital electronics and microprocessors, speed and torque control of electric motors can now be efficiently achieved through a process known as pulse width modulation (PWM). The PWM signals are used to turn ON and turn OFF the power electronic switches so as to control the average voltage applied at the motor terminals and thus achieve speed control. The entry of power electronic switches into the market has also led to gradual transition from brushed DC motors to brushless DC and AC motors since speed control of the later can now be achieved through variable frequency inverters. The electric motor along with the speed and current transducers, the power converter circuit and control electronics are referred to as an electric drive [3].

Despite the huge benefits that could be derived by the adoption of power electronic switches for both speed and torque control of electric motors, the PWM switching action makes the entire drive system to be time varying and nonlinear [4-8]. The topologies of such systems during the switch ON states are often different from those during the switch OFF states, thereby classifying these systems as non-smooth or piecewise smooth systems (PWS) (see Chapter 2 for details). Also due to the switching action, the trajectories of the state variables of the system will converge to a periodic orbit or limit cycle at the steady state instead of converging to an equilibrium point thus adding to the complexity of the system.

As some drive parameters such as the supply voltage or controller gains are being varied by the operators, this nominal orbit loses stability leading to the birth of new attracting orbit that is periodic, quasi-periodic or chaotic in nature. This change in qualitative behaviour of the system is referred to as a bifurcation [9, 10]. If the period of the new attracting orbit is double the period of the nominal orbit, the bifurcation will be referred to as period doubling bifurcation. But if the new attracting orbit is quasi-periodic in nature, the phenomena will be referred to as Neimark-Sacker or Hopf bifurcation [11-15]. While the period doubling route to chaos has been observed in virtually all drives operating with simple proportional control, the Neimark-Sacker bifurcation had been observed when a more practical proportional integral controller was employed. Also, the complex phenomena of co-existing attractors and fractal basin boundaries were observed in full-bridge converter DC drives operating within certain parameter ranges.

Since the desire of most electrical engineers is to maintain the system within the nominal period-1 behaviour, there is a need for thorough understanding of the mechanism through which this nominal orbit loses stability. One common approach for performing the stability analysis of the periodic orbit in switched mode power electronic (SMPE) systems including the electrical drives is to discard the switching details and retain only the average dynamics of the system. This is known as the averaging technique [16, 17]. This technique produces a model that can be easily analysed using several tools available from linear control theory, but is not suitable for detecting fast-scale instabilities that occur at the PWM frequency [18]. Also the state space averaging technique works well only within specific system topological configuration and parameter limits [19]. Consequently, a model based on the averaging technique will not be able to detect the subharmonics and chaotic dynamics of the state variables that could occur in SMPE systems.

In order to overcome the limitations of the averaging technique and also to obtain more information on the evolution of the state variables in SMPE systems, Deane and Hamill [5] introduced the Poincaré map based analytical technique. In this technique, the states of the system are sampled in synchronism with the PWM frequency to obtain a discrete time map of the form $\mathbf{X}_n=f(\mathbf{X}_{n-1})$. Once the nonlinear map is obtained, the stability of the system can be determined by evaluating the eigenvalues of the Jacobian matrix of the map at the fixed points. To date, the Poincaré map method has been the most widely used approach for performing the stability analysis of periodic orbits in SMPE systems. It has been successfully employed in the stability analysis of DC-DC converters [20, 21] and permanent magnet DC drives employing a simple DC chopper [7]. But for some higher order DC-DC converters and some electrical drives, this map cannot be derived in closed form due to the transcendental form of the equations involved.

In this project, an alternative analysis technique based on Filippov's method of differential inclusion [22] is adopted. This approach is referred to as the Monodromy matrix (MM) approach and is suitable for the stability analysis of both closed and non-closed orbits. The key idea is to obtain the state transition matrix (STM) around the nominal orbit (known as the Monodromy matrix) and obtain its eigenvalues (known as the Floquet multipliers). The nominal orbit is stable if the absolute value of the Floquet multipliers is within the unit circle and unstable otherwise. Since the nominal orbits of most SMPE systems are usually non-smooth, the STM at the switching manifold (known as the Saltation matrix) must also be taken into account in computing the MM. The MM approach has been successfully applied in the stability analysis of periodic orbits in both low order and high order DC-DC converters [23, 24]. This work represents its first application in electrical drive systems.

The stabilisation of the nonlinear dynamical phenomena (namely bifurcations and chaos) which occur in piecewise smooth systems such as electrical drives is of key interest to researchers in nonlinear dynamics. One approach proposed by Ott et. al. [25]is to locate and target the infinite unstable periodic orbit (UPO) embedded in the chaotic attractor. This technique was demonstrated in power electronic buck converter and boost converter circuit by Banerjee et. al. [26-28]. But this method has been found to be complex and has high sensitivity to noise. An interesting feature of the MM technique is the ease with which it can be applied in the stabilisation of the nonlinear phenomena. This could be achieved by manipulation of the Saltation matrix of the system and is well illustrated in this project. Thus the overall goal of the project is to analyse the nonlinear phenomena in some common electrical drive systems (namely *permanent magnet dc* (PMDC) *drives*, *series connected dc* (SCDC) *drives* and *switched reluctance motor* (SRM) *drives*) using the Monodromy matrix approach and to develop an efficient controller based on the Saltation matrix to stabilise the observed phenomena.

1.2 Analysis of Nonlinear Phenomena in Switched Mode Power Electronic Systems

The two most common SMPE systems are power converters (DC-DC and DC-AC) and electrical drive systems. The basic operation of these systems involve toggling between different sets of circuit topologies under the control of a feedback law [18]. Under closed loop control, the PWM duty ratio (*d*) is adjusted continuously thus making the entire closed loop system nonlinear. In this section, a brief overview will be given of past reports on the analysis of nonlinear phenomena in SMPE systems.

1.2.1 Analysis of Nonlinear Phenomena in Power Converters

The occurrence of nonlinear bifurcation and chaotic phenomena in SMPE systems were reported in DC-DC converters earlier than in electrical drives. In 1984, Brockett and Wood [29] reported that a DC-DC buck converter can exhibit nonlinear bifurcations and chaotic phenomena. The first detailed study of these nonlinear phenomena in DC-DC converter was conducted in 1988 by Hamill and Jefferies [30] . They showed for the first time that the concept of the iterative nonlinear map can be employed in the study of nonlinear phenomena in a first order DC-DC buck converter with wide band feedback control. Two years later (1990), Deane and Hamill [31], validated experimentally the initial analysis and simulation report of bifurcation and chaos in DC-DC converter using both first-order and second-order buck converters as example systems. Later, in 1992, Hamill, Deane and Jefferies [32] carried out further investigations on the nonlinear phenomena in a DC-DC buck converter by using both iterative maps and Lyapunov exponent computations, and the results were also experimentally validated.

The success of the trio (Dean, Hamill and Jefferies) in the analysis of the nonlinear phenomena in DC-DC buck converters stimulated much interest in the investigation of the nonlinear phenomena in other power converters. Further research and experimental validation of the nonlinear phenomena in buck converter [26, 33, 34], boost converters [13, 27, 35, 36], buck-boost [37, 38], Cuk converters [39, 40], and DC-AC inverter [41, 42] have been reported in literature.

1.2.2 Analysis of Nonlinear Phenomena in Electrical Drives

The success of the initial research on nonlinear phenomena in simple DC-DC buck converters stimulated research in other SMPE systems especially the electrical drives. Research on nonlinear bifurcation and chaotic phenomena in electrical drives started with AC drives in the pioneering work conducted in 1989 by Kuroe *et. al.* [43] in inverter-fed induction motor drive systems. Using the Poincaré map approach they analysed the period doubling bifurcation in a three-phase inverter-fed induction drive system employing V/F control. In 1994, Nagy [44] studied the bifurcation and chaotic phenomena in tolerance-band based current controlled induction motor drives. Also in 1994 Hemati [45] reported the strange attractors in a permanent magnet blushless DC drive system by transforming the drives mathematical model into a Lorenz system. In 1997, Chau *et al*. [7] investigated the bifurcation and chaotic phenomena in a simple DC drive using the proportional gain and the supply voltage as bifurcation parameters. Also in 1997, Chau *et al*. [46] investigated the subharmonics and chaotic phenomena in both voltage mode and current mode controlled DC drives. In 1999, Chau *et al*. [47] extended the nonlinear analysis to switched reluctance motor drives.

Later in 2000, Suto *et al*. [48] reported the period adding route to chaos in a hysteresis current controlled AC drive. In 2002, Li *et al*. [49] investigated the chaotic behaviour in a permanent magnet synchronous motor (PMSM) by reducing the system model to a Lorentz system. The paper looked at three different cases in which the trajectories of the state variables of the PMSM can approach an equilibrium point, a limit cycle or a chaotic attractor at steady state. In 2004, Gao *et al*. [50] reported the occurrence of a Hopf bifurcation and chaos in a synchronous reluctance drive. The paper showed that at some parameters of the drive, the attracting equilibrium point may lose stability and the trajectories begin to converge on a limit cycle. Further variation of the parameter caused the trajectories to depart from the limit cycle and converge on a strange or chaotic attractor. In 2009, Dai *et al*. [12] reported the Hopf bifurcation and chaos resulting from torus break down in a simple DC drive employing a PI controller. The phenomena of phase locking and period adding were also discussed in this paper.

1.3 Control of Nonlinear Phenomena in Electric Drives

These sub-harmonic and chaotic behaviours in electrical drive systems are viewed as undesirable by most engineers and some work has been conducted on how to stabilise such systems. Some common stabilization technique that have been tested on electrical drive are the Pyragas time delayed approach [51, 52], artificial intelligence techniques, nonlinear feedback, sliding mode and adaptive back-stepping. In 2000, Chen *et al*. [53] employed time-delayed feedback approach to stabilise the chaotic dynamics in an experimental DC drive. Also in 2000, Asakura *et al*. [54] employed neural networks to stabilize the chaotic dynamics of an induction drive system. Nonlinear feedback control [55], sliding mode control [56] and adaptive back-stepping control [57] have all been applied to the stabilization of chaos in a permanent magnet synchronous motor (PMSM). In this project, the nonlinear sub-harmonic and chaotic phenomena in the steady state trajectories of electrical drives were stabilised by manipulating the Saltation matrix component of the Monodromy matrix. This technique is less complex than existing methods and was successfully applied in stabilising the subharmonics and chaos in PMDC Drives, SCDC drives and SRM drives.

1.4 Objectives of the Nonlinear Analysis of Electrical Drives

The qualitative behaviour of all nonlinear systems including electrical drives often changes when some of the system parameters are being varied. Some of the needs for a thorough nonlinear analysis of drives are:

a. To help designers predict the dynamic behaviour as the system parameters are being varied.
b. To help designers in setting the operational parameter limits of the drives. For instance at some range of the system parameters the steady state behaviour will be the nominal period-T orbit, while at some other ranges the steady state trajectory will be either of period-nT, quasi-periodic or chaotic.
c. To develop methods to control the sub-harmonics and chaotic dynamics of the drives and thus extend the system parameter range for nominal period-T operation.

1.5 Contributions to Knowledge

The main contributions of this project are:

a. The first application of the Monodromy matrix approach in the analysis of the instability in steady state dynamics of electrical drives. Existing studies were all based on the Poincaré map technique.
b. The first analytical validation of the fast-scale bifurcation in a full-bridge converter PMDC drive. The existing report of the nonlinear phenomena in this drive is based on numerical simulation [58].
c. The first reporting of co-existing attractors and fractal basin boundaries in electrical drives.
d. The first application of the Monodromy matrix approach in the analysis of a fast-scale bifurcation in piecewise-smooth systems with nonlinear vector fields such as switched reluctance motor drives. Existing applications of this technique

were in piecewise-smooth systems with linear vector fields (such as DC-DC converters).

e. The first analytical validation of the fast-scale bifurcation in series connected DC drives.
f. The first experimental validation of Neimark-Sacker bifurcation in a dc chopper-fed DC drive operating with a PI controller.
g. The first application of the Saltation matrix manipulation technique in the control of fast scale instability and chaos in electrical drives.

1.6 Thesis layout

This thesis is structured as follows:

Chapter 2 gives background knowledge of complex dynamical phenomena in nonlinear system using examples from some popular physical systems. Some of the concepts discussed in this chapter will be applied throughout the thesis.

Chapter 3 gives an overview of electrical drives and their control techniques. A brief discussion of the various components of electrical drives is given. Also the various available power converter options and drives control strategies are discussed. The chapter is concluded with a brief review of the common modelling approaches for electric drives.

Chapter 4 presents the analysis of the nonlinear phenomena in an example piecewise linear electrical drives (namely DC chopper-fed PMDC Drives). The complex dynamical behaviour of the system when the simple proportional controller and the more practical proportional integral (PI) controller are employed is investigated. Also experimental validation of the observed phenomenon in the PI controlled drive was carried out using dsPIC30F3010 digital signal controller and details of the experimental set up is presented in Appendix A.

Chapter 5 gives an analysis of the steady state instabilities in three-phase SRM Drives. The chapter began with a brief overview of SRM operation followed by various SRM control strategies. Finally, a stability analysis of the period-1 orbit was carried out. Also, since this system is piecewise nonlinear, the state transition matrix (STM) along each vector fields in the periodic orbit was computed using matrix differential equations, instead of the simple exponential matrix applied in computing the STM in piecewise linear systems such as DC-DC converters and PMDC drives.

In Chapter 6, control of nonlinear sub-harmonics and chaotic phenomena in electrical drives are discussed. Three control options are discussed and applied to control the nonlinear phenomena in DC chopper PMDC Drives and SRM drives.

In Chapter 7, the nonlinear phenomena in SCDC drive is analysed and controlled using one of the control techniques discussed in Chapter 6. Also since this system is piecewise nonlinear, matrix differential equation was applied in computing the STM along each vector fields in the periodic orbit.

In Chapter 8, the analysis and control of nonlinear phenomena in a full-bridge converter PMDC drive is presented. Unlike the DC chopper-fed PMDC Drives, full-bridge converter PMDC drive can be used to achieve four quadrant operations.

Chapter 9 gives the conclusion of this study and suggestions for future work.

1.7 List of Publications

This project has led to the following publications:

[1] **Nelson Okafor**, Bashar Zahawi, Damian Giaouris and Soumitro Banerjee, “Chaos, Co-existing Attractors and Fractal Basin Boundary in DC Drives with Full-Bridge Converter ” *IEEE International Symposium on Circuits and Systems*, (ISCAS 2010), Paris, France, *May* 2010.

[2] **Nelson Okafor**, Bashar Zahawi, Damian Giaouris and Soumitro Banerjee, “Analysis of Fast-Scale Instability in DC Drives with Full-Bridge Converter using Filippov’s method” *IET Power Electronics Machine and Drives Conference (PEMD 2010), Brighton, UK, April 2010.*

CHAPTER 2

OVERVIEW OF NONLINEAR DYNAMICAL SYSTEMS

This chapter gives a general overview of nonlinear dynamical systems and the complex phenomena they exhibit. The concept of stability analysis of invariant sets will be discussed in detail. The background given here will be very useful when analysing the nonlinear behaviour of the various electrical drive systems discussed in later chapters.

2.1 Basic Ideas

Dynamics can be defined as a science of change [59] and dynamical systems are replete in nature. This includes the motion of the planets, the motion of fluids, the flow of current in electric circuit, the dissipation of heat in solids, the propagation and detection of seismic waves, and the increase and decrease of human or animal population [60]. Virtually all dynamic systems are composed of:

- A set of independent *state variables* which evolve with time and can be used to completely describe the behaviour of the system.
- A function which connects the rate of change of the state variables with the state variables themselves and other system inputs and parameters [18].

The time evolution of these state variables can be modelled by using either a *differential equation* or a *difference equation*, and such models are developed by applying some physical laws such as Newtons laws of motion, Kirchhoff's laws, Faradays laws etc. The block diagram of a typical dynamical system in state space representation is shown in Fig. 2.1

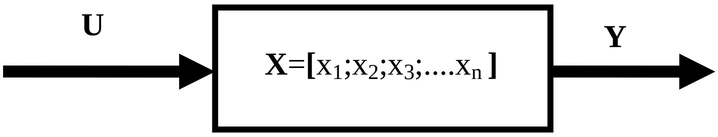

Fig. 2.1 Block diagram representation of a dynamical system

where **U** is a vector representation of all the possible external inputs to the system, **X** is the state vector containing the system state variables, and **Y** is the output vector containing all the possible system outputs. The state variables of a dynamical system are not necessarily the outputs of the system. Only measurable state variables are referred to as the system outputs and will depend on the number of available sensing devices [61].

2.2 Classifications of Dynamical systems

Dynamical systems can be classified using several criteria as discussed below:

2.2.1 Deterministic and Non-Deterministic Systems

Dynamical systems can be broadly classified as either deterministic or non-deterministic. A system is said to be deterministic if the future value of the state variables can be completely predicted once the initial or past states and other system parameters are known [62]. For instance, if the angular position ($\theta(t_0)$) of a simple pendulum at $t=t_0$ is known, then the position at any other time in the future ($\theta(\mathrm{t})$) should be predictable. Deterministic systems can be modelled using either ordinary differential equation or iterative maps depending on whether the state variables evolve in a continuous or discrete manner.

Similarly, systems whose behaviours are random in nature and cannot be easily predicted are referred to as non-deterministic or stochastic systems. A typical example of a non-deterministic system is the price of stocks in the stock market. Even if the price yesterday is known, the price today could be difficult to predict.

2.2.2 Continuous Time and Discrete Time Systems

Continuous time systems (CTS) are dynamical systems whose state variables evolve continuously with time. Continuous time systems are often modelled using ordinary differential equations of the form below [63].

$$\frac{d\mathbf{X}(t)}{dt} = \mathbf{f}(\mathbf{X}(t), t) \tag{2.1}$$

where $\mathbf{X}(t) = [x_1 \quad x_2 \quad \ldots\ldots\ldots \quad x_n]^T \in \mathbb{R}^n$ is the state vector, x_1, x_2... x_n are the state variables and the function $\mathbf{f}(\mathrm{X}(t),t)$ is the vector field. There are different possible solutions for a system of the form (2.1) depending on the initial values of the state variables. Such solutions (also referred to as the *flow* or *trajectory*) are used to predict future values of the state variables as $t \rightarrow \infty$. Assuming $\mathbf{X}(t_0) = \mathbf{X}_0$ is the initial state vector for system (2.1), the flow or solution will be expressed as $\mathbf{X}(t) = \varphi(t, t_0, \mathbf{X}_0)$. Such a solution can be evaluated analytically or numerically depending on whether the system is linear or nonlinear as discussed in section 2.2.3. Systems of the form (2.1) can be referred to as *autonomous* if the vector field does not depend on time and *non-autonomous* otherwise [60].

There are also dynamical systems where the state variables evolve in a discrete manner. Such systems are referred to as discrete time systems (DTS) and are often modelled using an *iterative map* or *difference equation* of the form below [62].

$$\mathbf{X}_{n+1} = \mathbf{f}(\mathbf{X}_n) \tag{2.2}$$

where n is an integer, $\mathbf{X}_n$ denotes the present state of the system, $\mathbf{X}_{n+1}$ denotes the state of the system at the next observation instant (hour, minute, second, etc.), and **f**(**X**) is the evolution rule that relates the present state to the next state.

2.2.3 Linear and Nonlinear Systems

Linear systems are dynamical systems in which the time evolution rules for the state variables are expressed as linear differential equations [60]. Such systems obey the principle of superposition [61] and a change in any of the system parameters causes only quantitative, but not qualitative change in the nature of the flow [10]. Linear systems usually have only one equilibrium point whose stability does not depend on the system parameter and they can be modelled using the *state equation* of the form (2.3) and *output equation* of the form (2.4) [61].

$$\frac{d\mathbf{X}(t)}{dt} = \mathbf{AX}(t) + \mathbf{BU}(t) \tag{2.3}$$

$$\mathbf{Y}(t) = \mathbf{CX}(t) + \mathbf{DU}(t) \tag{2.4}$$

where $\mathbf{X}(t) = [x_1 \quad x_2 \quad .... \quad x_n]^T \in \mathbb{R}^n$ is the state vector, $\mathbf{U} = [u_1 \ u_2 \mathbf{.....} u_m]^T$ is the input vector, $\mathbf{Y} = [y_1 \ y_2 \mathbf{.....} y_p]^T$ is the output vector, **A** is an ($n \times n$) state matrix, **B** is an ($n \times m$) input matrix, **C** is an ($p \times n$) output matrix and **D** is an ($p \times m$) feed forward matrix which is often zero in most systems.

Linear systems can be further classified as *linear time invariant* (LTI) and *linear time varying* (LTV) systems. If the parameters in the state matrix (**A**) vary with time, then the system will be referred to as LTV, but if the parameters in the state matrix remain constant over time, the system will be referred to as LTI. Also, if the input or external forcing function to the system is zero ($\mathbf{U}(t) = 0$), the system will be referred to as *homogenous*, and if ($\mathbf{U}(t) \neq 0$), the system will be referred to as *non-homogenous*. Linear systems usually have analytical solutions. Assuming $\mathbf{X}(t_0) = \mathbf{X}_0$ is the initial state for the non-homogenous LTI system (2.3), the solution $\mathbf{X}(t)$ can be expressed as $\mathbf{X}(t) = \varphi(t, t_0, \mathbf{X}_0) = e^{\mathbf{A}(t-t_0)}\mathbf{X}_0 + \int_{t_0}^{t} e^{\mathbf{A}(t-\lambda)}\mathbf{B}\mathbf{U}(\lambda)d\lambda$. Systems whose state equations cannot be expressed in the form (2.3) are considered as *nonlinear*. Precisely without exceptions, all systems in the real world are nonlinear at least to some extent. The evolution rule for the state variables in such systems are usually expressed as nonlinear differential equations. Unlike linear systems, nonlinear systems can only be solved using numerical techniques and are characterised by multiple equilibrium points. A small change in any of the system parameters can lead to sudden and dramatic changes in both the qualitative and quantitative behaviour of the system [10]. A very widely referred to nonlinear system is the Lotka-Volterra model of two competing species [9] which is expressed as

$$\frac{dx}{dt} = 3x - x^2 - 2xy$$
$$\frac{dy}{dt} = 2y - xy - y^2 \qquad (2.5)$$

where x and y represent the populations of the two species competing for the same food source or resources. The product terms (xy), and the square terms x^2 and y^2 make the system nonlinear.

2.2.4 Smooth and Non-smooth Systems

Dynamical systems can also be classified as either smooth or non-smooth. If the vector fields of the system (2.1) are differentiable everywhere in a given domain, the system will be referred to as smooth. On the other hand, a system is said to be non-smooth or piecewise smooth if it is described by differential equations with discontinuous right hand sides as shown below

$$\frac{d\mathbf{X}}{dt} = \mathbf{f}(\mathbf{X},t,\rho) = \begin{cases} f_1(\mathbf{X},t,\rho), & \textbf{for } \mathbf{X} \in \mathbf{R_1} \\ f_1(\mathbf{X},t,\rho), & \textbf{for } \mathbf{X} \in \mathbf{R}_2 \\ \cdot & \\ \cdot & \\ f_n(\mathbf{X},t,\rho), & \textbf{for } \mathbf{X} \in \mathbf{R_n} \end{cases} \tag{2.6}$$

where $\mathbf{R}_1$, $\mathbf{R}_2$,...$\mathbf{R}_n$ are different regions of the state space, separated by (n-1) dimensional surfaces given by algebraic equation of the form $\Gamma_n(X) = 0$ called switching manifolds. Systems of the form (2.6) are also referred to as Filippov's type systems [22, 23]. If the separate vector fields are linear, the system will be referred to as a *piecewise linear* system, and if the vector fields are nonlinear, the system will be referred to as a *piecewise nonlinear* system. Filippov type systems have very interesting practical applications. Typical examples include mechanical systems with dry friction, impact, and back lash, and switched mode power electronic systems including electrical drives.

2.3 The Concept of Invariant Sets

Consider the general equation (2.1) in $D \subset \mathbb{R}^n$. The set $M \subset D$ is invariant if the solution X(t) with $X(0) \in M$ is contained in M for $-\infty < t < +\infty$. If this property is valid only for $t \geq 0$, then M is called a positive invariant set, whereas if the property is valid for $t \leq 0$, then M is called a negative invariant set [63]. Invariant sets represent constant solution of the dynamical system and any solution that start on the invariant set always remain there forever. Typical examples of invariant sets are *equilibrium points*, *periodic orbit*, *quasi-periodic orbits*, and *chaotic orbits*. Invariant sets play a vital role in the overall behaviour of the system as system stability depends on the stability of the invariant set. Stable invariant sets can attract trajectories of nearby initial points and are referred to as *attractors* or *sinks* while unstable invariant sets repel trajectories of nearby initial points and are known as *repellers* or *sources* [10]. Some invariants sets in nonlinear dynamical systems are briefly discussed in the following subsections, while the stability analysis of invariant sets is discussed in sections 2.4 and 2.5.

2.3.1 Equilibrium Points

An equilibrium point (EP), also known as a *critical point* or *fixed point* (FP) is used to indicate the equilibrium or constant solution of a dynamical system. Assuming the initial state of the system is $\mathbf{X}_0 = \mathbf{X}^*$, then $\mathbf{X}(t) = \mathbf{X}^*$ for all time where $\mathbf{X}^*$ is the EP

[9]. For continuous type systems of the form (2.1), the EP occurs when $\mathbf{f}(\mathbf{X}^*) = 0$, where $\mathbf{f}(\mathbf{X}(t))$ is the vector field, while for a discrete type system or iterative map of the form (2.2) the fixed point occurs when $\mathbf{f}(\mathbf{X}^*) = \mathbf{X}^*$. While linear systems often have only one EP, nonlinear systems are characterised by multiple equilibrium points whose stability depends on the system parameters. For instance the competing species model (2.5) which is nonlinear have four equilibrium points at (0,0), (0,2), (3,0) and (1,1) [60]. All trajectories starting from an equilibrium point will remain there. The stability analysis of EPs is discussed in section 2.4.

2.3.2 Periodic Orbits

Another common steady state behaviour in higher order nonlinear systems (second order and above) is the periodic orbit or limit cycle. Suppose that $\mathbf{X}(t) = \phi(t)$ is a solution of the equation (2.1) and $\mathbf{X}(t) \in D \subset \mathbb{R}^n$ and suppose there exists a positive number *T* such that $\phi(t+T) = \phi(t)$ for all $t \in \mathbb{R}$, then $\phi(t)$ is called a periodic solution or periodic orbit of period *T* [63]. Since the value of the state variables are repeated every time period *T*, periodic solutions produce a closed trajectory or orbit in the state space. An isolated closed trajectory in the state space which other non-closed trajectories spiral either towards or away from as $t \to \infty$ is known as a *limit cycle* [9, 60].

2.3.3 Quasi-periodic Orbits

Another steady state behaviour that could occur in high order nonlinear dynamical systems is the quasi-periodic orbit. The steady state behaviour is said to be quasi-periodic if the trajectories move on the surface of a *torus*. This motion is often associated with two sets of frequencies that are related to one another by an irrational ratio [10, 18]. Quasi-periodic behaviour have been reported in the boost converter [13], Cúk converter [40] and in DC drives employing the proportional integral (PI) controller [12].

2.4 Stability Analysis of Equilibium Points

An EP can be said to be stable if it attracts the trajectories of nearby initial points and unstable otherwise. For linear systems of the form (2.3), the stability of the EP can be evaluated simply by obtaining the *eigenvalues* (λ) of the state matrix (**A**) or by finding the roots of the characteristic equation of the transfer function, while in nonlinear systems the stability analysis of EP can be performed by adding a small perturbation to the original system near the EP and then observing if the perturbation grows or shrinks over time. If the perturbation shrinks to zero as $t \to \infty$ then the EP is said to be *asymptotically stable*, but if the perturbation grows infinitely, then the EP will be said to be *unstable*. Assuming an autonomous nonlinear system of the form $\dot{\mathbf{X}}(t) = \mathbf{f}(\mathbf{X}(t))$ is perturbed near its EP ($\mathbf{X}^*$), then an *approximate linear system* of the form (2.7) will be obtained.

$$\frac{d\mathbf{P}(t)}{dt} = \mathbf{J}(\mathbf{X}^*)\mathbf{P}(t) \tag{2.7}$$

where $\mathbf{P}(t) = \mathbf{X}(t) - \mathbf{X}^*$ is a measure of the perturbation near the EP ($\mathbf{X}^*$), and $\mathbf{J}(\mathbf{X}^*)$ is the Jacobian matrix (2.8) of the system evaluated at the EP.

$$\mathbf{J}(\mathbf{X}(t)) = \begin{pmatrix} \frac{\partial f_1}{\partial x_1} & \frac{\partial f_1}{\partial x_2} & . & . & \frac{\partial f_1}{\partial x_n} \\ \frac{\partial f_2}{\partial x_1} & \frac{\partial f_2}{\partial x_2} & . & . & \frac{\partial f_2}{\partial x_n} \\ . & . & . & . & . \\ . & . & . & . & . \\ \frac{\partial f_n}{\partial x_1} & \frac{\partial f_n}{\partial x_2} & . & . & \frac{\partial f_n}{\partial x_n} \end{pmatrix} \tag{2.8}$$

The stability of the EP will depend on the eigenvalues (λ_1, λ_2, λ_3,.... λ_n) of $\mathbf{J}(\mathbf{X}^*)$ obtained by solving the characteristic equation $\det(\mathbf{J}(\mathbf{X}^*)-\mathbf{I}\boldsymbol{\lambda})=0$. For LTI system of the form (2.3), the Jacobian matrix is the same as the state matrix (**A**). The above linearization technique is suitable for studying the local behaviour of trajectories near the EP. For first order nonlinear systems of the form $\dot{x}(t) = f(x(t))$, the characteristic value or the eigenvalues can be simply obtained by evaluating the derivative of $f(x(t))$ with respect to $x(t)$ at the EP.

$$\lambda = \left.\frac{df(x)}{dx}\right|_{\mathbf{x}=\mathbf{x}^*} \tag{2.9}$$

If $\lambda<0$ the EP will be stable and will be referred to as *node* or *sink*, but if $\lambda>0$, then the EP will be unstable and will be referred to as a *repeller* or *source*.

2.5 Stability Analysis of Periodic Orbits

The stability analysis of periodic orbits or *limit cycles* is necessary as this steady state behaviour is common in practical systems such as SMPE systems including electrical drives. A periodic orbit of period (T) can lose stability as system parameters are varied and orbits of period (nT), quasi-periodic or chaotic orbits may emerge. If all the trajectories that start near the *limit cycle* (both inside and outside) spiral towards it as $t \to \infty$, then the *limit cycle* is said to be *asymptotically stable* [60] . If trajectories on one side spirals towards the limit cycle, while those on the other side spiral away as $t \to \infty$ then the limit cycle is said to be *semi-stable*. But, if the trajectories on both sides of the limit cycle spiral away as $t \to \infty$, then the limit cycle is said to be *unstable*. If nearby trajectories neither converges, nor departs from the *limit cycle*, then the limit cycle is said to be *stable*. The two common techniques for performing the stability analysis of limit cycles are the Poincaré map approach and the Floquet theory.

2.5.1 Poincaré Map Techniques

The Poincaré map technique is the most common method for performing the stability analysis of limit cycles. The idea is to reduce a continuous time dynamical systems into a discrete time system or a differential equation into a difference equation (*iterative map*). Once, the iterative map corresponding to the differential equation is derived, the stability of the periodic orbit of the continuous time system can be ascertained by analysing the stability of the fixed point of the iterative map [4, 62, 64]. If the fixed point is stable then the periodic orbit is stable and vice-versa.

Assuming that the trajectory of the state variables in a general non-autonomous nonlinear system $\dot{\mathbf{X}}(t) = \mathbf{f}(\mathbf{X}(t), t)$,$\mathbf{X}(t_0)$=$\mathbf{X}_0$) is a periodic orbit described by

$$\mathbf{X}(t) = \varphi(t, t_0, \mathbf{X}_0) = \mathbf{X_0} + \int_{t_0}^{t} f(\varphi(\tau, t_0, \mathbf{X}_0), \tau) d\tau \qquad (2.10)$$

then the iterative map equivalent of the continuous system can be obtained by placing a Poincaré section of order n-1(Fig. 2.2) in the state space or by sampling the states at every periodic interval (t=t_0+nT) where T is the period and n =0,1,2,..∞ [9, 10]. The state vector after the time interval (T) ($\mathbf{X}(T+t_0)$) can be expressed as a function of the initial state vector ($\mathbf{X}_0$) as follows

$$\mathbf{X}(T+t_0)=\varphi(T+t_0,t_0,\mathbf{X}_0)=\mathbf{X_0}+\int_{t_0}^{T+t_0} f(\varphi(\tau,t_0,\mathbf{X}_0),\tau)d\tau \tag{2.11}$$

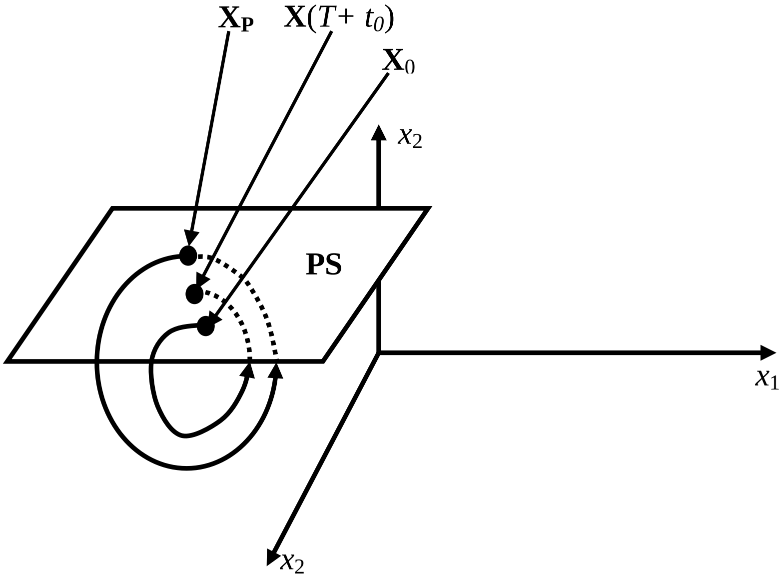

Fig. 2.2 Poincaré section (**PS**) for a simple 3rd order system.

Equation (2.11) can be generalised to an iterative map of the form (2.12) where $\mathbf{X_n}$ is the present state and $\mathbf{X_{n+1}}$ is the state of the system after the periodic interval (T).

$$\mathbf{X_{n+1}}=P(\mathbf{X_n})=\mathbf{X_n}+\int_{t_0}^{T+t_0} f(\varphi(\tau,t_0,\mathbf{X_n}),\tau)d\tau \tag{2.12}$$

At the fixed point of the iterative map, we have $P(\mathbf{X}_p)=\mathbf{X}_p$. Consequently,

$$\mathbf{X_P}+\int_{t_0}^{T+t_0} f(\varphi(\tau,t_0,\mathbf{X_P}),\tau)d\tau=\mathbf{X_P} \tag{2.13}$$

and

$$\int_{t_0}^{T+t_0} f(\varphi(\tau,t_0,\mathbf{X_P}),\tau)d\tau=0 \tag{2.14}$$

The fixed point of the map ($\mathbf{X_P}$) can be obtained by solving equation (2.14) numerically. To analyse the stability of the periodic orbit we need to analyse the stability of the fixed point of the map ($\mathbf{X_P}$). Since the iterative map (2.12) is a nonlinear map, the stability analysis of its fixed point will be achieved by evaluating the Jacobian matrix of the map $\left(\frac{\partial P(\mathbf{X_n})}{\partial \mathbf{X_n}}\right)$ at the fixed point and then obtaining its eigenvalues. The fixed point ($\mathbf{X_P}$) and thus the periodic orbit is stable if the absolute values of the eigenvalues are within the unit circle and unstable otherwise. The Poincaré map technique thus involves four key steps as outlined below:

- Convert the continuous time system to a discrete time system by deriving a nonlinear iterative map equivalent of the original differential equation.
- Obtain the fixed point of the map.
- Obtain the Jacobian matrix of the map and evaluate it at the fixed point.
- Obtain the eigenvalues of the Jacobian matrix.

The key limitation of this technique is that it may be difficult to derive the iterative map in closed form in some systems [23].

2.5.2 Floquet Theory

In the Poincaré map approach the orbital stability was deduced by transforming the continuous time system into a discrete time system (an iterative map) and the periodic orbit into a fixed point and thereafter linearizing the system around the fixed point. In Floquet theory the orbital stability is deduced by linearizing the system around the periodic orbit. The periodic orbit is first given an initial perturbation and the evolution of the perturbation is evaluated using the fundamental solution matrix or state transition matrix (STM).The STM is obtained by integrating the initial value problem of the variational equation [65]. Floquet theory is suitable for the stability analysis of both smooth and non-smooth orbits. The variational equation and the derivation of the STM will be discussed in section 2.5.2.1, while the application of the STM in the stability analysis of both smooth and non-smooth orbits will be discussed in sections 2.5.2.2 and 2.5.2.3, respectively.

2.5.2.1 *Variational Equation*

Assuming $\dot{\mathbf{X}}(t) = f(t, \mathbf{X}(t)),\ \mathbf{X}(t) \in \Re^n$ is the model of a general non-automous nonlinear dynamical system whose initial state vector is $\mathbf{X}(t_0) = \mathbf{X_0}$. Then the solution or the trajectory of the state varaibles in state space can be described by the function $\mathbf{X}(t) = \varphi(t, t_0, \mathbf{X}_0)$. By taking a time derivative of the solution we have the expression:

$$\frac{d\varphi(t, t_0, \mathbf{X}_0)}{dt} = f\left(t, \varphi(t, t_0, \mathbf{X}_0)\right), \qquad \varphi(t_0, t_0, \mathbf{X}_0) = \mathbf{X_0} \tag{2.15}$$

Then by taking partial derivative of (2.15) with respect to the initial state vector $\mathbf{X_0}$ we have the equation:

$$\frac{\partial\left(\dfrac{d\varphi(t,t_0,\mathbf{X}_0)}{dt}\right)}{\partial\mathbf{X}_0}=\frac{\partial f\left(t,\varphi(t,t_0,\mathbf{X}_0)\right)}{\partial\mathbf{X}}\times\frac{\partial\varphi(t,t_0,\mathbf{X}_0)}{\partial\mathbf{X}_0},\qquad\frac{\partial\varphi(t_0,t_0,\mathbf{X}_0)}{\partial\mathbf{X}_0}=\mathbf{I}_{n\times n}\tag{2.16}$$

The partial derivative of the solution with respect to the initial condition $\frac{\partial\varphi(t,t_0,\mathbf{X}_0)}{\partial\mathbf{X}_0}$ is known as the STM and is used to describe the time evolution of the state variables or the perturbation from $t= t_0$ to any other time (t) in the future. The STM can be abridged to $\Phi(t,t_0,\mathbf{X}_0)$.

Consequently, equation (2.16) can be re-arranged in the form below

$$\frac{d\Phi(t,t_0,\mathbf{X}_0)}{dt}=\frac{\partial f\left(t,\varphi(t,t_0,\mathbf{X}_0)\right)}{\partial\mathbf{X}}\times\Phi(t,t_0,\mathbf{X}_0),\qquad\Phi(t_0,t_0,\mathbf{X}_0)=\mathbf{I}_{n\times n}\tag{2.17}$$

The matrix differential equation (2.17) is known as the variational equation [65] and can be solved to obtain the STM. For simple LTI systems of the form (2.3) the STM ($\Phi(t,t_0,\mathbf{X}_0)$) can be obtained by solving an exponential matrix of the form ($e^{\mathbf{A}(t-t_0)}$), but for general non-autonomous systems of the form (2.1) the STM could be obtained by solving the matrix differential equation (2.17).

2.5.2.2 *Stability Analysis of Smooth Orbits*

Smooth and non-smooth dynamical systems were earlier discussed in section 2.2.4. In this section the stability analysis of a smooth periodic orbit using Floquet theory will be discussed. *As*suming the steady state trajectory of a smooth nonlinear dynamical systems $\dot{\mathbf{X}}(t)= f(t,\mathbf{X}(t)),\ \mathbf{X}(t)\in R^n$ is a periodic orbit of the form $\mathbf{X}_{\mathbf{ss}}(t)=\varphi(t,t_0,\mathbf{X}_0)$ where $\mathbf{X_0}$ is the initial condition. To analyse the stability of this orbit using Floquet theory, the system will be given an initial small perturbation (Fig. 2.3) and the difference between the original and perturbed trajectories after some time interval (T) corresponding to the period of the original orbit will be ascertained using the fundamental solution matrix.

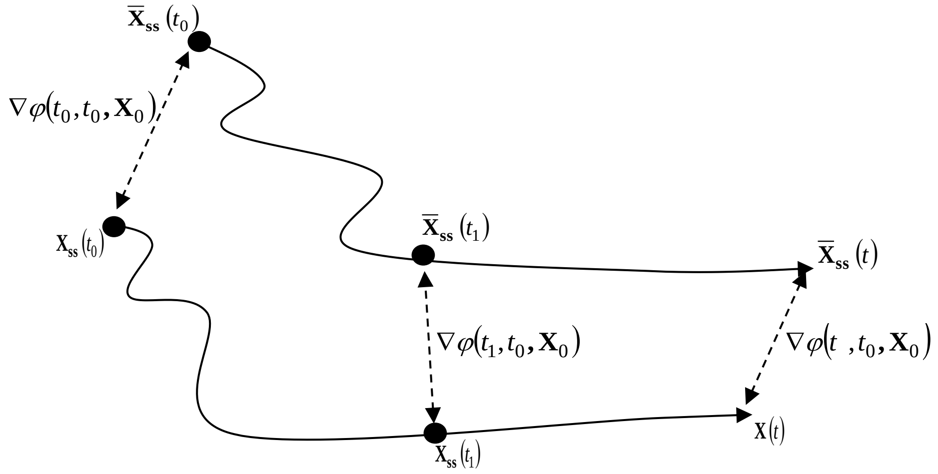

Fig. 2.3 Time evolution of a perturbation for a smooth dynamical system

If $\mathbf{X}_{\mathbf{ss}}(t_0)=\mathbf{X}_\mathbf{0}=\varphi(t_0,t_0,\mathbf{X}_0)$ is the initial state vector of the original orbit and $\overline{\mathbf{X}}_{\mathbf{ss}}(t_0)=\overline{\mathbf{X}}_\mathbf{0}=\varphi(t_0,t_0,\mathbf{X}_0+p(t_0))$ is a nearby initial point, then the initial perturbation ($p(t_0)$) will be expressed as (2.18), and the perturabtion at any time (t) will be expressed as (2.19).

$$p(t_0)=\varphi(t_0,t_0,\mathbf{X}_0+p(t_0))-\varphi(t_0,t_0,\mathbf{X}_0)=\nabla\varphi(t_0,t_0,\mathbf{X}_0) \tag{2.18}$$

$$p(t)=\nabla\varphi(t,t_0,\mathbf{X}_0)=\varphi(t\ ,t_0,\mathbf{X}_0+p(t_0))-\varphi(t,t_0,\mathbf{X}_0) \tag{2.19}$$

where $\overline{\mathbf{X}}_{\mathbf{ss}}(t)=\varphi(t,t_0,\mathbf{X}_0+p(t_0))$ is the perturbed trajectory and $\varphi(t,t_0,\mathbf{X}_0)$ is the original periodic orbit.The time evolution of the perturbation can be evaluated by using a linearization techinque such as the Taylor series around the periodic orbit as shown in (2.20) with the higher order terms being ignored.

$$\begin{aligned}\frac{dp(t)}{dt}&=\left.\frac{\partial f(\mathbf{X}(t),t)}{\partial \mathbf{X}}\right|_{X(t)=X_{ss}(t)} p(t\ )\\ &=A(\mathbf{X}_{ss}(t),t)\times p(t_0)\end{aligned} \tag{2.20}$$

Equation (2.20) is a simple homogenous linear time varying model with $\frac{\partial f(\mathbf{X}(t),t)}{\partial \mathbf{X}}=A(\mathbf{X}_{ss}(t),t)$ as the state matrix. The stability of the periodic orbit depends on the stability of this simple linear system and could be deduced by finding the eigenvalue of the state matrix $A(\mathbf{X}_{ss}(t),t)$. But, unfortunately $A(\mathbf{X}_{ss}(t),t)$ is a function of time and its eigenvalue cannot be easily ascertained. An alternative way of solving (2.20) is through the use of the fundamental solution matrix or the state transition matrix (STM)

$\Phi(t,t_0,\mathbf{X}_0)$ which has already been derived in section 2.5.2.1. By applying the STM, the time evolution of the perturbation will be expressed as

$$p(t)=\nabla\varphi(t,t_0,\mathbf{X}_0)=\Phi(t,t_0,\mathbf{X}_0)\times p(t_0) \tag{2.21}$$

If the orbit is periodic then the perturbation after some time interval *T*, $\left(p(t_0+T)=\Phi(t_0+T,t_0,\mathbf{X}_0)\times p(t_0)\right)$ will need to be evaluated to compute its stability, where *T* is the period of the orbit and $\Phi(t_0+T,t_0,\mathbf{X}_0)$is the state transition matrix around the orbit known as the *Monodromy matrix*. The stability of this orbit depends on the eigenvalue of the Monodromy matrix (also known as *Floquet multipliers*). The periodic orbit is stable if the absolute value of the Floquet multipliers is within the unit circle and unstable otherwise. The Monodromy matrix is thus the same as the Jacobian matrix of the *Poincaré* Map evaluated at the fixed point.

An interesting property of the STM is that if the evolution of the perturbation from the initial time (t_0) to any time (t) in the future is broken into smaller intervals (as shown in Fig. 2.3) then the total STM from t_0 to t is the product of the state transition matrices of each interval. This property is known as the *transition property* of the STM and is illustrated in the following equation:

$$\begin{aligned}\nabla\varphi(t,t_0,\mathbf{X}_0)&=\Phi(t,t_0,\mathbf{X}_0)\times p(t_0)\\&=\Phi(t,t_1,\mathbf{X}_1)\times\Phi(t_1,t_0,\mathbf{X}_0)\times p(t_0)\end{aligned} \tag{2.22}$$

where $\mathrm{X}_{ss}(t_0)=\mathrm{X}_0$ and $\mathrm{X}_{ss}(t_1)=\mathrm{X}_1$.

The transition property of STM is very useful in performing the stability analysis of non-smooth orbit where the STM along the different vector fields that make up the orbit are to be computed separately. Assuming Fig. 2.4 is an arbitrary periodic orbit produced by a smooth 3rd order nonlinear dynamical system of the form $\dot{\mathbf{X}}(t)=f(\mathbf{X}(t),t,\beta)$, $\mathbf{X}(t)\in R^3$ then the stability of this orbit as a system parameter such as β is varied can be determined simply by deriving the Monodromy matrix (2.23) and obtaining its eigenvalues.

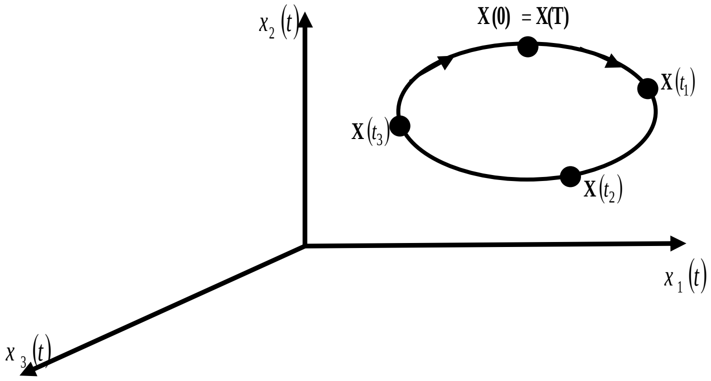

Fig. 2.4 Arbitrary periodic orbit of a smooth 3rd order nonlinear system

$$M(T,0) = \Phi(T,t_3) \times \Phi(t_3,t_2) \times \Phi(t_2,t_1) \times \Phi(t_1,0) \tag{2.23}$$

where $\Phi(t_B, t_A)$ is the state transition matrix from $t=t_A$ to $t=t_B$ and $M(T,0)$ is the state transition matrix round the arbitrary periodic orbit known as the *Monodromy matrix*. The state transition matrices $\Phi(t_B, t_A)$ are evaluated by solving matrix differential equations of the form (2.17).

2.5.2.3 *Stability Analysis of Non-Smooth Orbits*

The evolution of the state variables in non-smooth systems is often characterized by sharp bends and twists as the trajectory moves from one region of the state space to another thereby making the orbit non-smooth. The stability analysis of non-smooth orbits is necessary as such orbits are commonly encountered in switched mode power electronic systems including electrical drives. The procedure for performing the stability analysis of a non-smooth orbit is similar to that employed for the smooth orbit, but in this case the state transition matrix at the switching manifold (known as the *Saltation* or *jump* or *updating matrix* [65] [66]) must also be taken into consideration. The need for considering the Saltation matrix will be obvious if the time evolution of the perturbation of a non-smooth trajectory is considered. Assuming (2.24) defines a non-smooth system with two vector fields $f_1(\mathbf{X}, t, \rho)$ and $f_2(\mathbf{X}, t, \rho)$.

$$\frac{d\mathbf{X}}{dt} = \mathbf{f}(\mathbf{X}, t, \rho) = \begin{cases} f_1(\mathbf{X}, t, \rho), & \textbf{for } \mathbf{X} \in \mathbf{R}_- \\ \\ f_2(\mathbf{X}, t, \rho), & \textbf{for } \mathbf{X} \in \mathbf{R}_+ \end{cases} \tag{2.24}$$

where $f_1(\mathbf{X},t,\rho)$ is the vector field that governs the evolution of the state variables in region $\mathbf{R}_-$ of the state space, and $f_2(\mathbf{X},t,\rho)$ is the vector field that govern the evolution of the state variables in region $\mathbf{R}_+$ of the state space. The concept of solution for this type of system is defined by Filippov's method of differential inclusions [22]. Assuming the two regions are separated by a switching manifold $h(\mathbf{X}(t),t)$ such that:

$$\begin{aligned} &h(\mathbf{X}(t),t) < 0, \mathbf{X}(t) \in \mathbf{R_1} \\ &h(\mathbf{X}(t),t) > 0, \mathbf{X}(t) \in \mathbf{R_2} \\ &h(\mathbf{X}(t),t) = 0, \mathbf{X}(t) \in \Sigma \end{aligned} \tag{2.25}$$

where Σ is the switching hypersurface. If $\mathbf{X}(t_0) = \mathbf{X_0} = \varphi(t_0, t_0, \mathbf{X}_0)$ is the initial state vector of the original orbit and $\overline{\mathbf{X}}(t_0) = \overline{\mathbf{X}}_\mathbf{0} = \varphi(t_0, t_0, \mathbf{X}_0 + p(t_0))$ is the initial point when a small perturbation (p(t$_0$)) is applied (Fig. 2.5). To obtain the perturbation (p(t)) at future time (t), we need to compute the STM along the trajectory from the initial time (t_0) to time (t). For smooth systems (2.21) (p(t)) is given by $p(t) = \nabla\varphi(t, t_0, \mathbf{X}_0) = \Phi(t, t_0, \mathbf{X}_0) \times p(t_0)$ where $\Phi(t, t_0, \mathbf{X}_0)$ is the STM from the start time (t_0) to time (t) and is obtained by solving a matrix differential equation of the form (2.16). But, for a non-smooth system it could be seen from Fig. 2.5 that the perturbed trajectory and the original trajectory may hit the switching surface at different times and the vector field is discontinuous at the switching surface.

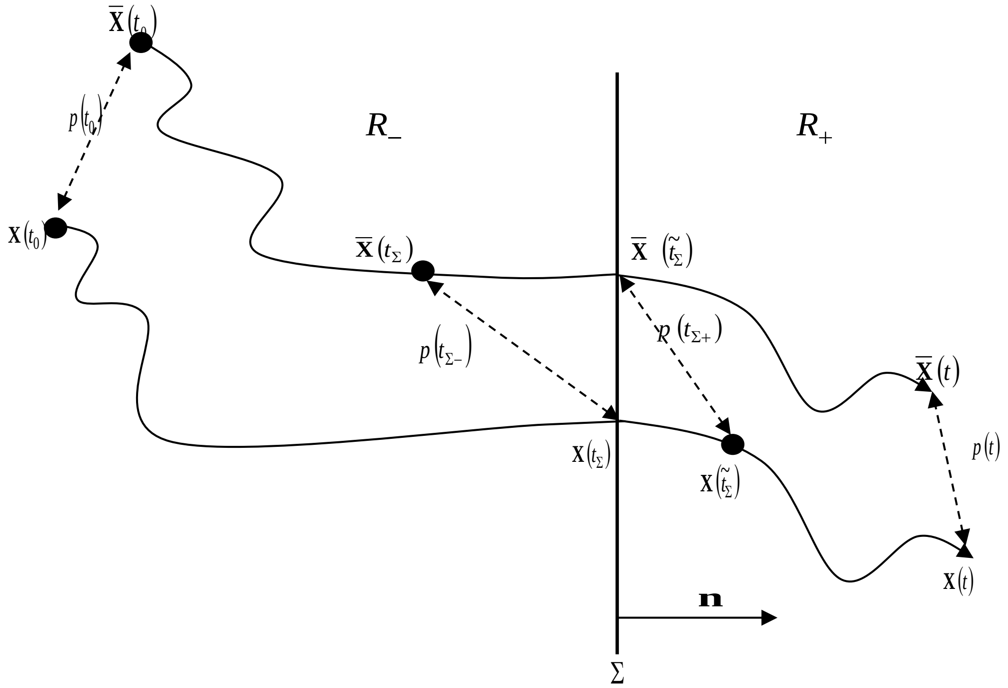

Fig. 2.5 Time evolution of a perturbation for a non-smooth dynamical system

Consequently, the STM will be discontinuous at the switching instant. Hence, there is a need for the *Saltation matrix* which relates the perturbation vector before the switching manifold $p\,(t_{\Sigma-})$ and the perturbation vector after the switching manifold $p\,(t_{\Sigma+})$ as shown below

$$p\,(t_{\Sigma+}) = \mathbf{S} \times p\,(t_{\Sigma-}) \tag{2.26}$$

where $\mathbf{S}$ is the Saltation matrix [65], and is expressed as shown below.

$$\mathbf{S} = \mathbf{I}_{n\times n} + \frac{(f_2 - f_1)\times \mathbf{n}^{\mathbf{T}}}{\mathbf{n}^{\mathbf{T}} f_1 + \left.\dfrac{\partial h(\mathbf{X}(t),t)}{\partial t}\right|_{t=t_{\Sigma}}} \tag{2.27}$$

where f_1 is the vector field before the switching manifold expressed as $f_1 = \lim_{t\downarrow t_\Sigma} f_1(\mathbf{X}(t),t,\rho)$, f_2 is the vector field after the switching manifold expressed as $f_2 = \lim_{t\uparrow t_\Sigma} f_2(\mathbf{X}(t),t,\rho)$, $\mathbf{n}$ is the normal to the hypersurface given by (2.28), $\mathbf{n}^{\mathbf{T}}$ is the transpose of the normal to the hypersurface and $\mathbf{I}_{n\times n}$ is an identity matrix of the same order as that of the system.

$$\mathbf{n} = \begin{bmatrix} \dfrac{\partial h(\mathbf{X}(t),t)}{\partial x_1(t)} \\ \cdot \\ \cdot \\ \dfrac{\partial h(\mathbf{X}(t),t)}{\partial x_n(t)} \end{bmatrix} \tag{2.28}$$

Consequently, the perturbation ($p(t)$) will be expressed as

$$\begin{aligned} p(t) &= \Phi\big(t, t_0, \mathbf{X}_0\big)\times p(t_0) \\ &= \Phi\big(t, t_\Sigma, \mathbf{X}(t_\Sigma)\big)\times \mathbf{S} \times \Phi\big(t_\Sigma, t_0, \mathbf{X}_0\big) \end{aligned} \tag{2.29}$$

Assuming Fig. 2.6 is an arbitrary non-smooth orbit of a non-smooth system, to determine the stability of this orbit we need to obtain the STM for $t \in [0,T]$ where T is the period of the orbit. Since the trajectory crosses the switching hypersurface twice in once cycle, the STM around the orbit (the Monodromy matrix) can be expressed as

$$M(T,0) = \mathbf{S}_2 \times \Phi(T, t_\Sigma, \mathbf{X}(t_\Sigma)) \times \mathbf{S}_1 \times \Phi(t_\Sigma, 0, \mathbf{X}_0) \tag{2.30}$$

where $\mathbf{S}_1$ is the Saltation matrix that govern the transition of the trajectory from region R_- to region R_+ and $\mathbf{S}_2$ is the Saltation matrix that govern the transition of the trajectory from region R_+ back to region R_- .

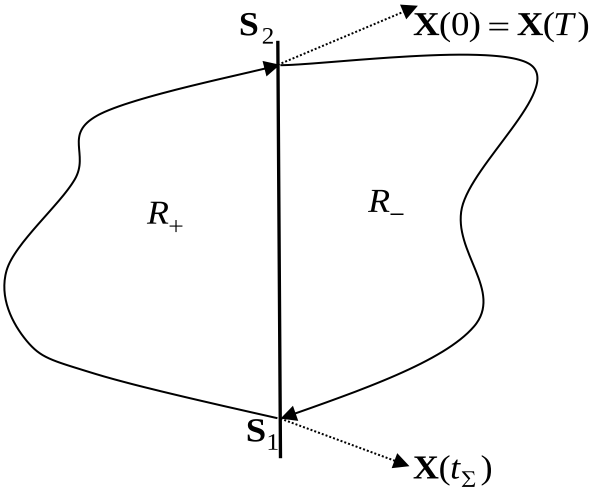

Fig. 2.6 Arbitrary periodic orbit of a non-smooth system

The stability of the non-smooth orbit will then be ascertained by computing the eigenvalues of the Monodromy matrix (the Floquet multipliers). The procedures outlined here will be applied in the stability analysis of non-smooth orbits in electrical drives discussed in chapters 4, 5, 7 and 8.

2.6 Complex Behaviour of Nonlinear Dynamical Systems

Unlike linear systems, nonlinear systems are prone to complex dynamical phenomena namely bifurcations, chaos, co-existing attractors and fractal basin boundaries. These phenomena can cause qualitative changes in the steady state trajectory of the system thereby making long time predictability difficult.

2.6.1 Bifurcations

A bifurcation can be defined as a change in the qualitative behavior of a nonlinear system as some system parameter is being varied thus leading to the birth or death of an *attracting set* [9, 60]. At some values of system parameters one of the invariant sets could be an *attractor* and trajectories of initial points converge on it at steady state, while at some other parameter values, the previous attractor may begin to repel and another invariant set begins to attract. It is also possible for all the invariant sets to vanish under parameter variation. The system parameter value at which a bifurcation occurs is referred to as a *bifurcation point*. The concept of the bifurcation can be used to explain some physical phenomena such as the buckling of beams as loads are varied. A graphical plot of the equilibrium state against the bifurcation parameters is referred to as a *bifurcation diagram*. The two main class of bifurcations are *smooth* and *non-smooth* bifurcation [4]. The former is very common in smooth dynamical systems and include *saddle node, transcritical, pitchfork, hopf* and *period-doubling* bifurcations. The later (including *border collisions*) could be found only in systems of non-smooth or Filippov's type. These types of bifurcation are explained below.

2.6.1.1 *Saddle Node Bifurcation*

This type of bifurcation is characterised by a sudden loss or acquisition of a stable attracting set as the system parameter moves across a critical value [67]. As the system parameter is varied, two EPs move towards each other, collide and mutually annihilate [9]. The saddle node bifurcation is also known as a *fold* bifurcation. Systems that exhibits saddle node bifurcation can be normalised to the form:

$$\frac{dx}{dt} = k + x^2 \tag{2.31}$$

where *k* is the bifurcation parameter and *x* is the state variable. For $k<0$, the system has two EPs, one stable $(x^* = -\sqrt{-k})$ and the other unstable $(x^* = +\sqrt{-k})$. But for $k>0$, all the EPs disappears. This qualitative change that occurs at $k=0$ is known as a *saddle node* bifurcation. The *bifurcation diagram* of the system of form (2.31) is shown in Fig. 2.7

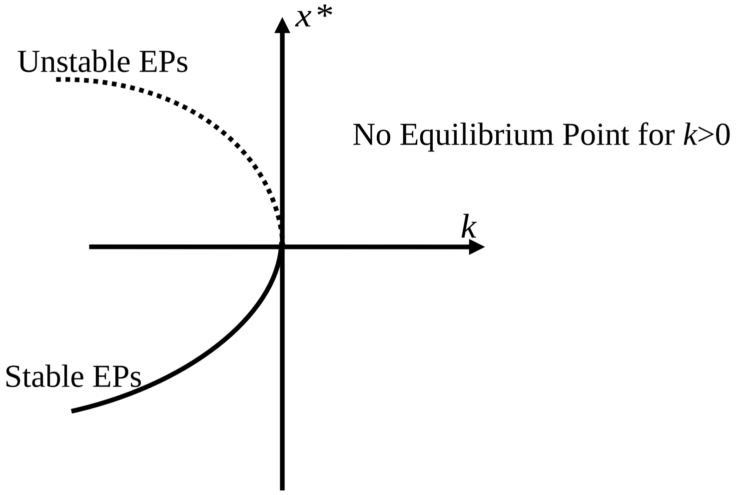

Fig. 2.7 Bifurcation diagram for a saddle node bifurcation.

2.6.1.2 *Transcritical Bifurcation*

This type of bifurcation involves the switching of stability status between two equilibrium solutions as the system parameters are being varied [9]. It often occurs in physical system where an equilibrium point exists for all the parameter values. Systems which exhibit this behaviour can be normalised to the form:

$$\frac{dx}{dt} = kx - x^2 \tag{2.32}$$

The two EPs of the system (2.8) occur at $(x^* = 0)$ and $(x^* = k)$. For k<0, the EP at $(x^* = 0)$ is stable and attract trajectories of initial points, while the EP at $(x^* = k)$ is unstable. But for k>0, the EP at $(x^* = 0)$ becomes unstable while the EP at $(x^* = k)$ becomes stable and thus attract trajectories. This exchange of stability at k=0 is known as a *transcritical bifurcation* and is illustrated in Fig. 2.8.

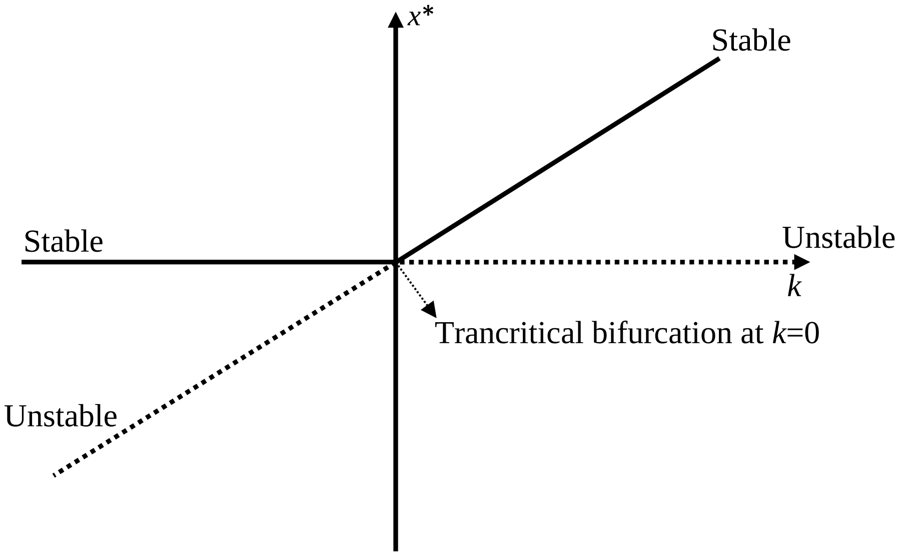

Fig. 2. 8 Bifurcation diagram for a transcritical bifurcation

2.6.1.3 *Pitch-Fork Bifurcation*

The Pitchfork bifurcation can be classified as either *supercritical* or *subcritical* [9] and is very common in systems that have spatial symmetry. A Supercritical pitchfork bifurcation occurs when a stable equilibrium point loses stability and two co-existing stable equilibrium points appear. Systems that exhibit supercritical pitchfork bifurcation can be normalised to:

$$\frac{dx}{dt} = kx - x^3 \tag{2.33}$$

As the system parameter (k) is varied from left to right, the stable equilibrium point at the origin loses stability and two stable equilibrium points emerge. This exchange of stability status between one equilibrium point and a pair of equilibrium points at k=0 is known as a Supercritical Pitch-Fork Bifurcation. The bifurcation diagram of the system is shown in Fig. 2.9.

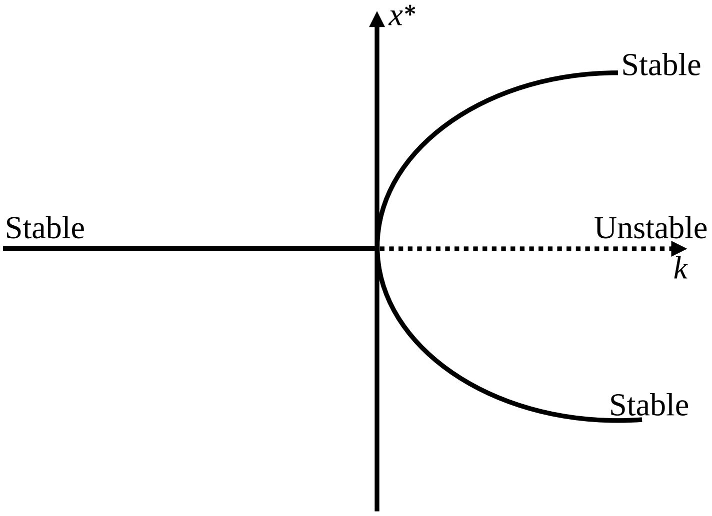

Fig. 2. 9 Bifurcation diagram for a supercritical pitchfork bifurcation

A Subcritical pitchfork bifurcation on the other hand occurs in systems of the form:

$$\frac{dx}{dt} = kx + x^3 \tag{2.34}$$

When the bifurcation parameter (k) is below the bifurcation point (k<0), we have three equilibrium points at $(x^* = 0)$ and $(x^* = \pm\sqrt{-k})$ with only the equilibrium point at the origin being stable and the other two unstable. But for (k>0), the two equilibrium points $(x^* = \pm\sqrt{-k})$ vanish and only the unstable equilibrium point at the origin remains. The bifurcation diagram of such a system is shown in Fig. 2.10.

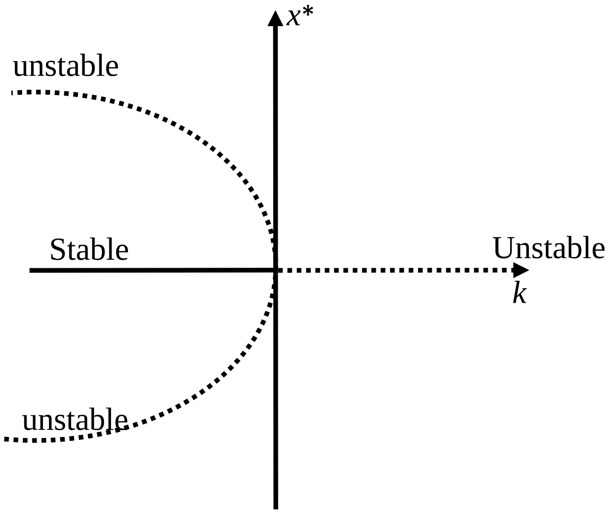

Fig. 2.10 Bifurcation diagram for a subcritical pitchfork bifurcation

2.6.1.4 *Hopf Bifurcation*

This type of bifurcation occurs when a stable spiral point loses stability and a stable limit cycle is born [67]. Systems that exhibit this kind of bifurcation can be normalized to a second-order equation of the form:

$$\begin{aligned}\frac{dx_1}{dt} &= -x_2 + x_1[\mu - (x_1^2 + x_2^2)] \\ \frac{dx_2}{dt} &= x_1 + x_2[\mu - (x_1^2 + x_2^2)]\end{aligned} \tag{2.35}$$

The stability of the EP in this system depends on the eigenvalues of the Jacobian matrix of the system. For $\mu < 0$, the EP at the origin is stable as the real part of the eigenvalues of the Jacobian matrix are negative, but for $\mu > 0$, the real part of the eigenvalues becomes positive and the EP at the origin loses stability. The trajectories of the various initial points will now depart from the origin and converge on a new attractor (a limit cycle). Another form of *Hopf* bifurcation that occurs in discrete systems is the *Neimark-Sacker* bifurcation and it occurs when pair of complex conjugate eigenvalues assume a magnitude of 1. The analysis and experimental validation of a Neimark-sacker bifurcation in a laboratory PI controlled permanent magnet DC drive is discussed in Chapter 4.

2.6.1.5 *Period Doubling Bifurcation*

This type of bifurcation is characterized by a sudden doubling of the period of a stable periodic orbit or limit cycle and it occurs when one of the eigenvalues of the system becomes -1. The Period doubling bifurcation is also known as a *flip* bifurcation or a *fast-scale instability* and is commonly observed in SMPE systems including electrical drives.

2.6.1.6 *Border Collision Bifurcation*

The border collision bifurcation is very common in non-smooth systems where two or more systems with different topologies operate at different parameter values. The *border collision* bifurcation is also referred to as a *non-smooth* bifurcation and is characterised by abrupt discontinuities, bending and jumps which do not resemble the patterns seen in standard or *smooth* bifurcations [18]. In PWM controlled electrical drives, border collisions occur due to saturation nonlinearities.

2.6.2 Chaos

Another complex behaviour peculiar to nonlinear systems is *chaos*. Chaos can be defined as an aperiodic behaviour of nonlinear deterministic systems that is highly sensitive to initial conditions [9]. An early example of chaos in nonlinear systems was the Lorenz system (2.36) [9]. A small change in the initial condition of the system can lead to significant change in the steady state trajectory thereby making long term predictability of chaotic systems nearly impossible.

$$\begin{aligned}\frac{dx_1}{dt} &= \rho(-x_1 + x_2)\\ \frac{dx_2}{dt} &= cx_1 - x_2 - x_1x_3\\ \frac{dx_3}{dt} &= -\beta x_3 + x_1x_2\end{aligned} \tag{2.36}$$

The occurrence of chaos in a system can be proved by examining the divergence of the trajectories of two nearby initial points in state space. A system is said to be chaotic if two nearby initial points to the chaotic attractor evolves into two uncorrelated trajectories after few iterations or if the *Lyapunov exponent* is positive [10, 18]**.** Chaos is said to be ubiquitous as it has been reported in many physical and biological systems including chemical systems [68], fetal heart rates [69], mechanical systems [70] and in power electronics systems [7, 20, 28, 30, 64, 71]. The two common routes to chaos are the period doubling route to chaos and the quasi-periodic route to chaos. These are discussed in Chapter 4. Chaotic attractors are also referred to as *strange attractors*.

2.6.3 Co-existing Attractors and Fractal Basin Boundaries

Co-existing attractors occur when two or more stable states exist at the same time in a dynamical system. For instance when the EP at the origin in system (2.33) loses stability via a supercritical pitchfork bifurcation, the two new attractors ($\pm\sqrt{k}$) could be referred to as co-existing attractors. When two or more attractors co-exist, the set of initial conditions whose trajectories converge on a given attractor is referred to as the *basin of attraction* for that attractor and the boundary separating the different basins is referred to as the *separatrix* [10]. For example the line x=0 separates the basin of the two attracting sets $\pm\sqrt{k}$ after the supercritical pitchfork bifurcation and all trajectories whose initial point is above zero converges on $+\sqrt{k}$ while all trajectories whose initial point is less than zero converge on $-\sqrt{k}$. If the boundary separating the different basins is highly irregular and difficult to isolate, then the phenomena will be referred to as *fractal*. In Chapter 4, the fractal phenomena associated with dc chopper-fed PMDC drive will be discussed, while the fractal phenomena in full-bridge converter PMDC drive is discussed in Chapter 8.

2.7 Summary

In this chapter the complex phenomena associated with nonlinear dynamical systems and the concept of invariant sets (*constant solution of dynamical systems*) were discussed. It has been shown that as system parameters are varied a stable invariant set may lose stability and a new stable invariant set may emerge or the invariant set may vanish completely. Also more than one stable invariant set may co-exist at the same time thereby making the system behaviour very uncertain and difficult to predict. These phenomena occur in most nonlinear systems including electrical drives. In the next chapter the fundamentals of electrical drives and the modelling techniques for nonlinear analysis of drives will be discussed.

CHAPTER 3

ELECTRICAL DRIVES FUNDAMENTALS

3.1 Introduction

Electrical drives are found in homes, industry, automobiles, aircrafts, space crafts, etc. Most modern homes often have several electrical drives hidden in devices such as vacuum cleaners, dishwashers, washing machines, refrigerators, air conditioning units, etc. The rotational speed and torque in modern electrical drives are controlled by the toggling ON and OFF of power electronic switches via pulse width modulated (PWM) signals.

The “switch ON” equivalent circuit topology is often different from the “switch OFF” circuit topology thus classifying these systems as non-smooth or Filippov’s type systems as discussed in section 2.2.4. Also due to the switching of the power electronic devices, electrical drives are inherently nonlinear in nature and are susceptible to complex nonlinear phenomena, namely *bifurcation* and *chaos*. Thus, special modeling techniques such as the average model [16, 17, 19] and nonlinear iterative mapping [20, 72] will be applied for a comprehensive analysis of the drives performance.

In this chapter, the fundamentals of electrical drives with emphasis on DC drives, and switched reluctance motor (SRM) drives will be discussed. The material provided here will be useful in Chapters 4-8 where the nonlinear phenomena in DC drives and SRM drives are analysed and controlled.

3.2 Components of an Electrical Drive System

A typical modern electrical drive (Fig.3.1) consist of an *electric motor*, a *power converter* and *control electronics*, working together to move a mechanical load [3]. An input power supply that provides the energy needed by the drive and sensors for closed-loop control, are also needed as integral parts of the system.

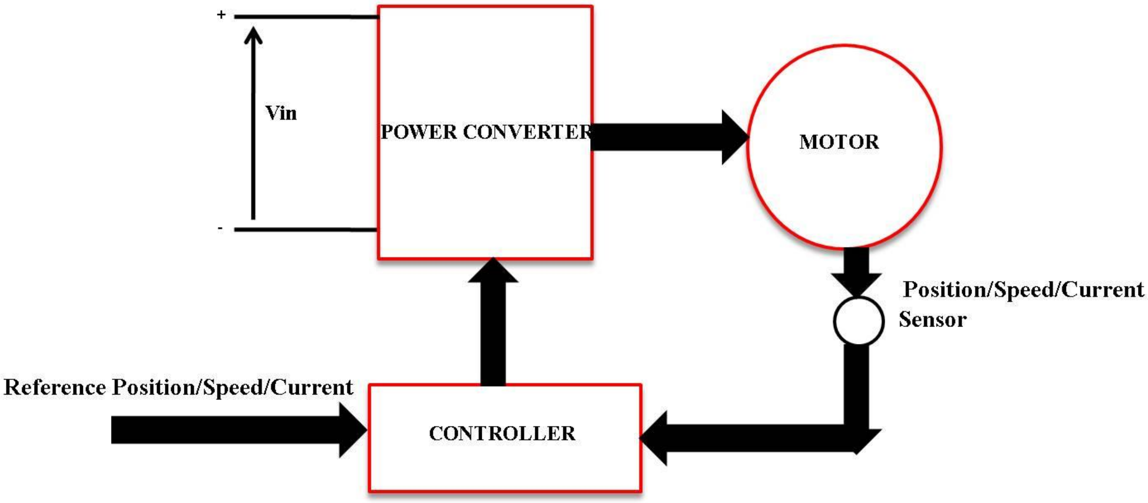

Fig. 3.1 Components of an electric drive system

3.2.1 Electric Motors

Electric motors are a key component of electric drive systems and they convert the input electrical energy into mechanical energy [2]. There are several variants of electrical motors in use today and possible classification criteria include the commutation strategy, the input power source and the type of torque being produced, as shown in Table 3.1. In terms of the commutation strategy, we typically have mechanical commutation and electronic commutation. An example of an electrical motor employing mechanical commutation is the conventional brushed DC motor (BDCM) which comes in four variants: separately excited (SE), series connected (SC), shunt connected (SHC), and compound motors (CM). Separately excited DC motors can also be subdivided into permanent magnet DC (PMDC) motors and field excited DC (FEDC) motors. The commutation strategy in those motors involves the use of mechanical commutators and carbon brushes. As the commutators and brushes wear out due to friction, conventional dc motors require routine maintenance. But, the ease at which the speed of conventional dc motors can be controlled makes them appealing for variable speed application and many industrial drives today still rely on brushed DC motors.

To overcome the problems caused by the wear and tear in mechanical commutators, electronic commutation is employed. Electronic commutation (brushless schemes) is based on the idea that a rotating magnetic field is produced by balanced three phase AC currents flowing in the stator coils. Typical examples of electrical motors employing electronic commutation are brushless DC motors (BLDCM), inverter-fed induction motors (IM) & permanent magnet synchronous motors (PMSM), and synchronous reluctance motors (SR). Other variants of electronically commutated motors include switched reluctance motors (SRM) and stepper motors (SM) that rely on the principle of reluctance torque.

Table 3.1 Classification of electric motors.

ELECTRIC MOTOR	INPUT POWER	COMMUTATION STRATEGY	FORM OF TORQUE
Brushed DC Motors	DC	Mechanical	Electromagnetic
Brushless DC Motors	DC	Electronic	Electromagnetic
Induction Motor(IM)	AC	Electronic	Electromagnetic
Permanent Magnet Synchronous Motors	AC	Electronic	Electromagnetic
Synchronous Reluctance Motors	AC	Electronic	Reluctance
Switched Reluctance Motors	DC	Electronic	Reluctance
Stepper Motors	DC	Electronic	Reluctance

In this thesis, the complex dynamics of electrical drives representing the two main commutation strategies are studied in details. Permanent magnet DC (PMDC) drives and Series connected DC (SCDC) drives are selected as examples of mechanically commutated motors while the SRM drive is selected as an example of an electronically commutated motor.

3.2.2 Power Converters

Power converters are used to adjust the voltage, current and frequency of the input electrical power for the purposes of motor speed and torque control. They receive electrical energy from the mains at constant voltage and frequency and then supply electrical energy to the motor at variable voltage and frequency [2]. The power conversion process could be DC-DC (*chopper*), DC-AC (*inverter*), or AC-DC-AC (*rectifier + inverter*).

3.2.3 Control Electronics

In general, the state variables of an electrical drive system can be controlled either in *open loop* or *closed loop*. In closed loop control, the controller compares the actual state of the system measured by sensors with the reference state to produce an error signal. Based on the error signal a pulse width modulated (PWM) signal of appropriate duty ratio will be produced to turn ON or OFF the power switches in the power converter and thus achieve the required speed or current control [2]. Control electronics can be implemented in analog form using operational amplifiers and comparators or in digital form using microprocessors. Most modern drives make use of the later.

3.2.4 Mechanical Loads

Electrical motors are designed to carry mechanical loads of one form or the other. The mechanical load imposes an opposing torque to the electrical torque produced by the motor. The load can be a constant load or may vary with the shaft speed. The load can also introduce nonlinearity in the drive’s dynamic model. For example the load torque imposed on the shaft by a fan or pump type load is proportional to the square of the speed ($T_L \alpha \omega^2$) thus making the system nonlinear.

3.3 Permanent Magnet DC Drives

Prior to the recent advances in power electronics and microprocessor technology, the most common drive system used for variable speed application was the DC drive. DC drives are relatively easy to analyse and control and are commonly used in several domestic and industrial applications (children toys, robots, paper mills, steel rolling mills etc). Typically PMDC drives consist of a permanent magnet DC motor, the power converter, and control electronics. The power converter can be a DC chopper (for first quadrant motoring operation), a full-bridge converter (for two quadrant operation) or even an active front end full-bridge converter (for four quadrant operation). The permanent magnet provides the field excitation, but since the permanent magnet flux is fixed, PMDC drives are widely used in low power applications [3]. In this section, the fundamentals of DC chopper fed PMDC drives will be discussed.

3.3.1 System Overview

The schematic diagram and equivalent circuit of DC-chopper fed PMDC drives (operating under open loop control) are shown in Fig. 3.2. The drive consists of the PMDC motor, an electronic switch (S**)** and free-wheeling diode (D). The switch (BJT, MOSFET, IGBT) is controlled by a PWM signal fed through an appropriate device driver. The PMDC motor consists of a field circuit (a permanent magnet), and an armature circuit comprising the armature coils, mechanical commutators (not shown) and brushes. The coils and the commutator are mounted on the rotor shaft and rotate with the rotor while the brushes are mounted on the stator and are stationary.

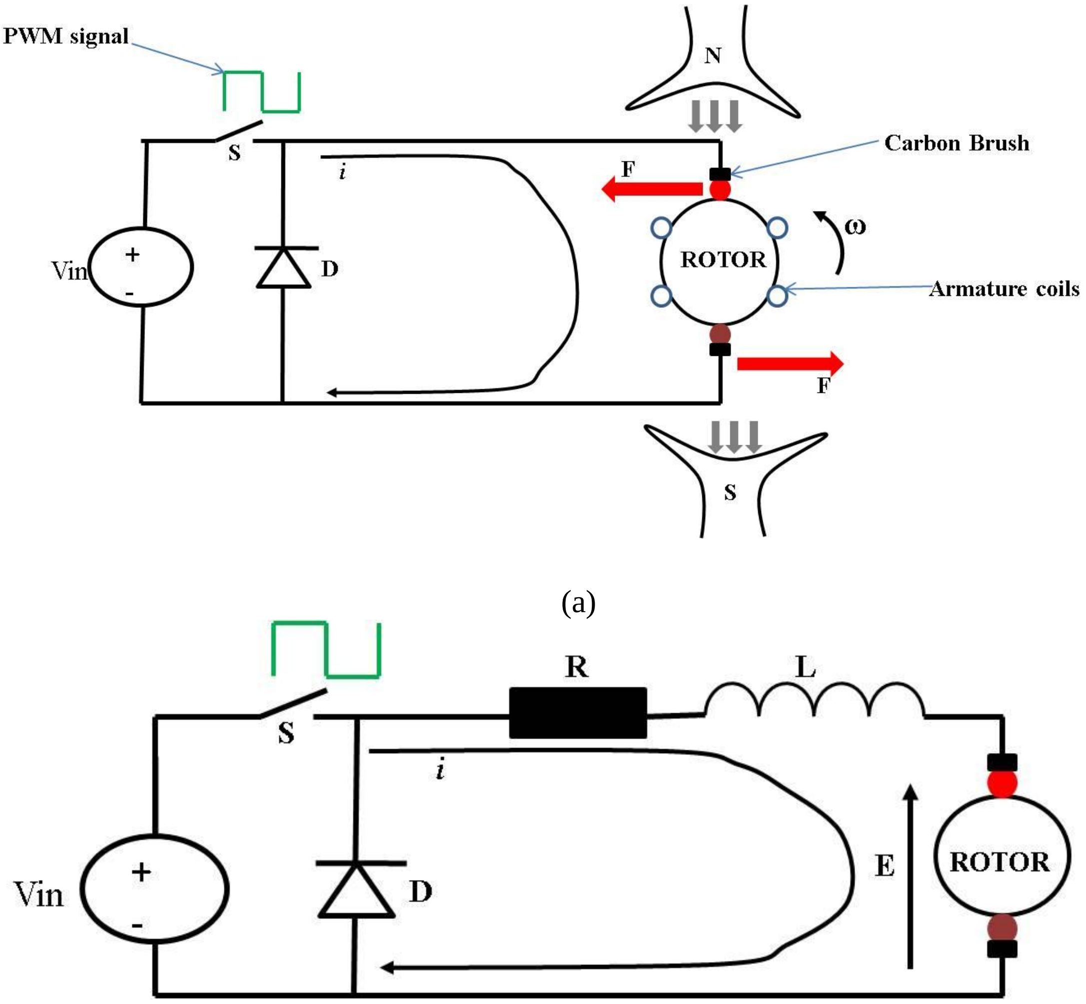

(a)

(b)

Fig. 3.2 Open loop PMDC drives (a) System schematic diagram (b) Equivalent circuit of the drive.

The speed of the motor depends on the average voltage applied at the armature terminals which depends on the duty cycle (*d*) of the PWM signal.

$$V_{avg} = V_{in} \times d \tag{3.1}$$

where *d* is the ratio of the switch ON time (T_{on}) to the period of the switching cycle (T).

$$d = \frac{T_{on}}{T} \tag{3.2}$$

and $T = T_{on} + T_{off}$

Since $d \in [0,\ 1]$, the average voltage applied at the armature terminals using the DC Chopper will be between 0 and V_{in}, thus making it possible to achieve a speed range from zero to full speed.

3.3.2 PMDC Drive Operation

The operation of the open loop PMDC drive can be described using Fig.3.2. When the PWM signal is High, the switch (S) is closed and $+V_{\text{in}}$ is applied at the terminals of the armature coil directly under the north pole of the permanent magnet (PM) thus causing current $i(t)$ to flow in the coil via the brushes. The interaction of the permanent magnet flux $\phi(t)$ and the armature current produces a force F (also known as Lorentz force) at both ends of the winding. The force produces an electrical torque (T_{e}) that causes anti-clockwise rotation of the shaft. When the PWM signal is Low, the switch opens and the diode (D) conducts thus causing zero volts to be applied at the armature coil terminals. The armature current thus decays via the diode. The switch ON and switch OFF circuit topologies are shown in Fig.3.3 and Fig.3.4, respectively.

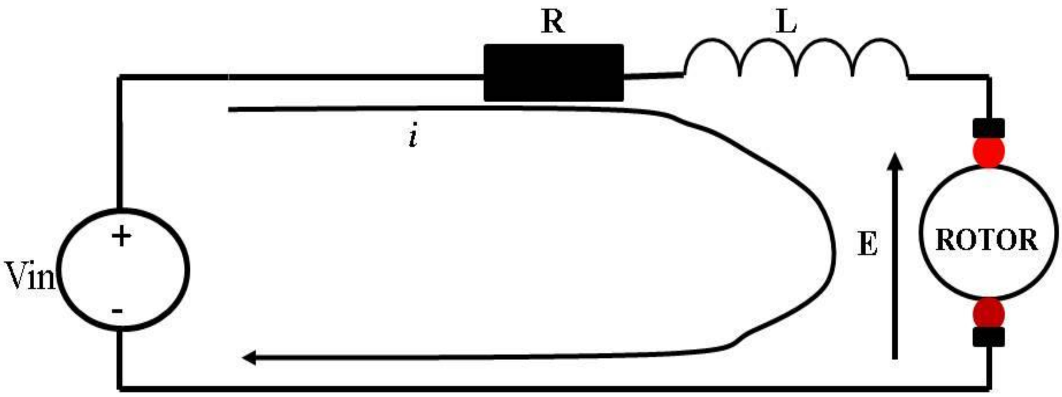

Fig. 3.3 Switch ON circuit topology of a PMDC drive

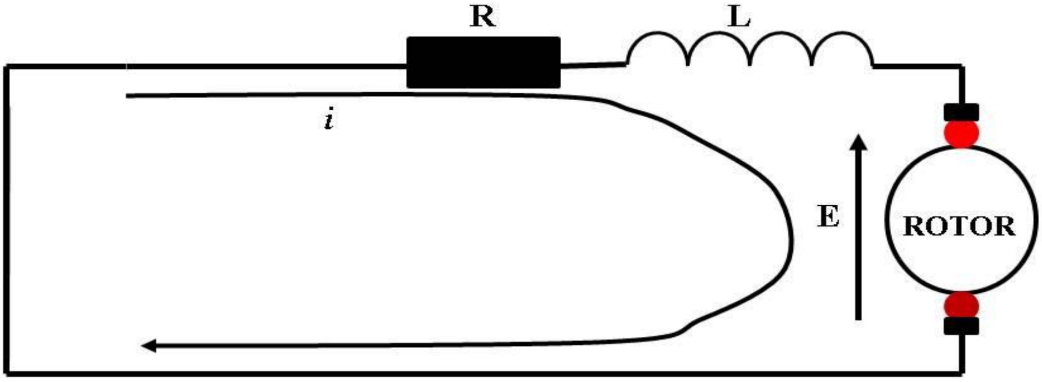

Fig. 3.4 Switch OFF circuit topology of a PMDC drive

If the armature current decays to zero during the switch OFF interval, the operational mode will be referred to as *discontinuous conduction mode* (DCM), otherwise it will be referred to as *continuous conduction mode* (CCM). In order for the drive to operate in CCM, the inductance of the motor winding must be high enough to ensure that the current does not drop to zero during the switch OFF interval.

The force (F) and the electrical torque (T_e) produced are functions of the armature current and field flux as shown below:

$$F = B \times i \times l \tag{3.3}$$

$$T_e = K_t \times \phi \times i \tag{3.4}$$

where $\phi(t)$ is the field flux, i is the armature current, B is the field flux density, l is the length of the armature coil being linked by the field flux and K_t is the torque constant. $\phi(t)$ is constant in PMDC motor and consequently the electrical torque produced will depend only on the armature current as expressed below:

$$T_e = K_t \times i \tag{3.5}$$

As the rotor rotates, an emf (E) will be induced at the terminals of the armature coil as it is being linked by the field flux $\phi(t)$. This emf is commonly referred to as back emf and is proportional to the field flux and the shaft angular velocity (ω(t)).

$$E_b = K_e \times \phi \times \omega \tag{3.6}$$

Since ϕ is constant for the PMDC motor the back emf can also be expressed as $E_b = K_e \times \omega$.

3.3.3 Mathematical Model of Open Loop PMDC Drive

Under CCM operation, the system will alternate between two different topological states as the switch is turned ON and OFF. The mathematical model depicting the switch ON state will be different from the mathematical model for the switch OFF state. When the switch is ON and the diode is OFF (Fig.3.3) the mathematical model will be expressed as:

$$\begin{aligned}\frac{d\omega(t)}{dt} &= \frac{\left(T_e - T_L - B\omega(t)\right)}{J} \\ &= \frac{\left(K_t i(t) - T_L - B\omega(t)\right)}{J}\end{aligned} \tag{3.7}$$

$$\begin{aligned}\frac{di(t)}{dt} &= \frac{-i(t)R - E_b + V_{in}}{L} \\ &= \frac{-i(t)R - K_e\omega(t) + V_{in}}{L}\end{aligned} \tag{3.8}$$

where $i(t)$ is the armature current, $\omega(t)$ is the shaft speed, L is the armature inductance, R is the armature resistance, K_e and K_t are the back emf and the torque constants, respectively, B is the viscous damping factor, T_L is the load torque, J is the moment of inertia, and V_{in} is the supply voltage.

But when the switch is OFF and the diode conducts (Fig.3.4), the mathematical model will be expressed as:

$$\frac{d\omega(t)}{dt} = \frac{\left(K_t i(t) - T_L - B\omega(t)\right)}{J} \tag{3.9}$$

$$\frac{di(t)}{dt} = \frac{-i(t)R - K_e\omega(t)}{L} \tag{3.10}$$

The switch ON model (3.7) and (3.8) and the switch OFF model (3.9) and (3.10) can be abridged in state space form as shown below:

$$\dot{\mathbf{X}}(t) = \mathbf{A_{on}}\mathbf{X}(t) + \mathbf{V_{on}} \tag{3.11}$$

$$\dot{\mathbf{X}}(t) = \mathbf{A_{off}}\mathbf{X}(t) + \mathbf{V_{off}} \tag{3.12}$$

$$\mathbf{X}(t) = \begin{bmatrix} x_1(t) \\ x_2(t) \end{bmatrix} = \begin{bmatrix} \omega(t) \\ i(t) \end{bmatrix} \tag{3.13}$$

$$\mathbf{A_{on}} = \mathbf{A_{off}} = \mathbf{A} = \begin{bmatrix} \frac{-B}{J} & \frac{K_t}{J} \\ \frac{-K_e}{L} & \frac{-R}{L} \end{bmatrix} \tag{3.14}$$

$$\mathbf{V_{on}} = \begin{bmatrix} \frac{-T_L}{J} \\ \frac{V_{in}}{L} \end{bmatrix} \tag{3.15}$$

$$\mathbf{V_{off}} = \begin{bmatrix} \frac{-T_L}{J} \\ 0 \end{bmatrix} \tag{3.16}$$

In order to ensure easy comparison of results, the parameters of the DC chopper-fed PMDC DC drive used in this thesis are the same as those used in [7] : K_e=0.1356Vs/rad, K_t=0.1324 NM/A, R=3.5 Ω, L=36 mH, B=0.000564 Nm.rad^{-1}.sec, V_{in}=100 V, T=4 msec, J=9.71×10^{-4} N.m.rad^{-1}.sec^{2}.

The steady state speed and current when the duty cycle (d=0.5) and Load torque (T_L=0.39 NM) are as shown in Fig.3.5 and Fig.3.6. From the Figures, it could be seen that the steady state behaviour of the state variables is a periodic ripple of the same period as the external clock signal. This is referred to as a *period-1 orbit*. In chapter 4 it will be shown that as some system parameters (such as the supply voltage and controller gains of the closed loop PMDC drive) are being varied, the nominal period-1 orbit may lose stability and a new stable orbit of period-nT or a quasi-periodic orbit may appear. The study of the mechanism through which such instability (or *bifurcation*) occurs is a major contribution of this thesis.

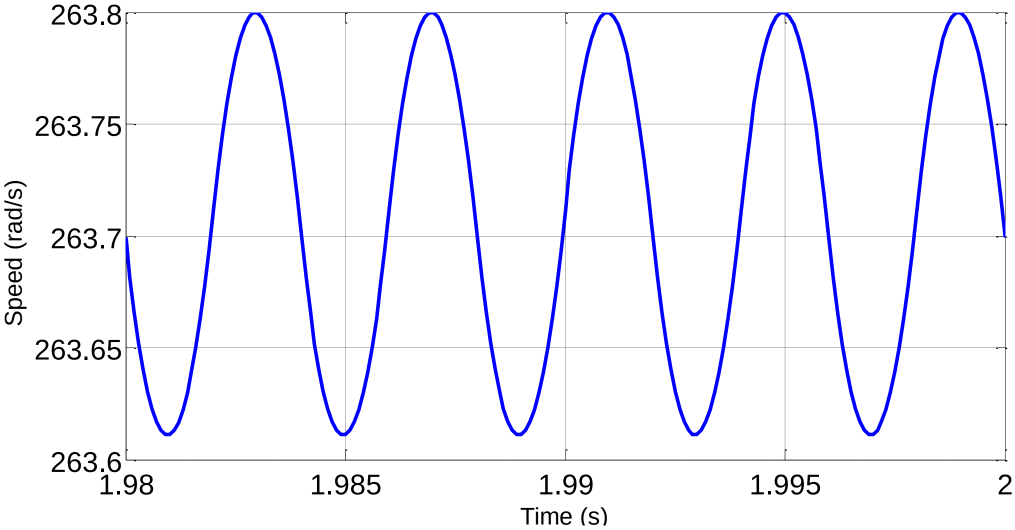

Fig. 3. 5 Open loop speed response (d=0.5, T_L=0.39 NM)

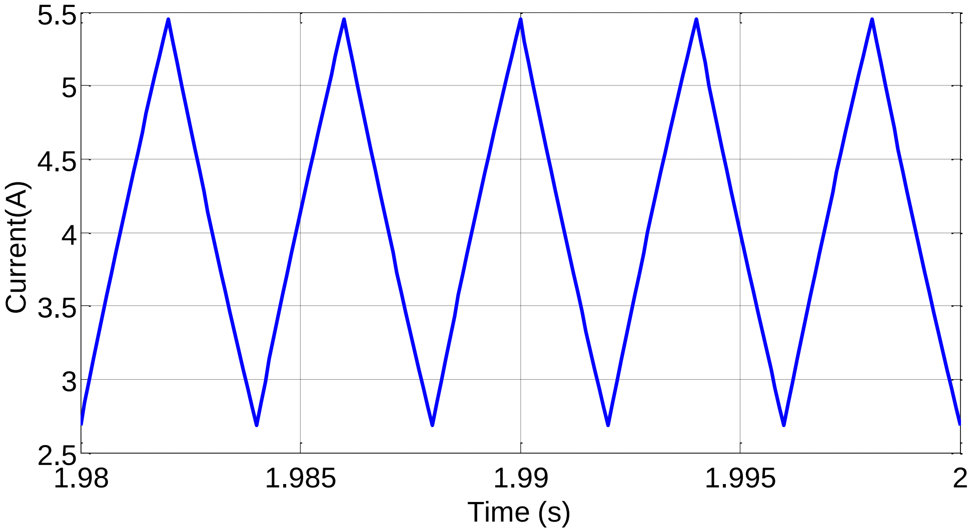

Fig. 3.6 Open loop current response (d=0.5, T_L=0.39 NM)

3.4 Series Connected DC Drives

A SCDC motor is a dc motor in which the field winding is connected in series with the armature circuit ($i_a = i_f = i$). This motor can produce high torque at low speed and is thus widely used in traction applications. The schematic diagram and equivalent circuit of the open loop SCDC drive are shown in Fig.3.7. The drive consists of the SCDC motor, an electronic switch (S**),** and free-wheeling diode (D). The motivation for investigation of the dynamics of the SCDC drive is due to the rich nonlinearity in the system [73, 74].

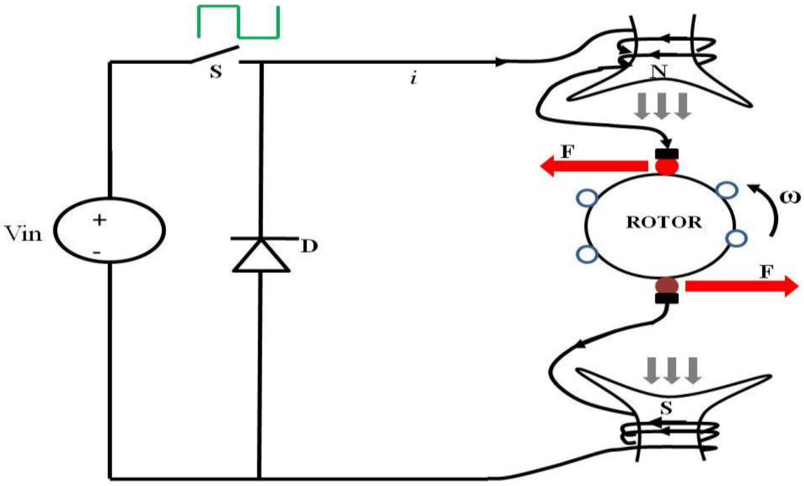

(a)

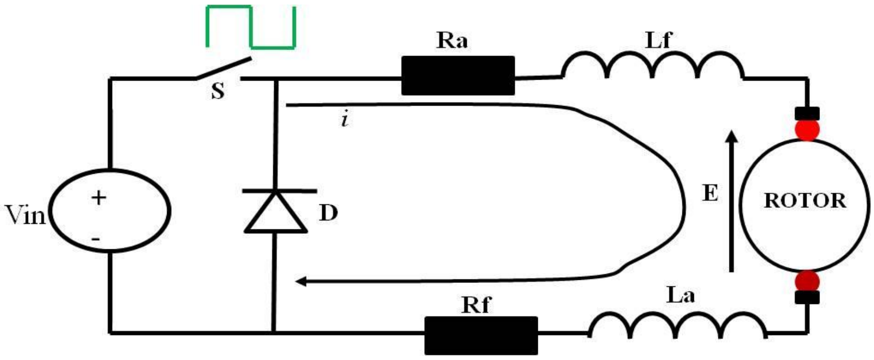

(b)

Fig. 3.7 Open loop SCDC drive (a) System schematic diagram (b) Equivalent circuit of the drive

There are three key sources of nonlinearity in a SCDC motor drive. First the electrical torque is proportional to the square of the current (below field saturation) and secondly the back EMF is proportional to the product of current and speed [74]. The third source of nonlinearity is introduced by the power electronic switching in the SCDC drive. Due to these nonlinearities, the SCDC drive is prone to complex nonlinear dynamical phenomena, namely *bifurcation* and *chaos*.

The expression for the electrical torque and back-emf is similar to (3.4) and (3.6), but in a SCDC motor, the field flux (ϕ) is not constant and varies with the armature current ($i_a=i_f=i$). As the load increases, the current (i) will increase and so will the field flux.

Under very heavy load and high current, the field flux will saturate as shown in Fig. 3.8. But, under light load and low current, the motor will operate in the linear region of the saturation curve and the field flux will be expressed as a linear function of current [3] [74] as shown:

$$\phi = C \times i \tag{3.17}$$

where C is the constant of proportionality.

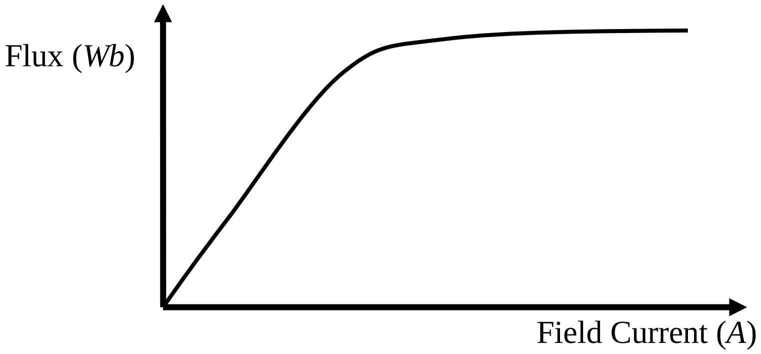

Fig. 3.8 Magnetic saturation curve of a SCDC motor

Consequently, the electrical torque and back-emf will be expressed as:

$$T_e = K \times \phi \times i = K \times C \times i^2 = K_t\, i^2 \tag{3.18}$$

$$E_b = K \times C \times i \times \omega = K_e i \omega \tag{3.19}$$

Thus when the switch is ON and the diode is OFF the system behaviour will be described by the dynamic equations:

$$\frac{d\omega(t)}{dt} = \frac{\left(K_t\, i^2 - T_L - B\omega\right)}{J} \tag{3.20}$$

$$\frac{di(t)}{dt} = \frac{-iR - K_e i \omega + V_{in}}{L} \tag{3.21}$$

But when the switch is OFF and the diode conducts the system behaviour will be described by the equations:

$$\frac{d\omega(t)}{dt} = \frac{\left(K_t\, i^2 - T_L - B\omega\right)}{J} \tag{3.22}$$

$$\frac{di(t)}{dt} = \frac{-iR - K_e i\omega}{L} \tag{3.23}$$

where $R=R_a+R_f$ (the sum of the resistances of the armature and field coils) and $L=L_a+L_f$ (the sum of the inductances of the armature and field coils). The square term for the electrical torque ($K_t i^2$) and the product term for the back-emf ($K_e i\omega$) make the SCDC drive inherently nonlinear. Assuming the state vector $\mathbf{X}(t) = \begin{bmatrix} x_1(t) \\ x_2(t) \end{bmatrix} = \begin{bmatrix} \omega(t) \\ i(t) \end{bmatrix}$ then the switch ON and switch OFF equations can be abridged as shown below:

$$\dot{\mathbf{X}}(t) = \mathbf{f}_{\mathbf{on}}(\mathbf{X}(t)) = \begin{bmatrix} \dfrac{\left(K_t\, x_2{}^2 - T_L - Bx_1\right)}{J} \\ \dfrac{-x_2R - K_e x_2 x_1 + V_{in}}{L} \end{bmatrix} \tag{3.24}$$

$$\dot{\mathbf{X}}(t) = \mathbf{f}_{\mathbf{off}}(\mathbf{X}(t)) = \begin{bmatrix} \dfrac{\left(K_t\, x_2{}^2 - T_L - Bx_1\right)}{J} \\ \dfrac{-x_2R - K_e x_2 x_1}{L} \end{bmatrix} \tag{3.25}$$

The investigation of the nonlinear bifurcation and chaotic phenomena of the SCDC drive is discussed in Chapter 7.

3.5 Closed Loop Control Schemes for DC Drives

Closed loop control of shaft speed (ω) and armature current (i) in DC drives is very important in most drives applications. The two commonly used control schemes are voltage mode control and current mode control [2]. Voltage mode control is designed for control of the shaft speed while current mode control is aimed at control of the rotational torque (T_e) produced by the motor. Also, the two control schemes can be combined to form what is commonly referred to as cascade or two loop control in which the inner feedback loop is for armature current (or torque) control while the outer feedback loop is for speed control. All closed loop control schemes involve the comparison of a reference state (speed or current) with the actual state obtained from sensors and then carrying out some compensation actions. The voltage mode control scheme is discussed in section 3.5.1 while the current mode control scheme is discussed in section 3.5.2.

3.5.1 Voltage Mode Control

Voltage mode control is aimed at speed control of DC drives. Assuming that the load torque (T_L) and friction constant (B) in the open loop PMDC drive are negligible then the steady state speed will be expressed as $\omega_{eq} = V_{avg} / K_e$ where $V_{avg} = V_{in} \times d$. Thus to control the steady state speed (ω_{eq}) we need to control the average voltage applied to the armature by adjusting the PWM duty cycle (d). This control strategy is described below using the DC chopper fed PMDC drive as an example system.

A schematic diagram of a DC chopper fed PMDC drive operating under voltage mode control is shown in Fig.3.9. The system consists of three main subsystems: the PMDC motor , the power converter (a dc chopper) and the control electronics [7]. The dc chopper comprises a dc source, power switch (BJT, MOSFET, IGBT) and a free-wheeling diode, while the control electronics comprise an operational amplifier (Op-Amp), comparator and a signal generator.

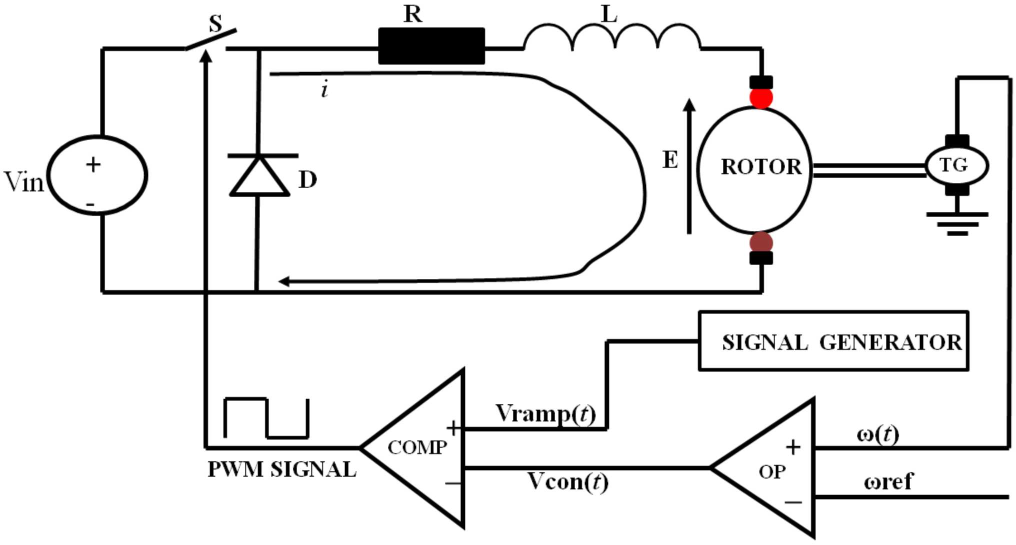

Fig. 3.9 Voltage mode controlled DC drive.

In this scheme, the output speed $\omega(t)$ in the form of an analogue voltage from a tacho-generator is compared with the reference speed ω_{ref} to obtain the speed error signal $(e(t) = \omega(t) - \omega_{ref})$. The speed error is then multiplied by the gain of the operational amplifier to obtain the control signal $V_{con}(t) = g \times (\omega(t) - \omega_{ref})$. The PWM signal is obtained by comparing a high frequency sawtooth signal $V_{\text{ramp}}(t)$ with the control signal. When the sawtooth signal is greater than the control signal, the PWM waveform goes high, the switch closes and the diode is reverse biased. But when the sawtooth signal is lower than the control signal, the PWM signal goes low, the switch opens and the diode is forward biased. The PWM duty cycle (*d*) is varied continuously to ensure that the actual speed $\omega(t)$ tracks the reference speed ω_{ref}. The comparison of the sawtooth signal and the control signal to produce the PWM signal is shown in Fig. 3.10.

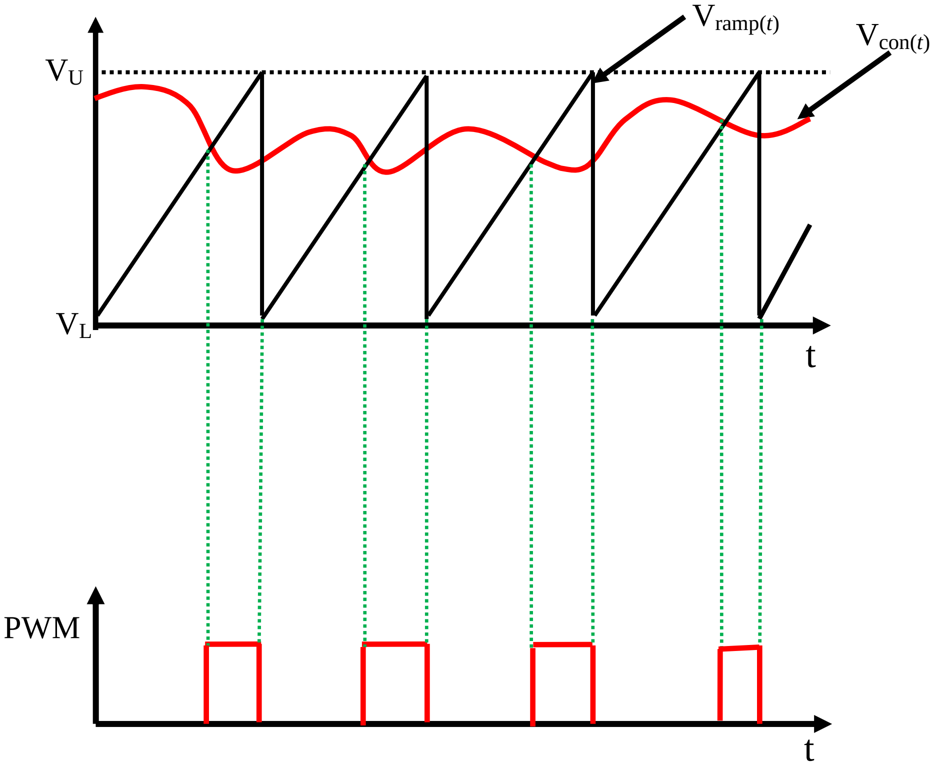

Fig. 3.10 PWM waveform generation

3.5.2 Current Mode Control

In applications where the DC motor is required to operate with a fixed torque regardless of the speed (for example in steel mill line tensioning) [2], current mode control is adopted. A schematic diagram of a current mode controlled DC drive is shown in Fig. 3.11. The reference current (I_{ref}) is compared with the actual armature current (i) to obtain a signal to reset a latch that was previously set by an external clock signal of period (T). When the S–R latch is set by the clock pulse, the power switch (S) is closed and the diode (D) is reverse biased. The armature current rises until it reaches the reference current (I_{ref}) causing the latch to be reset. When the latch is reset, the switch opens and the diode is forward biased. The armature current then decays through the diode. The switch will remain open until the arrival of the next clock pulse when it will close again and the cycle repeats. The interaction of the armature current, the reference current, and the external clock pulse is as shown in Fig. 3.12.

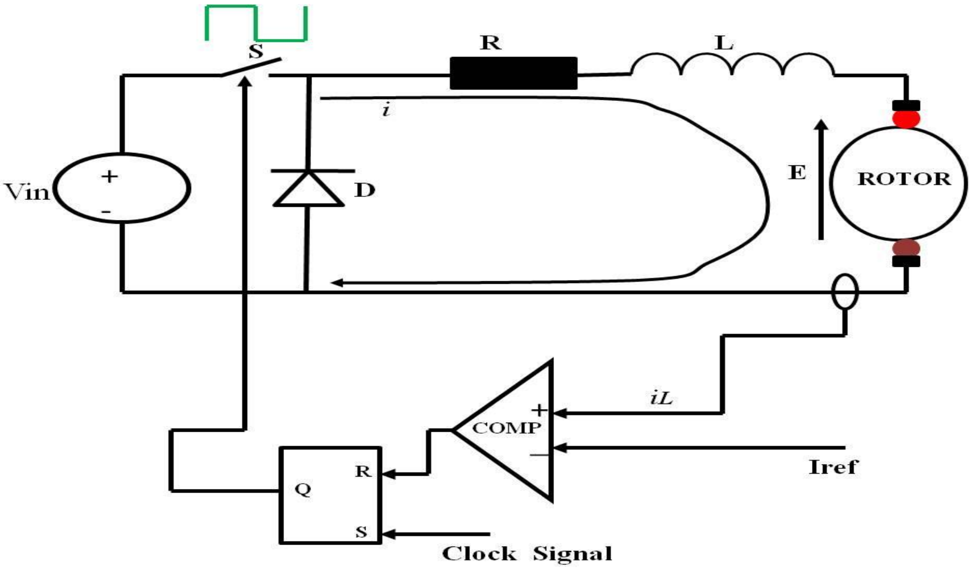

Fig. 3.11 Current controlled DC drive

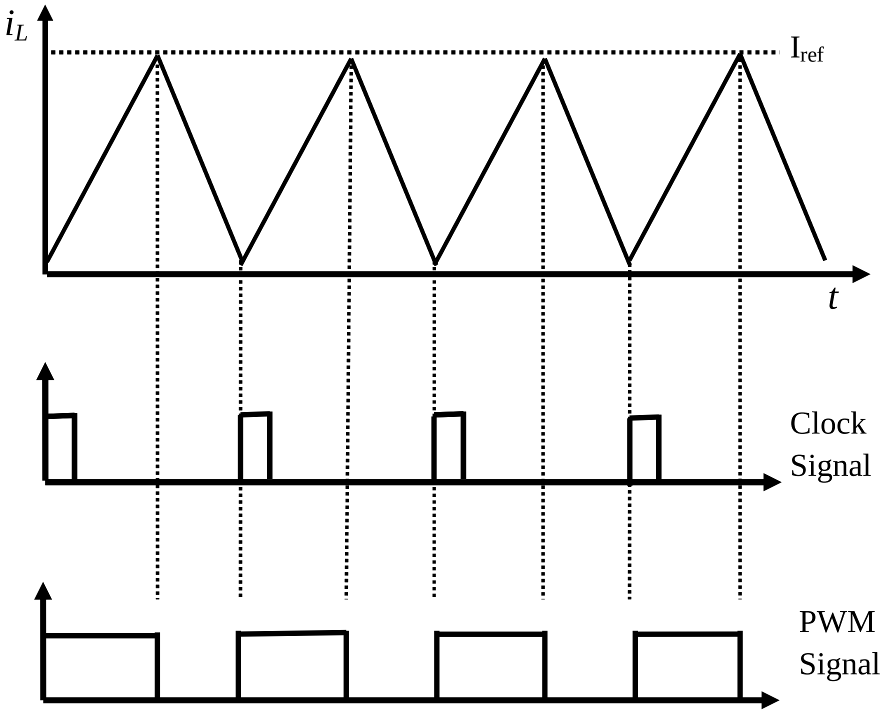

Fig. 3.12 Armature current, reference current and the external clock pulse in a current controlled DC drive.

In most practical applications, the current reference is provided by an outer speed control loop thereby forming what is referred to as cascade or two loop control. The inner current loop is always faster than the outer speed loop and the diagram of this arrangement is shown in Fig. 3.13.

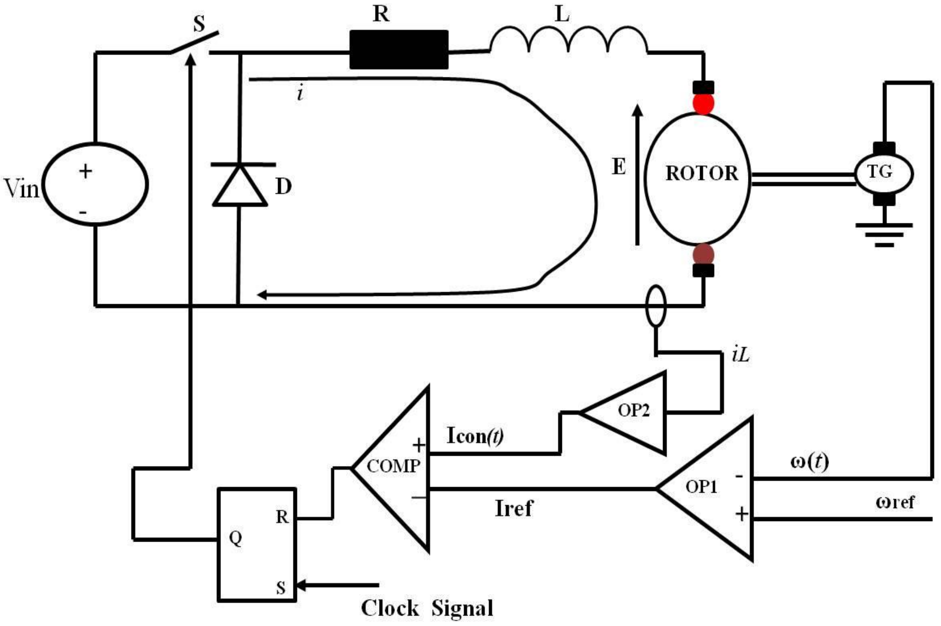

Fig. 3.13 Two loop control of a DC drive

3.6 Switched Reluctance Motor Drives

The Switched Reluctance Motor (SRM) is a low cost electronically commutated motor with a very simple mechanical structure. It has windings in the stator but the rotor is made up of stacked steel laminations and does not have any windings or permanent magnets [75, 76]. Both the stator and rotor poles are salient and torque is produced due to the tendency of the rotor poles to move to a position where the reluctance of the energized phase will be minimum [77]. Conventionally, the stator windings are grouped into phases. Each phase is energized separately and is electrically separate from the adjacent phase. A phase is energized (stroked) when its inductance is rising and de-energized when the inductance gets to its maximum value.

Owing to its simple mechanical structure and advances in power electronic technology the SRM is now seen as a viable candidate for variable speed applications and much research has been conducted in this area in the last two decades [75, 76, 78-84]. Moreover, the fault tolerance incorporated in most SRM drives make them suitable for some of the most sensitive applications including aerospace.

The mechanical simplicity of the machine is in sharp contrast to the complexity of its modelling and analysis caused by its inherent nonlinear characteristics. Such nonlinear systems are characterized by complex dynamical phenomena including bifurcation, chaos, co-existing attractors and fractal basin boundaries [9, 71]. In this section the basic characteristics of a SRM drive are discussed starting with its principles of operation in section 3.6.1 and the phase commutation logic in section 3.6.2. The different SRM drive operational modes are discussed in section 3.6.3. The information provided in this chapter will be useful in Chapter 5 where the complex nonlinear phenomena in a three-phase SRM drive are explored.

3.6.1 Principles of Operation of a SRM

As the name implies, the motion of a typical SRM (Fig.3.14) is produced as a result of the variable reluctance in the air gap between the stator and rotor poles [77, 80]. When current is applied to a phase winding, an *mmf* (*Ni*) is produced which in turn causes flux to flow through a magnetic path (the active phase poles, air gap and rotor structure). The expression for the *mmf* is:

$$mmf = N \times i = \phi \times R(\theta) \tag{3.26}$$

where N is the number of turns in the phase winding, i is the phase current, ϕ is the phase flux and $R(\theta)$ is the reluctance of the magnetic flux path. The reluctance (R) is a function of the rotor position (θ) due to the salient rotor and stator poles. The reluctance is maximum when the stator and rotor poles are unaligned (known as the unaligned position) and minimum when the stator and rotor poles are aligned. In order to minimize the reluctance of the magnetic circuit created by the energized phase, the magnetized stator pole pulls the adjacent rotor pole to alignment leading to the production of a reluctance torque [80]. If magnetic saturation effects are negligible (usually under light load conditions), then the instantaneous electrical torque produced by each phase [77] can be expressed as:

$$T = 0.5 i^2 \frac{dL(\theta)}{d\theta} \tag{3.27}$$

where $L(\theta) = \frac{N^2}{R(\theta)}$ is the inductance of the phase coil. The inductance is usually maximum at the aligned position (where the reluctance is minimum) and minimum at the unaligned position where the reluctance is maximum.

A SRM drive consist of a switched reluctance motor, a power converter circuit (usually an asymmetric drive circuit) and the control electronics. A standard asymmetric drive power converter circuit used for 3-phase SRM control is shown in Fig. 3.15. The circuit consist of six power electronic switches (BJT, MOSFET, IGBT) and six freewheeling diodes. The phase coils are connected between two of the power switches thereby eliminating the possibility of *shoot-through* faults that usually occur when two switches on the same leg of the power converter are switched ON at the same time.

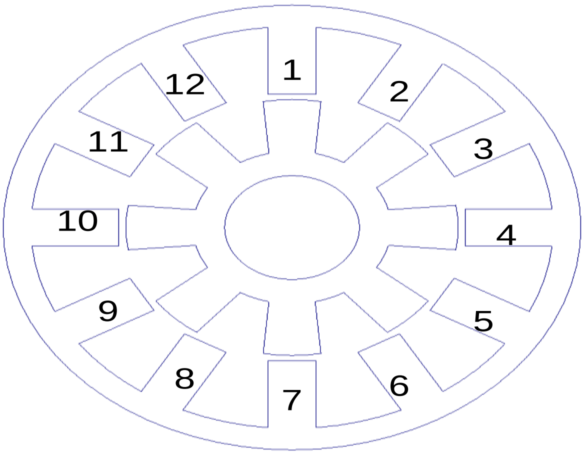

Fig. 3.14 Diagram of a 3-phase 12/8 SRM (2 stator poles pairs per phase)

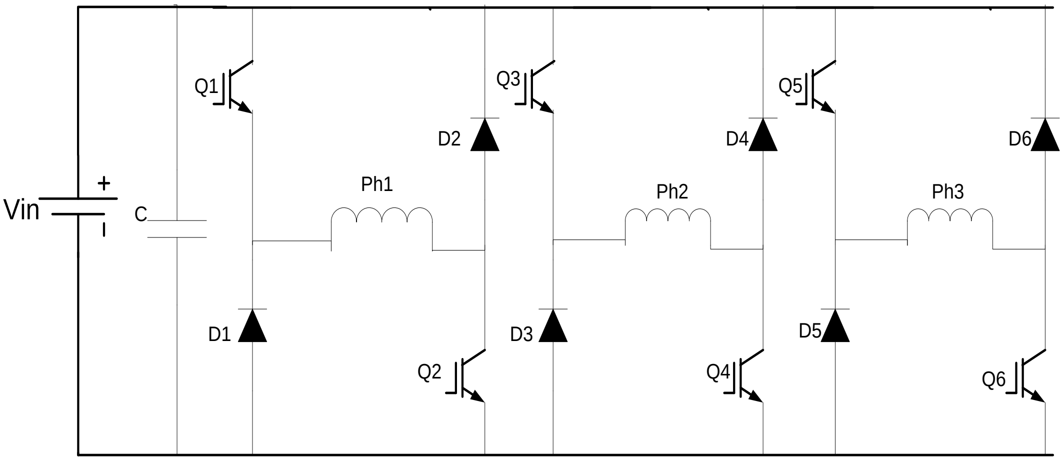

Fig. 3.15 Asymmetric drive power converter circuit

3.6.2 SRM Phase Commutation Strategy

The phase activation and de-activation of a SRM is controlled by the commutation logic using the rotor position and the phase inductance cycle as a guide. Each phase is activated at ($\theta=\theta_{on}$) when its inductance begins to rise and deactivated at ($\theta=\theta_{off}$) when the inductance reaches its' maximum value. The inductance cycle of each phase corresponds to the rotor pole pitch ($2\pi/N_r$) and the inductance cycle of adjacent phases are separated by an angle ($\theta_s=2\pi/mN_r$) known as the phase separating angle. Thus if the inductance cycle of phase A starts at ($\theta=\theta_1$), the inductance cycle of the adjacent phase will start at ($\theta=\theta_1+\theta_s$) and the inductance cycle for the third phase will start at ($\theta=\theta_1+$

$2\theta_s$). To keep the analysis simple, the conduction interval (θ_{off} - θ_{on}) or dwell angle of each phase is made to correspond with the phase separating angle. The phase commutation sequence of the three-phases of an 12/8 SRM within one inductance cycle of 45 mechanical degrees (or 360 electrical degrees) is shown in Fig.3.16 (θ_{on}=5.5˚, θ_{off} =20.5˚ and phase separating angle=15˚).

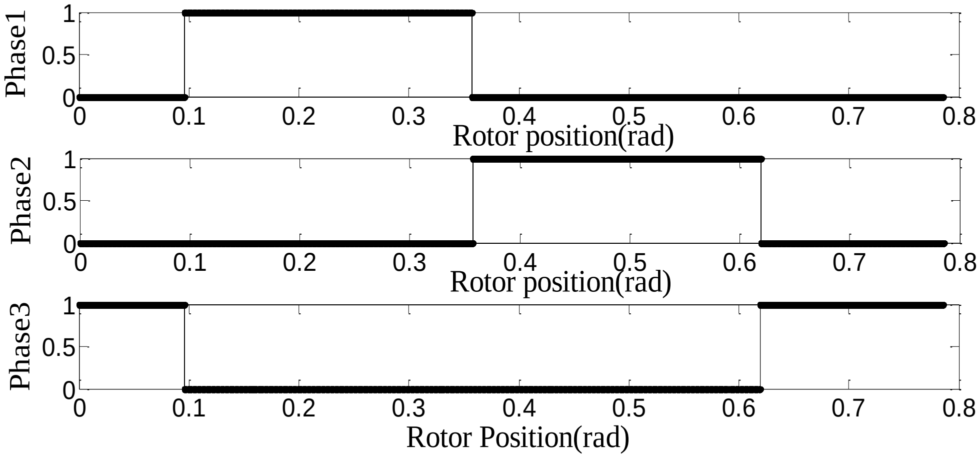

Fig. 3.16 SRM Commutation Sequence (the 3 phases are stroked once in one inductance cycle of 45 mechanical degrees).

3.6.3 SRM Drive Operational Modes

The three main operational modes of SRM drive are the single pulse operation, soft chopping operation and hard chopping operation [77].

3.6.3.1 *Single Pulse Operation*

The single pulse operational mode is usually employed in high speed SRM drive applications. In this mode, the upper and lower leg switches of the active phase are turned ON at the switch ON angle (θ_{on}) and OFF at the switch OFF angle (θ_{off}). This operational mode can be illustrated using phase1 of the SRM drive in Fig.3.15. At $\theta = \theta_{on}$, the two switches (Q1 and Q2) will be turned ON and $+V_{\text{in}}$ will be applied across the phase coil terminals. The two diodes (D1 and D2) will be reverse biased and the phase current will rise. Then at the end of the conduction interval ($\theta=\theta_{off}$), the two switches will be turned OFF and the two diodes will be forward biased. A negative voltage ($-V_{\text{in}}$) will be applied across the phase coil terminals and the phase current will decay to zero. Two different topological states can be identified in each phase (Table 3.2). Typical current and voltage waveforms for this mode of operation are shown in Fig.3.17.

Table 3.2 Topological states for single pulse operation

System States	Q1	Q2	D1	D2	V_{in}
State1	1	1	0	0	$+V_{in}$
State2	0	0	1	1	$-V_{in}$

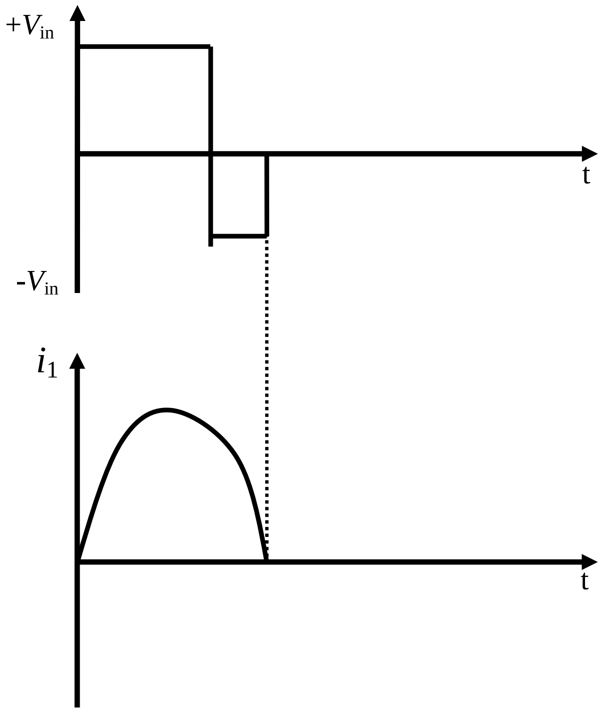

Fig. 3.17 Phase1 voltage and current waveforms for single pulse operation

3.6.3.2 *Soft Chopping PWM Operation*

The Soft chopping technique is used to regulate the phase current (by regulating the average voltage applied across the phase coils) and is widely used in low speed SRM drive applications. In this mode, the lower leg switch of the active phase is left ON, while the upper switch is turned ON and OFF by applying a PWM signal of constant or variable duty ratio. In closed loop operation, this PWM signal may be generated by comparing a control signal ($V_{con}(t)$) with a fixed frequency saw-tooth signal ($V_{ramp}(t)$) as detailed in Chapter 5. This operational mode can be illustrated (for a constant duty ratio PWM signal) using the asymmetric drive circuit shown in Fig.3.15. At $\theta = \theta_{on}$, the lower switch (Q2) is switched ON and a PWM signal of constant duty ratio will be applied to the upper switch (Q1). When the PWM signal is high, Q1 is turned ON and $+V_{in}$ will be applied across the phase coil terminals. The two diodes (D1 and D2) will then be reverse biased and the phase current will rise. When the PWM signal is low, Q1 is turned OFF and the winding will be short-circuited through the lower leg switch Q2 and the diode D1. At the end of the conduction interval ($\theta = \theta_{off}$), the two switches will be turned OFF and the two diodes will be forward biased. A negative voltage ($-V_{in}$) will be applied across the phase coil terminals and the phase current will decay to zero. Three different topological states can be identified in each phase (Table 3.3). Typical phase current and voltage waveforms for this mode of operation are shown in Fig.3.18.

Table 3. 3 Topological states for soft chopping operation

System State	Q1	Q2	D1	D2	V_{in}
State1	1	1	0	0	$+V_{in}$
State2	0	1	1	0	0
State3	0	0	1	1	$-V_{in}$

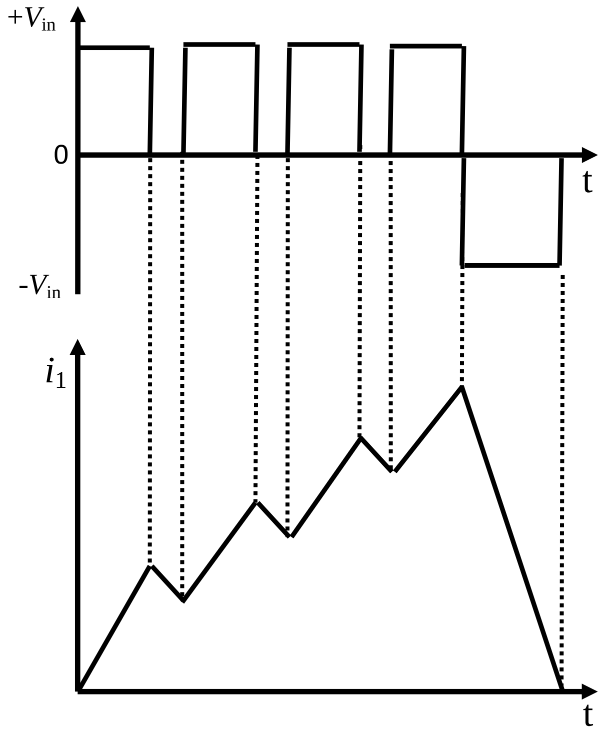

Fig. 3.18 Phase1 voltage and current waveforms for soft-chopping operation

3.6.3.3 *Hard Chopping PWM Operation*

The hard chopping operational mode is similar to the soft chopping mode, but in this mode both the upper and lower leg switches are turned ON when the PWM signal is high and turned OFF when the PWM signal is low. Thus $+V_{in}$ is applied when the PWM signal is high and $-V_{in}$ will be applied (as the two diodes conducts) when the PWM signal is low. The increased current and torque ripple are drawbacks of this mode of operation. The number of topological states for each phase is similar to the single pulse mode of operation and typical phase current and voltage waveforms are shown in Fig. 3.19.

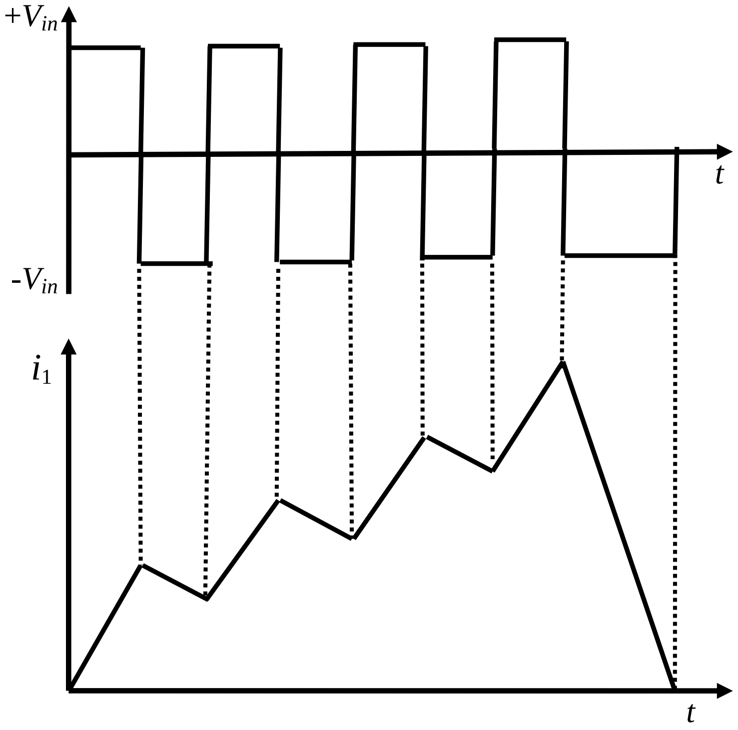

Fig. 3.19 Phase1 voltage and current waveforms for hard chopping operation.

3.7 Modelling Techniques for Nonlinear Analysis of Electrical Drives

Similar to other SMPE based systems, electrical drives adopt different topological states (multiple subsystems) as the power electronic switches are turned ON and OFF. The switch ON topology is often different from the switch OFF topology thereby making the system to be time varying and non-linear. Also due to the switching, the *invariant set* (steady state or constant solution of the system) is a periodic orbit rather than an equilibrium point. The common techniques for modelling the dynamic behaviour of SMPE based systems including electric drives are the state space average model [14, 16, 17, 19] and iterative mapping [20, 72].

3.7.1 State Space Average Model

Assuming there is only one switching during the PWM cycle period (T), the steady state behaviour of most electrical drives in CCM could be described by a non-smooth, time varying dynamic equation of the form:

$$\frac{d\mathbf{X}(t)}{dt} = \begin{cases} \mathbf{f_{ON}}(\mathbf{X}(t)), & \textbf{for } 0 \le t \le dT \\ \\ \mathbf{f_{OFF}}(\mathbf{X}(t)), & \textbf{for } dT < t \le T \end{cases} \tag{3.28}$$

where $\mathbf{f_{ON}}(\mathbf{X}(t))$ and $\mathbf{f_{OFF}}(\mathbf{X}(t))$ are the vector fields that describes the trajectories of the state variables when the switch is turned ON and OFF, respectively, dT is the switching instant, d is the duty cycle and T is the PWM switching period.

The time varying nature of the dynamic equation (3.28) makes the analysis of SMPE systems difficult. The state space average model (developed by R.D. Middlebrook [16]) is aimed at transforming the time varying system into a time invariant system thereby making analysis using conventional control theory tools (*Nyquist plot*, *Bode plot*, *Root locus* etc) possible. The main idea is to discard the switching details of the system and retain only the average dynamics [18]. Using the model (3.28) as an example, the state space average model could be described by the equation:

$$\frac{d\mathbf{X}(t)}{dt} = d \times \left(\mathbf{f_{ON}}(\mathbf{X}(t))\right) + \delta \times \left(\mathbf{f_{OFF}}(\mathbf{X}(t))\right) \tag{3.29}$$

where d is the fraction of the time the switch is turned ON or the fraction of time the vector field $\mathbf{f_{ON}}(\mathbf{X}(t))$ is active, and δ is the fraction of time the switch is turned OFF, which is also the time interval the vector field $\mathbf{f_{OFF}}(\mathbf{X}(t))$ is active.

$$\delta = 1 - d \tag{3.30}$$

By substituting the expression for δ in (3.29), the average model can be expressed as:

$$\frac{d\mathbf{X}(t)}{dt} = d \times \left(\mathbf{f_{ON}}(\mathbf{X}(t))\right) + (1-d) \times \left(\mathbf{f_{OFF}}(\mathbf{X}(t))\right) \tag{3.31}$$

To complete the derivation of the average model in closed loop drives applications, there is a need to obtain the expression that defines the duty cycle (d) as a nonlinear function of both the system state variables and the other parameters. The state space average modelling approach can be illustrated using the open-loop PMDC drive (Fig. 3.2) whose dynamic model can be expressed as:

$$\frac{d\mathbf{X}(t)}{dt} = \begin{cases} \mathbf{f_{ON}}(\mathbf{X}(t)) = \mathbf{A_{on}}\mathbf{X}(t) + \mathbf{V_{on}}, & \textbf{for } 0 \le t \le dT \\ \\ \mathbf{f_{OFF}}(\mathbf{X}(t)) = \mathbf{A_{off}}\mathbf{X}(t) + \mathbf{V_{off}}, & \textbf{for } dT < t \le T \end{cases} \tag{3.32}$$

Based on the open loop PMDC drive dynamic model (3.32), the state space average model can be expressed as:

$$\begin{aligned}\frac{d\mathbf{X}(t)}{dt} &= d\times\left(\mathbf{A_{on}}\mathbf{X}(t)+\mathbf{V_{on}}\right)+(1-d)\times\left(\mathbf{A_{off}}\mathbf{X}(t)+\mathbf{V_{off}}\right)\\ &= \mathbf{A}\mathbf{X}(t)+d(\mathbf{V_{on}}-\mathbf{V_{off}})+\mathbf{V_{off}}\end{aligned} \tag{3.33}$$

where $\mathbf{A_{on}}=\mathbf{A_{off}}=\mathbf{A}$ as defined in (3.14). $\mathbf{V_{on}}$ and $\mathbf{V_{off}}$ have also been previously defined in (3.15) and (3.16), respectively.

Using the state space average model for the open loop PMDC drive (3.33), the speed and current response when operating at a duty cycle (*d*=0.5) and a load torque of 0.39 NM are shown in Fig. 3.20 and Fig. 3.21, respectively.

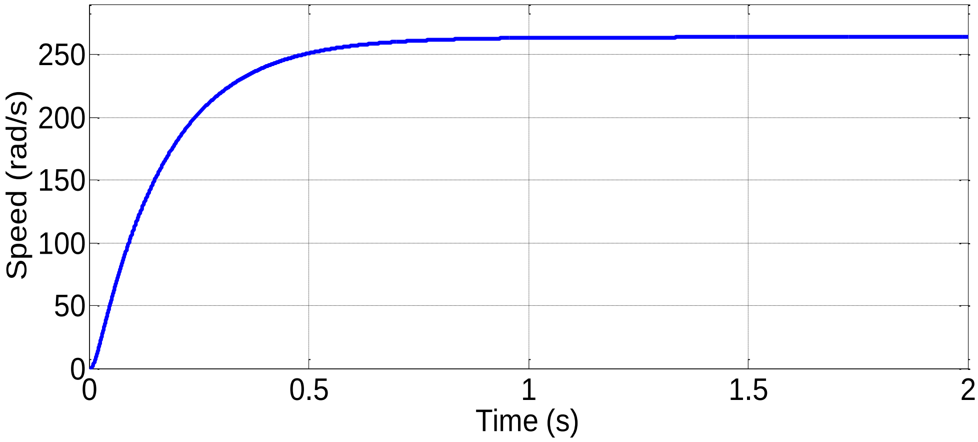

Fig. 3.20 Speed response using the average model

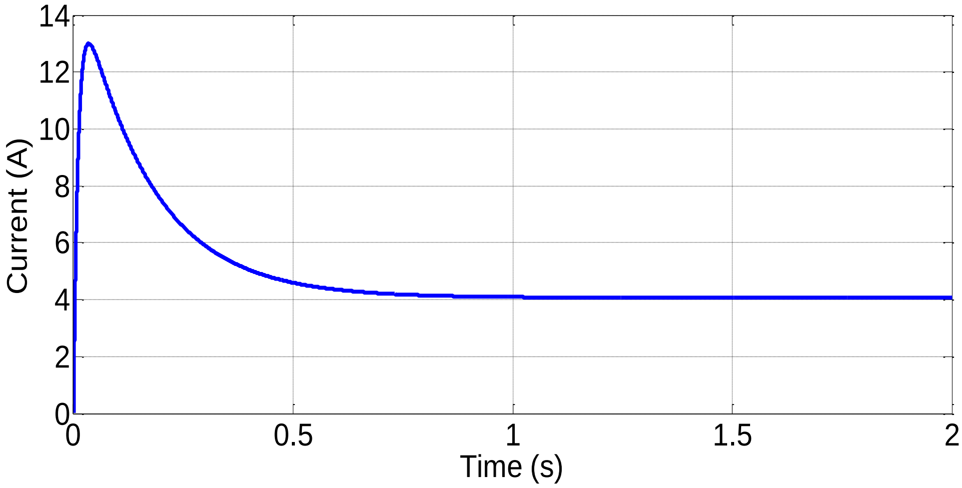

Fig. 3.21 Armature current response using the average model

The steady state value of the average model response (Fig. 3.20 and Fig. 3.21) is actually the average value of the periodic ripple in the original system (Fig. 3.5 and Fig. 3.6). The average model can be used to predict low frequency instabilities such as slow scale bifurcations but cannot predict fast-scale instabilities such as a period doubling bifurcation [18].

3.7.2 The Iterative Map Model

The iterative map or Poincaré map model is commonly used to study the complex dynamics of SMPE based systems including electrical drives. The idea is to convert the continuous time system to a discrete time system and the differential equation to a difference equation or iterative map. The periodic orbit of the continuous time system will correspond to the fixed point of the map thereby making the analysis easier. The iterative map model is suitable for predicting both slow scale and fast-scale instabilities in the system.

To derive the iterative map model of an electrical drive, the state variables will need to be sampled at a fixed time interval (*T*) corresponding to the period of the saw-tooth signal. The expression that relates the state at $t = nT$ to the state at $t = (n+1)T$ can then be obtained. The Poincaré map model of an electrical drive will be of the form:

$$\mathbf{X_{n+1}} = \mathbf{f}(\mathbf{X_n}, d_n) \tag{3.34}$$

where $\mathbf{X_n}$ is the state of the system at $t=nT$, $\mathbf{X_{n+1}}$ is the state of the system at $t = (n+1)T$ and d_n is the duty cycle. Since we are concerned mostly with the steady state behaviour of the drive system, the Poincaré map that describes the behaviour at steady state will suffice. The equivalent iterative map to describe the behaviour of the open-loop PMDC drive is described below. The approach is to solve the dynamic equation (3.32) over the intervals $t \in [0, dT]$ and $t \in [dT, T]$ and thereafter stacking the solutions over one switching period.

$$\begin{aligned} \mathbf{X}(T) &= \Phi(T, dT)\mathbf{X}(dT) + \int_{dT}^{T} \Phi(T, \lambda)\mathbf{V_{off}}\, d\lambda \\ &= K_1\mathbf{X}(dT) + M_1 \end{aligned} \tag{3.35}$$

$$\begin{aligned} \mathbf{X}(dT) &= \Phi(dT, 0)\mathbf{X}(0) + \int_{0}^{dT} \Phi(dT, \lambda)\mathbf{V_{on}}\, d\lambda \\ &= K_2\mathbf{X}(0) + M_2 \end{aligned} \tag{3.36}$$

By substituting (3.36) into (3.35), the solution at the end of the switching period can be expressed as:

$$\begin{aligned}\mathbf{X}(T) &= K_1K_2\mathbf{X}(0)+K_1M_2+M_1\\ &= \mathbf{f}(\mathbf{X}(0),d)\end{aligned} \tag{3.37}$$

where K_1, K_2, M_1, M_2 are derived from equations (3.35) and (3.36) and $\Phi(t_B,t_A)=e^{A(t_\mathbf{B}-t_\mathbf{A})}$. Equation (3.37) is the iterative map or Poincaré map that relates the state at t=0 to the state at t=T and can be written in the form $\mathbf{X_{n+1}}=\mathbf{f}(\mathbf{X_n},d_n)$ where d_n is the duty cycle at the end of each PWM cycle. If the steady state behaviour is periodic, then the present state $\mathbf{X_n}$ will be equal to the state at the end of the clock cycle $\mathbf{X_{n+1}}$ and the fixed point (FP) of the map will be derived as:

$$\begin{aligned}\mathbf{X_{n+1}} &= K_1K_2\mathbf{X_n}+K_1M_2+M_1\\ &= \mathbf{X_n}\end{aligned} \tag{3.38}$$

$$\mathbf{X_n}=\mathbf{X_{FP}}=[\mathbf{I}-K_1K_2]^{\mathbf{-1}}\times(K_1M_2+M_1) \tag{3.39}$$

To complete the derivation of the Poincaré map in closed loop SMPE based systems, we need to compute the duty cycle d_n, but the equation involved is usually nonlinear and transcendental [23] thereby making the derivation of the Poincaré map in closed form difficult.

3.8 Summary

In this chapter the fundamentals of electrical drive operation with emphasis on DC drives and SRM drives are discussed. The details covered include the operating principles, commutation strategies, mathematical models, and control schemes employed in electrical drive systems. The Chapter is concluded with an overview of the modelling techniques commonly used for the nonlinear analysis of electrical drives; state space average modelling and the iterative mapping approach. The state space average modelling technique is a much simpler approach but it is only useful in capturing slow scale instability, and connot detect fast-scale instabilities. The iterative map modelling technique is more complex but is capable of detecting both slow scale and fast-scale instabilities. In the next chapter the nonlinear phenomena that occur in a PMDC drive system will be analysed in detail.

CHAPTER 4

ANALYSIS OF NONLINEAR PHENOMENA IN DC CHOPPER-FED PERMANENT MAGNET DC DRIVES

4.1 Introduction

Switched mode power electronic based systems including electrical drives often exhibit complex, nonlinear behaviour. The nominal steady state behaviour of such systems is a periodic ripple with a mean value close to the reference state and the same period as the external clock. This operating regime is referred to as a period-1 operating mode, and the steady state trajectory in this operating mode is known as a period-1 orbit. As some system parameter (such as the supply voltage or controller gains) is being varied, this nominal orbit loses stability, and another attracting orbit of period-*nT* (*subharmonics*) or a quasiperiodic orbit emerges. This qualitative change in the steady state trajectory of the system under parameter variation (also known as bifurcation) is typical of all nonlinear systems, and was discussed in Chapter 2. Further variation of the parameter leads to the birth of an aperiodic or chaotic orbit.

In this Chapter, the nonlinear phenomena in DC chopper-fed PMDC drives employing simple proportional control and the more practical proportional integral (PI) control will be analysed. Apart from the *period doubling* (or *fast-scale bifurcation*) that was reported by Chau et al. [7, 8] when the proportional controller was employed, the phenomena of co-existing attractors and fractal basin boundary at some parameter values are observed and reported in this thesis for the first time in this simple deterministic system. Also, when employing a PI controller, a *Neimark-Sacker* (or *slow scale bifurcation*) was observed and experimentally validated. The analysis and experimental validation of the Neimark-Sacker bifurcation in a PI controlled PMDC drive which is presently absent from literature is one of the major contributions of this thesis. The first report of Neimark-Sacker bifurcation in DC drive was by Tse et. al. [3] but this was neither analysed nor experimentally validated.

Similar to other SMPE systems such as DC-DC converters, the analysis of the nonlinear phenomena in PMDC drives will involve the stability analysis of a limit cycle or periodic orbit rather than an equilibrium point, hence its complexity. The most common technique for performing the stability analysis of a limit cycle is the Poincaré map or iterative map approach [20, 30, 72]. But, as was discussed in Chapter 2 and Chapter 3, the iterative map will be difficult to derive in closed form in some power electronic systems (including electrical drives) due to the transcendental nature of the equations involved. Also, the iterative map approach is very complicated when applied to higher order drives such as the SRM drives. In this project, an alternative technique for stability analysis of the periodic orbit will be employed. This technique (also referred to as *Monodromy* matrix approach in some literature) is based on Filippov's method of differential inclusion [22] and will achieve the same objective as the Poincaré map technique, but in a much more straightforward way. It has been successfully employed in analysing stick-slip oscillations in mechanical systems [65], and subharmonics oscillations in DC-DC converters [23, 24, 66]. This represents its first application in an electrical drive system. The key idea is to obtain the state transition matrix (STM) around the nominal orbit (known as the *Monodromy matrix*) and evaluate its eigenvalues known as *Floquet multipliers*. The nominal orbit is stable if the absolute values of the Floquet multipliers is within the unit circle and unstable otherwise. The Monodromy matrix and its eigenvalues can be used to predict slow scale and fast-scale instabilities that occur in electrical drive systems.

This chapter is organized as follows: in section 4.2, nonlinear phenomena in DC chopper-fed PMDC drives operating under proportional control is investigated. The fast-scale bifurcation phenomenon in the drive will be initially investigated using numerical simulations and will be validated by the stability analysis of the nominal period-1 orbit of the drive using the Monodromy matrix approach. Also, the occurrence of co-existing attractors and fractal basin boundaries at some system parameter values are investigated both numerically and analytically. In section 4.3, the nonlinear phenomena in a more practical PI controlled PMDC drive is analyzed (using both the Monodromy matrix and state space averaging technique) and experimentally validated. Section 4.4 is the chapter summary.

4.2 Nonlinear Analysis of DC Chopper Fed PMDC Drives Employing the Proportional Controller

4.2.1 System Overview.

The schematic diagram of DC-chopper fed voltage mode controlled PMDC drive employing the proportional controller was earlier shown in Fig. 3.9 but will be repeated in Fig. 4.1 for easy reference. The system consists of three main components namely the PMDC motor, the power converter (a dc chopper) and the control electronics. The shaft speed ω(t) is controlled by control of the average voltage at the armature terminals via pulse width modulation (PWM). Under CCM, the system will alternate between two circuit topologies (detailed in Chapter 3) at steady state, depending on the relative magnitudes of the control signal $V_{\mathrm{con}}(t)$ and the sawtooth signal $V_{\mathrm{ramp}}(t)$.

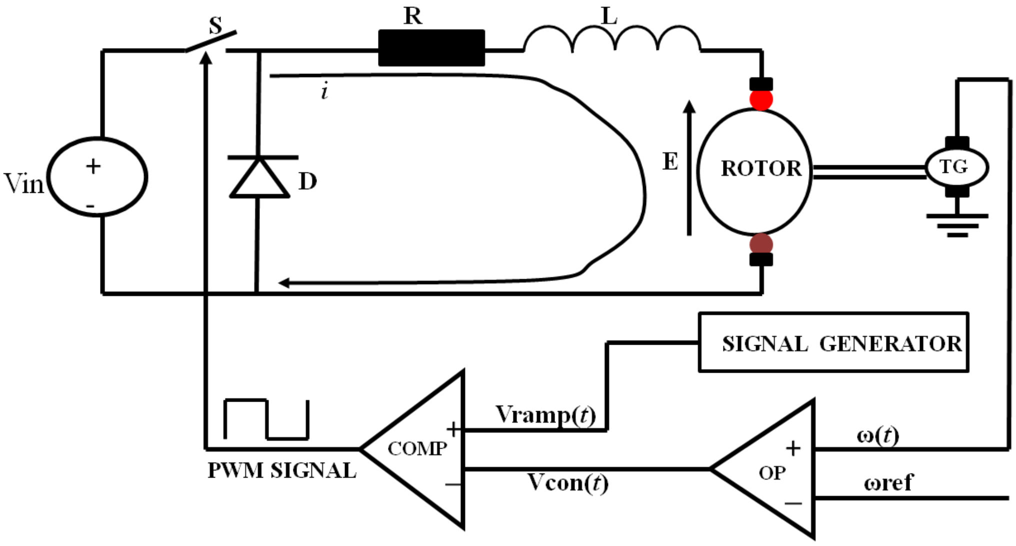

Fig. 4.1 Schematic diagram of voltage mode controlled DC chopper-fed PMDC drive.

When the sawtooth signal is greater than the control signal, the PWM output goes high, the switch (S) closes, the diode (D) opens (is reverse biased) and the system model will be described by the equation:

$$\frac{d\mathbf{X}(t)}{dt} = \mathbf{A_{on}}\mathbf{X}(t) + \mathbf{V_{on}}$$

(4.1)

But when the sawtooth signal is lower than the control signal, the PWM output goes low, the switch (**S**) opens, the diode (**D**) conducts (becomes forward biased) and the system model will be described by the equation:

$$\frac{d\mathbf{X}(t)}{dt} = \mathbf{A_{off}}\mathbf{X}(t) + \mathbf{V_{off}} \tag{4.2}$$

For the purpose of nonlinear analysis equations (4.1) and (4.2) can be combined leading to the equation below:

$$\frac{d\mathbf{X}(t)}{dt} = \begin{cases} \mathbf{f_{OFF}}(\mathbf{X}(t)) = \mathbf{A_{off}}\mathbf{X}(t) + \mathbf{V_{off}},\ V_{con}(t) > V_{ramp}(t) \\ \\ \mathbf{f_{ON}}(\mathbf{X}(t)) = \mathbf{A_{on}}\mathbf{X}(t) + \mathbf{V_{on}},\ \ V_{con}(t) < V_{ramp}(t) \end{cases} \tag{4.3}$$

where $\mathbf{f_{OFF}}(\mathbf{X}(t))$ is the vector field before the switching manifold, $\mathbf{f_{ON}}(\mathbf{X}(t))$ is the vector field after the switching manifold and $\mathbf{X(}t\mathbf{)} = [\omega(t)\ \ i(t)]^T = [x_1(t)\ \ x_2(t)]^T$ is the state vector.

$$V_{con}(t) = Kp \times (\omega(t) - \omega_{ref}) = Kp \times (x_1(t) - \omega_{ref}) \tag{4.4}$$

$$V_{ramp}(t) = V_L + (V_U - V_L)\frac{t}{T} \bmod 1 = V_L + V_D \times \frac{t}{T} \bmod 1 \tag{4.5}$$

where V_L is the lower voltage of the sawtooth signal, V_U is the upper voltage of the sawtooth signal, ($V_D = V_U - V_L$), and T is the PWM period.

$$\mathbf{A_{on}} = \mathbf{A_{off}} = \mathbf{A} = \begin{bmatrix} \frac{-B}{J} & \frac{K_t}{J} \\ \\ \frac{-K_e}{L} & \frac{-R}{L} \end{bmatrix},\ \mathbf{V_{on}} = \begin{bmatrix} \frac{-T_L}{J} \\ \\ \frac{V_{in}}{L} \end{bmatrix},\ \text{and}\ \mathbf{V_{off}} = \begin{bmatrix} \frac{-T_L}{J} \\ \\ 0 \end{bmatrix}$$

4.2.2 Dynamic Behaviour of DC Chopper-fed PMDC Drives

The nominal steady state behaviour of a DC chopper-fed PMDC drive is DC waveforms with periodic ripple at the same frequency as the PWM signal (Figs. 4.2 and 4.3). As some system parameters such as the proportional gain (Kp) or supply voltage (V_{in}) are being varied, this nominal orbit (also known as period-1 orbit) loses stability via a period doubling or fast-scale bifurcation [7] and a new orbit whose period is double the period of the original orbit emerges (Figs. 4.4 and 4.5). Further variation of the system parameter leads to period doubling bifurcation cascades and chaos (Figs. 4.6 and 4.7). In order to confirm the occurrence of chaos, the system response to slight variation in the initial condition was tested, and the result (Fig. 4.8) indicates that the steady state behaviour depends on the initial condition, thus satisfying the property of a chaotic system [9]. Also the chaotic phase portrait in Fig. 4.7 indicates that the occurrence of chaos does not imply that the steady state trajectory is unbounded, hence the term ‘strange attractor’ [9]. The bifurcation diagram of the system as the proportional gain is being varied is shown in Fig. 4.9, while the bifurcation diagram as the supply voltage is being varied is shown in Fig. 4.10. The fixed parameters of the system are: K_t=0.1324NM/A,L=36mH, R=3.5Ω, B=0.000564Nm.rad^{-1}.sec, K_e=0.1356Vs/rad,T=4ms, J=9.71×10^{-4}N.m.rad^{-1}.sec^{2}.

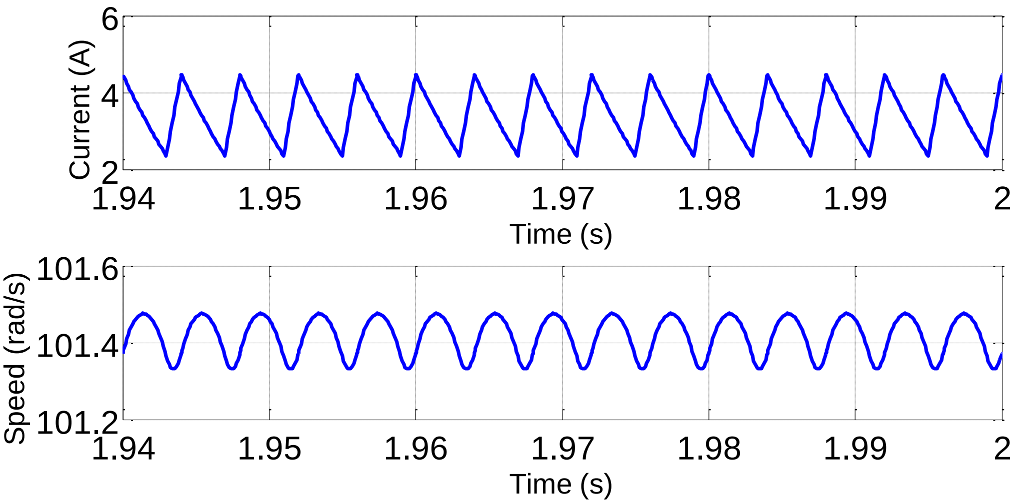

Fig. 4.2 Nominal period-1 current and speed trajectory in time domain; Kp=1.2 , V_{in}=100 V.

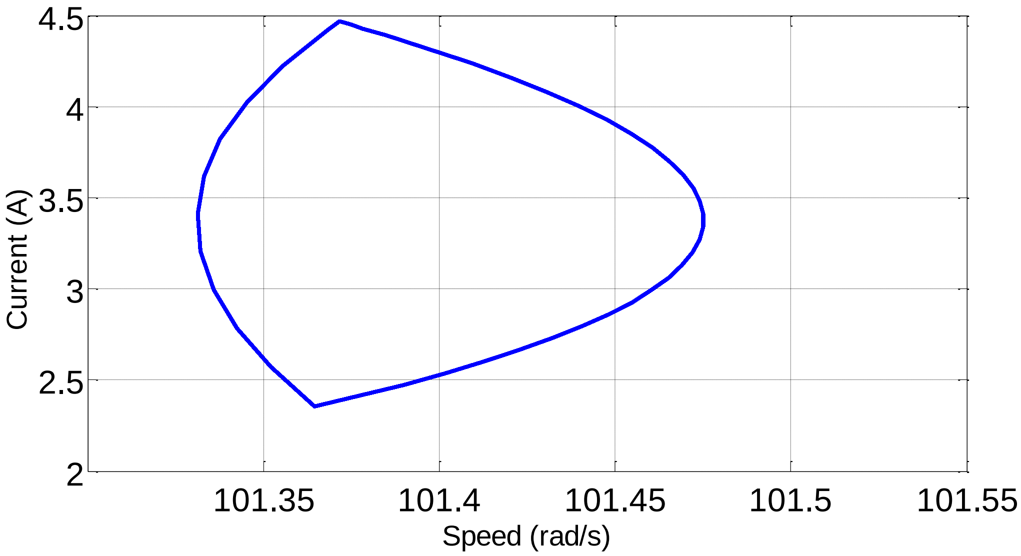

Fig. 4.3 Period-1 phase portrait.

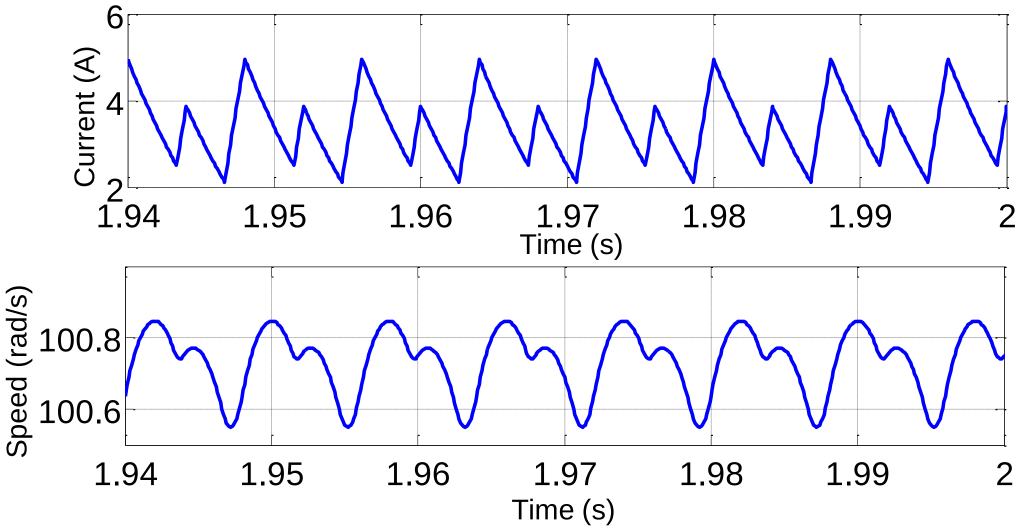

Fig. 4.4 Period-2 current and speed trajectory at *Kp*=2.4.

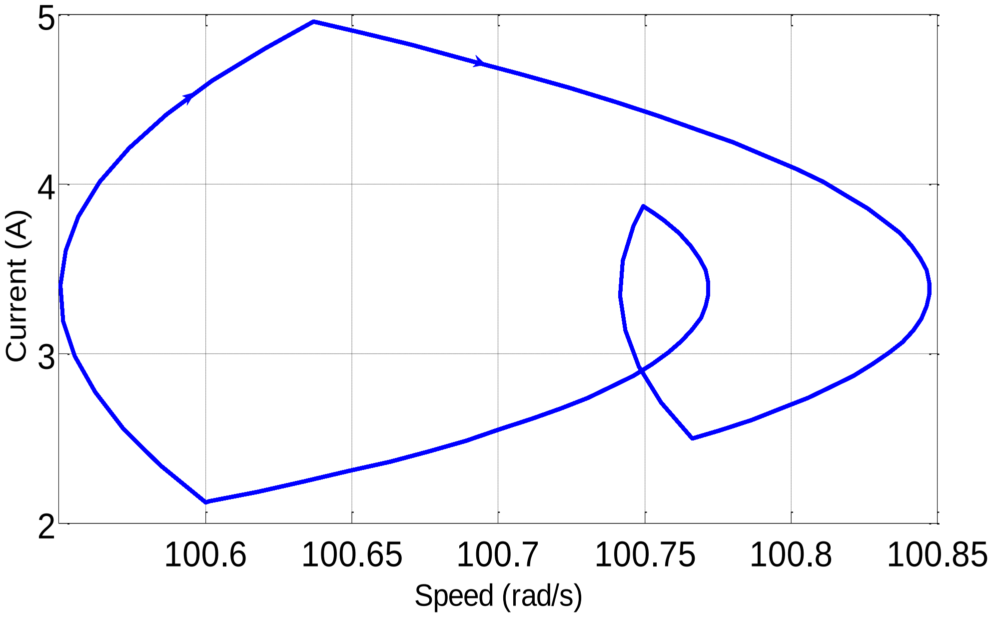

Fig. 4.5 Period-2 phase portrait**.**

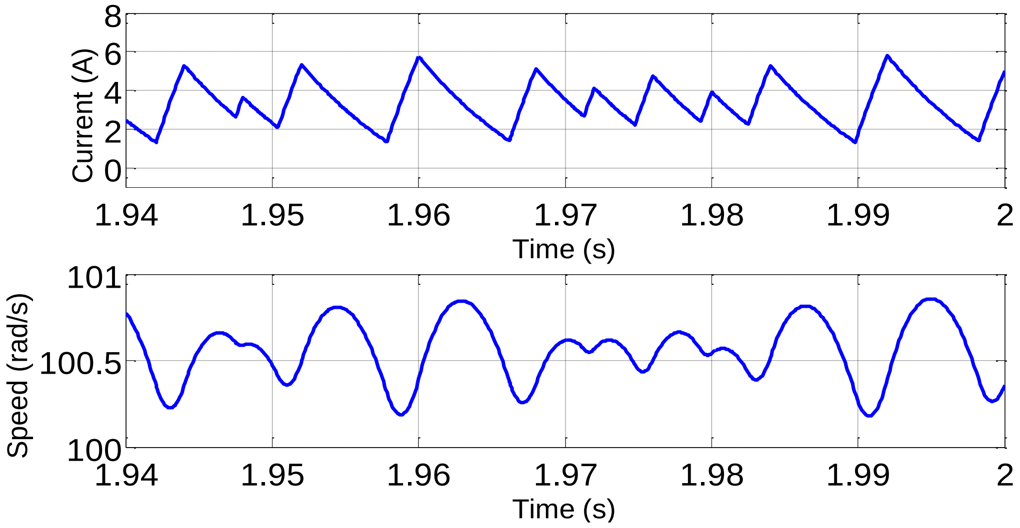

Fig. 4.6 Chaotic current and speed trajectory at *Kp*=3.2.

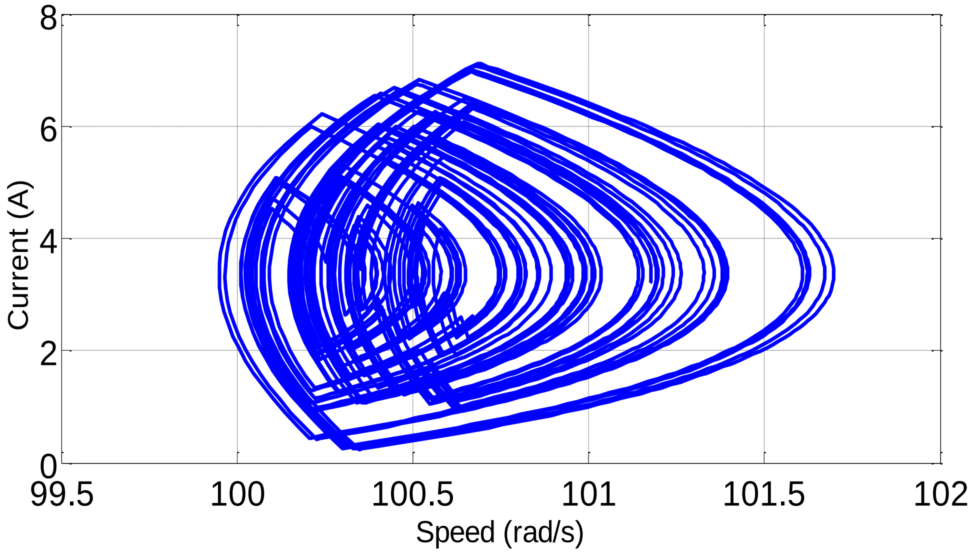

Fig. 4.7 Chaotic phase portrait

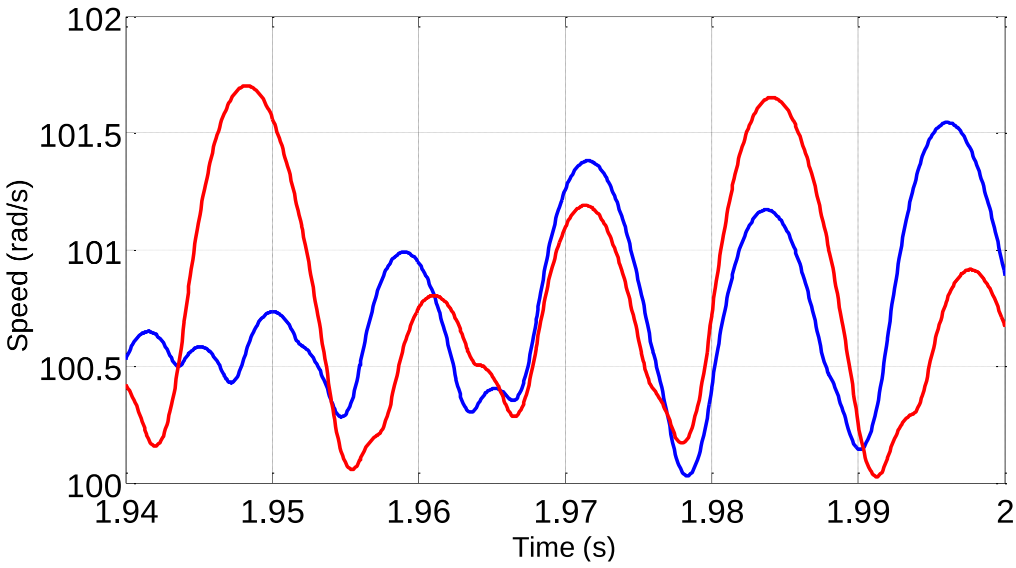

Fig. 4.8 Results of the sensitivity to initial conditions test at *Kp*=3.2 showing the divergence of the speed trajectories when $\omega(0)=0.55$Rad/s and $i(0)=0.55$A (blue) and when $\omega(0)=0.56$ Rad/s and $i(0)=0.56$ A (red).

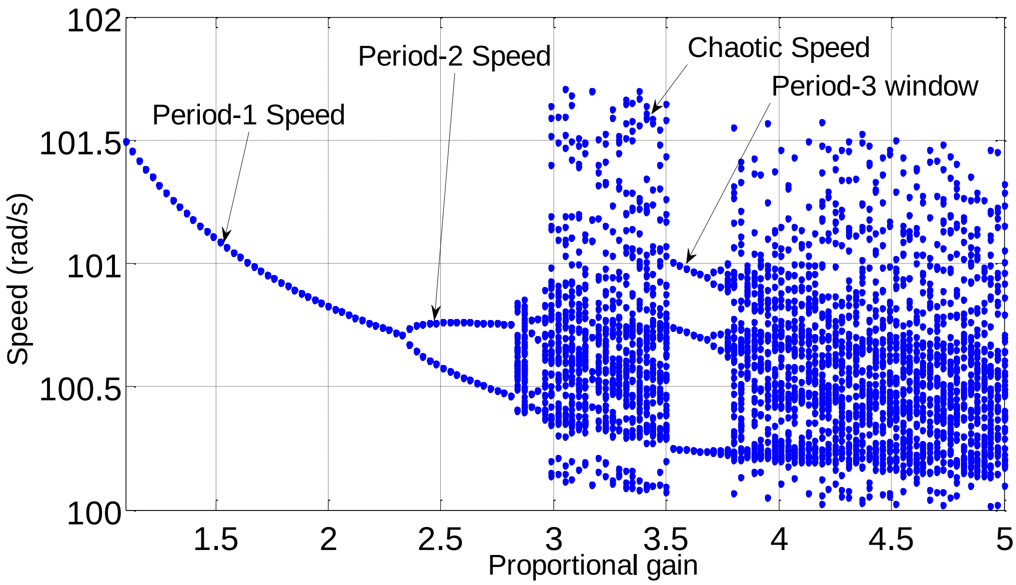

Fig. 4.9 Bifurcation diagram showing speed as the proportional gain is varied; $V_{in}=100$ V.

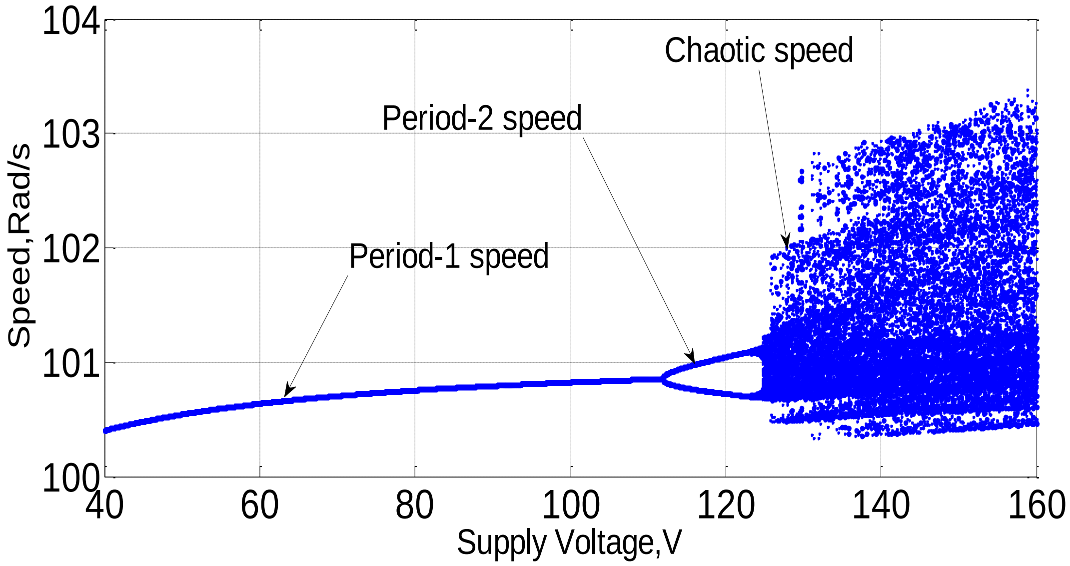

Fig. 4.10 Bifurcation diagram showing speed as the supply voltage is varied; *Kp*=2.

The bifurcation diagrams (Fig. 4.9 and Fig. 4.10) summarised the steady instability that occurs in DC Chopper-fed PMDC drives as the proportional gain or supply voltage are varied. The diagrams were obtained by varying the system's bifurcation parameter over some interval (1.1-5 for the proportional gain and 40V-160V for the supply voltage), and sampling the states at a discrete interval (*T*), corresponding to the period of the PWM signal. The steady state samples are then stored and plotted against the bifurcation parameter.

As the proportional gain (*Kp*) is varied (Fig. 4.9), the system operates at nominal period-1 orbit for $Kp \in [1.1, 2.34]$ and then loses stability via a period doubling bifurcation, leading to the birth of a period-2 attractor. From $Kp = 2.34$ to $Kp = 2.8$, the period-2 attractor is the only attracting set in the system. As *Kp* is varied further, the system undergoes period doubling bifurcation cascades leading to the birth of the chaotic attractor. At Kp=3.5, an intermittent *period-3 window* appeared which also undergoes period doubling route to chaos as the gain is varied further.

Similarly, as the supply voltage is varied (Fig. 4.10) it could be seen that the system operates at nominal period-1 behaviour for $V_{in} \in [40V, 111.83V]$, but at V_{in} =111.83V this nominal orbit loses stability and a period-2 orbit emerges. The period-2 orbit remains stable (attracts trajectories of initial points) until V_{in} =123.5V when it lost stability and begins to repel. For $V_{in} \in [125V, 160V]$, the system behaviour is aperiodic or chaotic and will be difficult to predict in the long term.

4.2.3 Stability Analysis of the Period-1 orbit using the Monodromy Matrix Approach

To analyze the fast-scale bifurcation in a DC chopper-fed PMDC drive employing the proportional controller, we have to perform a stability analysis of the period-1 orbit of the drive. In this thesis, the Monodromy matrix approach (detailed in Chapter2) will be employed in the analysis. The period-1 orbit of a DC Chopper-fed PMDC drive is shown in Fig. 4.3 but is repeated here (Fig. 4.11) for convenience, while a typical interaction of the control signal and the ramp signal for one PWM cycle is shown in Fig. 4.12. To analyze the stability of the orbit we need to study the system steady state dynamics for $t \in [0,T]$ where T is the period of the PWM cycle.

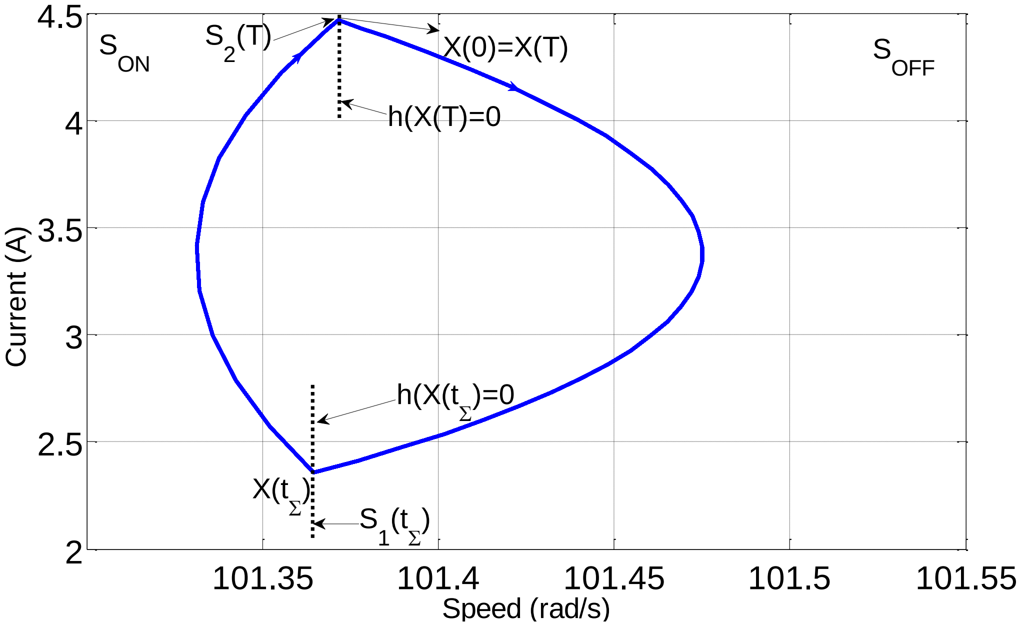

Fig. 4.11 Period-1 orbit of a DC Chopper-fed PMDC drive

From Figure 4.11, the state transition matrix (STM) over a complete cycle of the orbit (the so called Monodromy matrix) is expressed as:

$$M(T,0) = \mathbf{S}_2 \times \Phi(T,t_\Sigma) \times \mathbf{S}_1 \times \Phi(t_\Sigma,0) \tag{4.6}$$

where $\Phi(t_B,t_A)$ is the STM from $t=t_A$ to $t=t_B$ and is expressed as $\Phi(t_B,t_A) = e^{A(t_B-t_A)}$, $\mathbf{S}_1$ is the Saltation matrix that govern the transition of the trajectory from the switch OFF ($\mathbf{S}_{\mathbf{OFF}}$) region of the state space to the switch ON region ($\mathbf{S}_{\mathbf{ON}}$), and S2 is the Saltation matrix that govern the transition from region $\mathbf{S}_{\mathbf{ON}}$ to region $\mathbf{S}_{\mathbf{OFF}}$,

$t_\Sigma = (1-d)\times T = \delta \times T$ is the switching instant and $d = \dfrac{T_{ON}}{T}$. Consequently, the Monodromy matrix will be expressed as:

$$M(T,0) = \mathbf{S}_2 \times e^{A(T-t_\Sigma)} \times \mathbf{S}_1 \times e^{At_\Sigma} \tag{4.7}$$

where the Saltation matrices $\mathbf{S}_1$, $\mathbf{S}_2$ and the switching instant (t_Σ) are the only unknowns.

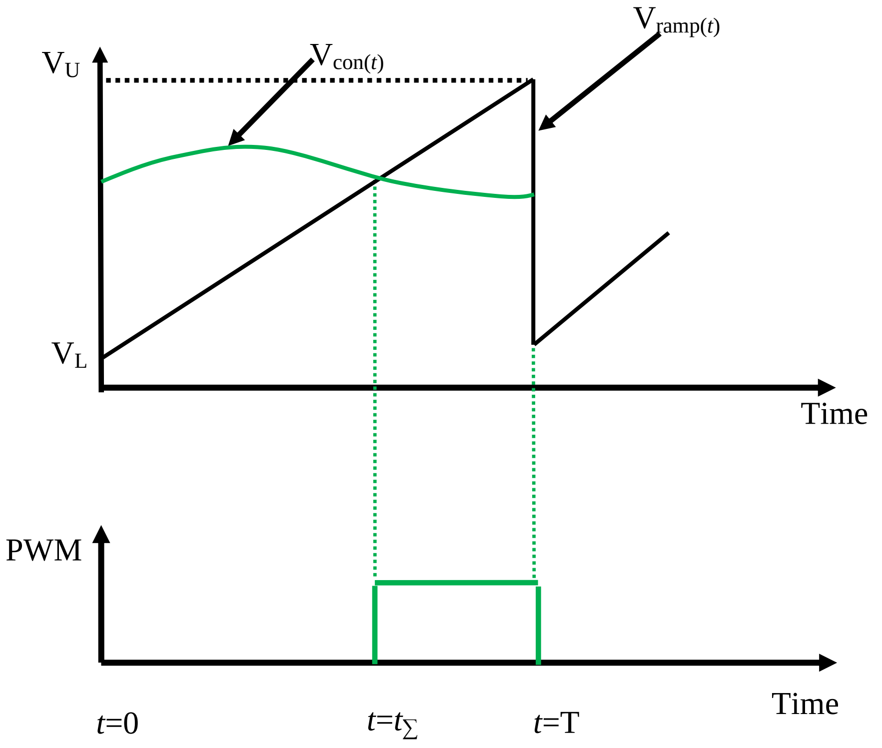

Fig. 4.12 Interaction of the control signal and the ramp signal for one PWM cycle.

As detailed in Chapter 2 and in [23, 65, 66] the Saltation matrix can be expressed as:

$$\mathbf{S} = \mathbf{I} + \frac{(\mathbf{f}_+ - \mathbf{f}_-)\mathbf{n}^T}{\mathbf{n}^T \mathbf{f}_- + \left.\dfrac{\partial h(\mathbf{X}(t))}{\partial t}\right|_{t=t_\Sigma}} \tag{4.8}$$

where h defines the location of the switching hypersurface, $\mathbf{n}$ is the normal vector to the hypersurface, $\mathbf{f}_-$ is the vector field before the switching instant and is given by $\lim_{t\downarrow t_\Sigma} \mathbf{f}_-(\mathbf{X}(t),t)$, $\mathbf{f}_+$ is the vector field after the switching instant and is given by $\lim_{t\uparrow t_\Sigma} \mathbf{f}_+(\mathbf{X}(t),t)$, and $\mathbf{I}$ is an identity matrix of the same order with the system. The

Saltation matrices for the DC chopper-fed PMDC drive can be derived following the procedure described below.

Assuming the initial state vector of the system is **X**(0) (Fig.4.11), then for $t \in [0, t_{\Sigma}]$ (Fig. 4.12) $V_{\text{con}}(t)$ is greater than $V_{\text{ramp}}(t)$, the PWM output is low, the switch is OFF and the system dynamics is described by $\overline{\mathbf{X}}(t) = \mathbf{f_{OFF}}(\mathbf{X}(t)) = \mathbf{A_{off}}\mathbf{X}(t) + \mathbf{V_{off}}$.

Similarly, for $t \in [t_{\Sigma}, T]$, $V_{\text{con}}(t)$ is less than $V_{\text{ramp}}(t)$, the PWM output is high, the switch is ON and the system dynamics is described by $\overline{\mathbf{X}}(t) = \mathbf{f_{ON}}(\mathbf{X}(t)) = \mathbf{A_{on}}\mathbf{X}(t) + \mathbf{V_{on}}$, with the last value of the state vector $\mathbf{X}(t_{\Sigma})$ serving as the initial state.

At $t = t_{\Sigma}$, the trajectory crossed from the switch OFF region of the state space to the switch ON region and the switching hypersurface expression is given by:

$$h(\mathbf{X}(t)) = V_{con}(t) - V_{ramp}(t) = Kp(x_1(t) - \omega_{ref}) - (V_L + (V_U - V_L))\frac{t}{T} \tag{4.9}$$

Since $V_{\text{con}}(t) = V_{\text{ramp}}(t)$ at the switching instant ($t = t_{\Sigma}$), the hypersurface or switching equation is given by:

$$h(\mathbf{X}(t_{\Sigma})) = x_1(t_{\Sigma}) - \omega_{ref} - \frac{V_L + (V_U - V_L)\delta}{Kp} = 0 \tag{4.10}$$

where $t_{\Sigma} = (1 - d) \times T = \delta \times T$.

From (4.9), the partial derivative of the hypersurface expression with respect to time $\frac{\partial h(\mathbf{X}(t))}{\partial t}$ and the normal (**n**) to the hypersurface can be expressed as:

$$\frac{\partial h(\mathbf{X}(t))}{\partial t} = \frac{-(V_U - V_L)}{T} \tag{4.11}$$

$$\mathbf{n} = \nabla h(X(t), t) = \begin{bmatrix} \dfrac{\partial h(X(t))}{\partial x_1} \\ \dfrac{\partial h(X(t))}{\partial x_2} \end{bmatrix} = \begin{bmatrix} Kp \\ 0 \end{bmatrix} \tag{4.12}$$

and the transpose of the normal to the hypersurface ($\mathbf{n}^T$) is given by $\mathbf{n}^T = [Kp \quad 0]$

$$\mathbf{f}_+ = \mathbf{f_{ON}} = \mathbf{A_{on}}\mathbf{X}(t_{\Sigma}) + \mathbf{V_{on}} \tag{4.13}$$

$$\mathbf{f}_- = \mathbf{f_{OFF}} = \mathbf{A_{off}}\mathbf{X}(t_{\Sigma}) + \mathbf{V_{off}} \tag{4.14}$$

$$\mathbf{f}_{+} - \mathbf{f}_{-} = \mathbf{f}_{\mathbf{ON}} - \mathbf{f}_{\mathbf{OFF}} = \mathbf{V}_{\mathbf{on}} - \mathbf{V}_{\mathbf{off}} = \begin{bmatrix} 0 \\ \\ \dfrac{V_{in}}{L} \end{bmatrix} \tag{4.15}$$

$$(\mathbf{f}_{\mathbf{ON}} - \mathbf{f}_{\mathbf{OFF}}) \times \mathbf{n}^{T} = \begin{bmatrix} 0 & 0 \\ \\ \dfrac{V_{in}Kp}{L} & 0 \end{bmatrix} \tag{4.16}$$

$$\mathbf{n}^{T} \times \mathbf{f}_{\mathbf{OFF}} = [Kp \quad \mathbf{0}] \times \begin{bmatrix} \dfrac{K_t x_2(t_\Sigma) - Bx_1(t_\Sigma) - T_L}{J} \\ \dfrac{-Rx_2(t_\Sigma) - K_e x_1(t_\Sigma)}{L} \end{bmatrix} = Kp\left(\frac{K_t x_2(t_\Sigma) - Bx_1(t_\Sigma) - T_L}{J}\right) \tag{4.17}$$

Consequently the Saltation matrix ($\mathbf{S}_1$) is given by:

$$\mathbf{S}_1 = \begin{bmatrix} 1 & 0 \\ \\ 0 & 1 \end{bmatrix} + \frac{(\mathbf{f}_{\mathbf{ON}} - \mathbf{f}_{\mathbf{OFF}})\,\mathbf{n}^{T}}{\mathbf{n}^{T}\,\mathbf{f}_{\mathbf{OFF}} + \left.\dfrac{\partial h(\mathbf{X}(t))}{\partial t}\right|_{t=t_\Sigma}} = \begin{bmatrix} 1 & 0 \\ \\ \mathbf{s}_{\mathbf{21}} & 1 \end{bmatrix} \tag{4.18}$$

$$\begin{aligned} s_{21} &= \frac{\dfrac{V_{in}Kp}{L}}{Kp\left(\dfrac{K_t x_2(t_\Sigma) - Bx_1(t_\Sigma) - T_L}{J}\right) - \dfrac{V_U - V_L}{T}} \\ &= \frac{\dfrac{V_{in}}{L}}{\left(\dfrac{K_t x_2(t_\Sigma) - Bx_1(t_\Sigma) - T_L}{J}\right) - \dfrac{V_U - V_L}{Kp \times T}} \end{aligned} \tag{4.19}$$

where the state vector at the switching instant $\mathbf{X}(t_\Sigma)$ is the only unknown and will be obtained by computing the initial state vector $\mathbf{X}(0)$ and the switching instant t_Σ. From Fig.4.11 we have:

$$\begin{aligned} \mathbf{X}(T) = \mathbf{X}(0) &= \Phi(T, t_\Sigma)\mathbf{X}(t_\Sigma) + \int_{t_\Sigma}^{T} \Phi(T, \lambda)\mathbf{V}_{\mathbf{on}}\, d\lambda \\ &= K_1\mathbf{X}(t_\Sigma) + M_1 \end{aligned} \tag{4.20}$$

$$\begin{aligned}\mathbf{X}(t_\Sigma) &= \Phi(t_\Sigma,0)\mathbf{X}(0)+\int_0^{t_\Sigma}\Phi(t_\Sigma,\lambda)\mathbf{V_{off}}\,d\lambda \\ &= K_2\mathbf{X}(0)+M_2\end{aligned} \tag{4.21}$$

By substituting (4.21) into (4.20) we get:

$$\begin{aligned}\mathbf{X}(0) &= K_1(K_2\mathbf{X}(0)+M_2)+M_1 \\ &= K_1K_2\mathbf{X}(0)+K_1M_2+M_1\end{aligned} \tag{4.22}$$

$$\mathbf{X}(0)=(\mathbf{I}-K_1K_2)^{\mathbf{-1}}\times(K_1M_2+M_1) \tag{4.23}$$

where $K_1=\Phi(T,t_\Sigma)=e^{\mathbf{A}(T-t_\Sigma)}$, $K_2=\Phi(t_\Sigma,0)=e^{\mathbf{A}t_\Sigma}$, $K_1K_2=e^{\mathbf{A}T}$, $M_1=\int_{t_\Sigma}^{T}\Phi(T,\lambda)\mathbf{V_{on}}\,d\lambda$

and $M_2=\int_0^{t_\Sigma}\Phi(t_\Sigma,\lambda)\mathbf{V_{off}}\,d\lambda$

Consequently the initial state **X**(0) will be expressed as :

$$\mathbf{X}(0)=(\mathbf{I}-e^{\mathbf{A}T})^{-1}\times\begin{pmatrix} e^{\mathbf{A}(T-t_\Sigma)}\int_0^{t_\Sigma}e^{\mathbf{A}(t_\Sigma-\tau)}\mathbf{V_{off}}\,d\tau \\ +\int_{t_\Sigma}^{T}e^{\mathbf{A}(T-\tau)}\mathbf{V_{on}}\,d\tau)\end{pmatrix} \tag{4.24}$$

Equation (4.24) expresses the initial condition **X**(0) in terms of the switching instant $t_\Sigma=(1-d)\times T=\delta\times T$. To obtain the value of the state vector at the switching instant $\mathbf{X}(t_\Sigma)$, the switching instant (t_Σ) and the initial state vector **X**(0) must be known. Thus the duty ratio δ will need to be calculated. This can be achieved by making use of the hypersurface expression (4.10) and the expression for the state vector at the switching instant (4.21), giving the equation:

$$x_1(t_\Sigma)=\begin{bmatrix}1 & 0\end{bmatrix}(e^{\mathbf{A}t_\Sigma}\mathbf{X}(0)+\int_0^{t_\Sigma}e^{\mathbf{A}(t_\Sigma-\tau)}\mathbf{V_{off}}\,d\tau)=\omega_{ref}+\frac{(V_L+(V_U-V_L)\delta)}{Kp} \tag{4.25}$$

By substituting the expression for **X**(0) in equation (4.24) into equation (4.25) we have the expression (4.26) with the duty ratio δ as the only unknown. This equation can be solved numerically for the duty ratio using the Newton-Raphson technique.

$$\begin{bmatrix}1 & 0\end{bmatrix}\times\left(e^{\mathbf{A}t_\Sigma}\times(\mathbf{I}-e^{\mathbf{A}T})^{-1}\times\begin{pmatrix} e^{\mathbf{A}(T-t_\Sigma)}\int_0^{t_\Sigma}e^{\mathbf{A}(t_\Sigma-\tau)}\mathbf{V_{off}}\,d\tau \\ +\int_{t_\Sigma}^{T}e^{\mathbf{A}(T-\tau)}\mathbf{V_{on}}\,d\tau)\end{pmatrix}+\int_0^{t_\Sigma}e^{\mathbf{A}(t_\Sigma-\tau)}\mathbf{V_{off}}\,d\tau\right)-\omega_{ref}-\frac{(V_L+(V_U-V_L)\delta)}{Kp}=0 \tag{4.26}$$

Once the duty ratio (δ) is known, the initial state vector $\mathbf{X}(0)$ will be easily evaluated from equation (4.24), and the state vector at the switching instant $\mathbf{X}(t_{\Sigma})$ will be computed from equation (4.21). The Saltation matrix ($\mathbf{S}_1$) will then be evaluated by substituting $\mathbf{X}(t_{\Sigma})$ into equation (4.18).

The Saltation matrix $\mathbf{S}_2$ governs the transition from the region $\mathbf{S_{ON}}$ back to the region $\mathbf{S_{OFF}}$ at the end of the switching cycle (t=T) as shown in Fig. 4.11.

$$\mathbf{S}_2 = \begin{bmatrix} 1 & 0 \\ 0 & 1 \end{bmatrix} + \frac{(\mathbf{f}_{\mathbf{OFF}} - \mathbf{f}_{\mathbf{ON}})\mathbf{n}^T}{\mathbf{n}^T \mathbf{f}_{\mathbf{ON}} + \left.\dfrac{\partial h(\mathbf{X}(t))}{\partial t}\right|_{t=T}} \tag{4.27}$$

But because of the sudden discontinuity of the sawtooth signal at t=T, $\left.\dfrac{\partial h(\mathbf{X}(t))}{\partial t}\right|_{t=T} = \infty$

and consequently $\mathbf{S}_2 = \begin{bmatrix} 1 & 0 \\ 0 & 1 \end{bmatrix}$.

By substituting the Saltation matrices ($\mathbf{S}_1$, $\mathbf{S}_2$) and the switching instant $(t_{\Sigma} = \delta \times T)$ into equation (4.7), the Monodromy matrix can be evaluated. The stability of the nominal period-1 orbit depends on the eigenvalues of the Monodromy matrix (the so called Floquet multipliers). The nominal orbit will be stable if the absolute value of the Floquet multipliers is within the unit circle and unstable otherwise.

The computed duty ratio (δ), initial state $\mathbf{X}(0)$, and the state vector at the switching instant $\mathbf{X}(t_{\Sigma})$ as the proportional gain (Kp) is varied are shown in Table 4.1, while the computed Saltation matrix, Monodromy matrix, and Floquet multipliers are shown in Table 4.2. A plot of the proportional gain against the duty ratio is shown in Fig. 4.13, while the eigenvalue loci are shown in Fig. 4.14.

Table 4.1 Changes in duty ratio, the initial state, and the state vector at the switching instant as the proportional gain is varied

Gain (Kp)	$\delta = t_\Sigma / T$	$d = 1 - \delta$	$\mathbf{X}(0)$	$\mathbf{X}(t_\Sigma)$
1.2	0.7443	0.2557	$\begin{bmatrix}101.3716\\4.4660\end{bmatrix}$	$\begin{bmatrix}101.3645\\2.3560\end{bmatrix}$
1.5	0.7447	0.2553	$\begin{bmatrix}101.0993\\4.4638\end{bmatrix}$	$\begin{bmatrix}101.0922\\2.3559\end{bmatrix}$
1.8	0.7449	0.2551	$\begin{bmatrix}100.9176\\4.4623\end{bmatrix}$	$\begin{bmatrix}100.9105\\2.3559\end{bmatrix}$
2.2	0.7452	0.2548	$\begin{bmatrix}100.7523\\4.4609\end{bmatrix}$	$\begin{bmatrix}100.7452\\2.3559\end{bmatrix}$
2.3	0.7452	0.2548	$\begin{bmatrix}100.7199\\4.4606\end{bmatrix}$	$\begin{bmatrix}100.7128\\2.3559\end{bmatrix}$
2.33	0.7453	0.2547	$\begin{bmatrix}100.7108\\4.4606\end{bmatrix}$	$\begin{bmatrix}100.7037\\2.3559\end{bmatrix}$
2.34	0.7453	0.2547	$\begin{bmatrix}100.7078\\4.4605\end{bmatrix}$	$\begin{bmatrix}100.7007\\2.3559\end{bmatrix}$

From Table 4.1, it could be seen that as the proportional gain is changed from 2.33 to 2.34 the duty ratio remains nearly constant. Consequently the product term $e^{A(T-t_\Sigma)} \times e^{At_\Sigma}$ in equation (4.7) does not change leading to the conclusion that the change in Monodromy matrix (Table 4.2) was mainly due to changes in the Saltation matrix as the system parameters are being varied. The sensitivity of the Saltation matrix to system parameter changes is the basis for the control of the fast-scale bifurcation and chaos that will be discussed in Chapter 6.

Table 4.2 Computed Saltation matrix and Monodromy matrix as the proportional gain is varied

Gain (*Kp*)	Saltation matrix	Monodromy Matrix	Floquet Multipliers
1.2	$\begin{bmatrix} 1.0000 & 0 \\ -4.6481 & 1.0000 \end{bmatrix}$	$\begin{bmatrix} 0.3795 & 0.2336 \\ -4.2034 & -0.8057 \end{bmatrix}$	-0.2131 + 0.7942i -0.2131 - 0.7942i
1.5	$\begin{bmatrix} 1.0000 & 0 \\ -5.4919 & 1.0000 \end{bmatrix}$	$\begin{bmatrix} 0.2691 & 0.1945 \\ -4.9650 & -1.0756 \end{bmatrix}$	-0.4033 + 0.7167i -0.4033 - 0.7167i
1.8	$\begin{bmatrix} 1.0000 & 0 \\ -6.2481 & 1.0000 \end{bmatrix}$	$\begin{bmatrix} 0.1701 & 0.1594 \\ -5.6475 & -1.3174 \end{bmatrix}$	-0.5737 + 0.5892i -0.5737 - 0.5892i
2.2	$\begin{bmatrix} 1.0000 & 0 \\ -7.1421 & 1.0000 \end{bmatrix}$	$\begin{bmatrix} 0.0530 & 0.1179 \\ -6.4544 & -1.6033 \end{bmatrix}$	-0.7751 + 0.2746i -0.7751 - 0.2746i
2.3	$\begin{bmatrix} 1.0000 & 0 \\ -7.3478 & 1.0000 \end{bmatrix}$	$\begin{bmatrix} 0.0261 & 0.1084 \\ -6.6401 & -1.6691 \end{bmatrix}$	-0.8215 + 0.0375i -0.8215 - 0.0375i
2.33	$\begin{bmatrix} 1.0000 & 0 \\ -7.4083 & 1.0000 \end{bmatrix}$	$\begin{bmatrix} 0.0182 & 0.1056 \\ -6.6946 & -1.6884 \end{bmatrix}$	-0.6897 -0.9805
2.34	$\begin{bmatrix} 1.0000 & 0 \\ -7.4283 & 1.0000 \end{bmatrix}$	$\begin{bmatrix} 0.0156 & 0.1047 \\ -6.7127 & -1.6948 \end{bmatrix}$	-0.6702 -1.0090

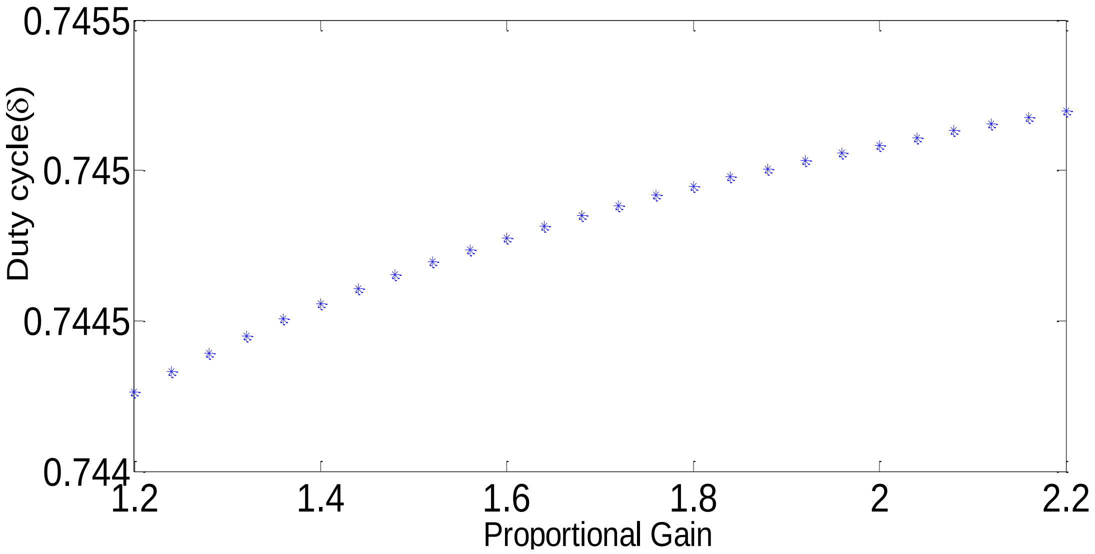

Fig. 4.13 Duty ratio against proportional gain

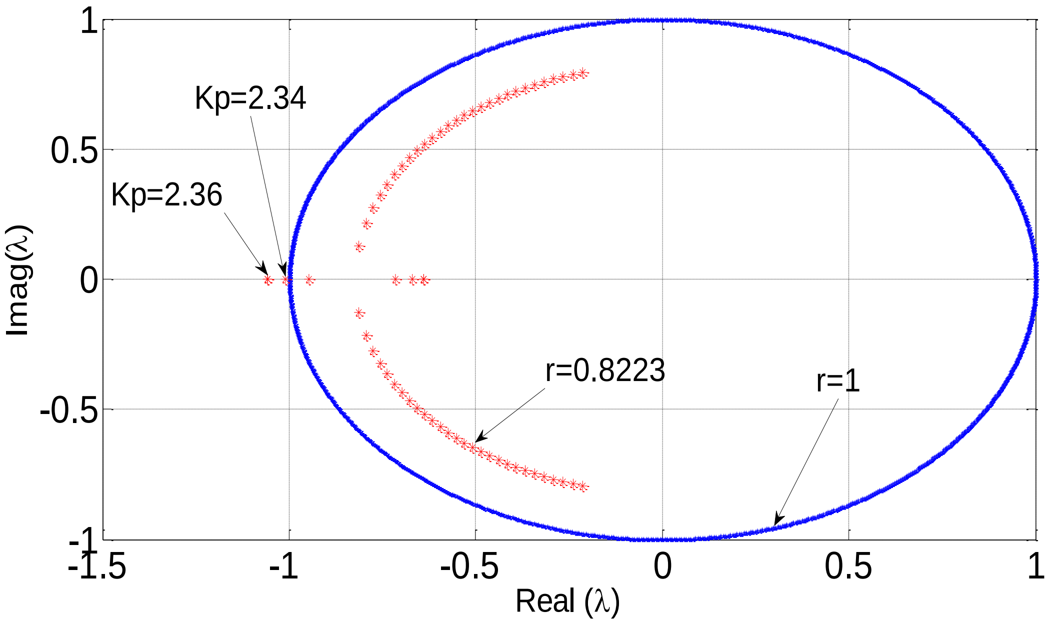

Fig. 4.14 Eigenvalue loci as the proportional gain is varied.

The analytical results shown in Table 4.2 and the eigenvalue loci (Fig.4.14) indicate that the period-1 orbit loses stability when Kp=2.34 (as one of the Floquet multipliers moves out of the unit circle at this parameter value). This is in full agreement with the numerically obtained bifurcation diagram shown in Fig. 4.9.

Also, when the proportional gain (Kp) is kept fixed at 2, and the supply voltage (V_{in}) is varied, the computed duty ratio, initial state, and the state vector at the switching instant are shown in Table 4.3, while the computed Saltation matrix, Monodromy matrix, and Floquet multiplier are shown in Table 4.4. The eigenvalue loci are shown in Fig. 4.15. The results in Table 4.4 and the eigenvalue loci in Fig. 4.15 indicate that the period-1 orbit loses stability when V_{in}=111.83V in agreement with the numerically obtained bifurcation diagram in Fig.4.10. The system stability boundary indicating the stable (nominal period-1) and unstable (*subharmonics*) regions as the supply voltage and proportional gain are varied is shown in Fig. 4.16.

Table 4.3 Changes in duty ratio, the initial state, and the state vector at the switching instant as the supply voltage is varied.

Supply Voltage (V)	$\delta = t_{\Sigma}/T$	$d = 1-\delta$	$\mathbf{X}(0)$	$\mathbf{X}(t_{\Sigma})$
85	0.7002	0.2998	$\begin{bmatrix}100.7776\\4.3895\end{bmatrix}$	$\begin{bmatrix}100.7702\\2.4119\end{bmatrix}$
90	0.7168	0.2832	$\begin{bmatrix}100.7958\\4.4161\end{bmatrix}$	$\begin{bmatrix}100.7885\\2.3911\end{bmatrix}$
95	0.7317	0.2683	$\begin{bmatrix}100.8121\\4.4399\end{bmatrix}$	$\begin{bmatrix}100.8049\\2.3725\end{bmatrix}$
100	0.7451	0.2549	$\begin{bmatrix}100.8267\\4.4615\end{bmatrix}$	$\begin{bmatrix}100.8196\\2.3559\end{bmatrix}$
105	0.7572	0.2428	$\begin{bmatrix}100.8399\\4.4811\end{bmatrix}$	$\begin{bmatrix}100.8329\\2.3409\end{bmatrix}$
110	0.7682	0.2318	$\begin{bmatrix}100.8519\\4.4990\end{bmatrix}$	$\begin{bmatrix}100.8450\\2.3273\end{bmatrix}$
111.83	0.7720	0.2280	$\begin{bmatrix}100.8560\\4.5051\end{bmatrix}$	$\begin{bmatrix}100.8492\\2.3226\end{bmatrix}$

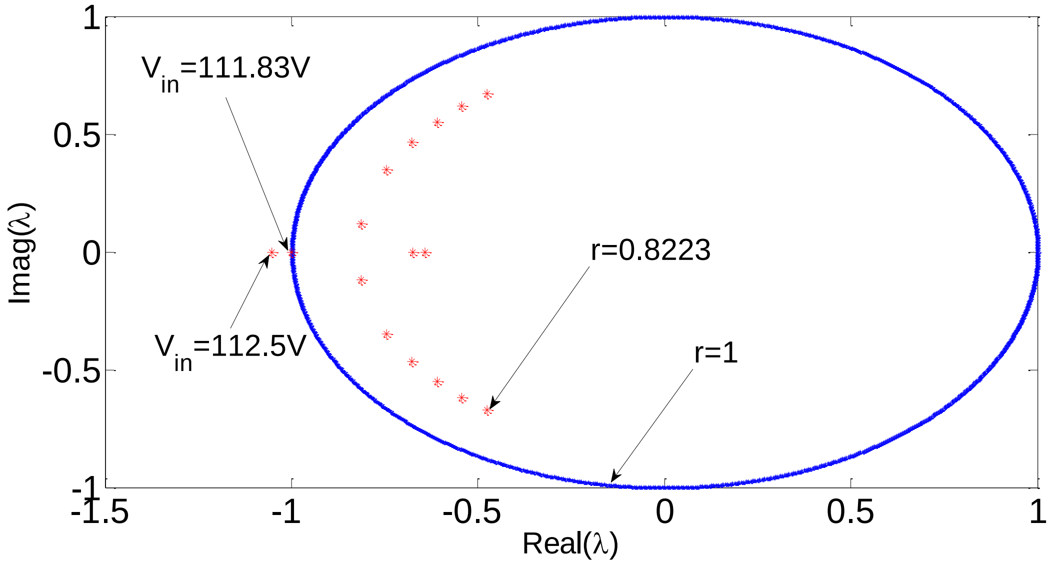

Fig. 4.15 Eigenvalue loci as the supply voltage is varied

Table 4.4 Computed Saltation matrix and Monodromy matrix as the supply voltage is varied.

Supply voltage	Saltation matrix	Monodromy Matrix	Floquet Multipliers
85V	$\begin{bmatrix} 1.0000 & 0 \\ -5.8111 & 1.0000 \end{bmatrix}$	$\begin{bmatrix} 0.1007 & 0.1514 \\ -5.1642 & -1.0511 \end{bmatrix}$	-0.4752 + 0.6711i -0.4752 - 0.6711i
90V	$\begin{bmatrix} 1.0000 & 0 \\ -6.1101 & 1.0000 \end{bmatrix}$	$\begin{bmatrix} 0.1041 & 0.1464 \\ -5.4639 & -1.1892 \end{bmatrix}$	-0.5426 + 0.6179i -0.5426 - 0.6179i
95V	$\begin{bmatrix} 1.0000 & 0 \\ -6.4098 & 1.0000 \end{bmatrix}$	$\begin{bmatrix} 0.1070 & 0.1420 \\ -5.7641 & -1.3272 \end{bmatrix}$	-0.6101 + 0.5514i -0.6101 - 0.5514i
100V	$\begin{bmatrix} 1.0000 & 0 \\ -6.7101 & 1.0000 \end{bmatrix}$	$\begin{bmatrix} 0.1096 & 0.1380 \\ -6.0645 & -1.4651 \end{bmatrix}$	-0.6778 + 0.4657i -0.6778 - 0.4657i
105V	$\begin{bmatrix} 1.0000 & 0 \\ -7.0108 & 1.0000 \end{bmatrix}$	$\begin{bmatrix} 0.1119 & 0.1344 \\ -6.3651 & -1.6030 \end{bmatrix}$	-0.7455 + 0.3470i -0.7455 - 0.3470i
110V	$\begin{bmatrix} 1.0000 & 0 \\ -7.3119 & 1.0000 \end{bmatrix}$	$\begin{bmatrix} 0.1140 & 0.1312 \\ -6.6660 & -1.7407 \end{bmatrix}$	-0.8134 + 0.1210i -0.8134 - 0.1210i
111.83V	$\begin{bmatrix} 1.0000 & 0 \\ -7.4222 & 1.0000 \end{bmatrix}$	$\begin{bmatrix} 0.1147 & 0.1301 \\ -6.7762 & -1.7911 \end{bmatrix}$	-0.6757 -1.0008
112.5V	$\begin{bmatrix} 1.0000 & 0 \\ -7.4626 & 1.0000 \end{bmatrix}$	$\begin{bmatrix} 0.1149 & 0.1297 \\ -6.8165 & -1.8096 \end{bmatrix}$	-0.6430 -1.0517

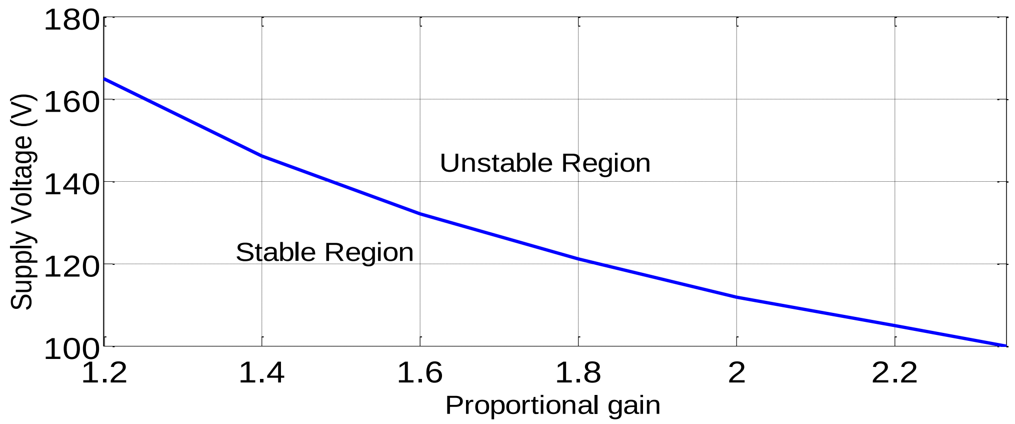

Fig. 4.16 System stability boundary (supply voltage against proportional gain).

4.2.4 Co-existing Attractors and Fractal Basin Boundary in DC Chopper-fed PMDC Drives

Apart from the period doubling route to chaos reported above, another form of complexity arises when two or more asymptotically stable periodic orbits or attracting sets co-exist as the system parameters are being varied. This is usually referred to as co-existing attractors [62], and when this occurs, trajectories of the system selectively converge on either of the attracting sets, depending on the initial state of the system [62], [60]. In a DC Chopper-fed PMDC Drive employing the proportional controller, three different co-existing attracting sets (period-1, period-3 and period-4 attractors) were identified when the proportional gain parameter was set to 2. Trajectories of the initial points of the system selectively converge on any of the attracting sets (Table 4.5), thus making future prediction of system performance nearly impossible. The period-3 attractor is born when the control signal skips one cycle of the ramp signal (Fig. 4.17) as a result of the change in the initial condition, while the period-4 attractor is born when the control signal skips two cycles of the ramp signal (Fig. 4.18). Efforts to isolate the basin of attractions of each of the attracting sets reveal the occurrence of a fractal phenomenon (Fig. 4.19). The basin of attraction of a given attractor is the set of initial conditions whose trajectories converge on the attractor. If co-existing attractors exist, the boundary demarcating the basins of the different attracting sets is referred to as separatrix.

Table 4.5 Possible attracting sets when Kp=2, for $\omega(0)\in[90,92.5]$ rad/s and $i(0)\in[2,4.5]$ A

Initial Speed $\omega(0)$, Rad/s	Initial Current $i(0)$,A	Attractor
90	2	Period-1
90.2	2.2	Period-4
90.4	2.4	Period-1
90.6	2.6	Period-4
90.8	2.8	Period-3
91	3	Period-3
91.5	3.5	Period-1
92	4	Period-1
92.5	4.5	Period-3

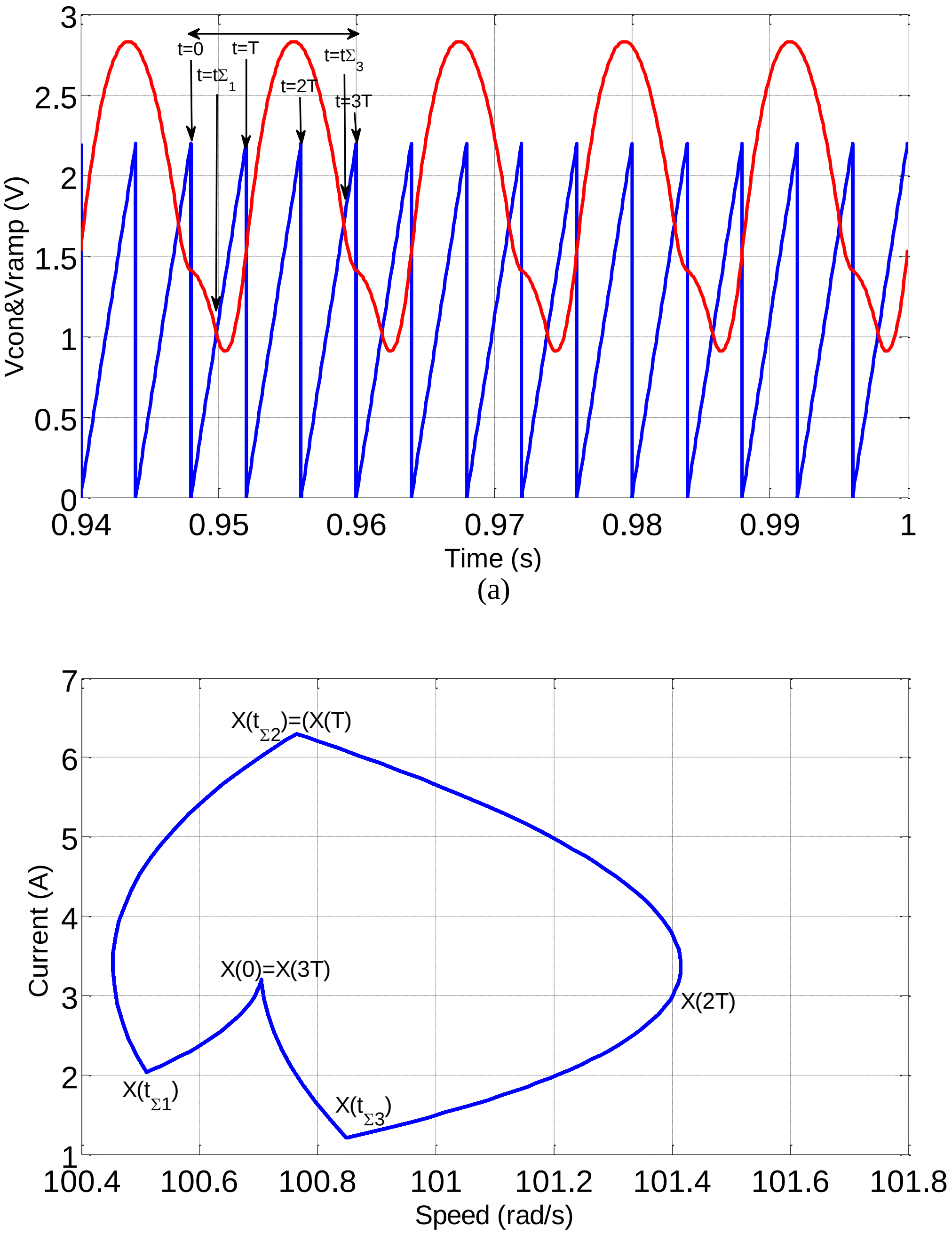

(a)

(b)

Fig. 4.17 Period-3 behaviour (a) Control and ramp signals (b) Period-3 phase portrait; *K*p=2, *ω*(0)=90.8 rad/s, *i*(0)=2.8 A.

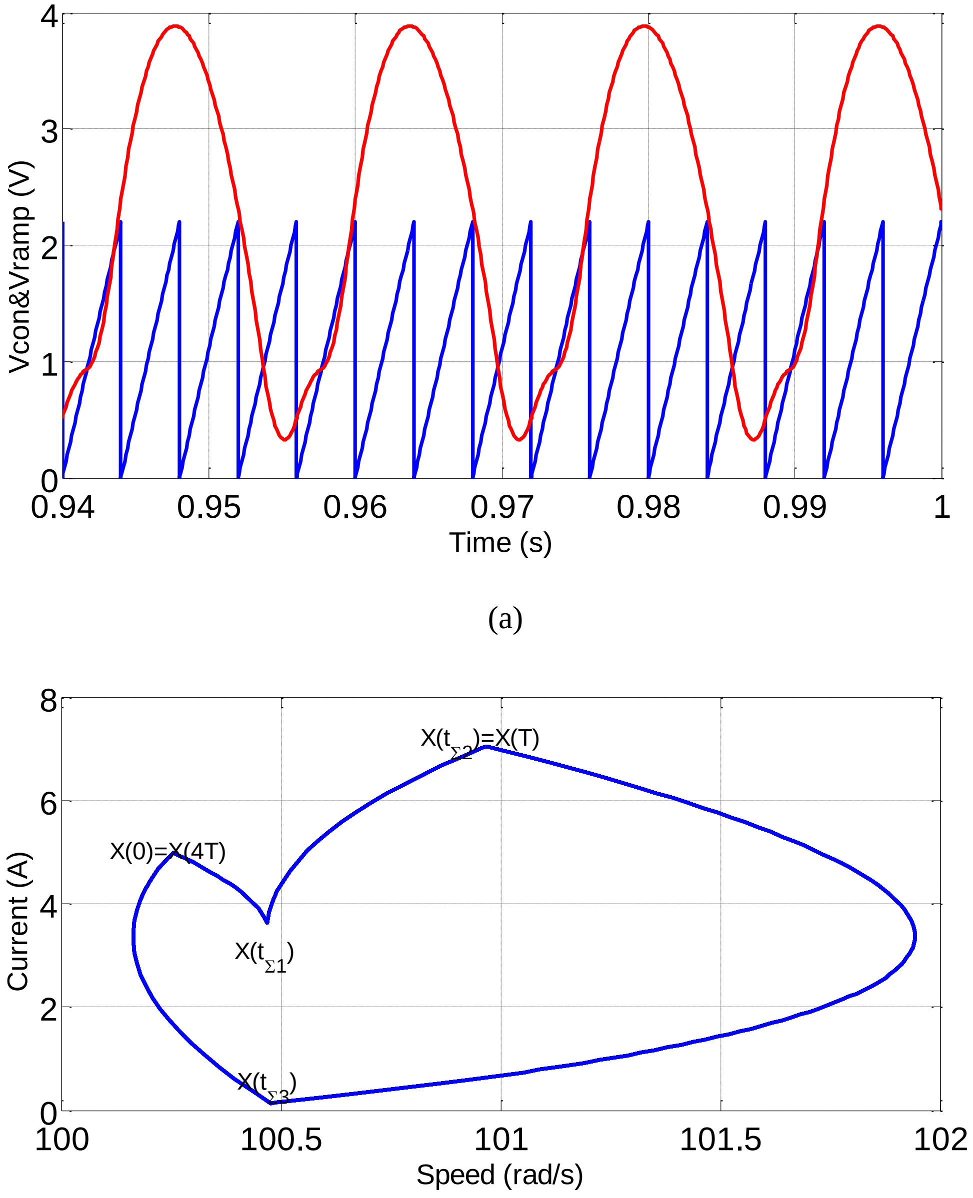

(a)

(b)

Fig. 4.18 Period-4 behaviour (a) Control and ramp signal (b) Period-4 phase portrait; Kp=2, $\omega(0)$=90.2 rad/s, $i(0)$=2.2 A.

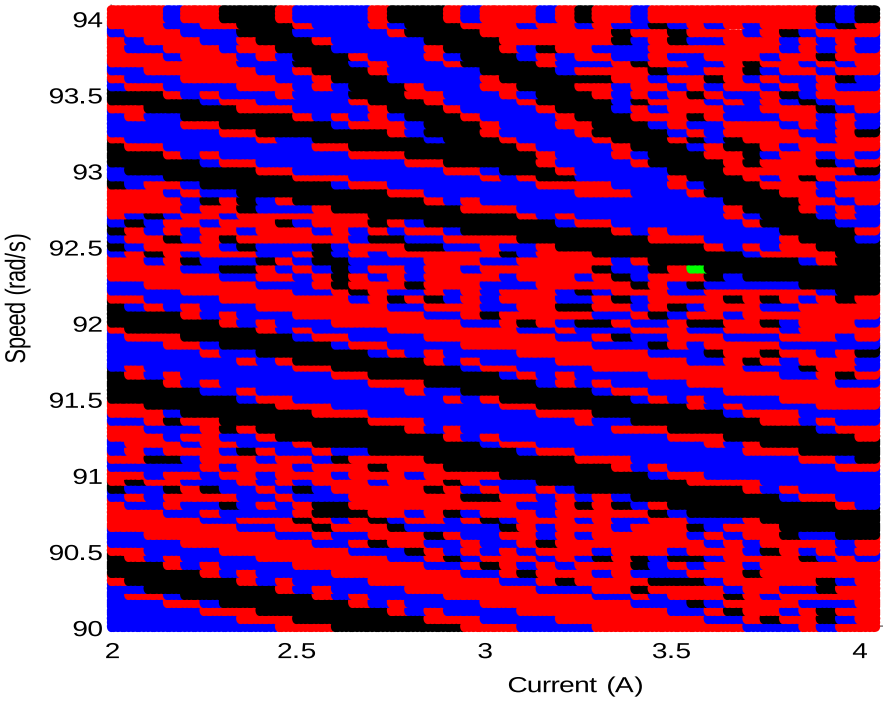

Fig. 4.19 Basin of attraction showing the co-existence of period-1(blue), period-3(red), and period-4 (black) attractors at *K*p=2, for ($\omega(0)\in[90,94]$ rad/s and $i(0)\in[2,4.1]$ A.

From Table 4.5 and Fig. 4.19, it could be seen that the boundary of demarcation between the basin of attractions of the three attracting sets is not clear, hence the *fractal* phenomenon. The bifurcation diagram of the system showing the birth and death of the co-existing period-3 attractor is shown in Fig. 4.20.

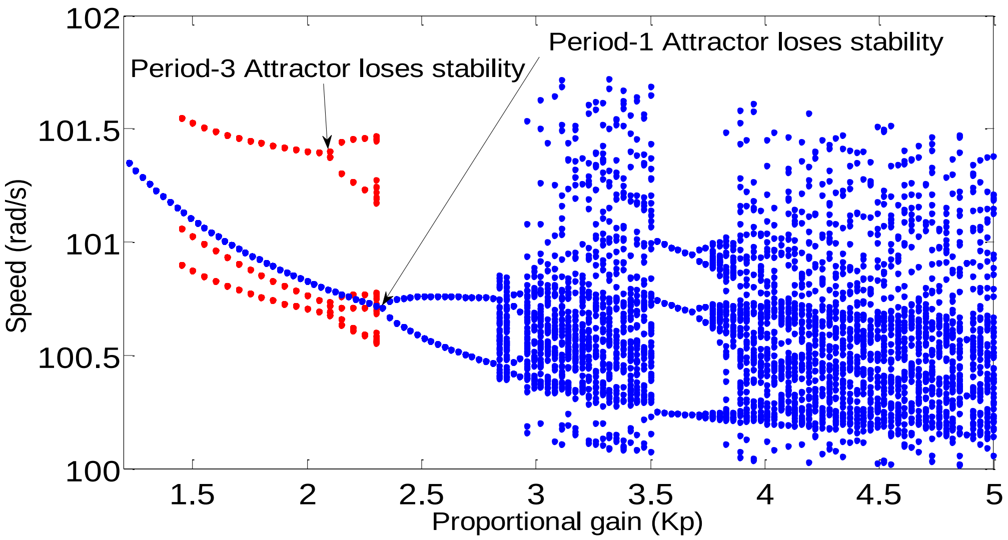

Fig. 4.20 Bifurcation diagram showing the birth and death of the period-3 attractor as the proportional gain is being varied.

4.2.5 StabilityAnalysis of the Period-3 orbit using the Monodromy Matrix Approach

In order to analytically ascertain the system parameter values at which the co-existing period-3 attractor loses its stability, we need to perform the stability analysis of the period-3 orbit of the drive. From Fig. 4.17b, the Monodromy matrix can be expressed as:

$$\begin{aligned}\mathbf{M}(3T,0) &= \Phi(3T,t_{\Sigma3})\times\mathbf{S}_3\times\Phi(t_{\Sigma3},T)\times\mathbf{S}_2\times\Phi(T,t_{\Sigma1})\times\mathbf{S}_1\times\Phi(t_{\Sigma1},0)\\ &= e^{A(3T-t_{\Sigma3})}\times\mathbf{S}_3\times e^{A(t_{\Sigma3}-T)}\times\mathbf{S}_2\times e^{A(T-t_{\Sigma1})}\times\mathbf{S}_1\times e^{A(t_{\Sigma1})}\end{aligned} \tag{4.28}$$

where **S**$_1$, **S**$_2$, and **S**$_3$ are the Saltation matrices at the three switching instants $t_{\Sigma1}=\delta_1 T$, $t_{\Sigma2}=T$ and $t_{\Sigma3}=2T+\delta_3 T$ respectively. δ_1 is the fraction of time the power switch will be OFF during the first PWM cycle and δ_3 is the fraction of time the switch will be OFF during the third PWM cycle. Since the switch is OFF throughout the second PMW cycle, $\delta_2=1$. **S**$_2$ is an identity matrix as the partial derivative of the switching hypersurface with respect to time is infinity at $t=T$, while **S**$_1$ and **S**$_3$ are derived following the same procedure adopted during the analysis of the period-1 orbit.

$$\mathbf{S}_1=\begin{bmatrix}1 & 0\\ \dfrac{\dfrac{V_{in}}{L}}{\left(\dfrac{K_t x_2(t_{\Sigma1})-Bx_1(t_{\Sigma1})-T_L}{J}\right)-\dfrac{V_U-V_L}{Kp\times T}} & 1\end{bmatrix} \tag{4.29}$$

$$\mathbf{S}_3=\begin{bmatrix}1 & 0\\ \dfrac{\dfrac{V_{in}}{L}}{\left(\dfrac{K_t x_2(t_{\Sigma3})-Bx_1(t_{\Sigma3})-T_L}{J}\right)-\dfrac{V_U-V_L}{Kp\times T}} & 1\end{bmatrix} \tag{4.30}$$

To complete the derivation of the Saltation matrices (**S**$_1$ and **S**$_3$), the switching instants $(t_{\Sigma 1})$ and $(t_{\Sigma 3})$, and the state vectors at the switching instants $\mathbf{X}(t_{\Sigma 1})$ and $\mathbf{X}(t_{\Sigma 3})$ are to be computed.

From Fig. 4.17b, we have:

$$\begin{aligned}\mathbf{X}(t_{\Sigma 1}) &= \Phi(t_{\Sigma 1},0)\mathbf{X}(0) + \int_0^{t_{\Sigma 1}} \Phi(t_{\Sigma 1},\lambda)\mathbf{V}_{\mathbf{off}}\,d\lambda \\ &= a_1\mathbf{X}(0) + b_1\end{aligned} \tag{4.31}$$

$$\begin{aligned}\mathbf{X}(T) &= \Phi(T,t_{\Sigma 1})\mathbf{X}(t_{\Sigma 1}) + \int_{t_{\Sigma 1}}^{T} \Phi(T,\lambda)\mathbf{V}_{\mathbf{on}}\,d\lambda \\ &= a_2\mathbf{X}(t_{\Sigma 1}) + b_2 = a_2a_1\mathbf{X}(0) + a_2b_1 + b_2\end{aligned} \tag{4.32}$$

$$\begin{aligned}\mathbf{X}(t_{\Sigma 3}) &= \Phi(t_{\Sigma 3},T)\mathbf{X}(T) + \int_{T}^{t_{\Sigma 3}} \Phi(t_{\Sigma 3},\lambda)\mathbf{V}_{\mathbf{off}}\,d\lambda \\ &= a_3\mathbf{X}(T) + b_3 = a_3a_2a_1\mathbf{X}(0) + a_3a_2b_1 + a_3b_2 + b_3\end{aligned} \tag{4.33}$$

$$\begin{aligned}\mathbf{X}(3T) &= \Phi(3T,t_{\Sigma 3})\mathbf{X}(t_{\Sigma 3}) + \int_{t_{\Sigma 3}}^{3T} \Phi(3T,\lambda)\mathbf{V}_{\mathbf{on}}\,d\lambda \\ &= a_4\mathbf{X}(t_{\Sigma 3}) + b_4 = a_4a_3a_2a_1\mathbf{X}(0) + a_4a_3a_2b_1 + a_4a_3b_2 + a_4b_3 + b_4\end{aligned} \tag{4.34}$$

where the expression for a_1,a_2, a_3,a_4,b_1, b_2, b_3, and b_4 can be deduced directly from equations (4.31-4.34). a_1, a_2, b_1 and b_2 are functions of the duty ratio (δ_1), while a_3, a_4, b_3 and b_4 are functions of the duty ratio (δ_3). Since the orbit is of period-3, **X**(3T)=**X**(0) and the initial state X(0) can be expressed as:

$$\begin{aligned}\mathbf{X}(0) &= \left[\mathbf{I} - a_4a_3a_2a_1\right]^{-1} \times (a_4a_3a_2b_1 + a_4a_3b_2 + a_4b_3 + b_4) \\ &= \left[\mathbf{I} - e^{3AT}\right]^{-1} \times \begin{pmatrix} (e^{A(3T-t_{\Sigma 1})} \times \int_0^{t_{\Sigma 1}} \Phi(t_{\Sigma 1},\lambda)\mathbf{V}_{\mathbf{off}}\,d\lambda) + (e^{2AT} \times \int_{t_{\Sigma 1}}^{T} \Phi(T,\lambda)\mathbf{V}_{\mathbf{on}}\,d\lambda) + \\ (e^{A(3T-t_{\Sigma 3})} \times \int_T^{t_{\Sigma 3}} \Phi(t_{\Sigma 3},\lambda)\mathbf{V}_{\mathbf{off}}\,d\lambda) + \int_{t_{\Sigma 3}}^{3T} \Phi(3T,\lambda)\mathbf{V}_{\mathbf{on}}\,d\lambda \end{pmatrix} \\ &= \mathbf{f}(\delta_1,\delta_3)\end{aligned} \tag{4.35}$$

where the two duty ratios δ_1 and δ_3 are the only unknowns, and will be obtained using the switching conditions and the expressions for the state vector at the switching instants in (4.31) and (4.33).

From Fig. 4.17a, the first switching occurs at $t=t_{\Sigma 1}$ when the control signal $V_{\mathrm{con}}(t)$ intercepts the ramp signal ($V_{\mathrm{con}}(t_{\Sigma 1})= V_{\mathrm{ramp}}(t_{\Sigma 1})$), while the third switching occurs at $t= t_{\Sigma 3}$ ($V_{\mathrm{con}}(t_{\Sigma 3})= V_{\mathrm{ramp}}(t_{\Sigma 3})$). Consequently, we have:

$$x_1(t_{\Sigma 1}) = \omega_{ref} + \frac{V_L + (V_U - V_L)\delta_1}{Kp} \tag{4.36}$$

$$x_1(t_{\Sigma 3}) = \omega_{ref} + \frac{V_L + (V_U - V_L)\delta_3}{Kp} \tag{4.37}$$

Using the expression for the state vector at the switching instants in (4.31) and (4.33) we have:

$$x_1(t_{\Sigma 1}) = [1 \quad 0] \times (a_1\mathbf{X}(0) + b_1) = \omega_{ref} + \frac{V_L + (V_U - V_L)\delta_1}{Kp} \tag{4.38}$$

$$x_1(t_{\Sigma 3}) = [1 \quad 0] \times (a_3 a_2 a_1\mathbf{X}(0) + a_3 a_2 b_1 + a_3 b_2 + b_3) = \omega_{ref} + \frac{V_L + (V_U - V_L)\delta_3}{Kp} \tag{4.39}$$

By substituting the expression for **X**(0) (equation 4.35) into equations (4.38) and (4.39) we will have two equations with the two duty ratios (δ_1 and δ_3) as unknowns. Equations (4.38) and (4.39) can be solved using the Newton-Raphson technique to obtain the two duty ratios. Once the two duty ratios are known, the two switching instants ($t_{\Sigma 1}$ and $t_{\Sigma 3}$), the state vector at the switching instants ($\mathbf{X}(t_{\Sigma 1})$ and $\mathbf{X}(t_{\Sigma 3})$), and the Saltation matrices ($\mathbf{S}_1$ and $\mathbf{S}_3$) can be evaluated. The Monodromy matrix for the period-3 orbit (4.28) will then be obtained.

The computed Saltation matrices, Monodromy matrix and Floquet multipliers as the proportional gain is varied are shown in Table 4.6, while the eigenvalue loci are shown in Fig. 4.21. From the tabulated result and the eigenvalue loci, it could be seen that the co-existing period-3 attractor loses stability when the proportional gain is set to 2.09, which is in agreement with the bifurcation diagram of the system (Fig. 4.20) obtained through numerical simulation.

Table 4.6 Monodromy matrix and Floquet multipliers showing the gain parameter value at which the co-existing period-3 orbit loses stability.

Gain (*Kp*)	**S$_1$**	**S$_3$**	Monodromy Matrix	Floquet Multipliers
1.45	$\begin{bmatrix} 1.0000 & 0 \\ -5.4959 & 1.0000 \end{bmatrix}$	$\begin{bmatrix} 1.0000 & 0 \\ -4.1328 & 1.0000 \end{bmatrix}$	$\begin{bmatrix} -1.4240 & -0.1311 \\ 9.9941 & 0.7032 \end{bmatrix}$	-0.3604 + 0.4235i -0.3604 - 0.4235i
1.5	$\begin{bmatrix} 1.0000 & 0 \\ -5.6313 & 1.0000 \end{bmatrix}$	$\begin{bmatrix} 1.0000 & 0 \\ -4.2124 & 1.0000 \end{bmatrix}$	$\begin{bmatrix} -1.4211 & -0.1387 \\ 10.5676 & 0.8141 \end{bmatrix}$	-0.3035 + 0.4660i -0.3035 - 0.4660i
1.9	$\begin{bmatrix} 1.0000 & 0 \\ -6.0400 & 1.0000 \end{bmatrix}$	$\begin{bmatrix} 1.0000 & 0 \\ -4.7704 & 1.0000 \end{bmatrix}$	$\begin{bmatrix} -1.6121 & -0.0958 \\ 14.7208 & 0.6827 \end{bmatrix}$	-0.4647 + 0.3054i -0.4647 - 0.3054i
2.05	$\begin{bmatrix} 1.0000 & 0 \\ -6.0786 & 1.0000 \end{bmatrix}$	$\begin{bmatrix} 1.0000 & 0 \\ -4.9251 & 1.0000 \end{bmatrix}$	$\begin{bmatrix} -1.9829 & -0.1162 \\ 16.0385 & 0.7840 \end{bmatrix}$	-0.8232 -0.3757
2.09	$\begin{bmatrix} 1.0000 & 0 \\ -6.0906 & 1.0000 \end{bmatrix}$	$\begin{bmatrix} 1.0000 & 0 \\ -4.9613 & 1.0000 \end{bmatrix}$	$\begin{bmatrix} -1.9811 & -0.0913 \\ 16.3849 & 0.5989 \end{bmatrix}$	-1.1014 -0.2808

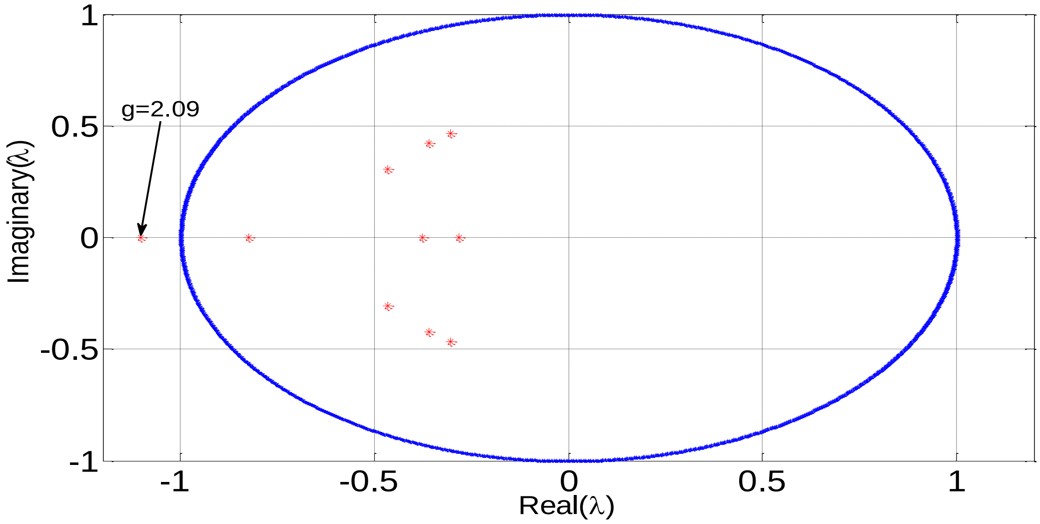

Fig. 4.21 Eigenvalue loci for the period-3 orbit.

4.3 Nonlinear Analysis of DC Chopper Fed PMDC Drives Employing the Proportional Integral Controller

The period doubling bifurcation route to chaos in DC chopper-fed PMDC drives employing the proportional controller was investigated in the last section using both numerical simulation and analytical techniques. In this section, the nonlinear analysis is extended to DC chopper-fed PMDC drives employing a more practical PI controller. Initial numerical simulations by Dong Dai et al. [12] confirmed the occurrence of a slow-scale (or *Neimark-Sacker*) bifurcation in a PI controlled PMDC drive, but the observation was neither analyzed nor experimentally validated. The purpose of this section is to analyze and experimentally validate for the first time the occurrence of a Neimark-Sacker bifurcation in a PMDC drive employing the PI controller. Both the Monodromy matrix approach and the state space averaging technique will be applied in the analysis.

4.3.1 System Overview

A schematic diagram of the DC chopper-fed PMDC drive operating with a proportional integral (PI) controller is shown in Fig. 4.22. The system is composed of three main components namely a permanent magnet brushed DC (PMDC) motor, power converter unit (DC chopper), and PI compensation network. The tacho-generator produces a voltage proportional to the actual speed, which is compared with the reference speed (an analog voltage from the potentiometer) to obtain an error signal. The error signal is used by the controller to produce a control voltage $V_{con}(t)$ that is compared with a 20kHz sawtooth signal $V_{ramp}(t)$ to produce the PWM signal $u(t)$.

The PWM signal will be high when the control signal is greater than the sawtooth signal and will be low otherwise. The power switch (S) and the freewheeling diode (D) operate in a cyclic and complementary manner depending on the PWM signal. When the PWM signal is high, the switch turns ON, and the diode will be reverse biased (OFF). But when the PWM signal is low, the switch turns OFF, and the diode will be forward biased (ON), thus providing a return path for the decaying armature current.

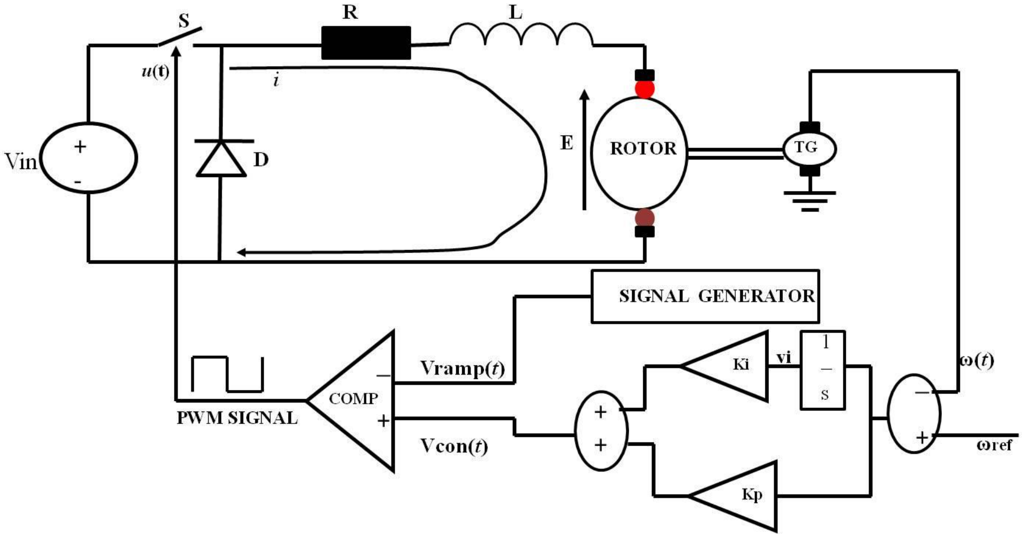

Fig. 4.22 DC chopper-fed PMDC drive employing the PI controller

Based on the condition of the switch (S) and the diode (D), the system is modelled by a 3rd order piecewise-affine set of equations as shown:

$$\frac{d\omega(t)}{dt} = \frac{\left(K_t i(t) - T_L - B\omega(t)\right)}{J} \tag{4.40}$$

$$\frac{di(t)}{dt} = \frac{-i(t)R - K_e\omega(t) + V_{in} \times u(t)}{L} \tag{4. 41}$$

$$\frac{dv_i(t)}{dt} = \omega_{ref} - \omega(t) \tag{4.42}$$

where *u*(*t*) is the PWM signal whose value is 1 when the switch is ON, and 0 when the switch is OFF. The 3rd state variable $v_i(t)$ is due to the integrator in the PI controller loop.

For the sake of compact notation, the mathematical model of the PI controlled PMDC drive can be expressed as:

$$\frac{d\mathbf{X}(t)}{dt} = \begin{cases} \mathbf{f}_1(\mathbf{X}(t)); V_{con}(t) > V_{ramp}(t) : \text{Switch ON} \\ \mathbf{f}_2(\mathbf{X}(t)); V_{con}(t) < V_{ramp}(t) : \text{Switch OFF} \end{cases} \tag{4.43}$$

where:

$$\mathbf{f}_1(\mathbf{X}(t)) = \mathbf{A}_1\mathbf{X}(t) + \mathbf{V}_1 \tag{4.44}$$

$$\mathbf{f}_2(\mathbf{X}(t)) = \mathbf{A}_2\mathbf{X}(t) + \mathbf{V}_2 \tag{4.45}$$

$$\mathbf{X}(t)=\begin{bmatrix}x_1(t)\\x_2(t)\\x_3(t)\end{bmatrix}=\begin{bmatrix}\omega(t)\\i(t)\\v_i(t)\end{bmatrix},\quad \mathbf{A}_1=\mathbf{A}_2=\begin{bmatrix}\frac{-B}{J} & \frac{K_t}{J} & 0\\ \frac{-K_e}{L} & \frac{-R}{L} & 0\\ -1 & 0 & 0\end{bmatrix},\quad \mathbf{V}_1=\begin{bmatrix}\frac{-T_L}{J}\\ \frac{V_{in}}{L}\\ \omega_{ref}\end{bmatrix},\quad \mathbf{V}_2=\begin{bmatrix}\frac{-T_L}{J}\\ 0\\ \omega_{ref}\end{bmatrix}$$

$$V_{con}(t)=Kp\times(\omega_{ref}-\omega(t))+K_i\times v_i(t)=Kp(\omega_{ref}-x_1(t))+K_i x_3(t) \qquad (4.46)$$

while V_{rampt}(t) has been previously defined in (4.5).

4.3.2 System Dynamic Behaviour

The nominal behaviour of a DC chopper-fed PMDC drive employing the PI controller is a period-1 orbit (Figs. 4.23 to 4.25). But as the integral gain (K_i) or the supply voltage(V_{in}) is varied, the Period-1 orbit loses stability via Neimark-Sacker or Hopf bifurcation [13-15, 85, 86] and a quasiperiodic orbit or the so called torus is born. While the supply voltage (V_{in}) is fixed at 24V and the integral gain is varied, the Neimark-Sacker bifurcation occurs at K_i=1612 (Figs. 4.26 to 4.28). Further variation of the integral gain causes the system to make a transition from CCM to DCM (Figs. 4.29 to 4.31). The bifurcation diagrams of the system as the integral gain is varied are shown in Figs. 4.32 and 4.33. Similarly, with the integral gain fixed at 1580 while varying the supply voltage, the Neimark-Sacker bifurcation occured at V_{in}=57V (Fig. 4.34 and 4.35). Further variation of the supply voltage caused the system to make a transition from CCM to DCM (Fig. 4.36 and 4.37). The bifurcation diagrams of the system as the supply voltage is varied are shown in Figs. 4.38 and 4.39.

It is also observed that the onset of the Neimark sacker bifurcation depends on the electrical time constant (T_e=L/R) of the PMDC motor. The higher the electrical time constant of the PMDC motor (high inductance and low resistance) the earlier the onset of the Neimark-Sacker bifurcation, as shown in Fig. 4.40. The figure confirms that Neimark-Sacker bifurcation occurs at low value of the integral gain if the electrical time constant of the PMDC motor is increased. The parameters of the system are: R=7.8 Ω, L=5mH, T_L=0.087NM, K_e=0.0984Vs/rad, K_t=0.09NM/A, ω_{ref}=100rad/s, B=0.000015Nm/rad/sec, J=4.8400e-005Nm/rad/sec^2, f_s=20kHz, T=0.05ms, V_L=0, V_U=8V, and Kp=1.

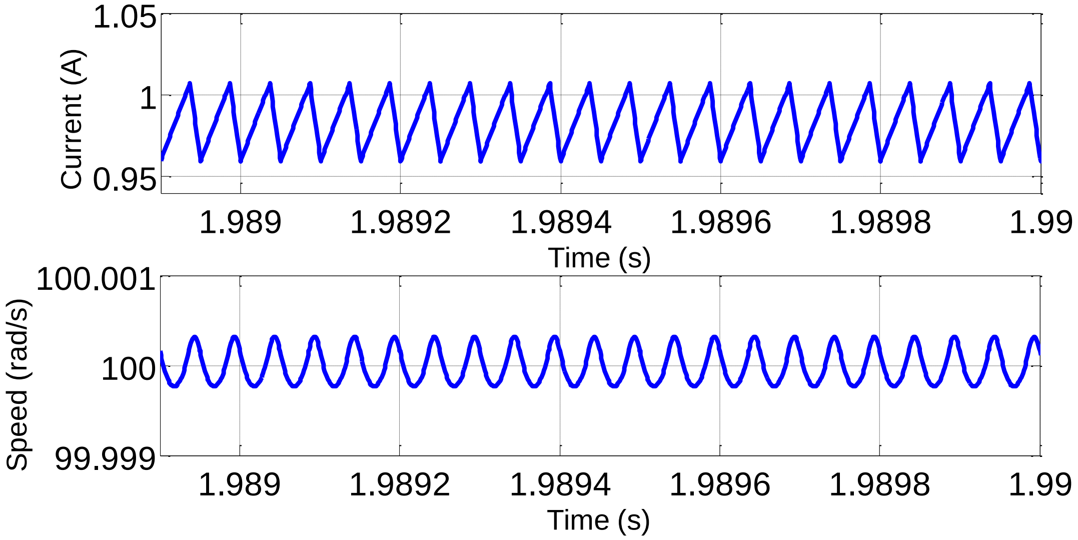

Fig. 4. 23 Period-1 speed and current trajectory; Ki=1000, V_{in}=24V, and T_e=0.641ms.

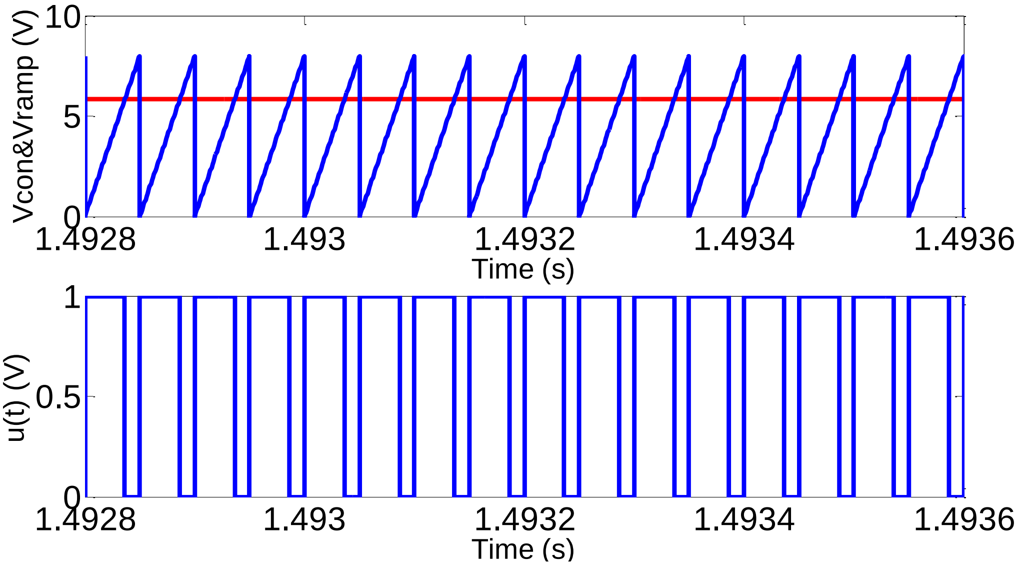

Fig. 4.24 Interaction of the control signal and the ramp signal; period-1 operating mode.

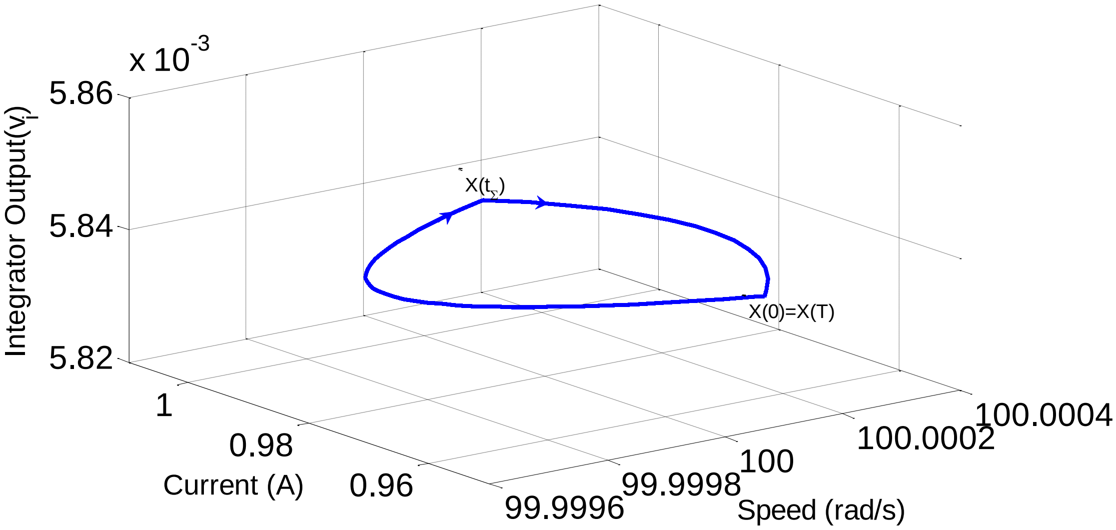

Fig. 4.25 Period-1 phase portrait.

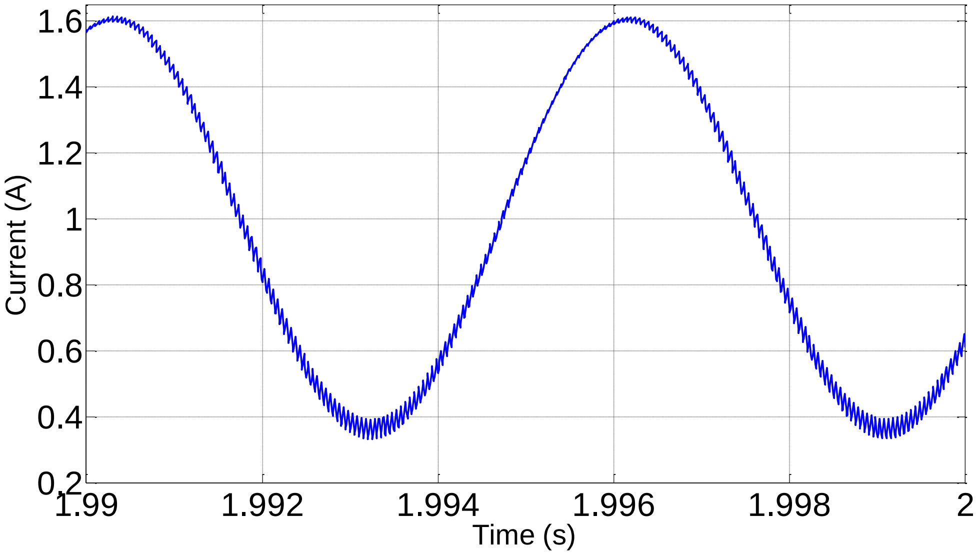

Fig. 4.26 Quasi-periodic current trajectory (CCM) at *Ki*=1612.

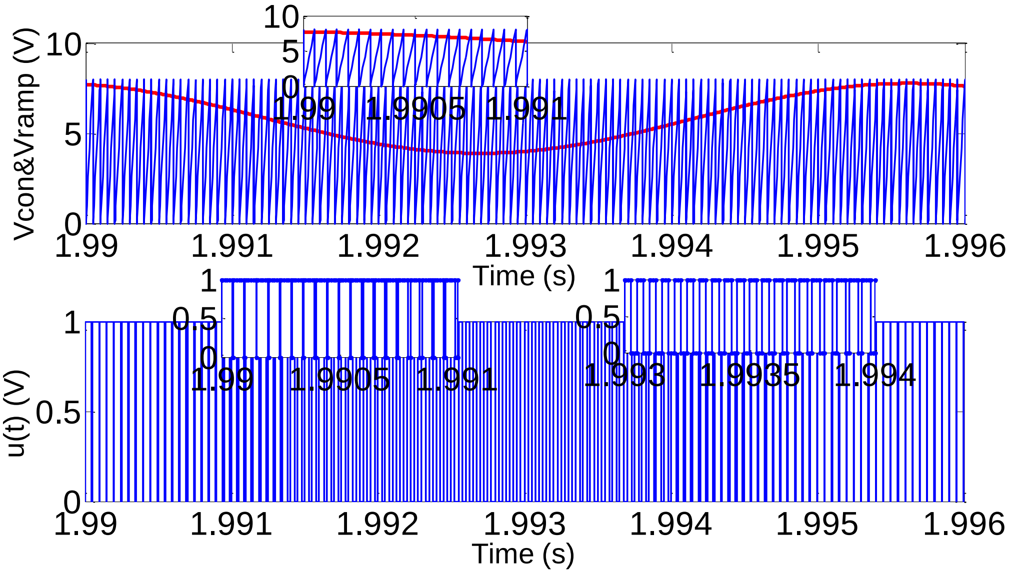

Fig. 4. 27 Interaction of control and ramp signal during quasi-periodic operation at *Ki*=1612.

c

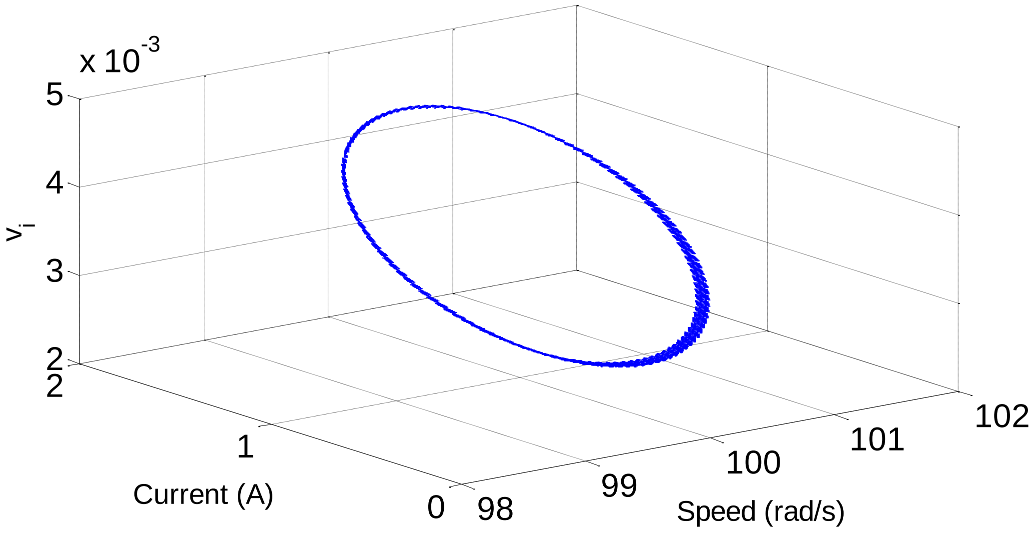

Fig. 4.28 Phase portrait of speed against current and integrator output (Torus) at *Ki*=1612.

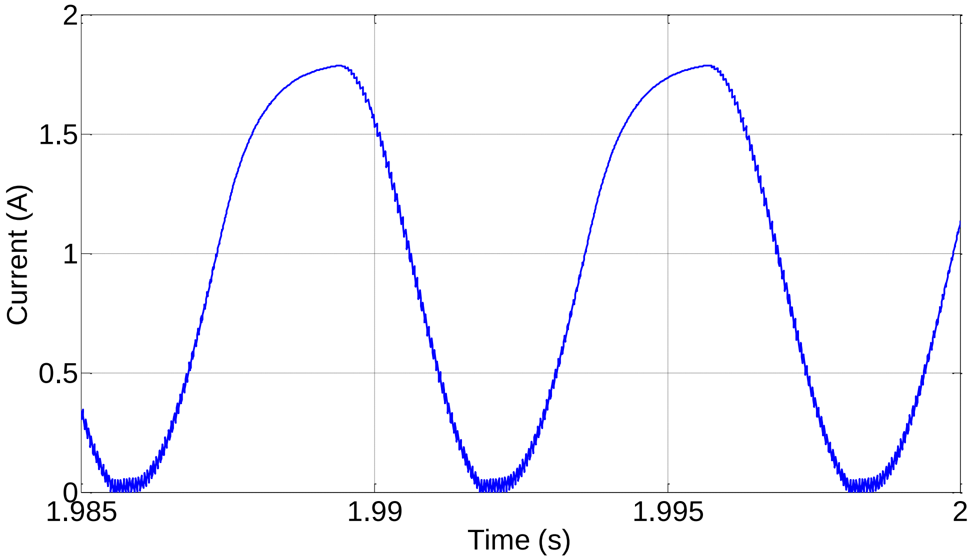

Fig. 4. 29 Transition from CCM to DCM at *Ki*=1640.

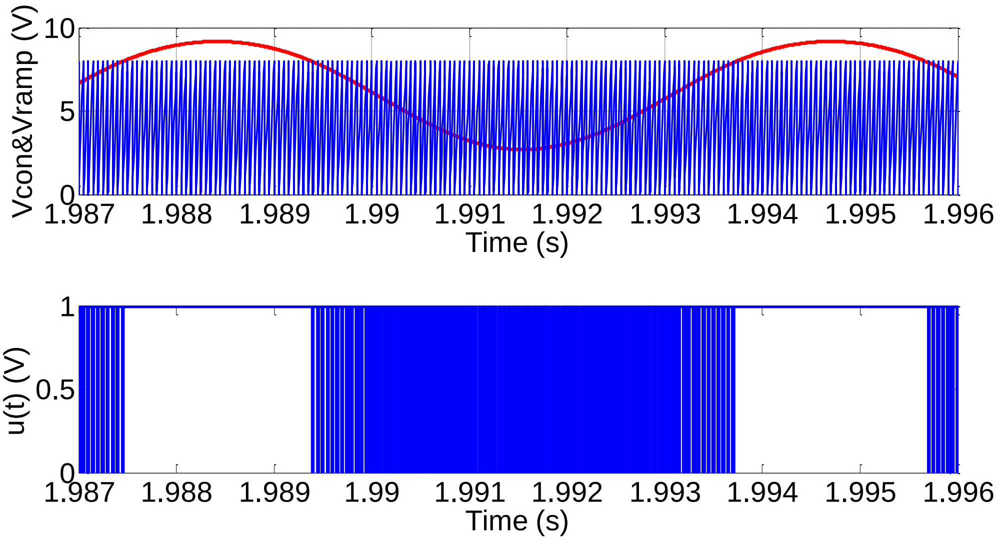

Fig. 4. 30 Interaction of control and ramp signal during quasi-periodic operation (DCM).

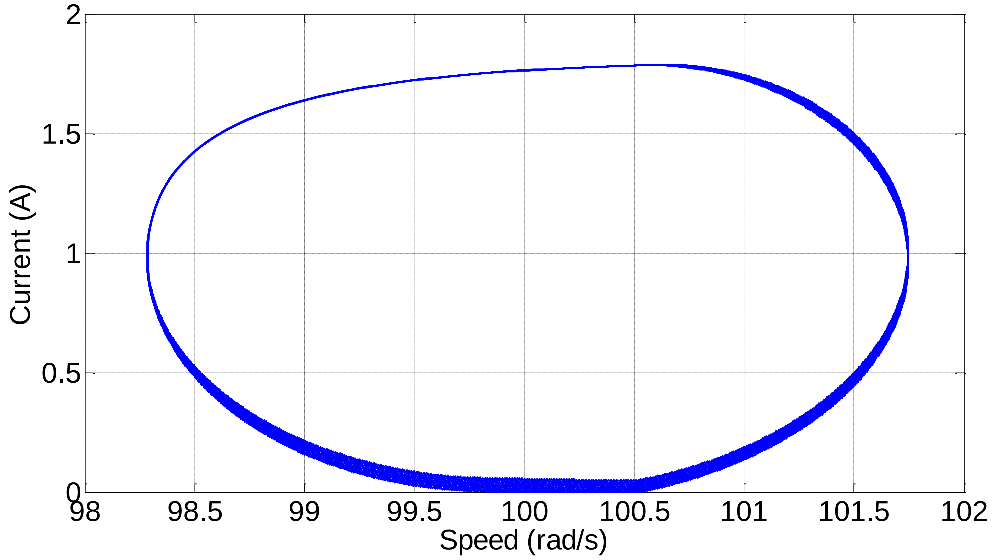

Fig. 4.31 Phase portrait of armature current against speed in DCM.

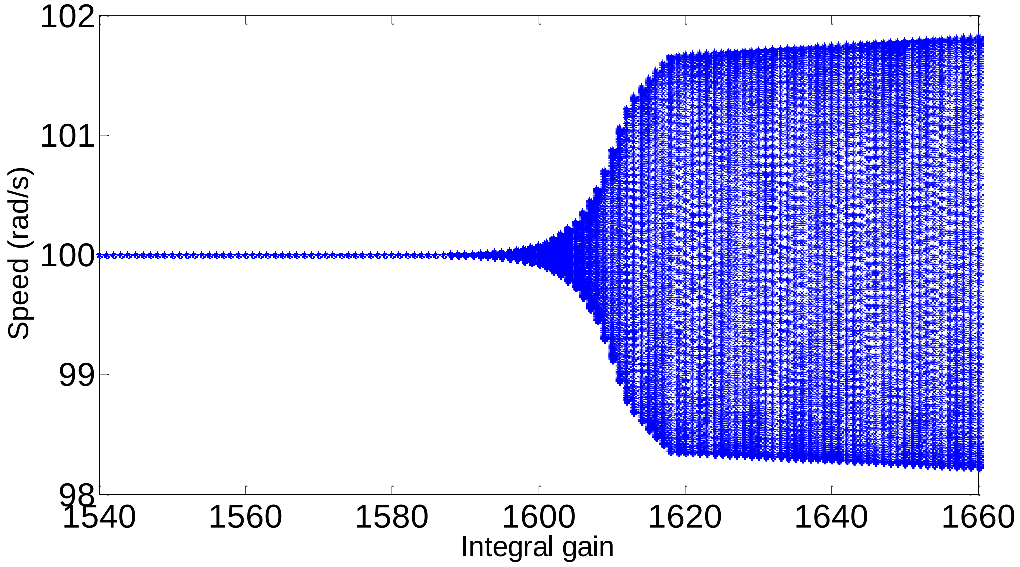

Fig. 4.32 Bifurcation diagram of speed against the integral gain (V_{in}=24 V).

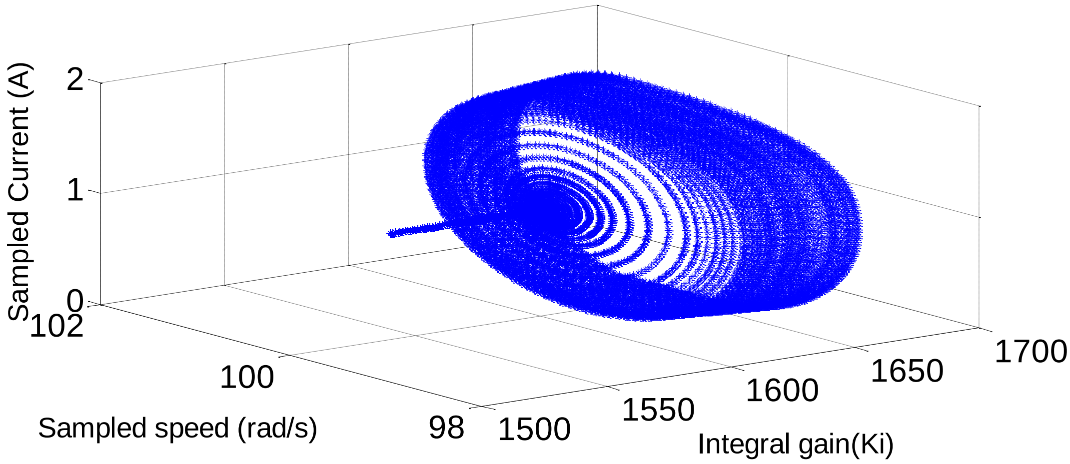

Fig. 4.33 Speed and current dynamics as the integral gain is varied (V_{in}=24V).

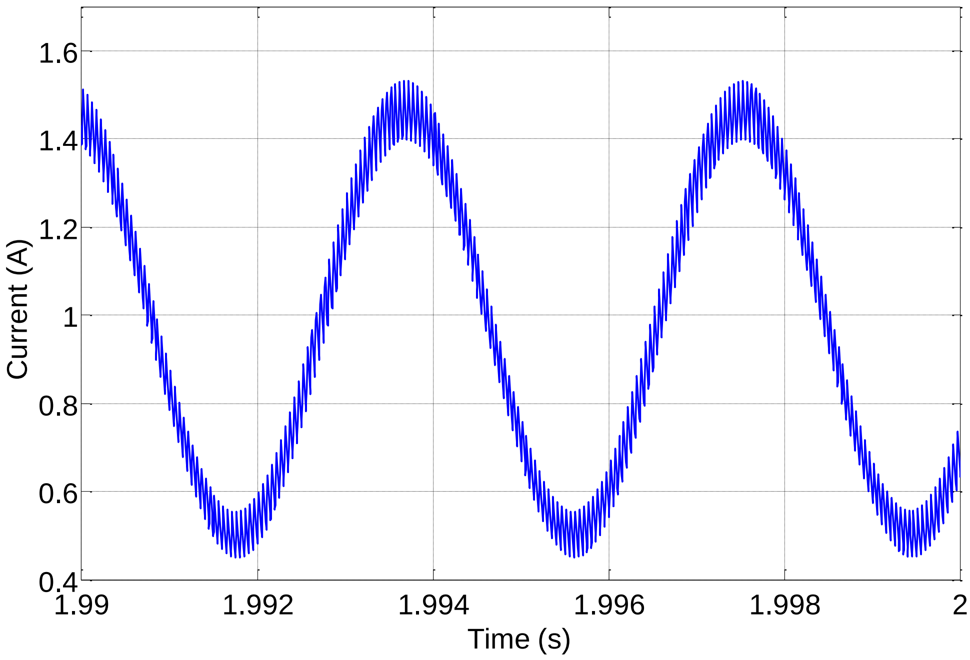

Fig. 4. 34 Quasi-periodic current at V_{in}=57 V (Ki=1580).

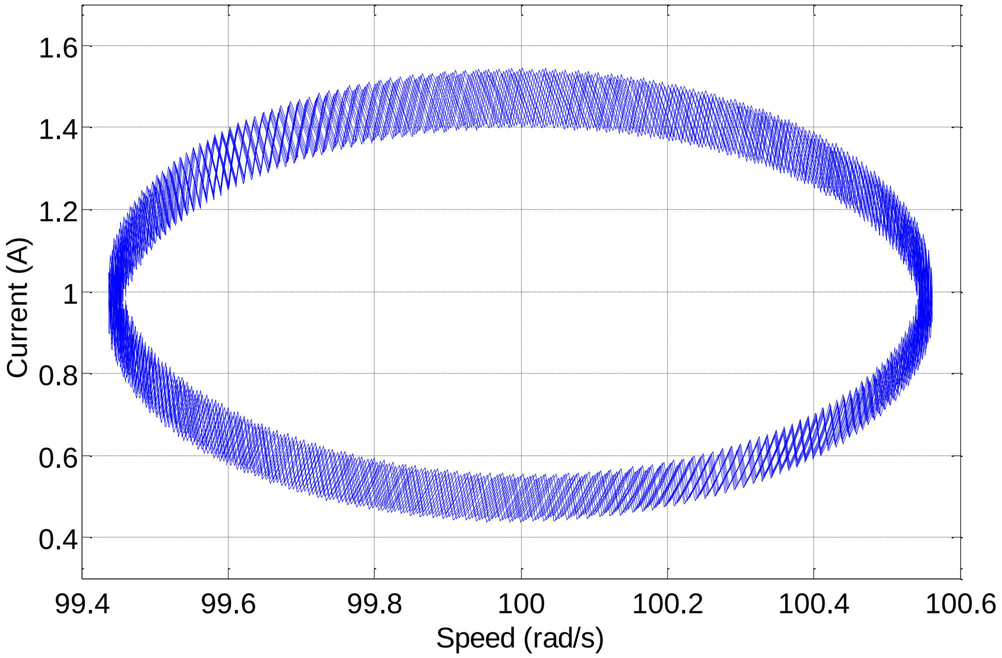

Fig. 4. 35 Phase portrait of armature current against speed at V_{in}=57 V (Torus).

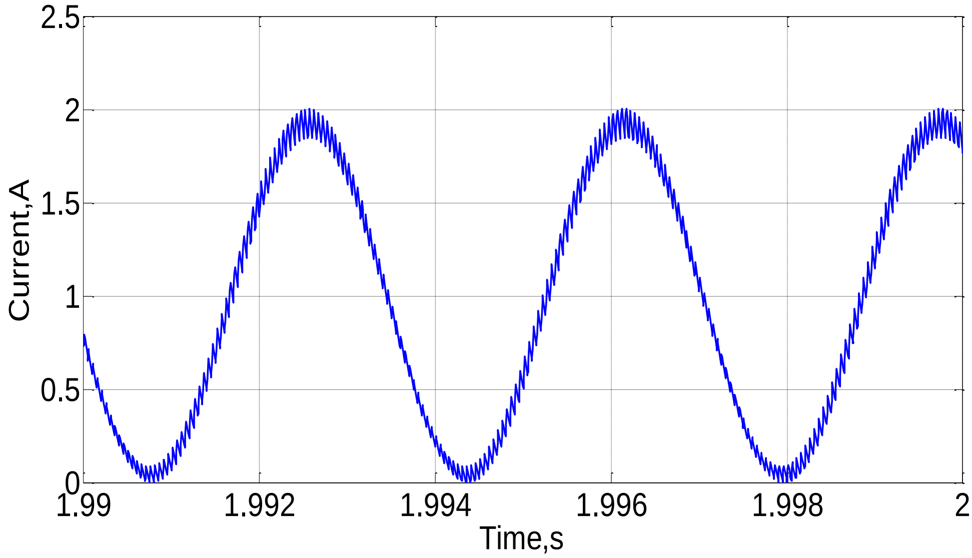

Fig. 4. 36 Transition from CCM to DCM at V_{in}=65 V.

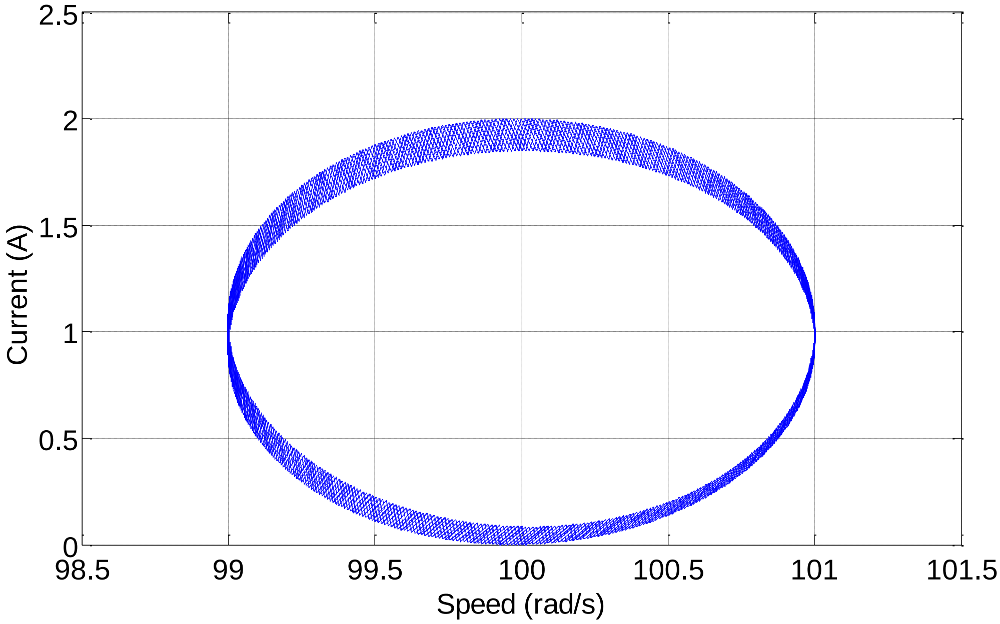

Fig. 4. 37 Phase portrait of armature current against speed (DCM) as the supply voltage is varied.

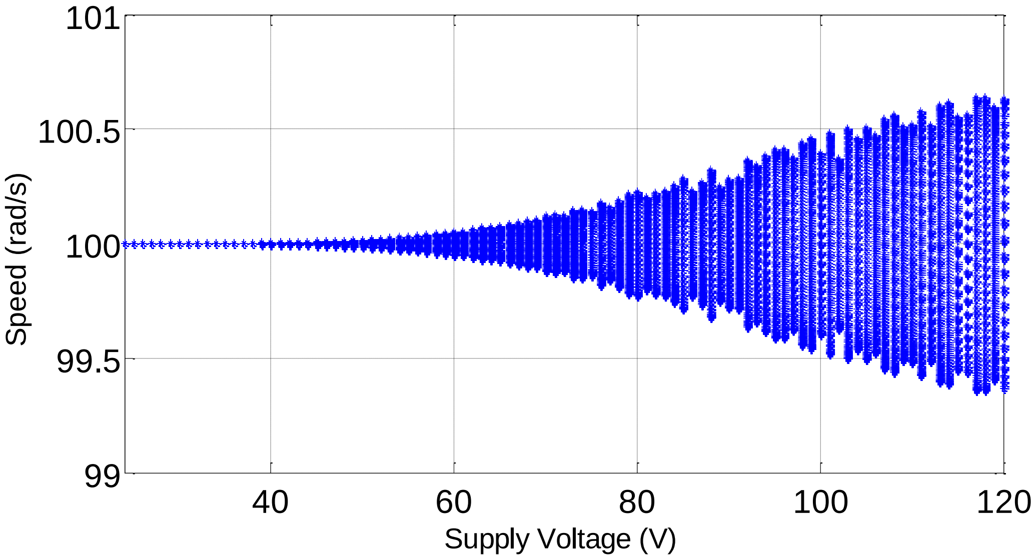

Fig. 4.38 Bifurcation diagram of speed against supply voltage (*K*i=1580).

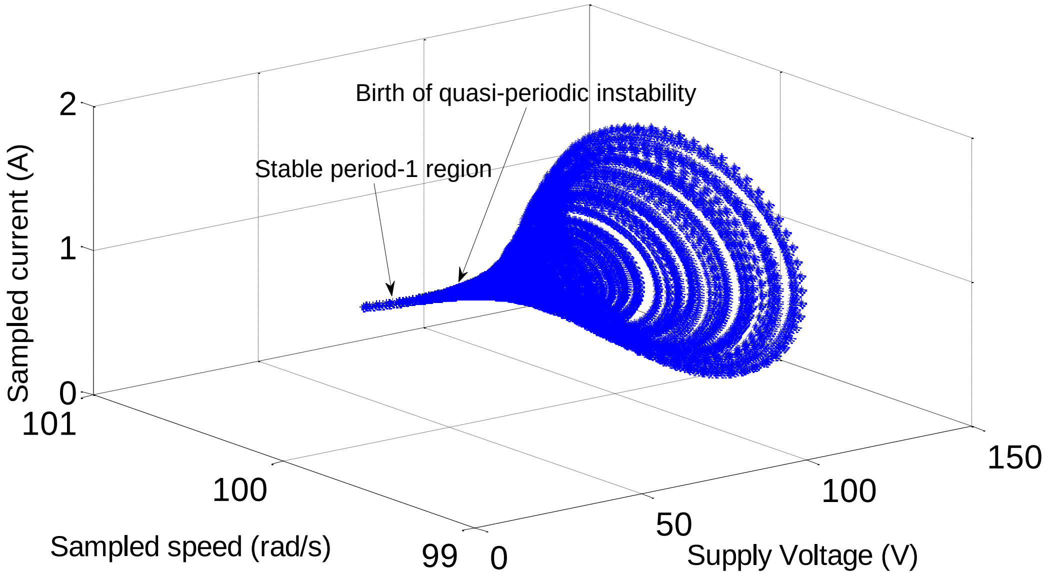

Fig. 4.39 Speed and current dynamics as the supply voltage is being varied (Ki=1580).

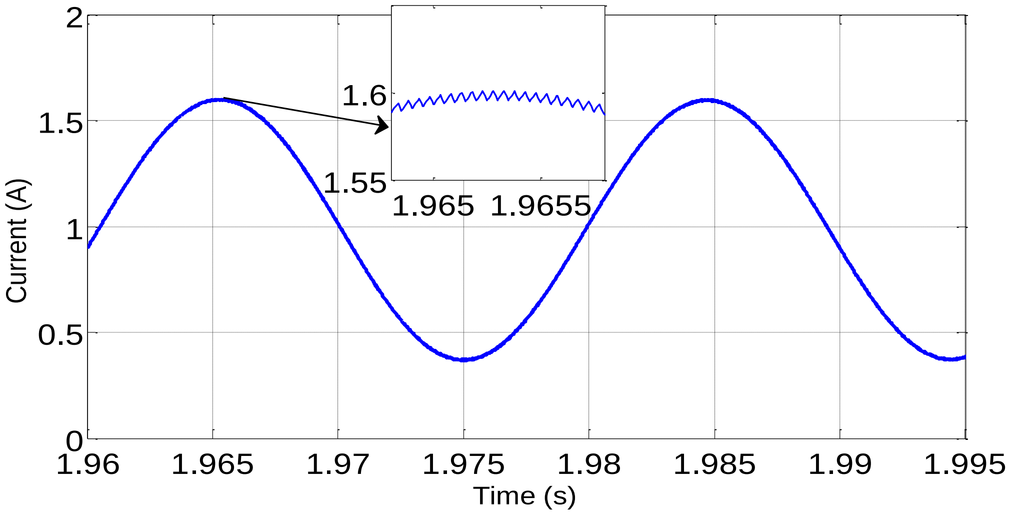

Fig. 4.40 Quasiperiodic current at Ki=56.2, R=3 Ω, L=55 mH, T_e=18.33 ms.

4.3.3 Experimental Validation of the Neimark-Sacker Bifurcation in a PMDC drive

To validate the occurrence of the Neimark-Sacker bifurcation (slow scale instability) in a PI controlled PMDC drive, the experimental set up shown in Fig. 4.41 was built. The rig consisted of a PMDC motor (Fig. 4.42), a power converter unit, and a dsPIC30F3010 digital signal controller (DSC). A dc generator was connected to the PMDC motor to act as a load. Though the analysis presented was based on analog controller, a digital controller was adopted due to its flexibility and the built-in peripherals that are suitable for motor speed control. Also the qualitative behaviour of the system under parameter variation (which is the key emphasis of this research) is the same for both analog and discrete PI implementation.

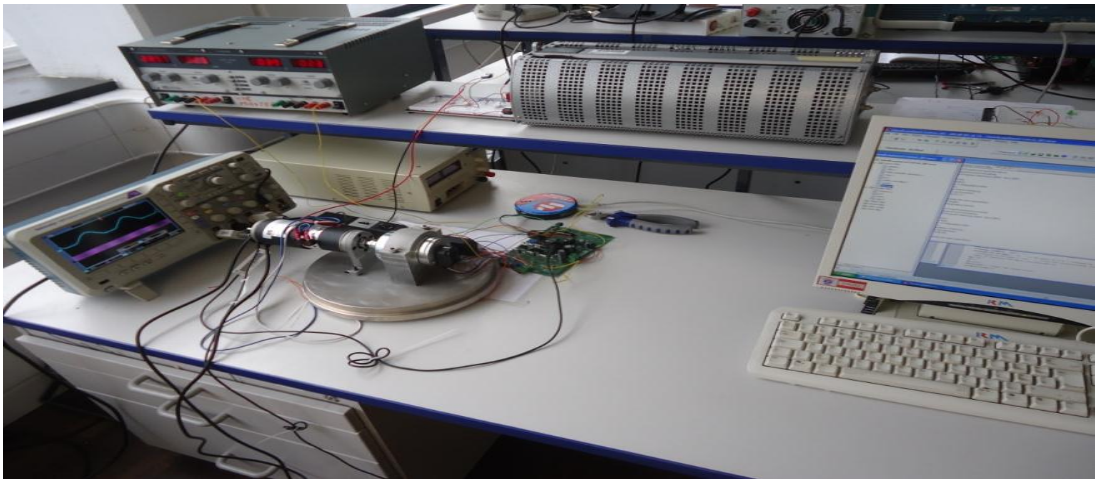

Fig. 4.41 The experimental set up.

The power converter and the DSC were mounted on a flexible dsPIC30F3010 development board (Fig. 4.43) which can be easily configured as a dc chopper, a full bridge converter or a 3 phase inverter (depending on the application). The PI control algorithm was implemented in C language, and the executable program was downloaded to the DSC via a Microchip ICD2 debugger device. Details of the experimental setup are discussed in appendix A. The measured period-1 behaviour of the system is shown in Figs. 4.44 to 4.45, while the measured quasi-periodic behaviour as the integral gain and supply voltage are varied is shown in Figs. 4.46 to 4.55.

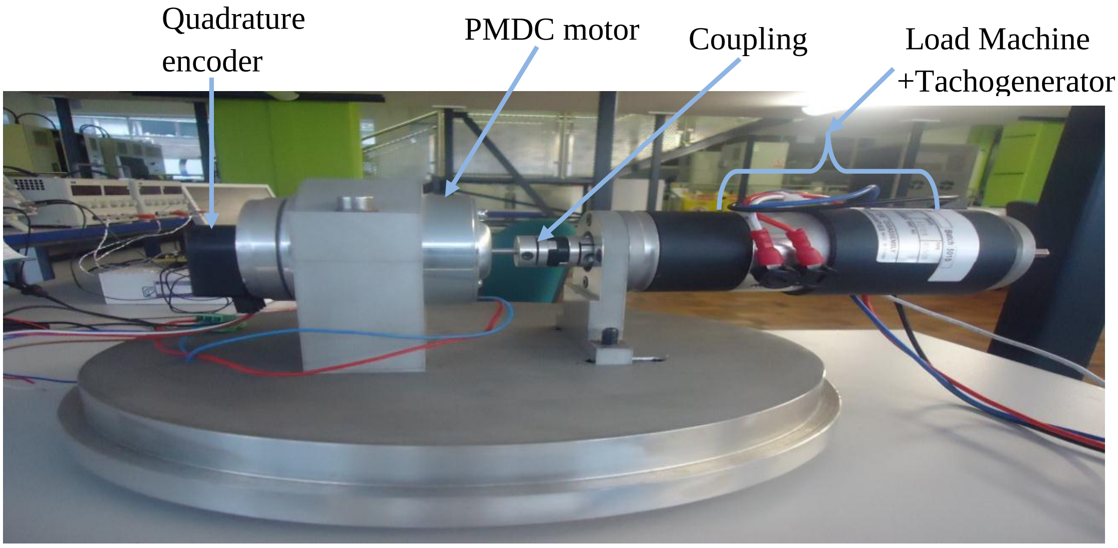

Fig. 4.42 PMDC motor and DC generator unit

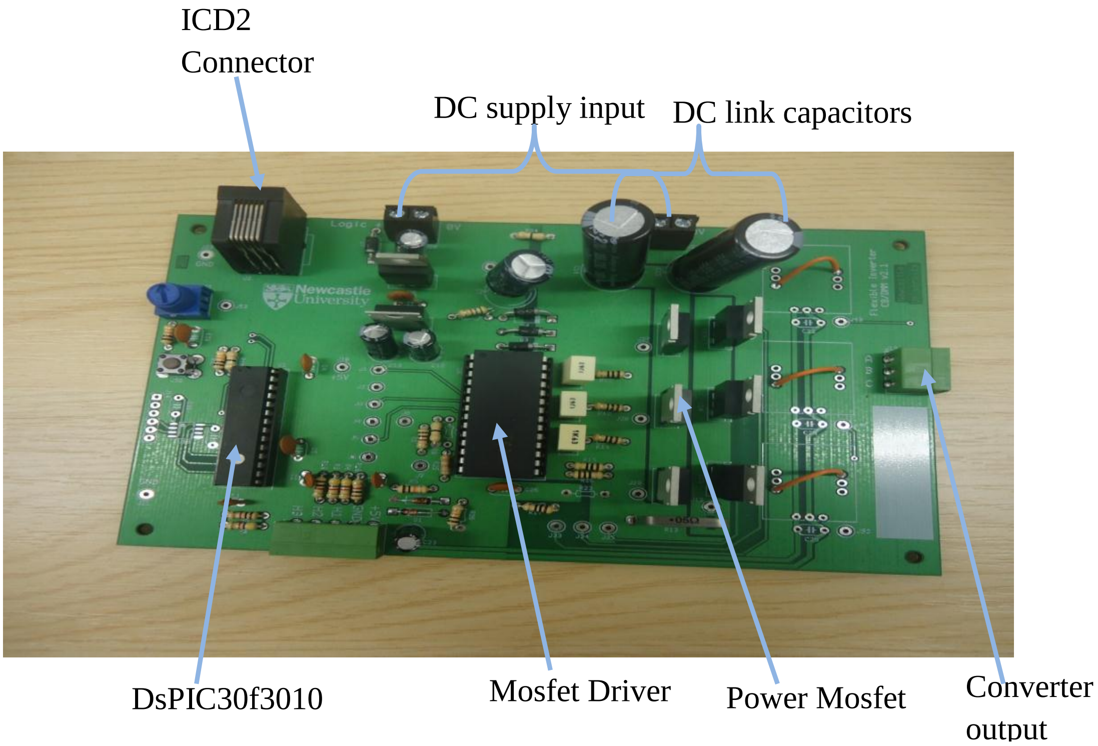

Fig. 4.43 Flexible DsPIC30F3010 development board.

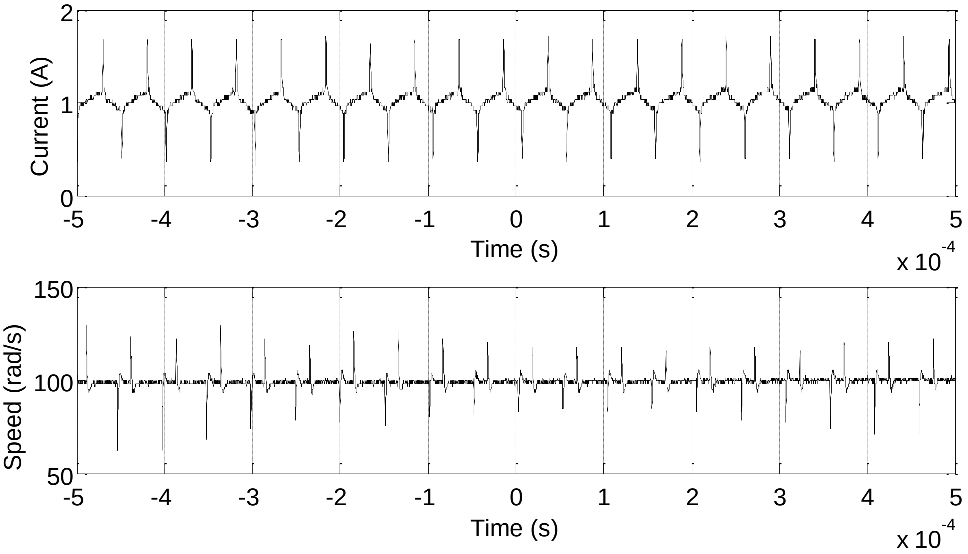

Fig. 4.44 Measured period-1 current and speed at Kp=328, Ki= 3933, and V_{in}=24 V (ω_{ref} =100 rad/s).

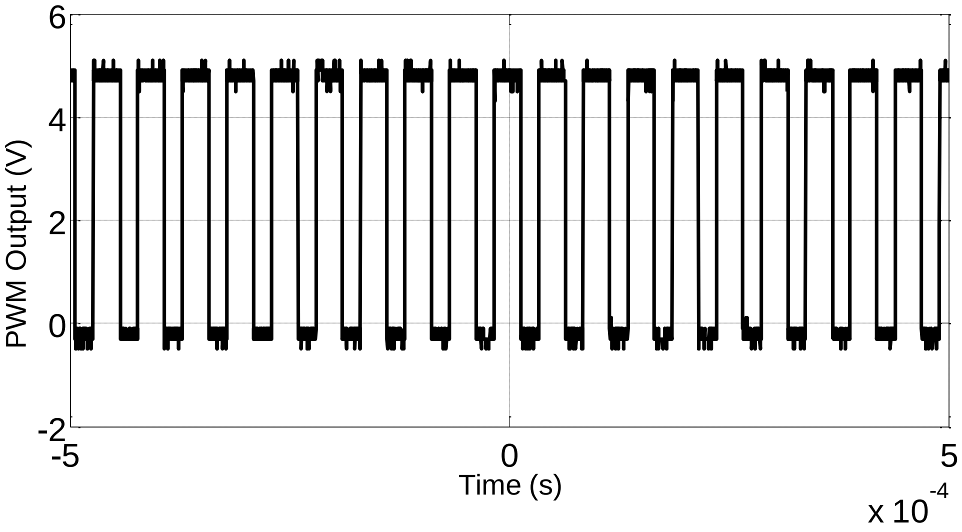

Fig.4. 45 Measured PWM output for period-1 operation.

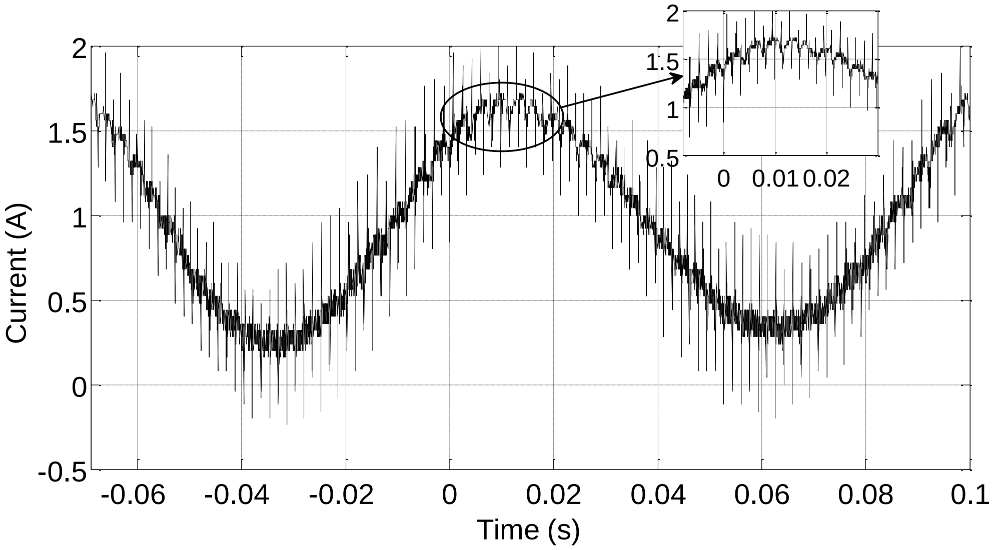

Fig. 4.46 Measured quasi-periodic current (CCM) at *Ki*=9175 corresponding to Fig. 4.26.

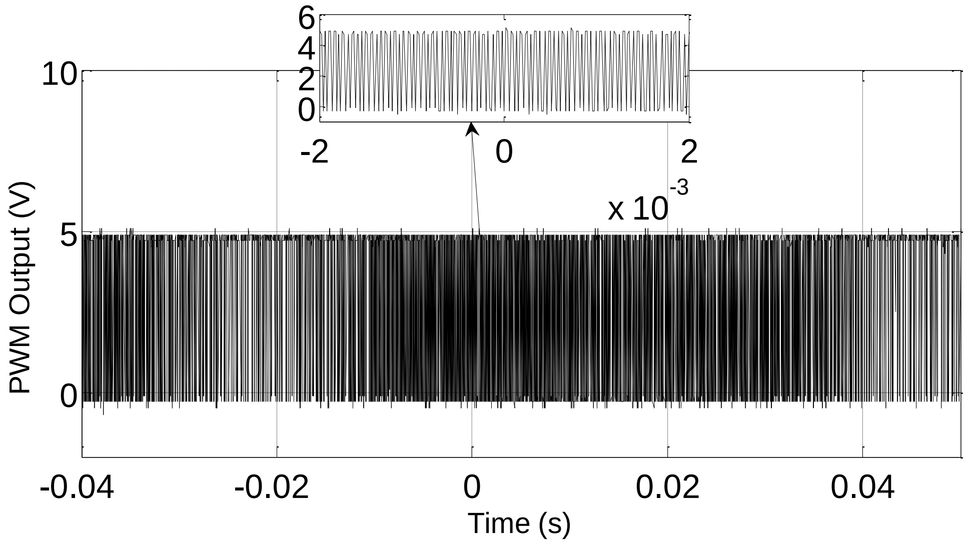

Fig. 4. 47 Measured PWM output during quasi-periodic operation (CCM) corresponding to Fig. 4.27.

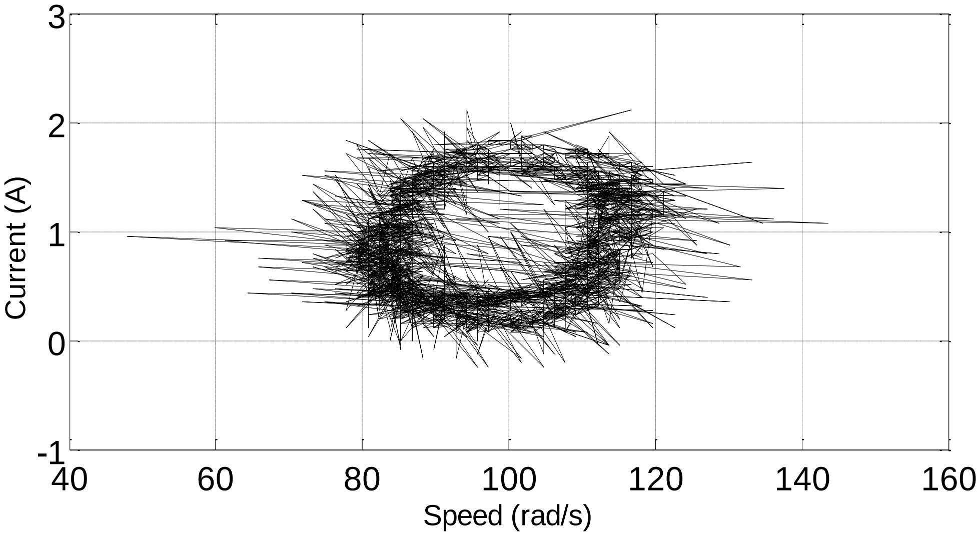

Fig. 4.48 Measured phase portrait of armature current against speed (or the so called *Torus*) at *Ki*=9175 corresponding to Fig. 4.28.

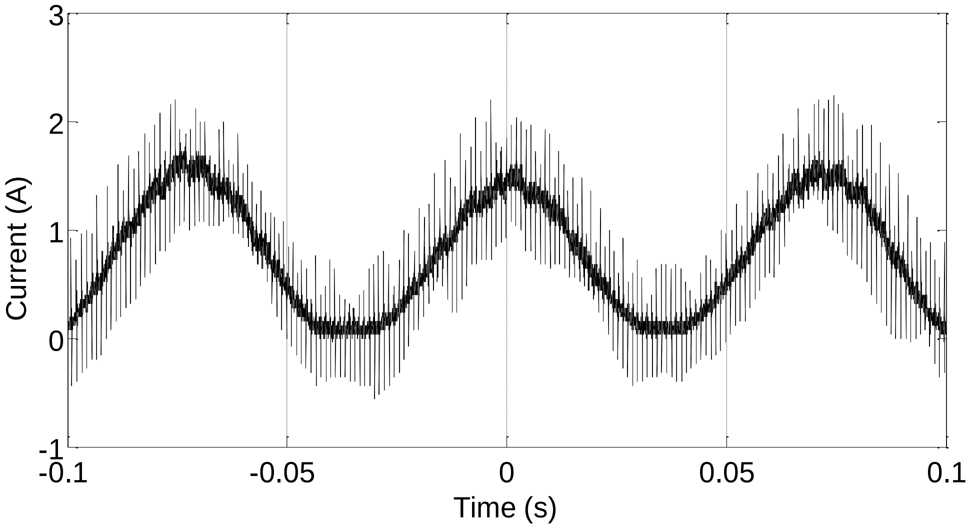

Fig. 4.49 Measured quasi-periodic current (DCM) at *Ki*=9831 corresponding to Fig. 4.29

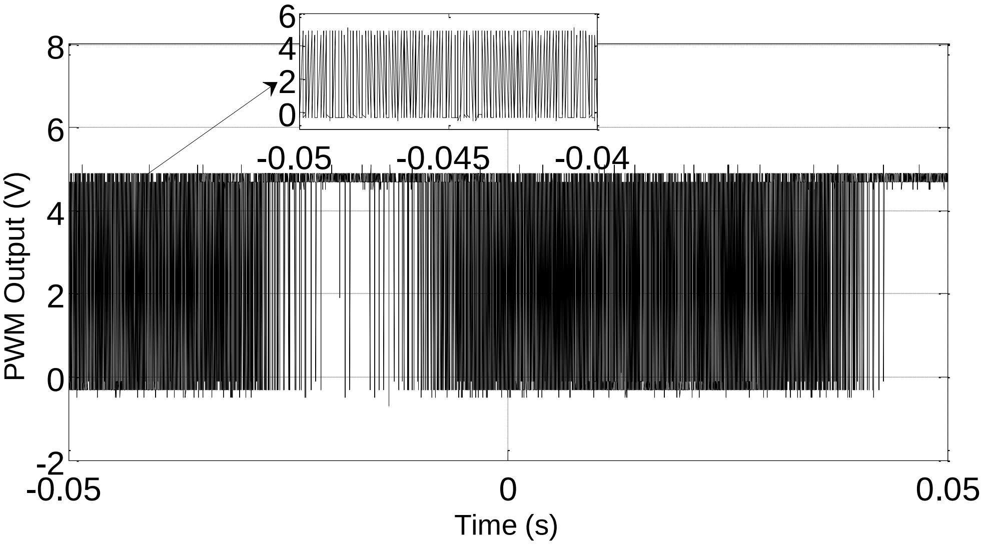

Fig. 4.50 Measured PWM output during quasi-periodic operation in DCM (corresponding to Fig. 4.30).

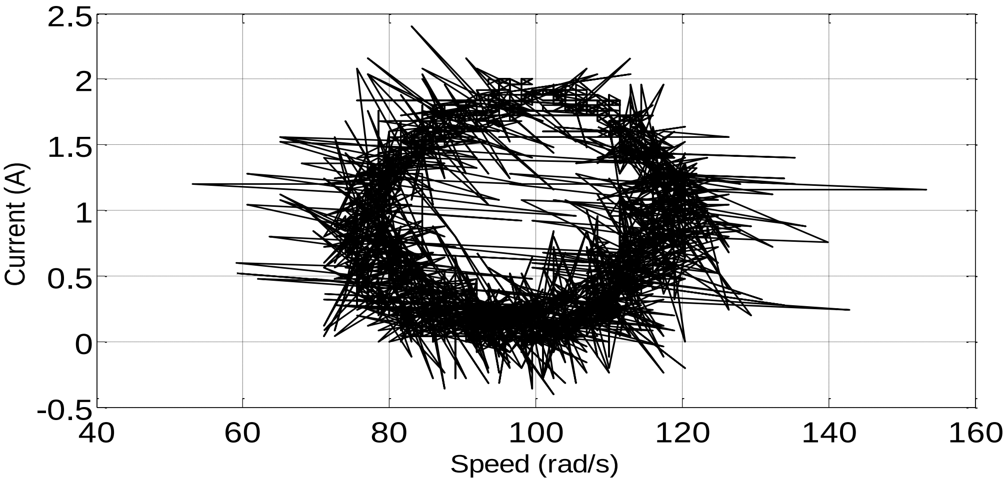

Fig. 4.51 Measured quasi-periodic phase portrait in DCM (*Torus*) at *Ki*=9831 corresponding to Fig. 4.31.

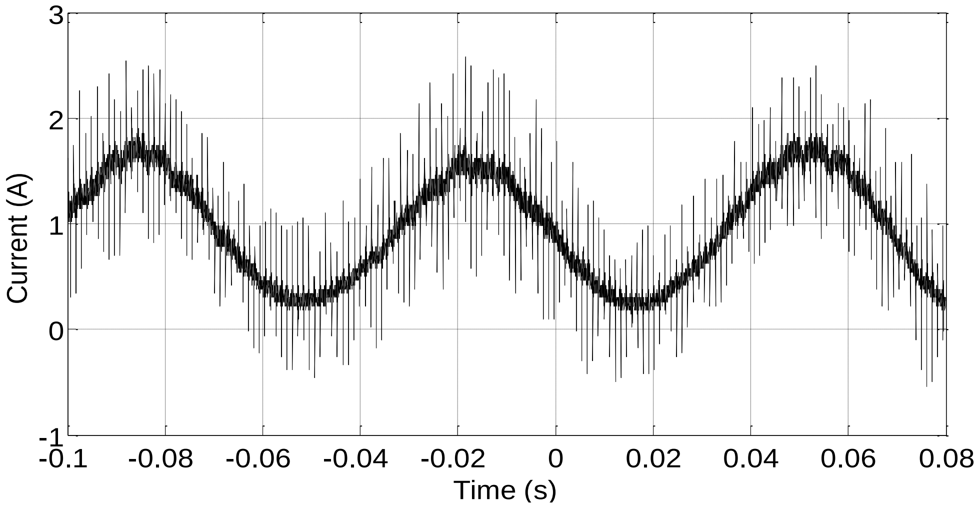

Fig. 4. 52 Measured quasi-periodic current (CCM) as V_{in} is increased to 56.07 V while *Ki* is fixed at 3933 (corresponds to Fig. 4.34).

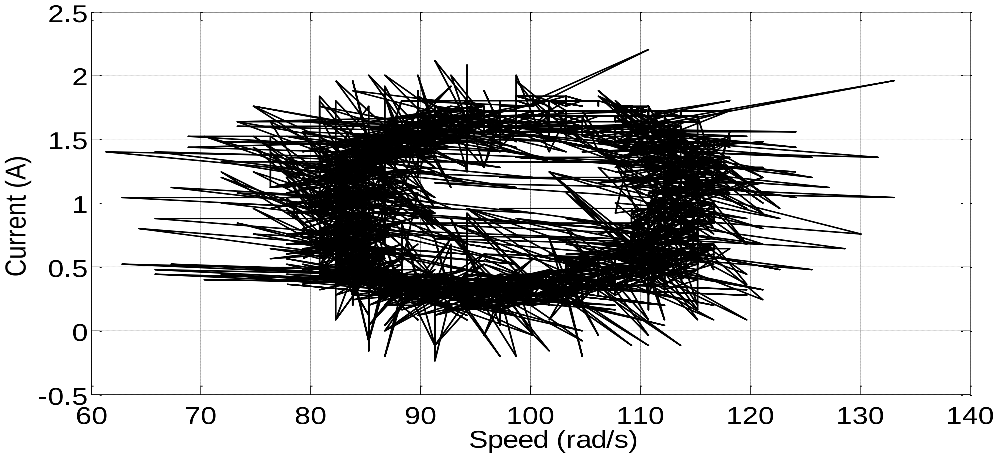

Fig. 4.53 Measured quasi-periodic phase portrait at V_{in} =56.07 V (corresponding to Fig. 4.35).

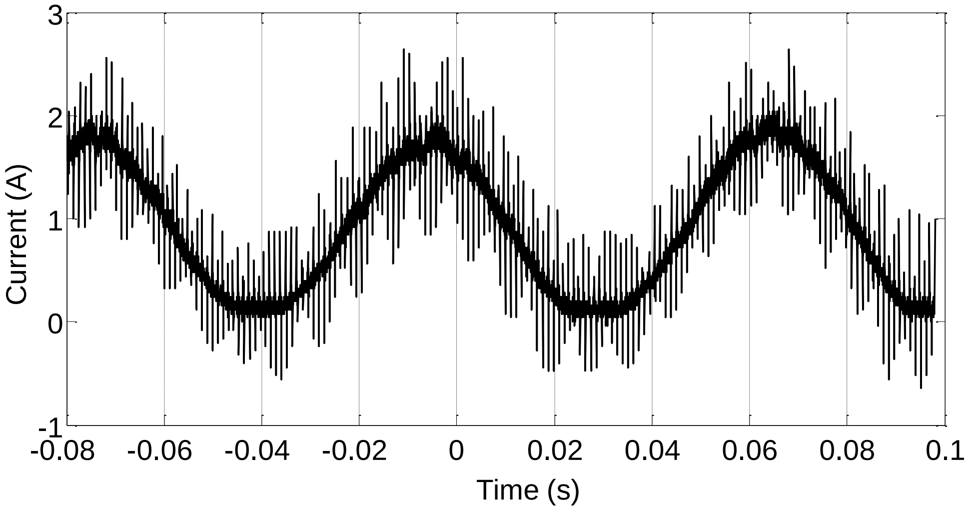

Fig. 4. 54 Measured quasi-periodic current (DCM) at V_{in}=61.5V (corresponding to Fig. 4.36).

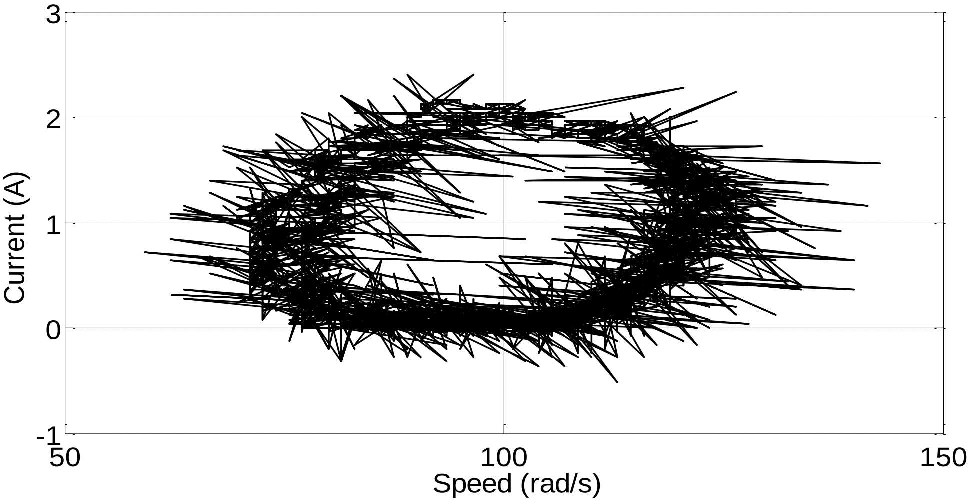

Fig. 4. 55 Measured quasi-periodic orbit (DCM) at V_{in}=61.5V (corresponding to Fig. 4.37).

As can be seen, the qualitative behaviour of the experimental system as the integral gain and supply voltage are varied corresponds with the simulation results. Even though the critical parameter values at which the qualitative change occurred are not expected to be the same in the analog simulation and the digital implementation, the qualitative behaviour of the two systems are the same. An increase in integral gain or supply voltage up to some critical values leads to the birth of a quasi-periodic orbit in both the analog simulation and digital implementation. Further variation of the parameters causes a qualitative change from CCM to DCM. The measured period-1 current and PMW output (Figs. 4.44 and 4.45) correspond with the numerical results (Figs. 4.23 and 4.24), while the measured quasi-periodic orbits as the integral gain is varied (Figs. 4.46

to 4.51) are in agreement with the numerical results presented in Figs. 4.26-4.31. Similarly, the measured quasi-periodic orbits as the supply voltage is varied (Figs. 4.52 to 4.55) correspond well with the numerical results (Figs. 4.34-4.37).

4.3.4 Analysis of the Neimark-Sacker Bifurcation

In this section, the occurrence of the Neimark-Sacker bifurcation will be analysed using both the Monodromy matrix approach and the state space averaging technique. The Monodromy matrix approach can detect both fast-scale and slow-scale instabilities, while the state space averaging technique (see Chapter3 for details) can detect only slow-scale instabilities such as a Neimark-Sacker bifurcation.

4.3.4.1 *Analysis of the Neimark-Sacker Bifurcation Using the Monodromy Matrix Approach*

To analyse the Neimark-Sacker bifurcation using the Monodromy matrix approach, we need to obtain the STM around the nominal period-1 orbit for $t \in [0, T]$ and calculate its eigenvalues. A Neimark-Sacker bifurcation is said to occur when two of the eigenvalues of the system leave the unit circle at the same time. From Fig.4.25, the Monodromy matrix can be expressed as:

$$M(T,0) = \Phi_{\mathbf{off}}(T, t_\Sigma) \times \mathbf{S} \ \times \Phi_{\mathbf{on}}(t_\Sigma, 0) \tag{4.47}$$

where $\Phi(t_B, t_A)$ is the STM from t=t_A to t=t_B and is expressed as $\Phi(t_B, t_A) = e^{A(t_\mathbf{B} - t_\mathbf{A})}$, S is the Saltation matrix that govern the transition of the trajectory from the switch ON region of the state space to the switch OFF region, and $t_\Sigma = d \times T$ is the switching instant. Thus:

$$M(T,0) = e^{A(T - t_\Sigma)} \times \mathbf{S} \ \times e^{At_\Sigma} \tag{4.48}$$

where the Saltation matrice (S) and the switching instant (t_Σ) are the only unknowns. The Saltation matrix can be expressed as:

$$\mathbf{S} = \mathbf{I} + \frac{(\mathbf{f}_2 - \mathbf{f}_1)\mathbf{n}^T}{\mathbf{n}^T \mathbf{f}_1 + \left.\dfrac{\partial h(\mathbf{X}(t))}{\partial t}\right|_{t=t_\Sigma}} \tag{4.49}$$

where h defines the location of the switching hypersurface, $\mathbf{n}$ is the normal vector to the hypersurface, $\mathbf{f}_1$ is the vector field before the switching instant, $\mathbf{f}_2$ is the vector field after the switching instant, and $\mathbf{I}$ is an identity matrix of the same order of the system.

$$\mathbf{f}_1 = \lim_{t\downarrow t_\Sigma} \mathbf{f}_1(\mathbf{X}(t),t) = \mathbf{A}_1\mathbf{X}(t_\Sigma) + \mathbf{V}_1 \tag{4.50}$$

$$\mathbf{f}_2 = \lim_{t\uparrow t_\Sigma} \mathbf{f}_2(\mathbf{X}(t),t) = \mathbf{A}_2\mathbf{X}(t_\Sigma) + \mathbf{V}_2 \tag{4.51}$$

where $\boldsymbol{A}_1$, $\boldsymbol{A}_2$, $\mathbf{V}_1$, and $\mathbf{V}_2$ have been previously defined, and $\mathbf{X}(t_\Sigma)$ is the state vector at the switching instant. The transition from the first sub-system (switch ON state) to the second sub-system (switch OFF state) occurs when $V_{\mathrm{con}}(t)=V_{\mathrm{ramp}}(t)$, and thus the switching hypersurface is expressed as:

$$h(X(t)) = Kp(\omega_{ref} - x_1(t)) + K_i x_3(t) - V_L - (V_U - V_L)\frac{t}{T} \tag{4.52}$$

$$n = \begin{bmatrix} \dfrac{\partial h}{\partial x_1} \\ \dfrac{\partial h}{\partial x_2} \\ \dfrac{\partial h}{\partial x_3} \end{bmatrix} = \begin{bmatrix} -Kp \\ 0 \\ Ki \end{bmatrix} \tag{4.53}$$

$$\frac{\partial h}{\partial t} = \frac{-(V_U - V_L)}{T} \tag{4.54}$$

Consequently to obtain the Saltation matrix (**S**) and the Monodromy matrix, the only unknown is the switching instant t_Σ, and this can be obtained following the same procedure outlined in section 4.2.3. The computed Saltation matrix, Monodromy matrix, and Floquet multipliers as the integral gain is varied are as shown in Table 4.7. From the Table it could be seen that the Neimark-Sacker bifurcation occurs at *K*i=1612 which is in agreement with the bifurcation diagram of Fig. 4.32.

Table 4.7 Saltation matrix and Monodromy matrix as the integral gain is varied.

K_i	Saltation matrix	Monodromy Matrix	Abs(Floquet Multipliers)
1000	$\begin{bmatrix} 1.0000 & 0 & 0 \\ -0.0300 & 1.0000 & 29.9917 \\ 0 & 0 & 1.0000 \end{bmatrix}$	$\begin{bmatrix} 0.9992 & 0.0894 & 0.7467 \\ -0.0314 & 0.9229 & 29.3653 \\ -0.0000 & -0.0000 & 1.0000 \end{bmatrix}$	0.9941 0.9941 0.9359
1200	$\begin{bmatrix} 1.0000 & 0 & 0 \\ -0.0300 & 1.0000 & 35.9901 \\ 0 & 0 & 1.0000 \end{bmatrix}$	$\begin{bmatrix} 0.9992 & 0.0894 & 0.8960 \\ -0.0316 & 0.9229 & 35.2383 \\ -0.0000 & -0.0000 & 1.0000 \end{bmatrix}$	0.9964 0.9964 0.9317
1500	$\begin{bmatrix} 1.0000 & 0 & 0 \\ -0.0300 & 1.0000 & 44.9876 \\ 0 & 0 & 1.0000 \end{bmatrix}$	$\begin{bmatrix} 0.9992 & 0.0894 & 1.0766 \\ -0.0320 & 0.9229 & 44.0843 \\ -0.0000 & -0.0000 & 1.0000 \end{bmatrix}$	0.9991 0.9991 0.9266
1570	$\begin{bmatrix} 1.0000 & 0 & 0 \\ -0.0300 & 1.0000 & 47.0870 \\ 0 & 0 & 1.0000 \end{bmatrix}$	$\begin{bmatrix} 0.9992 & 0.0894 & 1.1722 \\ -0.0320 & 0.9229 & 46.1034 \\ -0.0000 & -0.0000 & 1.0000 \end{bmatrix}$	0.9997 0.9997 0.9256
1600	$\begin{bmatrix} 1.0000 & 0 & 0 \\ -0.0300 & 1.0000 & 47.9868 \\ 0 & 0 & 1.0000 \end{bmatrix}$	$\begin{bmatrix} 0.9991 & 0.0894 & 1.1946 \\ -0.0320 & 0.9229 & 46.9844 \\ -0.0000 & -0.0000 & 1.0000 \end{bmatrix}$	0.9999 0.9999 0.9251
1612	$\begin{bmatrix} 1.0000 & 0 & 0 \\ -0.0300 & 1.0000 & 48.3467 \\ 0 & 0 & 1.0000 \end{bmatrix}$	$\begin{bmatrix} 0.9991 & 0.0894 & 1.2036 \\ -0.0320 & 0.9229 & 47.3368 \\ -0.0000 & -0.0000 & 1.0000 \end{bmatrix}$	1.0000 1.0000 0.9250
1618	$\begin{bmatrix} 1.0000 & 0 & 0 \\ -0.0300 & 1.0000 & 48.5566 \\ 0 & 0 & 1.0000 \end{bmatrix}$	$\begin{bmatrix} 0.9991 & 0.0894 & 1.2088 \\ -0.0320 & 0.9229 & 47.5423 \\ -0.0000 & -0.0000 & 1.0000 \end{bmatrix}$	1.0001 1.0001 0.9249

4.3.4.2 *Analysis of the Neimark-Sacker Bifurcation Using the State Space Average Model*

To analyse the Neimark-Sacker bifurcation using the state space averaging technique [16], we need to obtain an average or time invariant equivalent model of the original time varying model of the system (equation 4.43). If the new model is linear time invariant then its stability can be deduced by finding the eigenvalue of the state matrix or by applying other tools such as root locus or the Routh stability criterion. The period-*T* state space average model of the PI controlled PMDC drive is expressed as follows:

$$\begin{aligned}\frac{d\overline{\mathbf{X}}(t)}{dt} &= d\times\mathbf{f_1}(\overline{\mathbf{X}}(t))+(1-d)\times\mathbf{f_2}(\overline{\mathbf{X}}(t))\\ &= d\times(\mathbf{A}_1\overline{\mathbf{X}}(t)+\mathbf{V_1})+(1-d)\times(\mathbf{A}_2\overline{\mathbf{X}}(t)+\mathbf{V_2})\\ &= \mathbf{A}\overline{\mathbf{X}}(t)+(\mathbf{V_1}-\mathbf{V_2})d+\mathbf{V_2}\end{aligned} \tag{4.55}$$

where (d) is the fraction of time sub-system1 (switch ON state) is active, 1- d is the fraction of time sub-system 2 (switch OFF state) is active, $\overline{\mathbf{X}}(t)$ is the period-T averaged state vector and $\mathbf{A}_1$=**A**2=**A.** The expressions for $\mathbf{V}_1$, $\mathbf{V}_2$, and the state matrix **A** have been previously defined.

To complete the average model, we need to derive the expression for the duty cycle (d) using the switching condition $V_{\mathrm{con}}(t)$=$V_{\mathrm{ramp}}(t)$, where $V_{con}(t)=Kp(\omega_{ref}-x_1(t))+K_i x_3(t)$.

$$d=\frac{Kp\times(\omega_{ref}-\overline{x}_1)+Ki\times\overline{x}_3-V_L}{V_D} \tag{4.56}$$

where $V_D=V_U-V_L$. Thus, the duty cycle is a function of the state variables of the system. By substituting the expression for the duty cycle (d) in equation (4.55), the average model is expressed as:

$$\frac{d\overline{\mathbf{X}}(t)}{dt}=\mathbf{A}_{avg}\overline{\mathbf{X}}(t)+V_{avg} \tag{4.57}$$

$$\mathbf{A}_{avg}=\begin{bmatrix}\frac{-B}{J} & \frac{K_t}{J} & 0\\ \left(\frac{-K_e}{L}-\frac{Kp\times V_{in}}{L\times V_D}\right) & \frac{-R}{L} & \frac{Ki\times V_{in}}{L\times V_D}\\ -1 & 0 & 0\end{bmatrix} \tag{4.58}$$

$$V_{avg} = \begin{bmatrix} \dfrac{-T_L}{J} \\ \\ \left(\dfrac{-V_L \times V_{in}}{L \times V_D} + \dfrac{Kp \times \omega_{ref} \times V_{in}}{L \times V_D} \right) \\ \\ \omega_{ref} \\ \\ \end{bmatrix} \qquad (4.59)$$

From (4.58), it could be seen that the state matrix ($\mathbf{A}_{avg}$) of the average model is a function of the integral gain (*K*i), the proportional gain (*K*p), and the supply voltage (V_{in}). Assuming *K*p and V_{in} are kept constant, the response of the average model at *K*i=1400 and *K*i=1612 are as shown in Figs. 4.56 and 4.57, respectively.

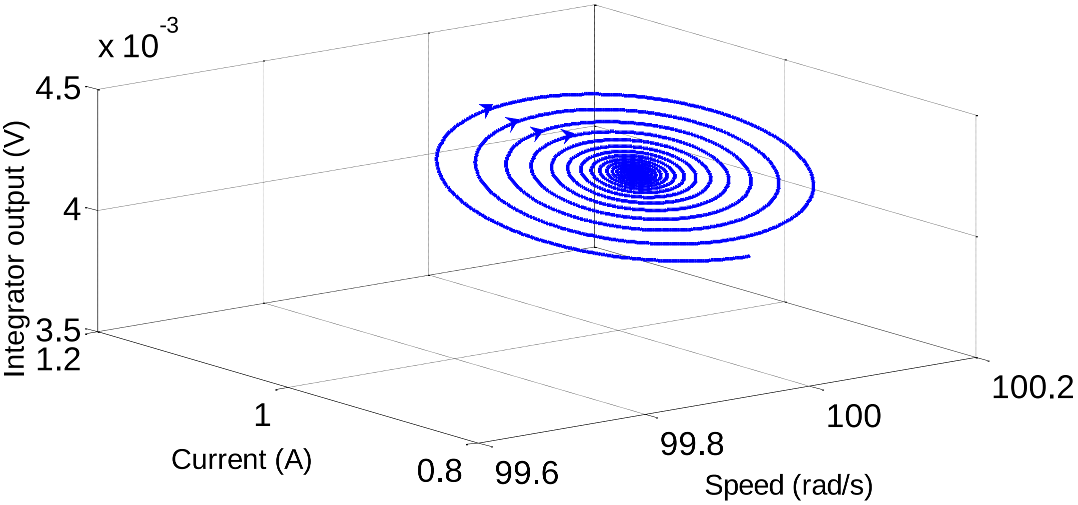

Fig. 4. 56 Stable spiral point at Ki=1400, Kp=1, V_{in}=24 V.

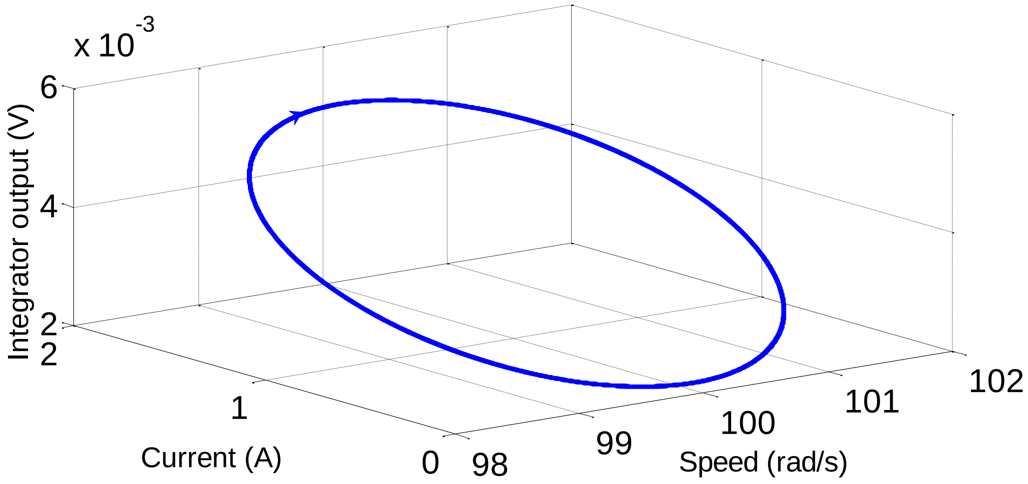

Fig. 4.57 Stable limit cycle (Torus) due to the Neimark-Sacker bifurcation at *K*i=1612, *K*p=1, V_{in} =24 V.

The simulation results indicate the existence of a stable spiral point at *K*i=1400, and a stable limit cycle due to the Neimark-Sacker bifurcation at *K*i=1612, in agreement with the bifurcation diagram of Fig. 4.32.

To analytically validate the occurrence of the Neimark-Sacker bifurcation using the average model, the eigenvalue of the state matrix ($\mathbf{A}_{\text{avg}}$) will be computed as the system parameters (*K*i, V_{in}, *K*p) are being varied. As discussed in Chapter 2, a Neimark-Sacker bifurcation is said to occur if a stable spiral point loses stability and a stable limit cycle appears. The spiral point is stable (attracts) when the real part of all the eigenvalues of the state matrix is negative, and unstable when the real part suddenly becomes positive. Assuming V_{in}=24V, *K*p=1, and the integral gain is varied, the computed eigenvalues of the state matrix are shown in Table 4.8, and the eigenvalue loci are shown in Fig. 4.58.

Table 4.8 Eigenvalues of the state matrix as the integral gain is varied.

Integral Gain (Ki)	Eig($\mathbf{A}_{avg}$)	Remarks
1400	$\begin{bmatrix} -0.0351 + 1.0232i \\ -0.0351 - 1.0232i \\ -1.4901 \end{bmatrix} \times 10^3$	Stable Spiral point
1500	$\begin{bmatrix} -0.0180 + 1.0477i \\ -0.0180 - 1.0477i \\ -1.5243 \end{bmatrix} \times 10^3$	Stable Spiral point
1600	$\begin{bmatrix} -0.0019 + 1.0709i \\ -0.0019 - 1.0709i \\ -1.5565 \end{bmatrix} \times 10^3$	Stable Spiral point
1610	$\begin{bmatrix} -0.0003 + 1.0732i \\ -0.0003 - 1.0732i \\ -1.5596 \end{bmatrix} \times 10^3$	Stable Spiral point
1612	$\begin{bmatrix} 1.0736i \\ 1.0736i \\ -1.5603 \end{bmatrix} \times 10^3$	Unstable Spiral point
1613	$\begin{bmatrix} 0.0001 + 1.0739i \\ 0.0001 - 1.0739i \\ -1.5606 \end{bmatrix} \times 10^3$	Stable limit cycle

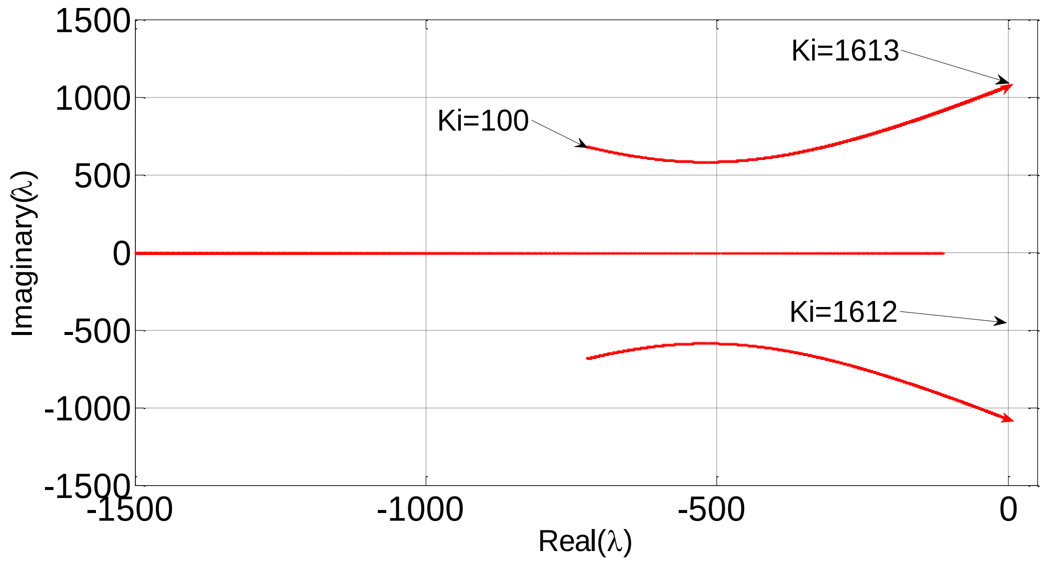

Fig. 4. 58 Eigenvalue loci as the integral gain is varied from 100 to 1615.

From Table 4.8 and Fig. 4.58, it could be seen that the Neimark-Sacker bifurcation occurs at Ki=1612 as the real part of the complex conjugate eigenvalues is zero at that parameter value. At Ki=1613, the real part of the complex conjugate eigenvalues crosses to the positive side of the complex eigenvalue plane, indicating the occurrence of the Neimark-Sacker bifurcation.

4.4 Summary

In this chapter, the nonlinear phenomena in DC chopper-fed PMDC drive have been investigated. When the simple proportional controller was employed, the drive exhibited a period doubling bifurcation cascades route to chaos, as well as co-existing attractors with fractal basin boundaries. But when the proportional integral controller was employed, a slow scale instability or Neimark-Sacker bifurcation was observed. The Neimark-Sacker bifurcation was analysed (using both the Monodromy matrix and state space averaging techniques) and experimentally validated using a dsPIC30F3010 DSC. The experimental results are in good agreement with the analytical and simulation results thus confirming the occurrence of Neimark-Sacker bifurcation in the PI controlled PMDC drive. In the next chapter, the nonlinear analysis will be extended to a switched reluctance drive which is an example of a piecewise nonlinear system.

CHAPTER 5

ANALYSIS OF NONLINEAR PHENOMENA IN SWITCHED RELUCTANCE DRIVES

5.1 Introduction.

In Chapter 4, nonlinear phenomena in a typical piecewise linear electrical drive, namely PMDC drives were analyzed. In this chapter, the nonlinear analysis is extended to a three-phase 12/8 switched reluctance drive (Fig. 5.1), which is an example of a piecewise nonlinear system.

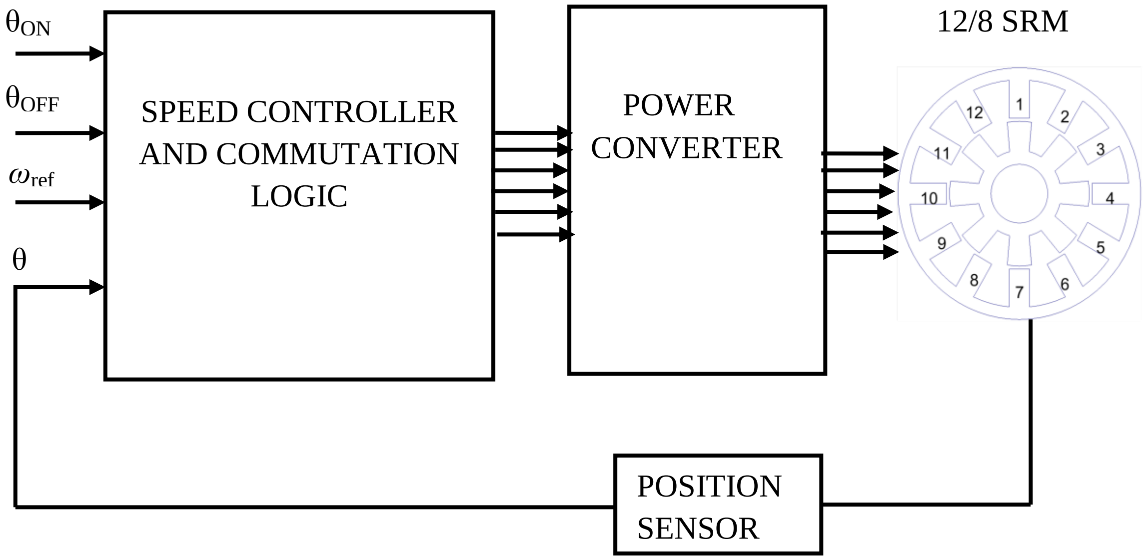

Fig. 5.1 Architecture of the three-phase 12/8 SRM drive.

The system consists of a conventional 12/8 SRM, asymmetric drive power converter circuit, speed controller and commutation logic circuits, and position sensor. θ_{ON} is the phase switch ON angle, θ_{OFF} is the phase switch OFF angle, ω_{ref} is the reference speed ,θ is the actual shaft position, and four of the stator poles make one phase. In digital implementation, the speed controller and the commutation logic will be implemented within the microprocessor. The expanded view of the controller and power converter circuit is shown in Fig. 5.2.

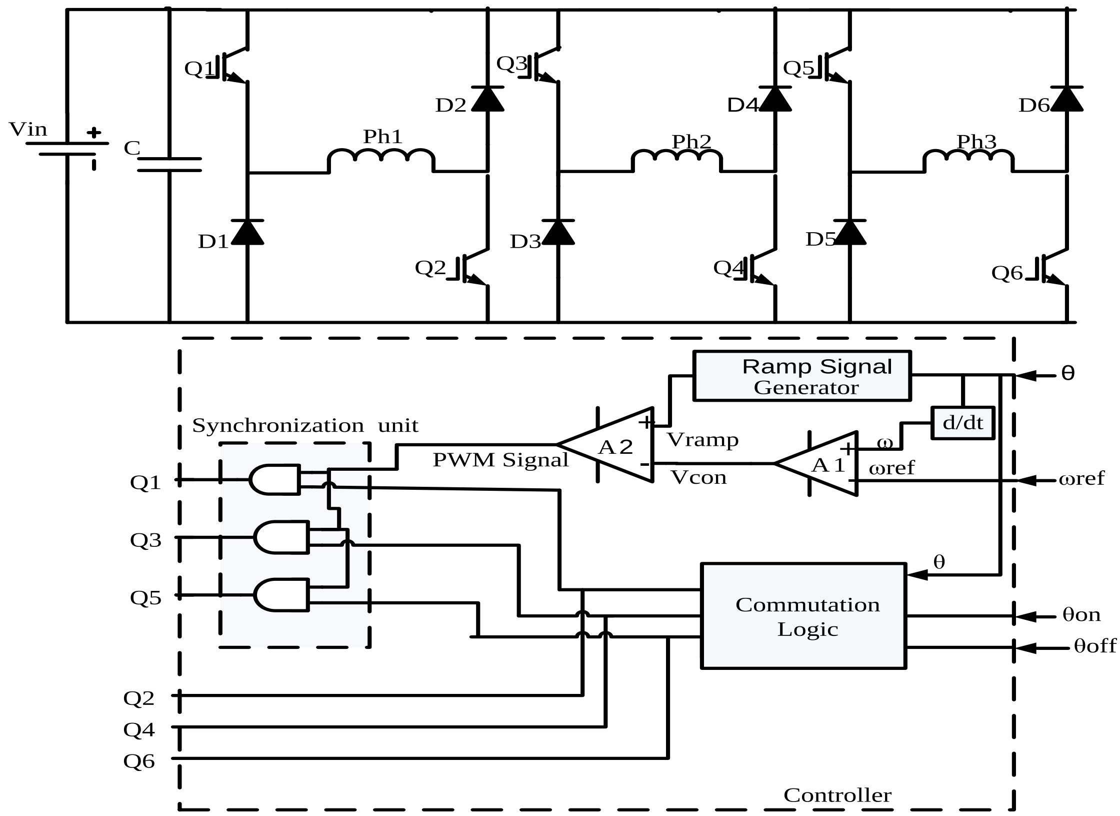

Fig. 5.2 Expanded view of the controller and power converter circuit

The nominal behaviour of the system is a period-1 orbit, but this nominal orbit can lose stability via fast-scale or period doubling bifurcation as some system parameter such as the proportional gain is being varied, as initially reported in [47]. Further variation of the parameter leads to period doubling bifurcation cascades and chaos. In this Chapter, the Monodromy matrix approach will be applied in analysing the fast-scale bifurcation in the 3-phase, 12/8 SRM drive. The complexity of the analysis is compounded by the fact that the SRM drive model consist of nonlinear vector fields, and thus the state transition matrix (STM) along the orbit will be computed by solving matrix differential equation (MDE), instead of the simple exponential matrix used in piecewise linear systems such as PMDC drive and DC-DC converters.

This chapter is structured as follows. In section 5.2, the operation of the 12/8 SRM drive will be described, while the system mathematical model is derived in section 5.3. The dynamic behaviour of the drive is discussed in section 5.4, and the fast-scale bifurcation is analysed in section 5.5 using the Monodromy matrix technique.

5.2 System Operation

As shown in Fig.5.1, closed loop operation of the SRM drive relies on rotor position feedback. In this project, the soft-chopping SRM operational mode (see Chapter 3 for details) is considered. Once the actual rotor position is obtained from the position sensor, the commutation logic (detailed in Chapter3) will determine which SRM phase is to be activated, and the appropriate lower leg switch (Q2, Q4 or Q6) will be switched ON. The inputs to the commutation logic are the rotor position (θ), the phase switch ON angle (θ_{on}), and the phase switch OFF angle (θ_{off}). While the commutation logic is running, the PWM generator will compare the ramp signal ($V_{ramp}(t)$) and the control signal ($V_{con}(t)$), to obtain the required PWM signal. When the ramp signal is greater than the control signal, the PWM output will be high, and the upper leg switches (Q1, Q3 or Q5) will be switched ON, but when the control signal is greater than the ramp signal, the PWM output will be low, and the upper leg switch will be switched OFF. To ensure that the ramp signal always starts from its lowest value at the beginning of the conduction interval $\theta\in[\theta_{on,}\ \theta_{off}]$ of any given phase, the ramp signal is made to be a function of the angle (θ). The synchronization unit ensures that the PWM operation takes place only in the upper switch of the energized phase, while the other phases will be idle.

For efficient operation of the drive, the switch ON angle (θ_{on}) corresponds to the angle when the phase inductance begins to rise, and the switch OFF angle (θ_{off}) corresponds to the angle when the phase inductance gets to maximum. Each phase must be stroked (energized) once within one inductance cycle of $2\pi/N_r$, where N_r is the number of rotor poles. The commutation sequence of the 12/8 SRM whose dynamic behavior is studied in this project was shown earlier in section 3.6.2, but repeated here (Fig.5.3) for convenience, for θ_{on}=5.5° and θ_{off} =20.5°**.** The possible topological states, during the drive operation, can be illustrated by considering only one phase of the drive.

Assuming the shaft position θ=5.5°= θ_{on}, the lower leg switch Q2 will be turned ON, and the diode (D2) will be reverse biased (OFF) (phase1 activated). Then, if the PWM signal is high, the upper leg switch Q1 will be switched ON, and diode (D1) will be reverse biased (OFF), thus causing +Vin to be applied at the phase coil terminal. But, if the PWM signal is low, Q1 will be turned OFF, and D1 will be forward biased (switched ON), thus causing 0V to be applied at the phase1 coil terminal. At θ=20.5°= θ_{off}, phase1 will be de-energized by switching OFF the upper and lower leg switches, thus causing D1 and D2 to be forward biased, and -Vin to be applied at the phase1 coil terminal. The phase1 switch OFF angle (θ=20.5°) corresponds to the phase2 switch ON angle. The three possible topological states applicable to any of the energized phases due to the soft-chopping operation are shown in Table 5.1.

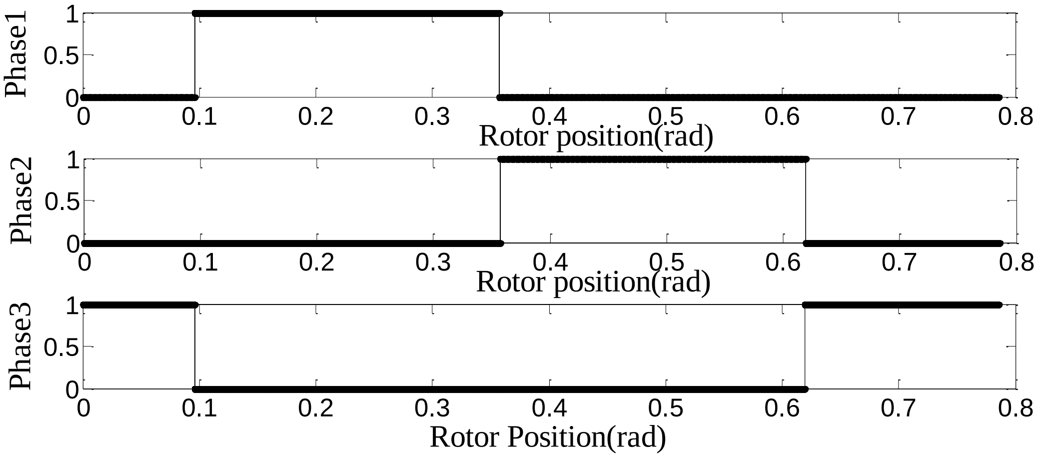

Fig. 5.3 SRM commutation sequence for one inductance cycle of 45° mechanical. (θ_{on}=5.5°=0.095rad, θ_{off} =20.5°=0.3577rad and phase separating angle=15°).

Table 5.1 Possible topological states during the conduction interval of any phase.

System State	Q1	Q2	D1	D2	Vin
$V_{r\,amp} > V_{con}$	1	1	0	0	+Vin
$V_{r\,amp} < V_{con}$	0	1	1	0	0
Defluxing	0	0	1	1	-Vin

5.3 System Mathematical Model

The mathematical model of the SRM comprises the electromagnetic equations of the phase windings and the mechanical equations. Assuming that mutual inductance effects are ignored, the electromagnetic circuit created by any energized phase in an n-phase SRM can be described by [78, 80, 82] :

$$\frac{d\lambda_j(i_j,\theta)}{dt} = V_j - Ri_j \Big|_{j=1,2,..n} \tag{5.1}$$

where V_j is the voltage across the phase coil terminals, R is the electrical resistance of the phase coil, i_j is the phase current, λ_j is the phase flux linkage, and θ is the rotor position. The flux linkage is a function of the phase current and inductance and is given by

$$\lambda(i_j,\theta) = N \times \phi(\theta,i_j) = L(\theta,i_j) \times i_j \tag{5.2}$$

where *N* is the number of turns in the stator poles, ϕ is the magnetic flux produced, and $L(\theta,i_j)$ is the inductance of the phase coil. Since the phase flux linkage is a function of two independent variables, its derivative with time can be expressed as:

$$\begin{aligned}\frac{d\lambda(i_j,\theta)}{dt} &= \frac{\partial\lambda(i_j,\theta)}{\partial i}\frac{di_j}{dt} + \frac{\partial\lambda(i_j,\theta)}{\partial\theta}\frac{d\theta}{dt} \\ &= L(\theta,i_j)\frac{di_j}{dt} + i_j\omega\frac{dL(\theta,i_j)}{dt}\end{aligned} \tag{5.3}$$

When operating under low speed and light load conditions, the magnetic saturation effect will be negligible and the inductance of the phase coil will be expressed as a function of the rotor position only. Consequently, the phase flux linkage will be expressed as a linear function of the phase current and the rotor position as shown below:

$$\lambda(i_j,\theta) = L(\theta) \times i_j \tag{5.4}$$

The electromagnetic equation (5.1) will thus be expressed as:

$$\frac{di_j}{dt} = \frac{V_j - Ri_j - i_j\omega\dfrac{dL(\theta)}{d\theta}}{L(\theta)} \tag{5.5}$$

where the term $i_j\omega dL(\theta)/d\theta$ is the back EMF produced at the phase coil terminals. The phase inductance profile ($L(\theta)$) for the 12/8 SRM, based on the linear flux linkage model is a function of the rotor position [47] and is as expressed below:

$$L(\theta) = \begin{cases} L_{\min};0 < \theta \le \theta_x \\ L_{\min} + G(\theta - \theta_x);\theta_x < \theta \le \theta_y \\ L_{\max};\theta_y < \theta \le \dfrac{\pi}{N_r} \end{cases} \tag{5.6}$$

$$G = \frac{L_{\max} - L_{\min}}{\theta_y - \theta_x} \qquad (5.7)$$

where G is the slope of the rising portion of the inductance profile, L_{min} is the minimum inductance, and L_{max} is the maximum inductance. The angular interval $0<\theta<\theta_x$ is the unaligned position while the angular interval $\theta_y<\theta<\pi/N_r$ is the aligned position. The inductance cycle of 12/8 SRM is $(2\times pi/N_r = 0.7583rad = 45\,\text{deg})$. Assuming θ_x=5.5°, θ_y=20.5°, $L_{\min}$=0.34mH, and G=7.8mH/rad, then the inductance profile for one phase of the 12/8 SRM is as shown in Fig.5.4.

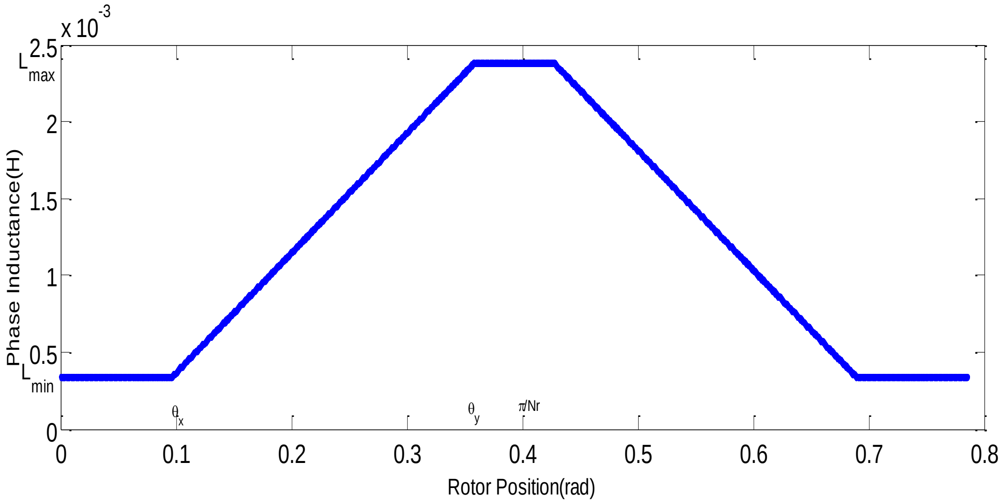

Fig. 5.4 Inductance profile for one phase of the 12/8 SRM.

The mechanical equations of the system are:

$$\frac{d\theta}{dt} = \omega(t) \qquad (5.8)$$

$$\frac{d\omega}{dt} = (T_e - T_L - B\omega)/J \qquad (5.9)$$

where T_e is the total electrical torque produced by all the phases, T_L is the load torque, B is the friction coefficient, and J is the load inertia. Based on the linear flux linkage model, the expression for the electrical torque produced by each energized phase is:

$$T_j = \left.\frac{\partial W_j}{\partial \theta}\right|_{j=1,2,3} \qquad (5.10)$$

where W is the co-energy or the total energy under the magnetisation curve of each phase [77].

$$\begin{aligned} W_j &= \int_0^i \lambda(i_j,\theta)di = \int_0^i L(\theta)idi \\ W_j &= 0.5L(\theta)i^2 \end{aligned} \tag{5.11}$$

Thus, the per phase torque will be given by

$$T_j = 0.5i^2 \left.\frac{dL(\theta)}{d\theta}\right|_{j=1,2,3} \tag{5.12}$$

Since the phase inductance is a piecewise linear function of the rotor position (5.6), the torque produced by each phase will also be a piecewise linear function of the rotor position as shown below.

$$T_j(\theta) = \begin{cases} 0;\ 0 < \theta \le \theta_x \\ 0.5{i_j}^2G;\ \theta_x < \theta \le \theta_y \\ 0;\ \theta_y < \theta \le \dfrac{\pi}{N_r} \end{cases} \tag{5.13}$$

This implies that the per phase torque is zero during the aligned and unaligned positions. To avoid zero starting torque most SRM drives usually employ a special start-up algorithm. The mechanical equation for the linear flux linkage model is thus:

$$\frac{d\omega}{dt} = \left(T_e - T_L - B\omega\right)/J \tag{5.14}$$

where T_e is the total torque produced by all the separate phases in an n-phase SRM expressed as [78] :

$$T_e = 0.5\sum_{j=1}^{n} \frac{dL(\theta + (n-j-1)\theta_s)}{d\theta} i_j^2 \tag{5.15}$$

where θ_s is the phase separating angle. Assuming the firing angles (θ_{on} and θ_{off}) correspond with θ_x and θ_y, and the phase separating angle (θ_s) is equal to the dwell angle ($\theta_D = \theta_{off} - \theta_{on}$), then the torque produced by any energized phase during the dwell angle or conduction interval is given by

$$T_j = 0.5Gi_j^2 \tag{5.16}$$

Within the period of maximum inductance, i.e. the aligned position ($\theta \in [\theta_y, \pi/N_r]$), the torque produced will be zero as $dL/d\theta$ is zero. If the phase current of the energized phase decays to zero within the period of maximum inductance, then the total torque produced at any instant is the same as the torque produced by the energized phase. Also, there will be no overlap among the different phase currents and the sum of all the phase currents ($i = i_1 + i_2 + \dots i_n$) at any instant will be same as the current in the activated phase [87]. As a result, the mathematical model for the SRM based on the three possible topological states during the conduction interval of any of the phases is expressed as

$$\begin{cases} \dfrac{d\theta}{dt} = \omega(t) \\ \dfrac{d\omega}{dt} = \begin{cases} \dfrac{0.5Gi^2 - T_L - B\omega}{J} \\ \dfrac{-T_L - B\omega}{J};\theta \in [\theta_{off}, \dfrac{\pi}{N_r}] \end{cases} \\ \dfrac{di}{dt} = \begin{cases} \dfrac{V_{in} - iR - G\omega i}{L_{\min} + G(\theta - \theta_{on})};V_{ramp} > V_{con} \\ \dfrac{-iR - G\omega i}{L_{\min} + G(\theta - \theta_{on})};V_{ramp} < V_{con} \\ \dfrac{-iR - V_{in}}{L_{\max}};\theta \in [\theta_{off}, \dfrac{\pi}{N_r}] \end{cases} \end{cases} \tag{5.17}$$

where $\theta(t)$ is the shaft position, $\omega(t)$ is the angular speed, and $i(t)$ is the sum of all phase currents at any instant t.

To express the system in a form suitable for the stability analysis, the system equation (5.17) can be rearranged as

$$\frac{dX(t)}{dt} = \begin{cases} f_1(\mathbf{X}(t));\ V_{con}(t) > V_{ramp}(t) \\ f_2(\mathbf{X}(t));V_{con}(t) < V_{ramp}(t \\ f_3(\mathbf{X}(t));\theta_{off} < \theta < \dfrac{\pi}{N_r} \end{cases} \tag{5.18}$$

where $X(t) = [\theta(t)\ \ \omega(t)\ \ i(t)]^T = [x_1(t)\ \ x_2(t)\ \ x_3(t)]^T$ is the state vector.

$$f_1(X(t)) = \begin{bmatrix} x_2 \\ \dfrac{0.5Gx_3^2 - Bx_2 - T_L}{J} \\ \dfrac{-Rx_3 - Gx_2x_3}{L_{\min} + G(x_1 - \theta_{on})} \end{bmatrix} \tag{5.19}$$

$$f_2(X(t)) = \begin{bmatrix} x_2 \\ \dfrac{0.5Gx_3^2 - Bx_2 - T_L}{J} \\ \dfrac{V_{in} - Rx_3 - Gx_2x_3}{L_{\min} + G(x_1 - \theta_{on})} \end{bmatrix} \tag{5.20}$$

$$f_3(X(t)) = \begin{bmatrix} x_2 \\ \dfrac{-Bx_2 - T_L}{J} \\ \dfrac{-V_{in} - Rx_3}{L_{\max}} \end{bmatrix} \tag{5.21}$$

$$V_{con}(t) = g(\omega(t) - \omega_{ref}) = g(x_2(t) - \omega_{ref}) \tag{5.22}$$

$$\begin{aligned} V_{ramp}(t) &= V_{Low} + (V_{Up} - V_{Low})\left(\frac{(\theta(t) - \theta_{on}}{\theta_T}\right) \bmod 1 \\ &= V_{Low} + (V_{Up} - V_{Low})\left(\frac{(x_1(t) - \theta_{on}}{\theta_T}\right) \bmod 1 \end{aligned} \tag{5.23}$$

$$\theta_T = \frac{(\theta_{off} - \theta_{on})}{C} \tag{5.24}$$

where C is an integer constant that determines the number of cycles of the ramp signal within the conduction interval of each phase.

5.4 System's Dynamic Behaviour

Under soft-chopping operation, the nominal steady state dynamics of the state variables is a period-1 orbit (Figs. 5.5 to 5.7). But as some system parameter such as the proportional gain (g) is varied, the nominal orbit loses stability via a period doubling or fast-scale bifurcation leading to the birth of a new attractor whose period is double the period of original orbit (Figs. 5.8 to 5.10). Further variation of the system parameter leads to period doubling bifurcation cascades and chaos (Fig. 5.11 to 5.13). The bifurcation diagram of the system as the proportional gain is varied is shown in Fig.5.14, and the system parameters used in the simulation are shown in Table 5.2.

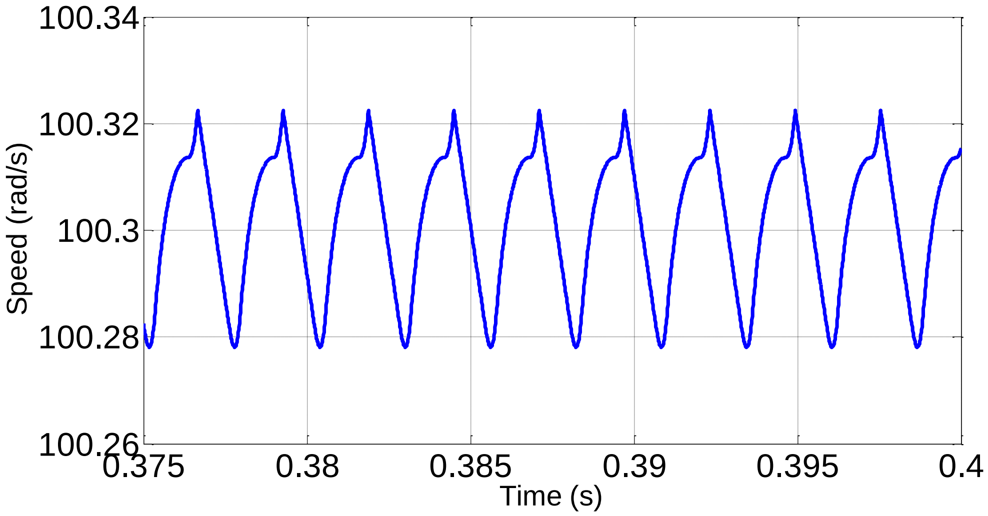

Fig. 5.5 Period-1 speed trajectory at g=10.

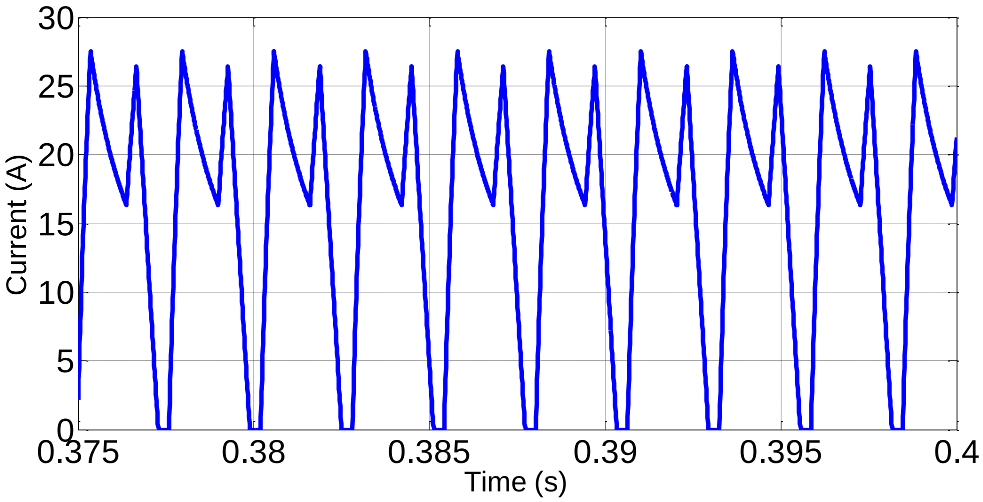

Fig. 5. 6 Sum of all phase current (i=i_1+i_2+i_3) against time during period-1 operation.

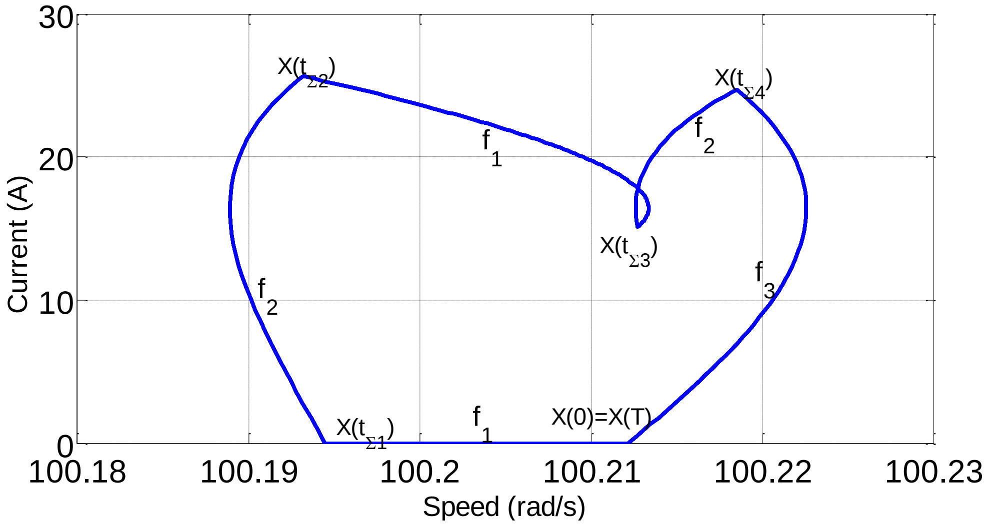

Fig. 5. 7 Trajectory of speed against the sum of all phase current during one inductance cycle of the drive $(\theta \in [0, \frac{2\pi}{N_r}])$.

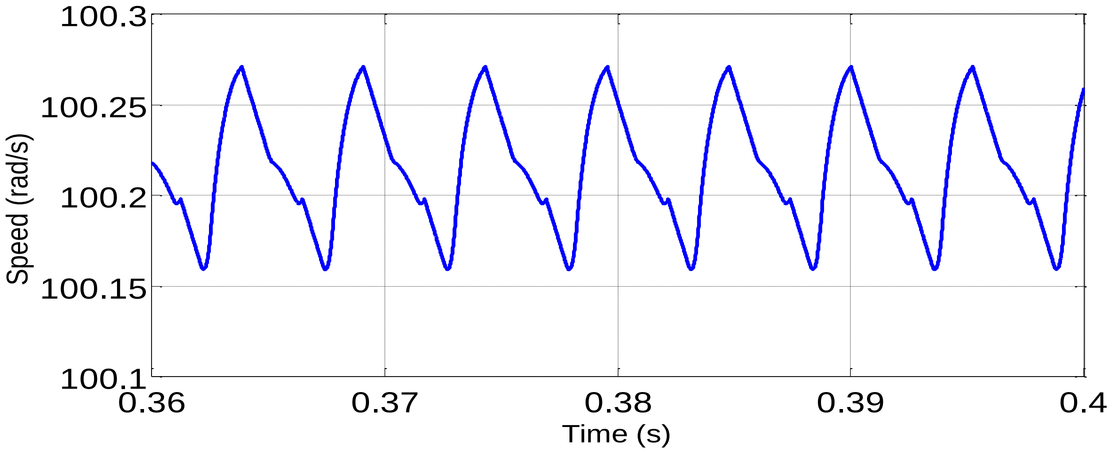

Fig. 5.8 Period-2 speed trajectory of 12/8 SRM at g=15.

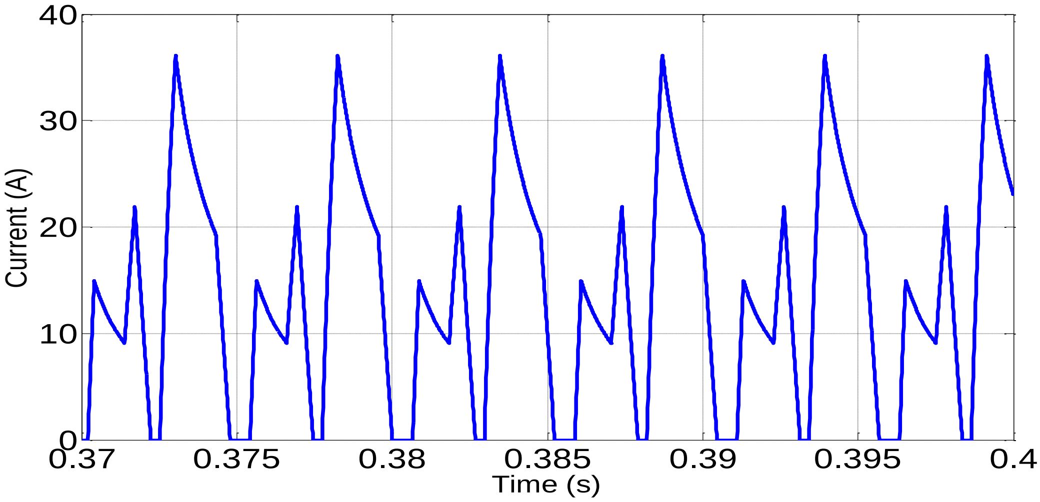

Fig. 5. 9 Sum of all the phase current against time during period-2 operation.

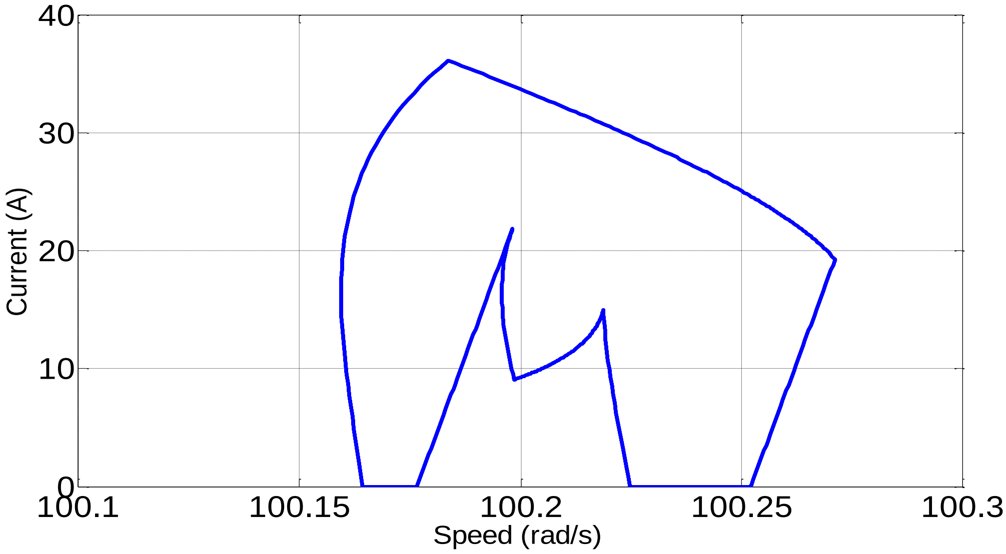

Fig. 5.10 Period-2 phase portrait.

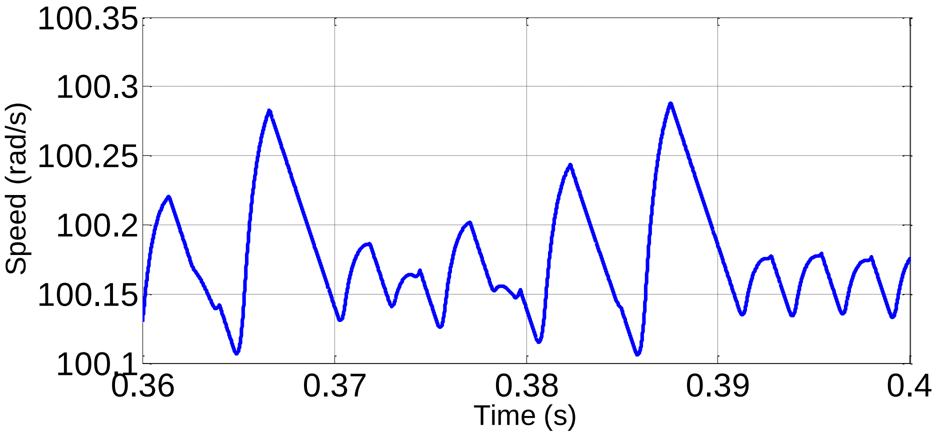

Fig. 5.11 Chaotic speed trajectory of 12/8 SRM at g=20.

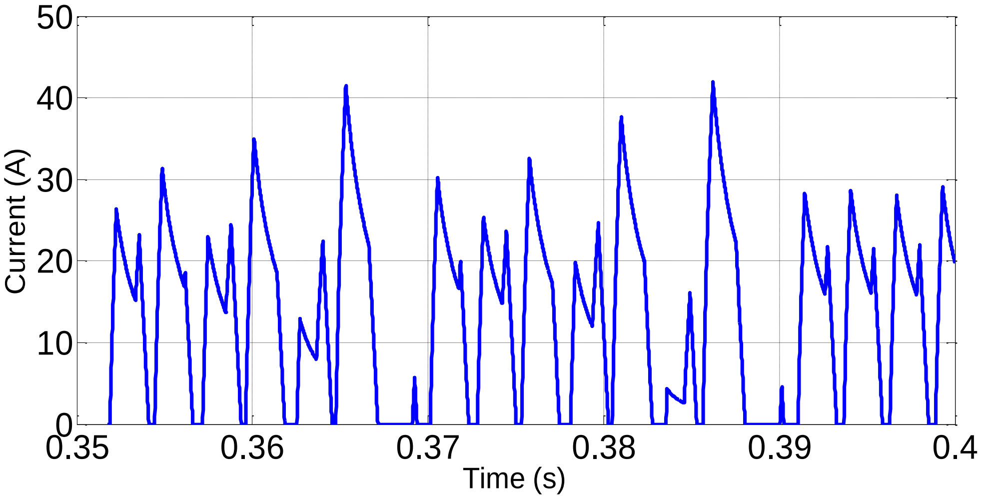

Fig. 5.12 Chaotic current trajectory.

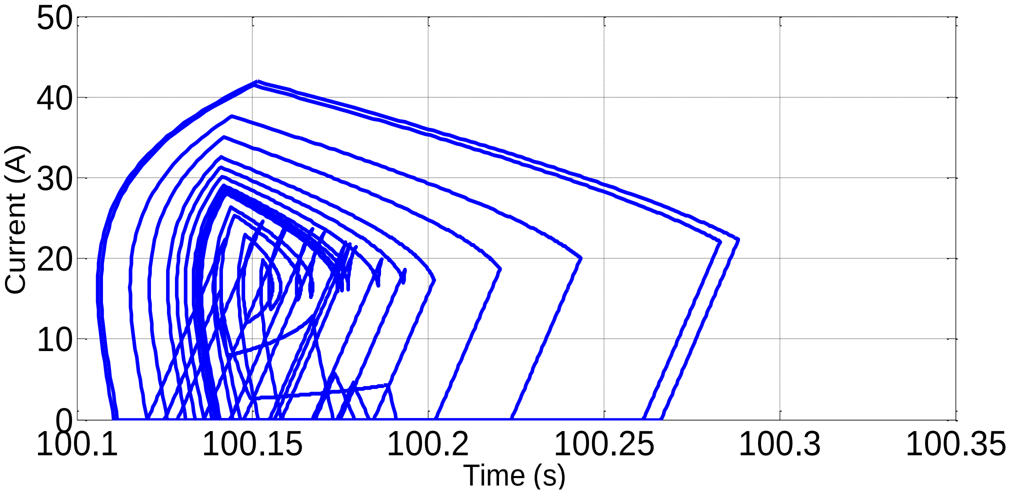

Fig.5.13 Chaotic phase portrait.

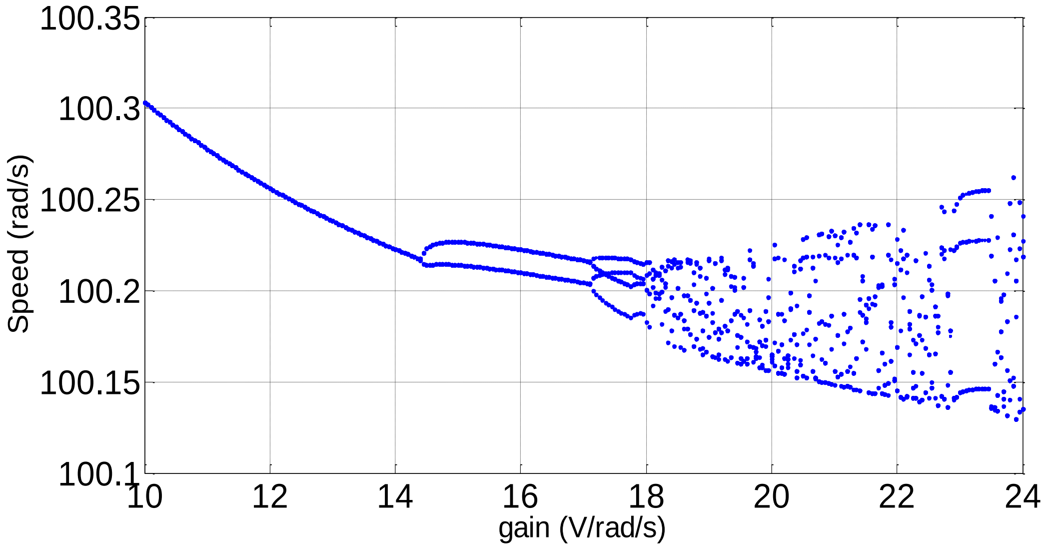

(a)

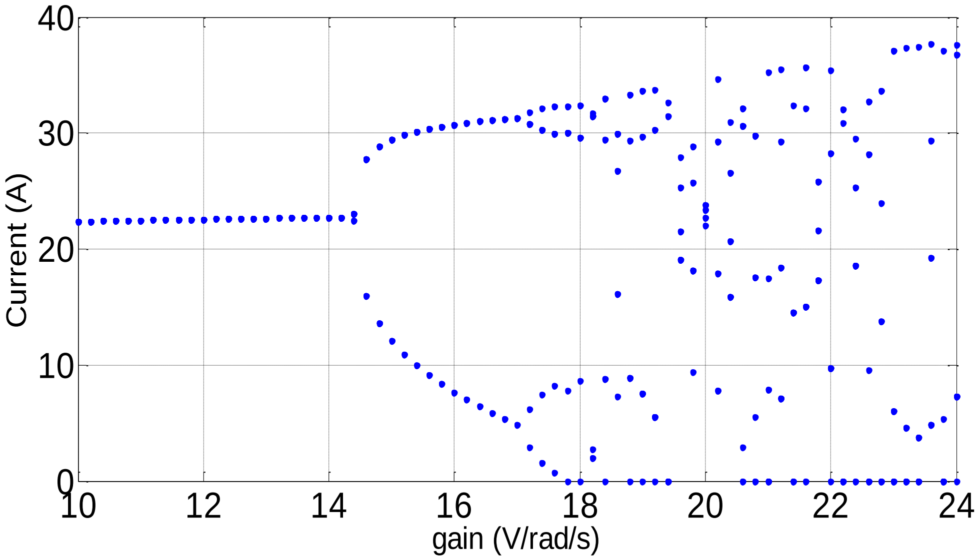

(b)

Fig. 5.14 Bifurcation diagrams of the system (a) Speed against proportional gain (b) Sum of all phase current against proportional gain.

Table 5.2 SRM drive parameters.

V_{in}(V)	100
$R(\Omega)$	0.1
L_{min}(mH)	0.34
ω_{ref}(rad/s)	100
G(mH/rad)	7.8
T_L(NM)	1
J(kgm^2)	0.025
B(Nm/rads^{-1})	0.0005
N_s	12
N_r	8
θ_{on}(degree)	5.5
θ_{off} (degree)	20.5
θ_T(degree)	7.5
V_U(V)	4
V_L(V)	0
C	2

5.5 Analysis of the Fast-Scale Bifurcation

To analyse the fast-scale bifurcation in the 12/8 SRM drive, we have to perform the stability analysis of the of the period-1 orbit of the system (Fig. 5.7). By employing the Monodromy matrix approach [23, 88] the key task is to obtain the state transition matrix (STM) along the entire orbit and its eigenvalues (Floquet multipliers). The orbit is stable if the absolute value of the Floquet multipliers falls within the unit circle and unstable otherwise. From Fig. 5.7, the Monodromy matrix can be expressed as

$$\begin{aligned} M(T,0) &= \Phi(T,t_{\Sigma 4}) \times S_4 \times \Phi(t_{\Sigma 4},t_{\Sigma 3}) \times S_3 \times \Phi(t_{\Sigma 3},t_{\Sigma 2}) \\ &\times S_2 \times \Phi(t_{\Sigma 2},t_{\Sigma 1}) \times S_1 \times \Phi(t_{\Sigma 1},0) \end{aligned} \tag{5.25}$$

where $M(T,0)$ is the STM from $t=0$ to $t=T$, $\Phi(t_B,t_A)$ is the STM from $t=t_A$ to $t=t_B$, $\mathbf{S}_1$, $\mathbf{S}_2$, $\mathbf{S}_3$ and $\boldsymbol{S}_4$ are the STM across the switching manifolds (the Saltation matrices).

5.5.1 Computing the State Transition Matrix $\Phi(t_B,t_A)$

If the vector field describing the trajectory of the system is linear, the STM along any section of the orbit ($\Phi(t_B,t_A)$) can be simply obtained by computing the exponential matrix of the form ($e^{A(tB-tA)}$). But for the SRM and other systems with nonlinear vector fields, the STM is obtained by solving a matrix differential equation of the form below

$$\frac{d\Phi(t,t_0)}{dt} = J(t)\Phi(t,t_0);\Phi(t_0,t_0) = I_{n\times n} \tag{5.26}$$

where $J(t)$ is the Jacobian matrix evaluated along the orbit from $t = t_0$ to any other future time(t) and is given by:

$$J(t) = \left.\frac{\partial f(X,t)}{\partial X}\right|_{X=\phi(t,t_0,X_0)} \tag{5.27}$$

Based on (5.26), $\Phi(t_{\Sigma1},0)$, $\Phi(t_{\Sigma2}, t_{\Sigma1})$, $\Phi(t_{\Sigma3}, t_{\Sigma2})$, $\Phi(t_{\Sigma4}, t_{\Sigma3})$, and $\Phi(t_{\Sigma T}, t_{\Sigma4})$ are evaluated as shown below.

$$\frac{d\Phi(t_{\Sigma1},0)}{dt} = J_1(t)\Phi(t_{\Sigma1},0);\Phi(0,0) = I_{n\times n} \tag{5.28}$$

where $\Phi(0,0)$ is an identity matrix of order 3 and $J_1(t)$ is the Jacobian matrix of the first vector field (f_1(X(t)) evaluated along the orbit from t=0 to t= $t_{\Sigma1}$.

$$J_1(t) = \left.\frac{\partial f_1(X)}{\partial X}\right|_{X=\phi(t_{\Sigma1},0,X_0)} \tag{5.29}$$

$$\frac{\partial f_1(X)}{\partial X} = \begin{bmatrix} 0 & 1 & 0 \\ 0 & \frac{-B}{J} & \frac{Gx_3}{J} \\ K & P & Q \end{bmatrix} \tag{5.30}$$

where

$$K = \frac{-G(-x_3R - Gx_3x_2)}{(L_{\min} + G(x_1 - \theta_{on}))^2}\ , \quad P = \frac{-Gx_3}{(L_{\min} + G(x_1 - \theta_{on}))}\ , \quad Q = \frac{-R - Gx_2)}{(L_{\min} + G(x_1 - \theta_{on}))}$$

The STM from $t = t_{\Sigma 1}$ to $t = t_{\Sigma 2}$ ($\Phi(t_{\Sigma 2}, t_{\Sigma 1})$) is also evaluated following a similar approach as shown below

$$\frac{d\Phi(t_{\Sigma 2},t_{\Sigma 1})}{dt} = J_2(t)\Phi(t_{\Sigma 2},t_{\Sigma 1});\Phi(t_{\Sigma 1},t_{\Sigma 1}) = I_{n\times n} \qquad (5.31)$$

where $J_2(t)$ is the Jacobian matrix of the second vector field (f_2(X(t)) and is to be evaluated along the orbit from t= $t_{\Sigma 1}$ to t= $t_{\Sigma 2}$.

$$J_2(t) = \left.\frac{\partial f_2(X)}{\partial X}\right|_{X=\phi(t_{\Sigma 2},t_{\Sigma 1},X_0)} \qquad (5.32)$$

$$\frac{\partial f_2(X)}{\partial X} = \begin{bmatrix} 0 & 1 & 0 \\ 0 & \frac{-B}{J} & \frac{Gx_3}{J} \\ V & P & Q \end{bmatrix} \qquad (5.33)$$

where $V = \frac{-G(V_{in} - x_3 R - G x_3 x_2)}{(L_{\min} + G(x_1 - \theta_{on}))^2}$, while P and Q have been earlier defined.

$\Phi(t_{\Sigma 3}, t_{\Sigma 2})$, $\Phi(t_{\Sigma 4}, t_{\Sigma 3})$, and $\Phi(t_{\Sigma T}, t_{\Sigma 4})$ are evaluated by following a similar procedure.

5.5.2 Computing the Saltation Matrices.

Since there are interactions of different vector fields in the period-1 orbit of the SRM, the state transition matrices at the switching manifolds must be evaluated.

$$S_1 = I + \frac{\left(\lim\limits_{t\downarrow t_{\Sigma 1}}(f_2(X(t))) - \lim\limits_{t\uparrow t_{\Sigma 1}}(f_1(X(t))\right)\mathbf{n}_1^T}{\mathbf{n}_1^T \lim\limits_{t\uparrow t_{\Sigma 1}}(f_1(X(t))) + \left.\frac{\partial h_1(X(t))}{\partial t}\right| t = t_{\Sigma 1}} \qquad (5.34)$$

where $h_1(X(t))$ is the first switching hypersurface, $\mathbf{n}_1$ is the normal vector to the hypersurface, and I is a (3x3) identity matrix. The first switching occurs when $V_{\mathrm{con}}(t) = V_{\mathrm{ramp}}(t)$ and thus the switching hypersurface is given by

$$h_1(X(t)) = (x_2(t) - \omega_{ref}) - \frac{1}{g}\left[V_{Low} + (V_{Up} - V_{Low})\left(\frac{(x_1(t) - \theta_{on}}{\theta_T}\right)\right] = 0 \qquad (5.35)$$

The normal $\mathbf{n_1}$ to the hypersurface is expressed as

$$\mathrm{n}_1 = \nabla h_1(X(t)) = \begin{bmatrix} \dfrac{\partial h_1(X(t))}{\partial x_1} \\ \dfrac{\partial h_1(X(t))}{\partial x_2} \\ \dfrac{\partial h_1(X(t))}{\partial x_3} \end{bmatrix} = \begin{bmatrix} \dfrac{-(V_{up} - V_{low})}{g\theta_T} \\ 1 \\ 0 \end{bmatrix} \tag{5.36}$$

$$\mathbf{n_1}^T = \begin{bmatrix} \dfrac{-(V_{up} - V_{low})}{g\theta_T} & 1 & 0 \end{bmatrix} \tag{5.37}$$

where

$$\frac{\partial h_1(X(t)}{\partial t} = 0 \tag{5.38}$$

$$\lim_{t \uparrow t_{\Sigma 1}} (f_1(X(t)) = \begin{bmatrix} x_2(t_{\Sigma 1}) \\ \dfrac{0.5Gx_3^2(t_{\Sigma 1}) - Bx_2(t_{\Sigma 1}) - T_L}{J} \\ \dfrac{-Rx_3(t_{\Sigma 1}) - Gx_2(t_{\Sigma 1})x_3(t_{\Sigma 1})}{L_{\min} + G(x_1(t_{\Sigma 1}) - \theta_{on})} \end{bmatrix} \tag{5.39}$$

$$\lim_{t \downarrow t_{\Sigma 1}} (f_2(X(t)) = \begin{bmatrix} x_2(t_{\Sigma 1}) \\ \dfrac{0.5Gx_3^2(t_{\Sigma 1}) - Bx_2(t_{\Sigma 1}) - T_L}{J} \\ \dfrac{V_{in} - Rx_3(t_{\Sigma 1}) - Gx_2(t_{\Sigma 1})x_3(t_{\Sigma 1})}{L_{\min} + G(x_1(t_{\Sigma 1}) - \theta_{on})} \end{bmatrix} \tag*{5.40)}$$

$$\lim_{t\downarrow t_{\Sigma 1}}(f_2(X(t))) - \lim_{t\uparrow t_{\Sigma 1}}(f_1(X(t))) = \begin{bmatrix} 0 \\ 0 \\ \dfrac{V_{in}}{L_{\min} + G(x_1(t_{\Sigma 1}) - \theta_{on})} \end{bmatrix} \tag{5.41}$$

By substituting equations (5.37), (5.38), (5.39) and (5.41) into (5.34), the Saltation matrix (S_1) can be evaluated. S_2, $S_{3,}$ and S_4 were computed following a similar procedure. The computed Monodromy matrix and Floquet multipliers at different values of the proportional gain are shown in Table 5.3 and the eigenvalue loci are shown in Fig. 5.15.

Table 5.3 Computed Monodromy matrix and Floquet multipliers

G	Monodromy Matrix	Floquet Multipliers
10	$\begin{bmatrix} 1.0003 & 0.0002 & 0.0000 \\ -0.6909 & -0.6511 & 0.0028 \\ -437.4463 & -38.9344 & -0.1916 \end{bmatrix}$	0.9983 -0.4203 ± 0.2403i
12	$\begin{bmatrix} 1.0001 & -0.0002 & 0.0000 \\ -0.7507 & -0.7916 & 0.0028 \\ -415.0809 & 0.7179 & -0.2934 \end{bmatrix}$	0.9984 -0.2880 -0.7954
13	$\begin{bmatrix} 1.0000 & -0.0003 & 0.0000 \\ -0.7790 & -0.8204 & 0.0026 \\ -409.3241 & 12.9489 & -0.3187 \end{bmatrix}$	0.9985 -0.2584 -0.8792
14.1	$\begin{bmatrix} 0.9999 & -0.0006 & 0.0000 \\ -0.7952 & -0.8973 & 0.0024 \\ -388.8347 & 55.9577 & -0.3984 \end{bmatrix}$	0.9987 -0.2035 -1.0910

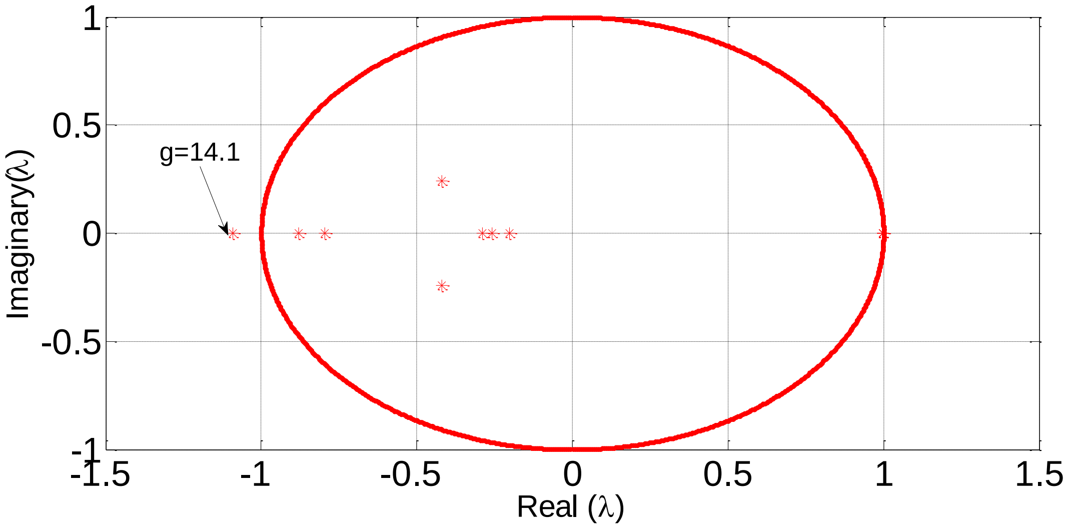

Fig. 5.15 Eigenvalue loci at different values of the proportional gain

From Table 5.3 and Fig. 5.15 it could be seen that the nominal period-1 orbit losses stability at g=14.1V/rad^{-1} as the absolute value of one of the Floquet multipliers fell outside the unit circle at that value of the proportional gain. This is in agreement with the bifurcation diagram of the system (Fig. 5.14) that was obtained via numerical simulation.

5.6 Summary

In this chapter, the fast scale bifurcation in a three-phase 12/8 SRM has been investigated using the Monodromy matrix approach. It has been found that the stability of the nominal period-1 orbit depends on the eigenvalues of the state transition matrix around the entire orbit (the Monodromy matrix). This technique can be applied to the stability analysis of other SRM drives such as 4/2, 6/4, and 8/6 SRM drives. In the next chapter, the control of nonlinear phenomena in electrical drives will be discussed.

CHAPTER 6

CONTROL OF NONLINEAR PHENOMENA IN ELECTRICAL DRIVES

6.1 Introduction

In Chapter 4 and Chapter 5 the nonlinear bifurcation and chaotic phenomena in two selected electrical drive systems, namely a DC chopper-fed PMDC drive and a three-phase 12/8 SRM drive were extensively discussed. As some system parameter such as the controller gains or the supply voltage is being varied, the nominal period-1 orbit in the drives may lose stability leading to the birth of period-nT or chaotic orbits. Hence there is a need to develop controllers that are capable of compensating for the parameter variations.

The development of controllers to extend the period-1 operation of switched mode power electronic systems over a wider range of system parameters have been a challenging topic. Popular techniques are the OGY (Ott, Grebogi and Yorke) method [25] and the Pyragas techniques [51-53, 89]. The basis of these control techniques lies in the fact that a chaotic attractor contains several unstable periodic orbits (UPO) which can be located and stabilized. But these techniques have been found to be complex as so many computations are to be performed online [28].

In this thesis, the Monodromy matrix based stabilization technique [23, 24, 88] will be applied. The goal of this stabilization technique is to ensure that the absolute values of the eigenvalues of the Monodromy matrix (the Floquet multipliers) remain within the unit circle irrespective of the system parameter variation. This can be achieved by manipulating the Saltation matrix (the state transition matrix at the switching manifold of the UPO) component of the Monodromy matrix. Thus, the key task is to locate the UPO and then stabilize it by manipulating the Saltation matrix. This chapter is organised as follows: in section 6.2 the control of fast-scale bifurcation in DC chopper-fed PMDC drive employing the proportional controller will be discussed, while the control of fast-scale bifurcation in the three-phase 12/8 SRM is discussed in section 6.3. Section 6.4 is the chapter summary.

6.2 Control of Fast-scale Bifurcation in a DC Chopper-fed PMDC Drive Employing a Proportional Controller

The nominal behaviour of a DC chopper-fed PMDC Drive employing the proportional controller is a period-1 orbit. But as was reported in Chapter 4, this nominal behaviour can lose stability via fast-scale bifurcation when the supply voltage (V_{in}) is greater than 111.83V or when the proportional gain (Kp) is greater than 2.34. In this section, the Monodromy matrix based stabilization approach will be applied to control this instability. As the system parameter is varied, the controller will ensure that the Floquet multipliers lie on a circle of radius 0.8223 (chosen as a radius of stable eigenvalues).

6.2.1 Locating the Unstable Periodic Orbit of the PMDC Drive

Locating the UPO as system parameters are being varied simply involves enforcing periodicity and then computing analytically the duty ratio that will ensure period-1 operation. Once the duty ratio is computed, the initial state vector ($\mathbf{X}(0)$) and the state vector at the switching instant ($\mathbf{X}(t_{\sum})$ for the UPO will be determined using the procedure described in Chapter4. For instance, when the supply voltage (V_{in}) was 100V, the attractor was a period-1 orbit, but when the supply voltage was changed to 113V (see Fig.4.10), the attractor was a period-2 orbit and the previously stable period-1 orbit began to repel (unstable). By enforcing periodicity (or assuming that $X(0)=X(T)$) and following the procedure outlined in Chapter 4, the unstable period-1 orbit (at V_{in}=113V) embedded in the period-2 attractor could be located (Fig. 6.1). The switching instant ($t_{\sum}=\delta T$), the initial state X(0), and the state vector at the switching instant ($\mathbf{X}(t_{\sum}$) of the UPO are: $t_{\sum}$=0.0031s, $\mathbf{X}(0)=[\ \ 100.8586\ \ \ 4.5090]^{T}$ and $\mathbf{X}(t_{\sum})=[\ \ 100.8518\ \ \ 2.3197]^{T}$.

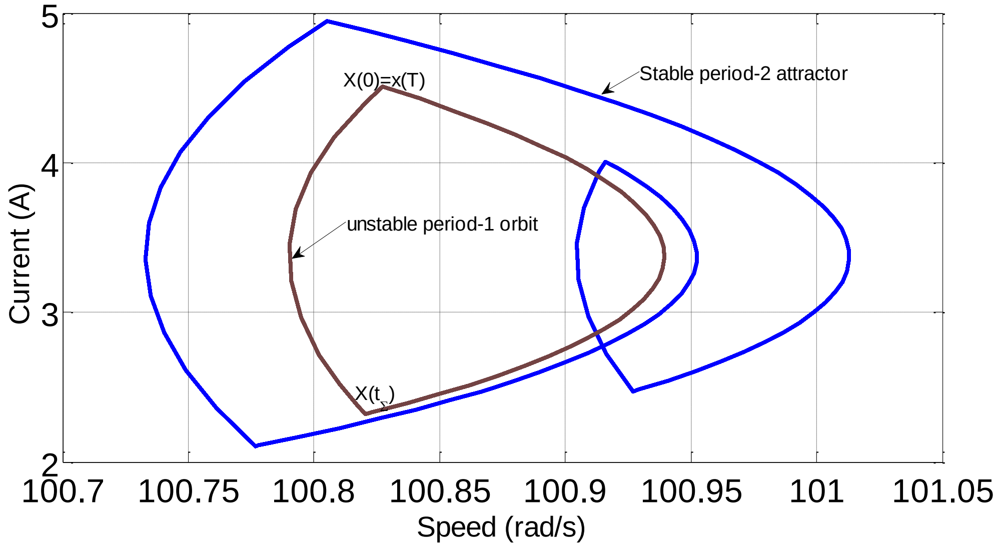

Fig. 6.1 Unstable period-1 orbit embedded in the period-2 attractor at V_{in} =113V.

Once the UPO is located, it will be stabilized by manipulating the Saltation matrix components of the Monodromy matrix. The Monodromy matrix of the UPO is expressed as:

$$M(T,0)=\Phi(T,t_{\Sigma})\times \mathbf{S} \times \Phi(t_{\Sigma},0) \tag{6.1}$$

where $\Phi(t_B,t_A)$ is the STM from t=t_{A} to t=t_{B} and is expressed as $\Phi(t_B,t_A)=e^{A(t_{\mathrm{B}}-t_{\mathrm{A}})}$, and **S** is the Saltation matrix that govern the transition of the trajectory from the switch OFF region of the state space to switch ON region. As discussed in Chapter4, the Saltation matrix can be expressed as:

$$\mathbf{S}=\mathbf{I}+\frac{(\mathbf{f}_{ON}(\mathbf{X}(t_{\Sigma}))-\mathbf{f}_{OFF}(\mathbf{X}(t_{\Sigma})))\mathbf{n}^{T}}{\mathbf{n}^{T}\,\mathbf{f}_{OFF}(\mathbf{X}(t_{\Sigma}))+\left.\dfrac{\partial h(\mathbf{X}(t))}{\partial t}\right|_{t=t_{\Sigma}}} \tag{6.2}$$

where the switching hypersurface (h(X(t)) and its normal (**n**) are expressed as:

$$h(\mathbf{X}(t))=V_{con}(t)-V_{ramp}(t)=(x_1(t)-\omega_{ref})-\frac{1}{Kp}\left(V_L+(V_U-V_L)\frac{t}{T}\right)=0 \tag{6.3}$$

$$\mathbf{n}=\nabla h(X(t),t)=\begin{bmatrix}\dfrac{\partial h(X(t))}{\partial x_1}\\[2ex]\dfrac{\partial h(X(t))}{\partial x_2}\end{bmatrix} \tag{6.4}$$

In order to ensure that the absolute value of the Floquet multipliers is within the unit circle for a wide range of system parameters, the Saltation matrix is to be manipulated. Some of the possible approaches for manipulating the Saltation matrix are discussed in section 6.2.2.

6.2.2 Manipulating the Saltation Matrix

From equation (6.2), the Saltation matrix can be manipulated without causing major structural change in the system by adding a small time varying signal to the switching hypersuface $h(\mathbf{X}(t)$ or by adding a signal that is a function of the state variable to $h(\mathbf{X}(t)$. The addition of small time varying signal will cause a change in the term $\partial h(\mathrm{X}(t)/\partial t$), while adding a signal that is a function of the state variable will cause a change in the term $\partial h(\mathrm{X}(t)/\partial \mathrm{X}$. The changes in the switching hypersurface should be small in order to keep the switching instant $(t_\Sigma = \delta \times T)$, the initial state vector (X(0)), and the state vector at the switching instant $(\mathbf{X}(t_\Sigma))$ unchanged (so as to maintain the location of the UPO), but should be significant enough to cause change in either $\partial h(\mathrm{X}(t)/\partial t$ or $\partial h(\mathrm{X}(t)/\partial \mathrm{X}$. Techniques for the Saltation matrix manipulation are discussed in [23, 88]. In this thesis three of these methods are explored.

6.2.2.1 *Saltation Matrix Manipulation Based on the Injection of a Low Amplitude Sinusoidal Signal*

In this scheme, a low amplitude sinusoidal signal is added to the switching hypersurface by replacing the reference speed (ω_{ref}) with $\omega_{\mathrm{ref}}(1+ \alpha\sin(\omega t))$ where $\omega=2\pi/T$, T is the period of the sawtooth signal and the parameter α is chosen to determine the desired location of the Floquet multipliers. Since the parameter α is usually very small, this change will have little effect on the control signal ($V_{\mathrm{con}}(t)$) and the location of the switching instant $(t_\Sigma = \delta \times T)$, but can cause significant change in the Saltation matrix as illustrated in equations below:

$$h(\mathbf{X}(t)) = \left(x_1(t) - \omega_{ref}(1+\alpha\sin(\omega t)\right) - \frac{1}{Kp}\left(V_L + (V_U - V_L)\frac{t}{T}\right) = 0 \qquad (6.5)$$

$$\left.\frac{\partial h(\mathbf{X}(t)}{\partial t}\right|_{t=t_\Sigma} = -\omega_{ref} \times \alpha \times \omega \times \cos(\omega \times t_\Sigma) - \frac{\left(V_U - V_L\right)}{T \times Kp} \qquad (6.6)$$

$$\mathbf{S} = \begin{bmatrix} 1 & 0 \\ \mathbf{P} & 1 \end{bmatrix} \tag{6.7}$$

where $\mathbf{P} = \dfrac{\dfrac{V_{in}}{L}}{\left(\dfrac{K_t x_2(t_\Sigma) - B x_1(t_\Sigma) - T_L}{J}\right) - \omega_{ref}\alpha\omega\cos(\omega t_\Sigma) - \dfrac{(V_U - V_L)}{T \times Kp}}$

From (6.7), it could be seen that the introduction of a low amplitude sinusoidal signal will have a significant effect on the Saltation matrix. Since the Monodromy matrix of the UPO is expressed as $M(T,0) = e^{\mathbf{A}(T-t_\Sigma)} \times \mathbf{S} \times e^{\mathbf{A}t_\Sigma}$ and the switching instant $(t_\Sigma = \delta \times T)$ is unchanged, then it could be deduced that the Monodromy matrix is only influenced by the Saltation matrix.

To design a controller based on this approach the value of the parameter (α) necessary to force the Floquet multipliers to lie on a radius of 0.8223 (see Fig.4.14 and Fig.4.15), as the system parameters are varied will be computed. Thus, we need to solve (6.8) to obtain the required value of the parameter (α) using Newton-Raphson or other numerical techniques.

$$abs(eig(M(T,0))) = 0.8223 \tag{6.8}$$

where $M(T,0)$ is a function of α. If the supply voltage (V_{in}) is used as the bifurcation parameter, then the value of the parameter (α) will be computed offline for selected values of the supply voltage, and a polynomial equation that relates (α) with V_{in} will be developed using the Matlab Polyfit function. By using this polynomial function, a look up table will be developed to obtain the value of the parameter (α) that is necessary to ensure period-1 operation (an eigenvalue radius of 0.8223) as V_{in} is being varied. The third order polynomial function that relates V_{in} and the control parameter (α) is as shown in (6.9), and the computed optimal values of the parameter (α) as V_{in} is being varied are shown in Fig. 6.2.

$$\alpha(V_{in}) = 1.47 \times 10^{-8}(V_{in})^3 - 5.88 \times 10^{-6}(V_{in})^2 + 8.65 \times 10^{-4} V_{in} - 0.0431 \tag{6.9}$$

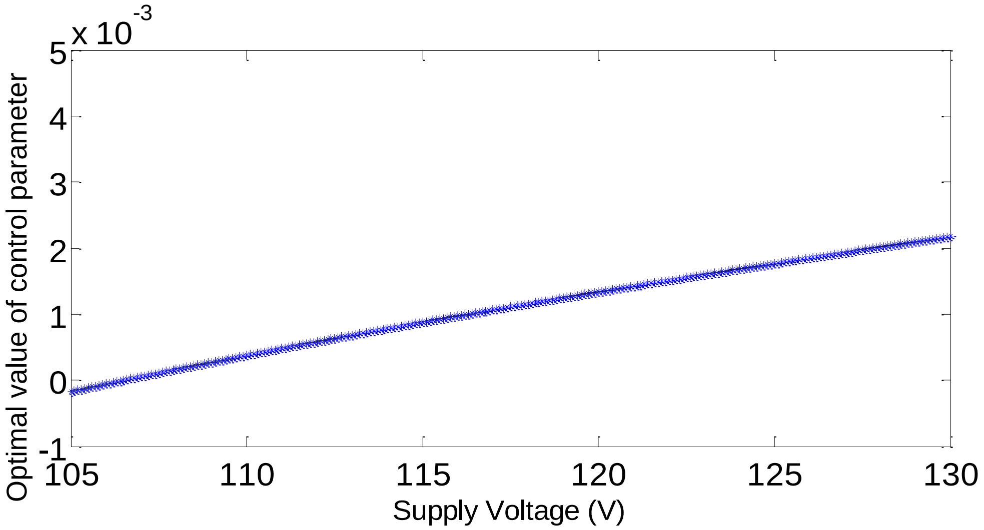

Fig. 6.2 Required values of (α) against supply voltage

From Fig.6.2, the required value of the control parameter when the supply voltage is 113V is 1×10^{-3}. By substituting this value into (6.7) and using the value of the state vector at the switching instant of the UPO ($\mathbf{X}(t_{\Sigma}) = [\ 100.8518 \quad 2.3197]^T$) computed earlier, the Saltation matrix will be $\left(\mathbf{S} = \begin{bmatrix} 1.0000 & 0 \\ -7.0876 & 1.0000 \end{bmatrix}\right)$, and the Monodromy matrix thus becomes $M(T,0) = \begin{bmatrix} 0.1626 & 0.1468 \\ -6.4771 & -1.6883 \end{bmatrix}$. The eigenvalue of the Monodromy matrix is a complex conjugate pair $\lambda = \begin{bmatrix} -0.7628 + 0.3071i \\ -0.7628 - 0.3071i \end{bmatrix}$ whose absolute value is 0.8223. This confirms that the injection of a low amplitude sinusoidal signal in the switching hypersurface is capable of stabilising the UPO at V_{in}=113V as the Floquet multiplier now lies on a circle of radius 0.8223 as desired.

This new controller can be referred to as a supervising controller and could easily be implemented using a digital signal processor. The inputs to the supervising controller are the supply voltage (V_{in}) and the reference speed (ω_{ref}), and the output of the controller is $\omega_{ref}\times\alpha\times\sin(\omega t)$. The control parameter (α) is computed by solving (6.9). A schematic diagram of the DC chopper-fed PMDC drive based on the new controller is shown in Fig. 6.3.

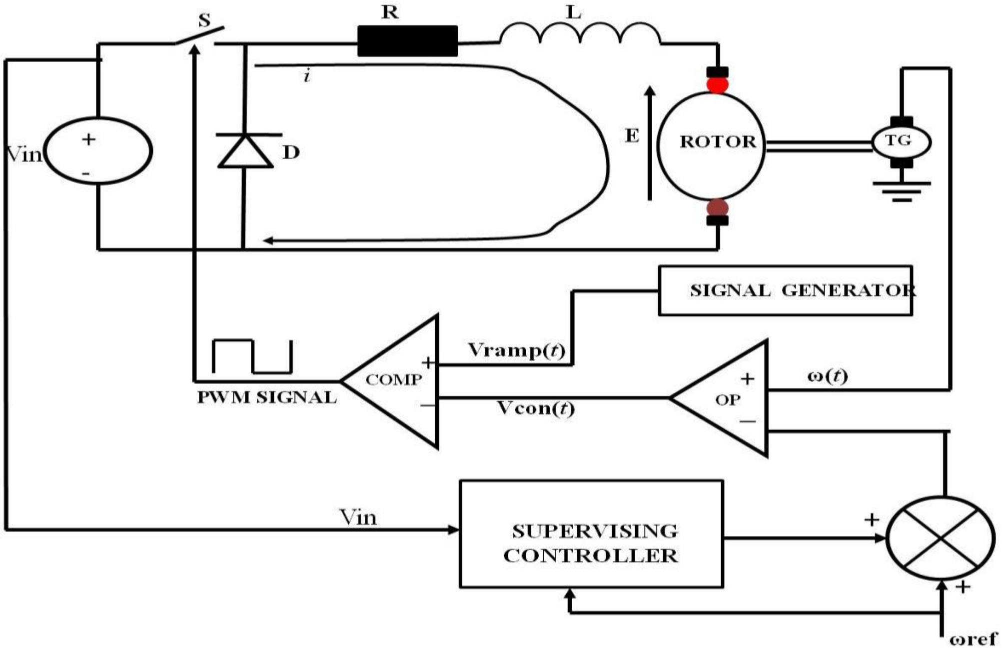

Fig. 6.3 Schematic diagram of DC chopper-fed PMDC drive with the supervisory controller.

To test the response of the new control scheme to system parameter variation, the supply voltage was changed to 113V and the system response is as shown in Fig. 6.4.

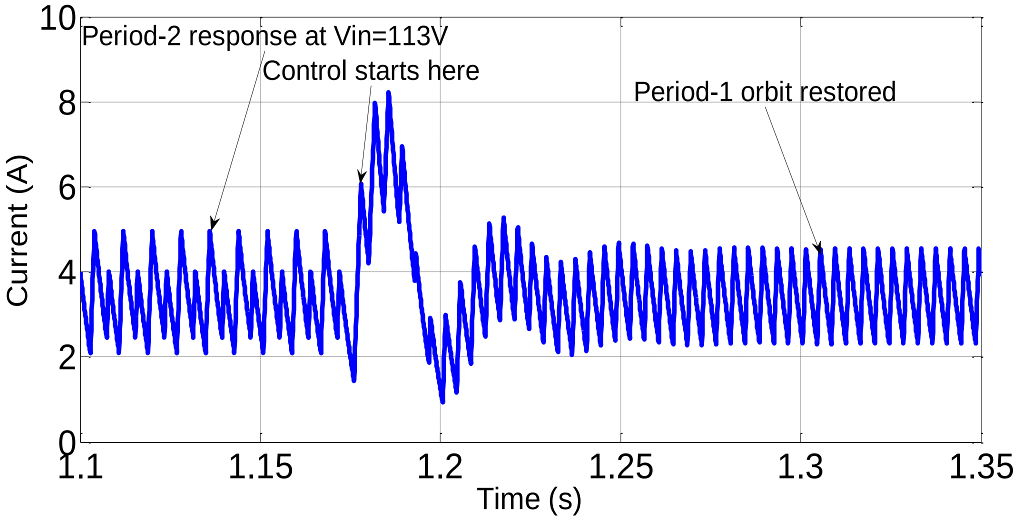

Fig. 6.4 Response of the supervising controller at V_{in} =113V

From Fig.6.4, it could be seen that the system trajectories approached the period-2 attractor without the supervising controller, but after the introduction of the supervising controller at t = 1.18s, the trajectories approached a period-1 orbit. Thus, it is clear that the introduction of the low amplitude sinusoidal signal was able to stabilize the unstable period-1 orbit embedded in the period-2 attractor with little effect on the location of the

UPO. This control technique is also suitable for stabilizing the unstable period-1 orbit embedded in the chaotic attractor of the DC chopper-fed PMDC drive as shown in Fig.6.5

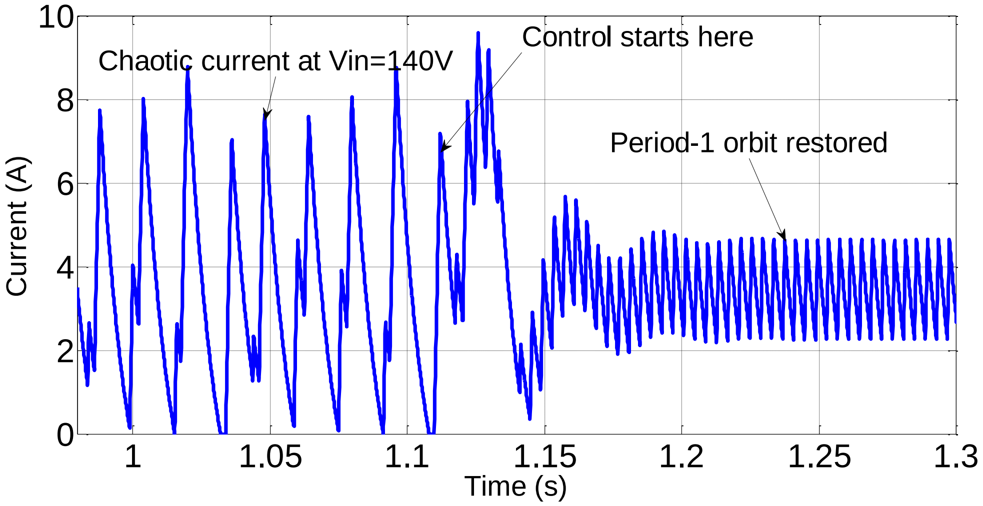

Fig. 6.5 Stabilization of unstable period-1 orbit embedded in a chaotic attractor at Vin=140V.

6.2.2.2 *Saltation Matrix Manipulation Based on changing the slope of the Ramp Signal*

Another technique for changing the time derivative of the switching hypersurface ($\partial h(\mathrm{X}(t)/\partial t$) and thus the Saltation matrix (**S**) is by changing the slope of the sawtooth or ramp signal $(V_r = V_L + (V_U - V_L)\frac{t}{T})$. This can be achieved by manipulating either the upper or the lower values of the ramp signal (V_U or V_L). To illustrate this control technique, the upper value of the ramp signal is replaced with $(k \times V_U)$ where k is the control parameter. Consequently, the time derivative of the switching hypersurface $\partial h(\mathrm{X}(t)/\partial t$ becomes $-\frac{(k \times V_U - V_L)}{T \times Kp}$, and the Saltation matrix will be expressed as shown below:

$$\mathbf{S} = \begin{bmatrix} 1 & 0 \\ \dfrac{\dfrac{V_{in}}{L}}{\left(\dfrac{K_t x_2(t_\Sigma) - Bx_1(t_\Sigma) - T_L}{J}\right) - \dfrac{(k \times V_U - V_L)}{T \times Kp}} & 1 \end{bmatrix} \tag{6.10}$$

To design the controller based on this approach, the value of the parameter (k) necessary to force the Floquet multipliers to lie on a radius of 0.8223 as system parameters are varied, will be computed. Thus, we need to solve (6.8) with k as the unknown parameter.

If the supply voltage (V_{in}) is still used as the bifurcation parameter, the required value of the parameter (k) will be computed offline for selected values of V_{in} and a polynomial equation that relates (k) with V_{in} will be developed using the Matlab Polyfit function. The 3rd order polynomial function that relates V_{in} and the control parameter (k) is as shown in (6.11) and the computed optimal values of the parameter (k) necessary to ensure period-1 operation are shown in Fig.6.6.

$$k(V_{in}) = \text{-}2.28 \times 10^{\text{-}5}(V_{in})^3 + 8.28 \times 10^{\text{-}3}(V_{in})^2 - 0.987 \times V_{in} + 39.81 \tag{6. 11}$$

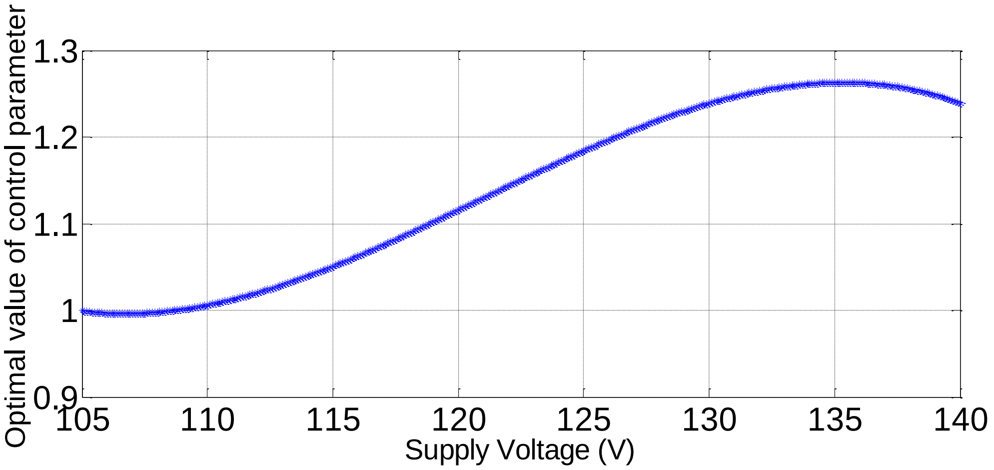

Fig. 6.6 Computed values of the parameter (k) as the supply voltage is varied.

The schematic diagram of the DC chopper-fed PMDC drive based on this second controller is as shown in Fig.6.7.

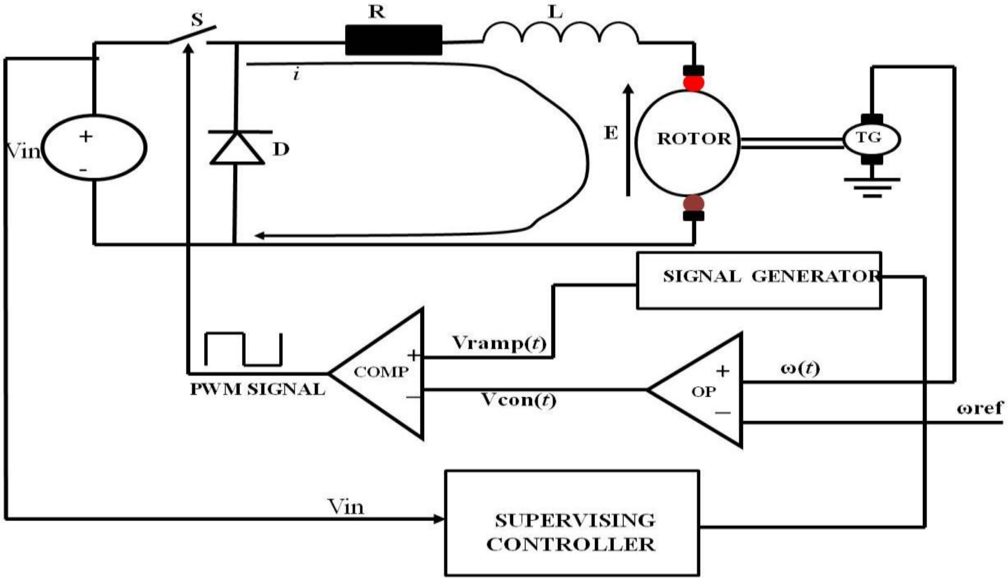

Fig. 6.7 Schematic diagram of the DC chopper-fed PMDC drive based on the second control approach

To test the response of the new control scheme the supply voltage was changed to 113V and the system response is as shown in Fig. 6.8.

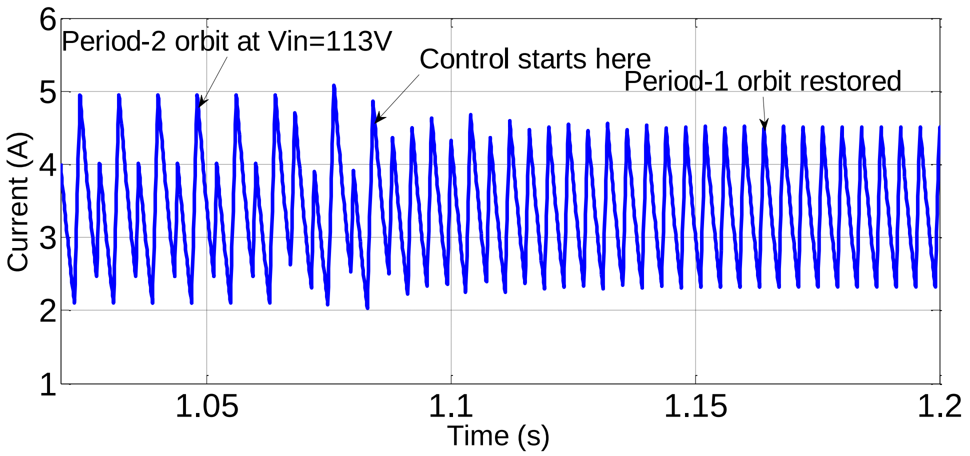

Fig. 6.8 Response of the second controller at V_{in}=113 V

From Fig.6.8, it could be seen that the supervising controller can effectively stabilise the unstable period-1 orbit embedded in the period-2 attractor. This control approach is also suitable for stabilizing the unstable period-1 orbit embedded in the chaotic attractor of the PMDC drive, as shown in Fig.6.9.

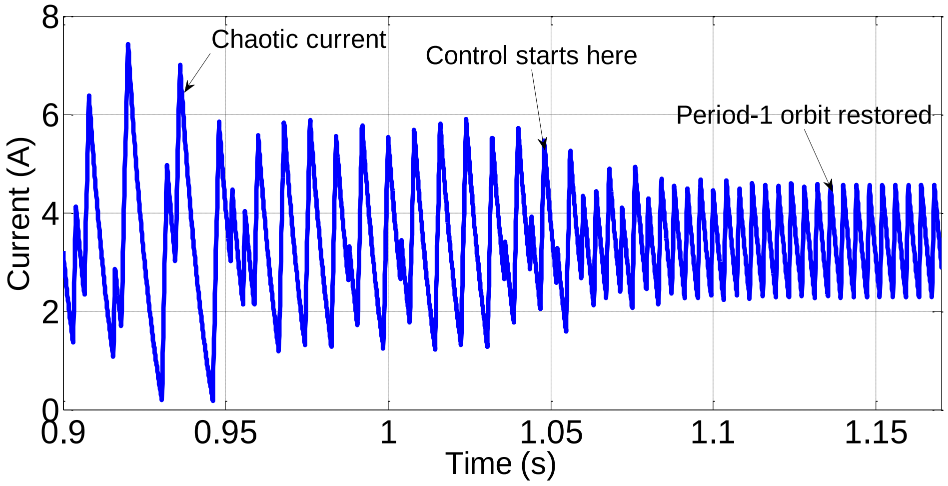

Fig. 6.9 Stabilization of the chaotic attractor at V_{in} =130 V.

6.2.2.3 *Saltation Matrix Manipulation by Adding a Signal Proportional to the Shaft Speed*

Apart from manipulating the time derivative of the switching manifold ($\partial h(\mathbf{X}(t)/dt$), the Saltation matrix (**S**) can also be altered by manipulating the normal to the switching hypersurface $\left(\mathbf{n} = \nabla h(X(t),t) = \begin{bmatrix} \dfrac{\partial h(X(t))}{\partial x_1} & \dfrac{\partial h(X(t))}{\partial x_2} \end{bmatrix}^T\right)$. This can be achieved by adding a constant signal (β) to the feedback speed ($x_1(t)$). Based on this alteration, the control signal $V_{con}(t) = Kp(x_1 - \omega_{ref})$ becomes $V_{con}(t) = Kp(x_1(1+\beta) - \omega_{ref})$, and the switching hypersurface will be expressed as:

$$h(\mathbf{X}(t)) = V_{con}(t) - V_{ramp}(t) = (x_1(1+\beta) - \omega_{ref}) - \frac{1}{Kp}\left(V_L + (V_U - V_L)\frac{t}{T}\right) = 0 \tag{6.12}$$

The normal to the switching surface (**n**) will then be expressed as:

$$\mathbf{n} = \begin{bmatrix} \dfrac{\partial h(X(t))}{\partial x_1} \\ \dfrac{\partial h(X(t))}{\partial x_2} \end{bmatrix} = \begin{bmatrix} 1+\beta \\ 0 \end{bmatrix} \tag{6.13}$$

Based on the expression for the normal to the switching hypersurface (6.13), the Saltation matrix will be expressed as:

$$\mathbf{S} = \begin{bmatrix} 1 & 0 \\ \dfrac{(1+\beta)\dfrac{V_{in}}{L}}{(1+\beta)\left(\dfrac{K_t x_2(t_\Sigma) - Bx_1(t_\Sigma) - T_L}{J}\right) - \dfrac{(V_U - V_L)}{T \times Kp}} & 1 \end{bmatrix} \tag{6.14}$$

To design the supervising controller based on this approach the value of the parameter (β) necessary to force the Floquet multipliers to lie on a radius of 0.8223, as the system parameters are varied will be computed. Thus, we need to solve (6.8) with β as the unknown parameter

The 3rd order polynomial function that relates the supply voltage (V_{in}) and the control parameter (β) is as shown in (6.15), and the computed optimal values of the parameter (β) necessary to ensure period-1 operation are shown in Fig.6.10.

$$\beta(V_{in}) = 2.32\times10^{-5}(V_{in})^3 - 8.3\times10^{-3}(V_{in})^2 + 0.98V_{in} - 38.15 \tag{6.15}$$

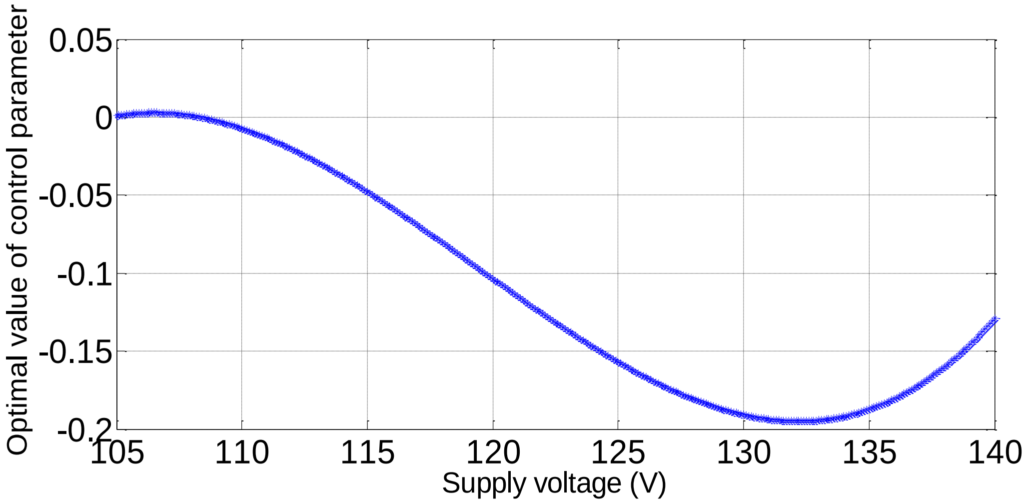

Fig. 6.10 Computed values of the control parameter (β)

The schematic diagram of the DC chopper-fed PMDC drive based on the 3rd control approach is as shown in Fig.6.11. To test the response of the 3rd controller the supply voltage was changed to 113 V and the system response is as shown in Fig.6.12.

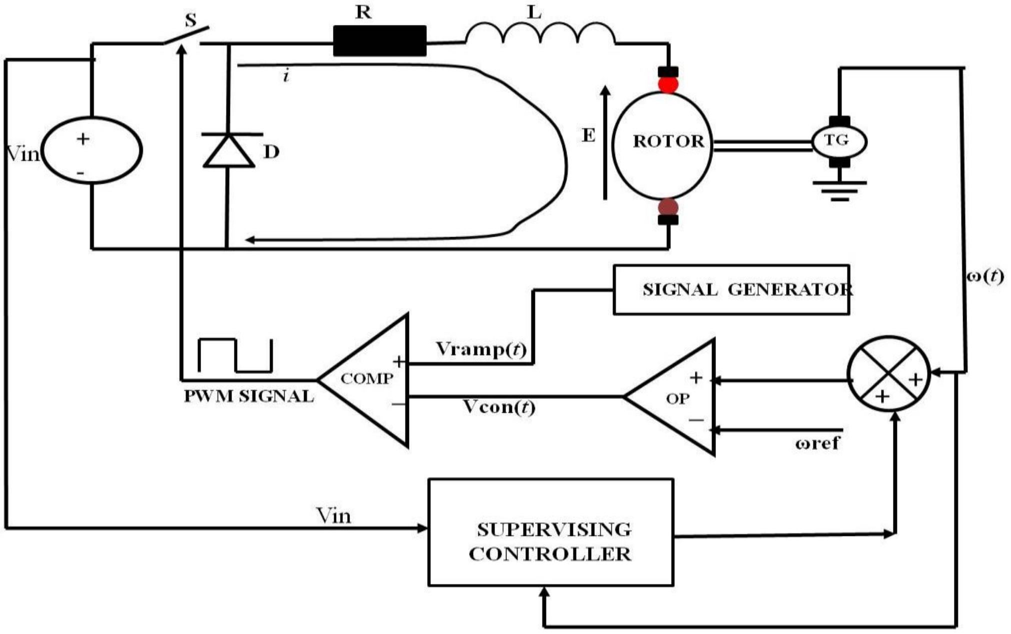

Fig. 6.11 Schematic diagram of the DC chopper-fed PMDC drive based on the 3rd controller

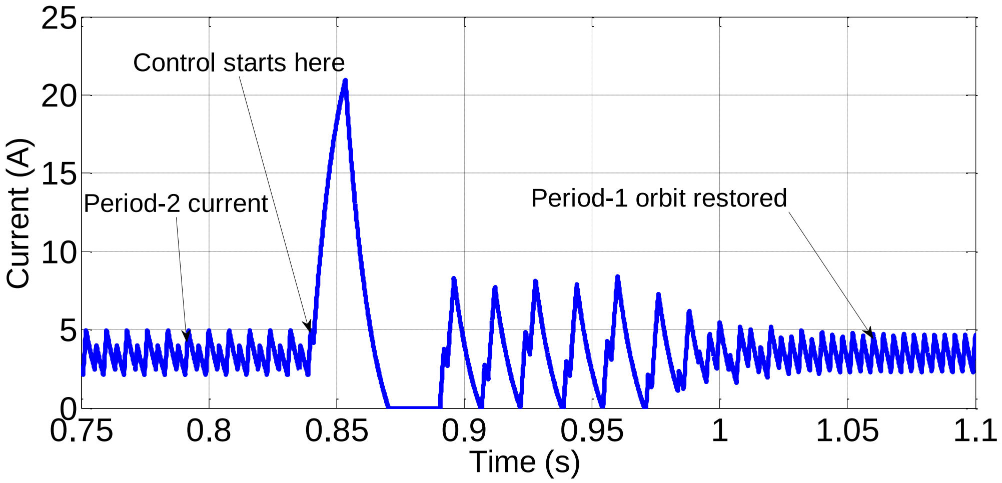

Fig. 6.12 Response of the 3^{rd} controller when the supply voltage was changed to 113V.

As could be seen from Fig.6.12, the manipulation of the normal to the switching surface can effectively stabilise the unstable period-1 orbit embedded in the period-2 attractor.

The UPO stabilization steps based on the three techniques described above are summarized below:

- Locate the UPO by finding the initial state X(0) and the state vector at the switching instant X($t_{\sum}$).
- Manipulate the Saltation matrix and thus the Monodromy matrix of the UPO using any of the three techniques described above, while ensuring that the location of the UPO remains unchanged.
- Using the new expression for the Monodromy matrix, determine the required value of the control parameter necessary to ensure stable period-1 operation as the system parameters are being varied.
- Develop a look up table that relates the control parameter to the bifurcation parameter.

6.3 Control of Fast-scale Bifurcation in a SRM Drive

The Saltation matrix based stabilization approach can also be extended to piecewise nonlinear electrical drives like the SRM drive. As discussed in Chapter 5, the nominal period-1 behaviour in the SRM drive (Fig.5.5) can lose stability as the proportional gain is being varied leading to the birth of a new orbit whose period is double the period of the nominal period-1 orbit (Fig.5.6). By using the first stabilization approach (introduction of a low amplitude sinusoidal signal) and selection of the required value of the control parameter (α), the Saltation matrix (5.34), and thus the Monodromy matrix (5.25) can be manipulated with little influence on the location of the UPO. The hypersurface expression (5.35) and its time derivative (5.38) thus become:

$$h_1(X(t)) = (x_2(t) - \omega_{ref} - \alpha\omega_{ref}\sin(\omega t) - \frac{1}{g}\left[V_{Low} + \left(V_{Up} - V_{Low}\right)\left(\frac{(x_1 - \theta_{on})}{\theta_T}\right)\right] \tag{6.16}$$

$$\frac{\partial h_1(X(t),t)}{\partial t} = -\alpha\omega\omega_{ref}\cos(\omega t) \tag{6.17}$$

where $\omega = 2\pi / T$ and T is the duration of the period-1 orbit. With the introduction of the low amplitude sinusoidal signal, the time derivative of the switching hypersurface that was initially zero (5.38), has now been changed to $(-\alpha\omega\omega_{ref}\cos(\omega t))$ thus influencing the Saltation matrix (**S**$_1$). The system response for a sudden change in the proportional gain from g=10 to g=15 is as shown in Fig.6.13. From Fig.6.13a, it could be seen that without the supervising controller, the step change will lead to the birth of a period-2 orbit. Fig.6.13b shows how the period-2 orbit is stabilised back to the nominal period-1 orbit due to the supervising controller. The result confirms the effectiveness of this control technique in stabilizing the SRM drive.

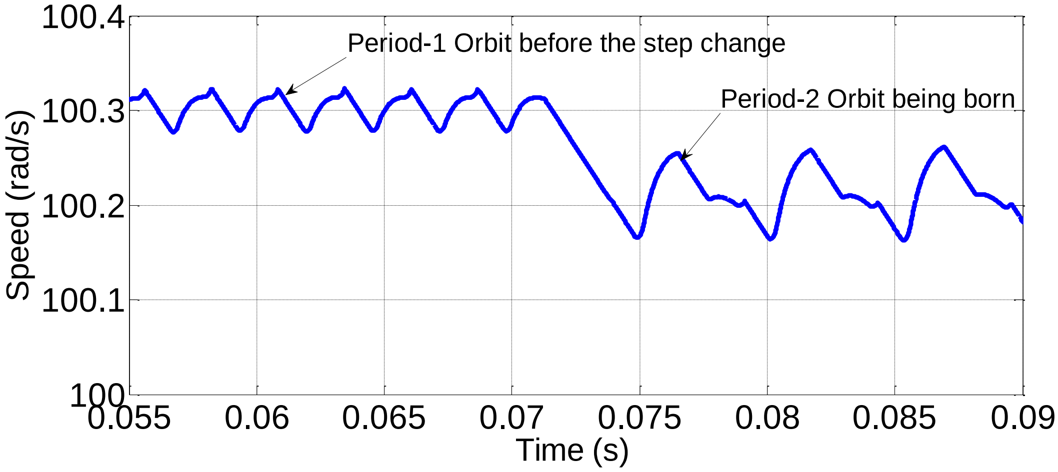

(a)

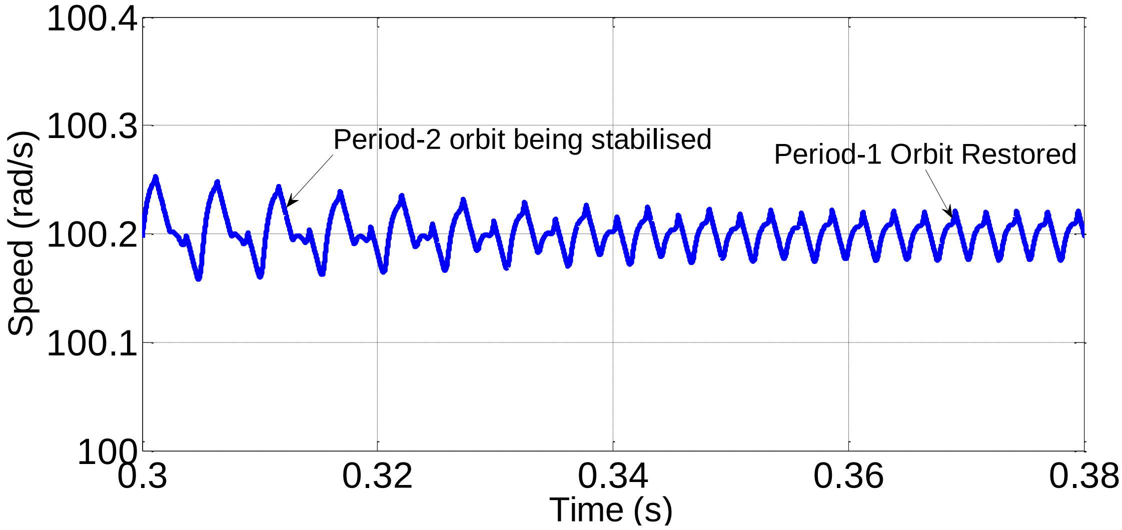

(b)

Fig. 6.13 System response due to step change in proportional gain from g=10 to g=15 (a) Without the supervising controller (b) With the supervising controller.

6.4 Summary

In this chapter, the control of the fast-scale (period doubling) bifurcation in the DC chopper-fed PMDC drive and the SRM drive (by the alteration of the Saltation matrix component of the Monodromy matrix) is discussed. Three stabilization options based on Saltation matrix manipulation were explored, and the results of the control action confirmed the effectiveness of these stabilization techniques.

CHAPTER 7

ANALYSIS AND CONTROL OF NONLINEAR PHENOMENA IN A SERIES CONNECTED DC MOTOR DRIVE

7.1 Introduction

In Chapter 4, nonlinear phenomena in a PMDC drive were investigated. In this Chapter, the nonlinear analysis is extended to a series connected DC (SCDC) motor drive whose mathematical model was derived in Chapter 3. As discussed in Chapter 3, there are three key sources of nonlinearity in an SCDC drive. Firstly, the electrical torque is proportional to the square of the current (below field saturation). Secondly, the back EMF is proportional to the product of current and speed. The last source of nonlinearity is introduced by the power electronic switching in the SCDC drive.

Due to these nonlinearities the SCDC drive is prone to complex, nonlinear dynamical phenomena, namely bifurcation and chaos. The first report of bifurcation behaviour in an SCDC drive was presented in 2011 [90], but no analytical validation of this phenomenon exists in the literature. The key reason could be that unlike PMDC drives and DC-DC converters (whose model is piecewise linear), the mathematical model of an SCDC drive is piecewise nonlinear making the analysis more difficult.

In this chapter, the fast-scale instability (period doubling bifurcation) in an SCDC is analysed using the Monodromy matrix approach [23, 66]. The complexity of the analysis is compounded by the fact that the SCDC drive model comprises nonlinear vector fields, thereby making the computation of the STM along each vector field difficult. Unlike the simple exponential matrix approach used in piecewise linear systems, the STM along each vector field in an SCDC drive is obtained by solving a matrix differential equation (MDE). Analytical results obtained using this approach are compared with the numerically obtained bifurcation diagram of the system, and the two show good agreement. Also, by manipulating the Saltation matrix component of the Monodromy matrix, the fast-scale instability was controlled.

This chapter is structured as follows. In section 7.2, a brief description of the SCDC drive and its mathematical formulation is given, while the bifurcation behaviour of the system is discussed in section 7.3. The analysis of the fast-scale bifurcation is discussed in section 7.4, and bifurcation control is discussed in section 7.5. Section 7.6 is the summary of the chapter.

7.2 System Description

The schematic diagram of the DC chopper-fed SCDC drive is shown in Fig. 7.1. The system consists of three main components, namely the SCDC motor, the power converter (a dc chopper) and the control electronics. Speed control is achieved by regulating the average voltage applied at the armature terminals via control of the power electronic switches.

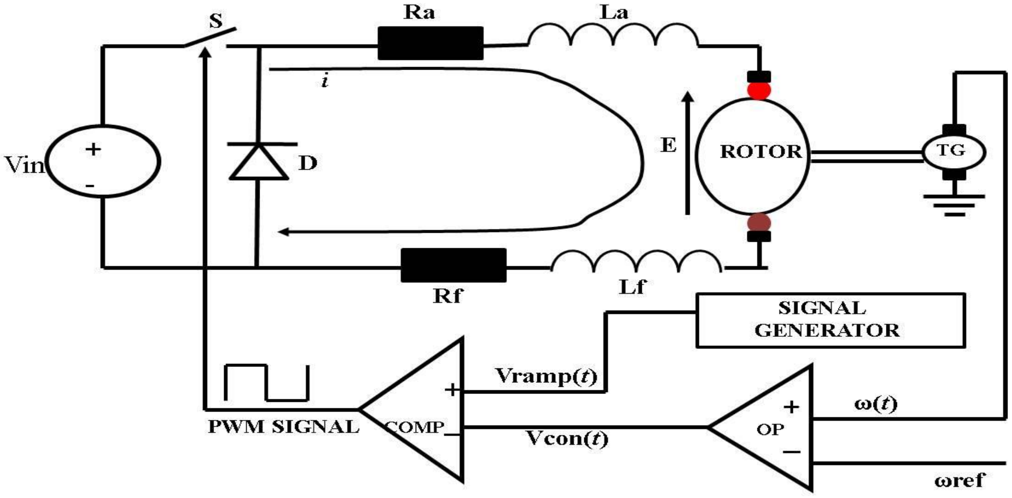

Fig. 7.1 Schematic diagram of an SCDC drive

As a result of the power electronic switching, the system will toggle between two different subsystems in the steady state. The mathematical model of the system is given by a differential equation with a discontinuous right hand side as shown:

$$\frac{d\mathbf{X}(t)}{dt} = \begin{cases} \mathbf{f}_{\mathbf{off}}(\mathbf{X}(t)), \; V_{con}(t) > V_{ramp}(t) \\ \\ \mathbf{f}_{\mathbf{on}}(\mathbf{X}(t)), \; V_{con}(t) < V_{ramp}(t) \end{cases} \tag{7. 1}$$

$$\mathbf{f}_{\mathbf{off}}(\mathbf{X}(t)) = \begin{bmatrix} \dfrac{\left(K_t \, x_2{}^2 - T_L - Bx_1\right)}{J} \\ \dfrac{-x_2 R - K_e x_2 x_1}{L} \end{bmatrix} \tag{7. 2}$$

$$\mathbf{f}_{\mathbf{on}}(\mathbf{X}(t)) = \begin{bmatrix} \dfrac{\left(K_t\, x_2{}^2 - T_L - Bx_1\right)}{J} \\ \dfrac{-x_2 R - K_e x_2 x_1 + V_{in}}{L} \end{bmatrix} \tag{7. 3}$$

$$V_{con}(t) = g(\omega(t) - \omega_{ref}) = g(x_1(t) - \omega_{ref}) \tag{7. 4}$$

$$V_{ramp}(t) = V_L + (V_U - V_L)\frac{t}{T} \operatorname{mod} 1 \tag{7. 5}$$

and $\mathbf{X}(t) = \begin{bmatrix} x_1(t) \\ x_2(t) \end{bmatrix} = \begin{bmatrix} \omega(t) \\ i(t) \end{bmatrix}$.

where $i(t)$ is the armature and field current, $\omega(t)$ is the motor speed, $R = R_a + R_f$ is the sum of the resistances of the armature and field coils, $L = L_a + L_f$ is the sum of the armature and field coil inductances, K_E and K_T are the back emf constant and the torque constant, respectively, B is the friction coefficient, V_L and V_U are the lower and upper ramp signal voltages, T_L is the load torque, J is the moment of inertia, T is the period of the PWM signal, V_{con} is the output of the proportional controller, g is the gain of the operational amplifier, and ω_{ref} is the reference speed. The parameters of the system are: R=7.2Ω, L=0.0917H, T_L=0.2NM, K_E= K_T =0.1236N.m/A^2, J=7.046e-4Kg-m^2,B=4e-4N.m.rad.sec, J=0.000557 N.m.rad.sec^2, T=10msec,V_L=0, V_U=8V and ω_{ref}=100rad/sec.

7.3 Bifurcation Behaviour of Series Connected DC drive

The nominal behaviour of an SCDC drive is a period-1 orbit (Fig. 7.2) whose mean value is close to the reference value and with the same period as the external clock signal. But as some system parameters such as the proportional gain is being varied, this nominal orbit loses stability and a new orbit whose period is double the period of the original orbit (Fig. 7.3) emerges. Further variation of the system parameter leads to period doubling bifurcation cascades and chaos (Fig. 7.4). The bifurcation diagram of the system is shown in Fig. 7.5.

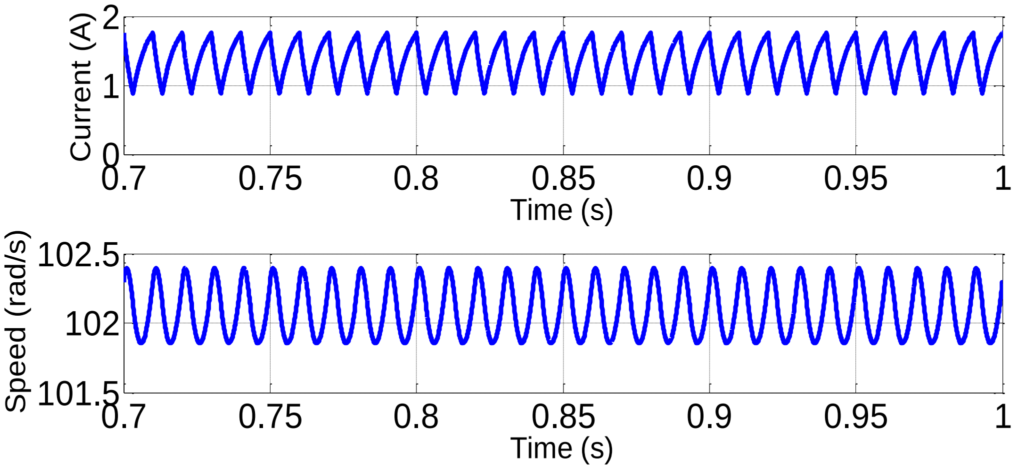

(a)

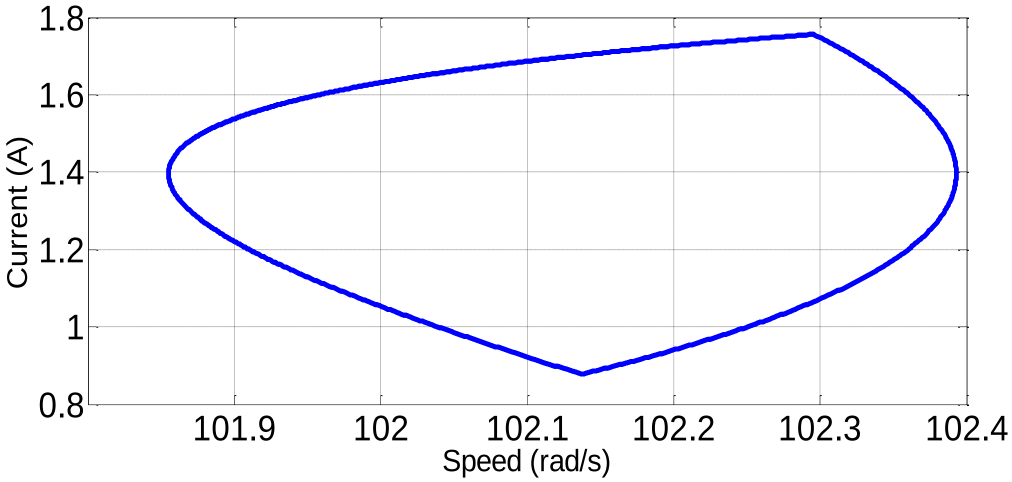

(b)

Fig. 7. 2 Nominal period-1 behaviour of the SCDC drive at g=1.2 (a) Current and speed (b) Trajectory of speed against current.

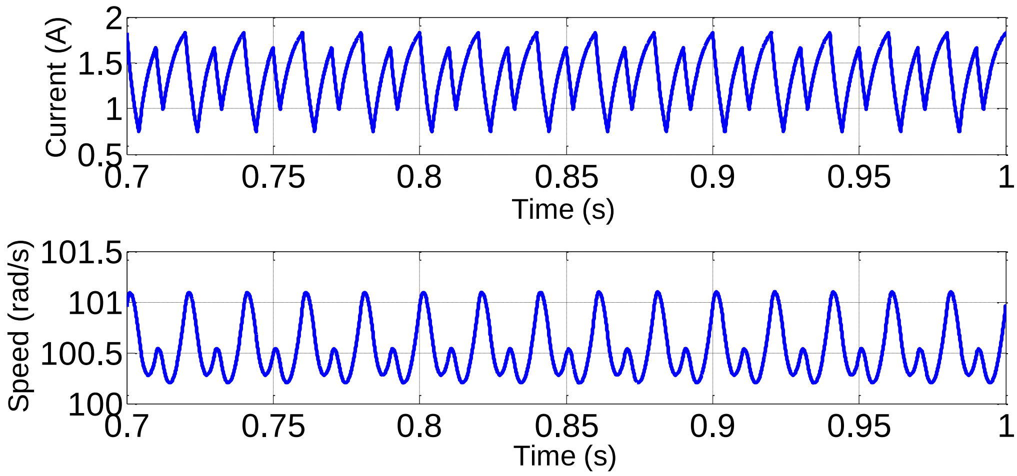

(a)

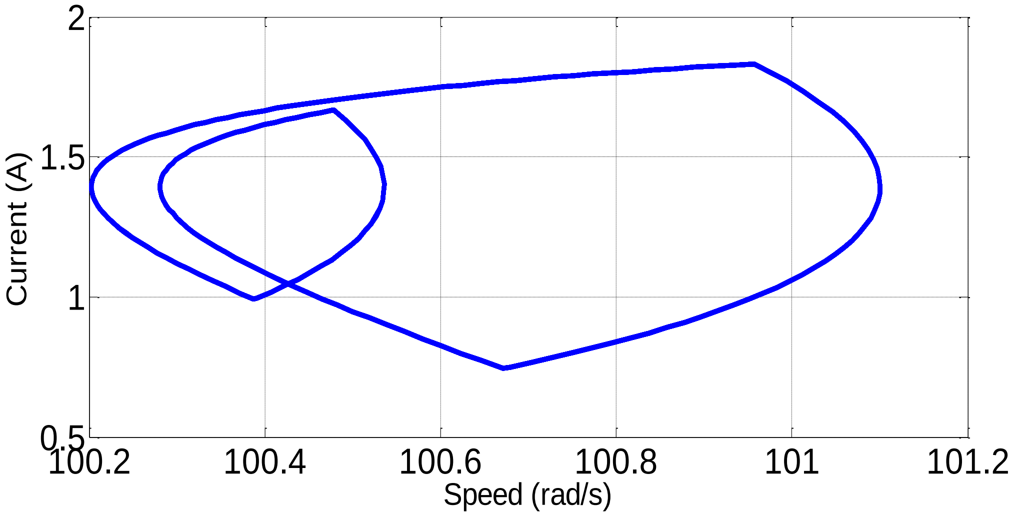

(b)

Fig. 7. 3 Period-2 behaviour of the SCDC drive at g=5 (a) Current and speed (b) Trajectory of speed against current.

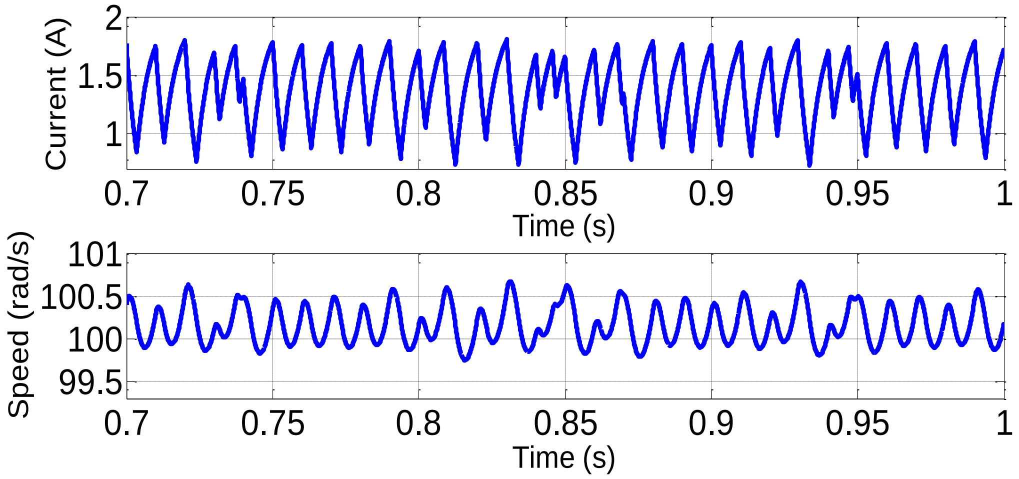

(a)

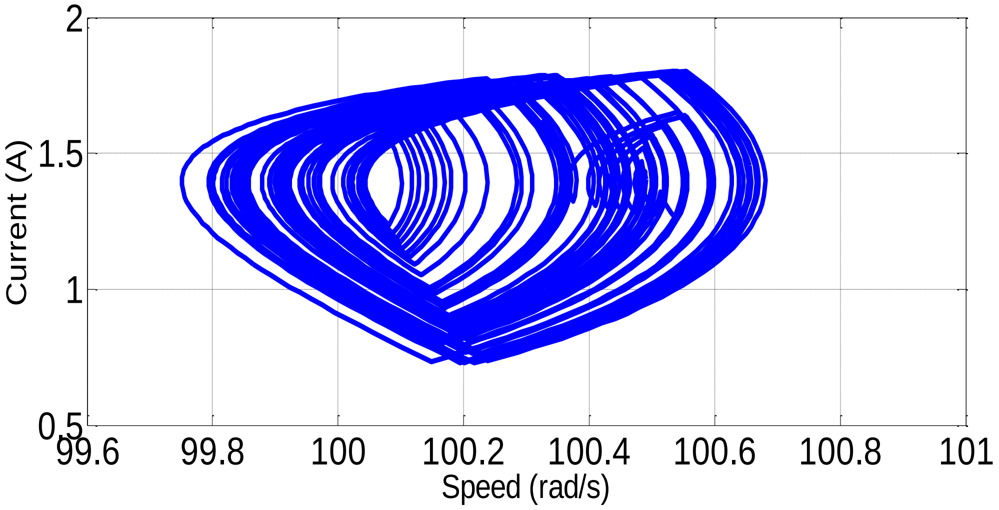

(b)

Fig. 7. 4 Chaotic response of the SCDC drive at g=14 (a) Current and speed (b) Phase portrait of speed against current.

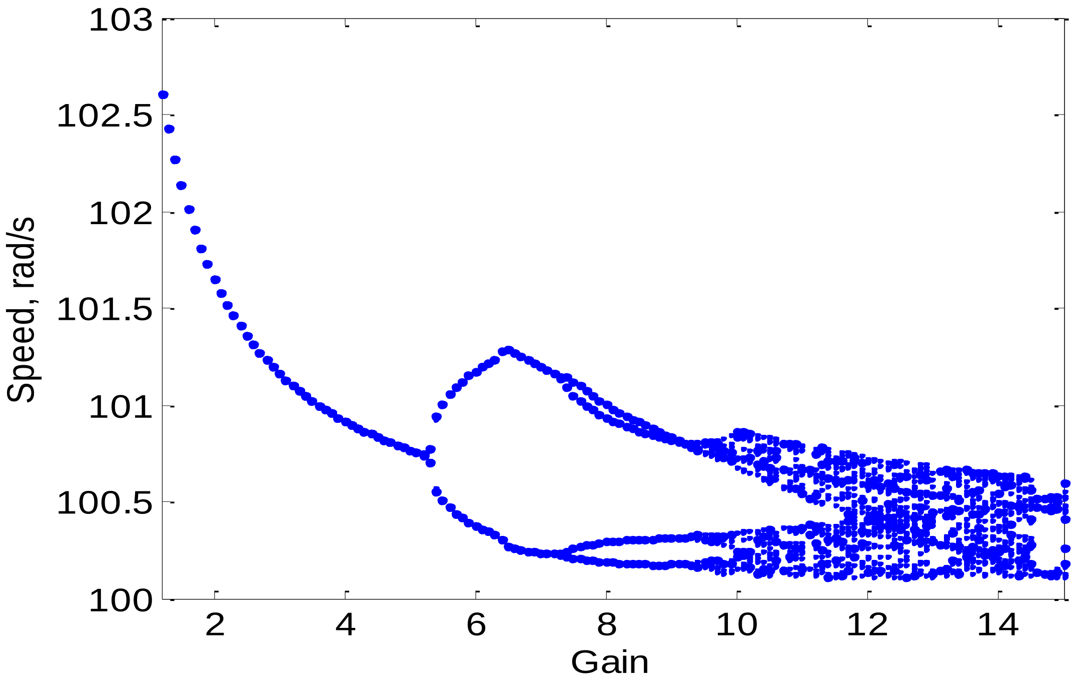

Fig. 7.5 Bifurcation diagram of speed against proportional gain

7.4 Analysis of the Period Doubling Bifurcation in a Series Connected DC Drive via the Monodromy Matrix Approach

To analytically ascertain the bifurcation parameter value at which the nominal period-1 orbit (Fig. 7.2b) loses stability we have to study the system dynamics for $t \epsilon$ [0, T] where T is the period of the orbit. By employing the Monodromy matrix approach [23, 88] the key task is to compute the state transition matrix (STM) along the entire orbit and obtain its eigenvalues. The nominal orbit is stable if the absolute values of the eigenvalues fall within the unit circle and is unstable otherwise. From Fig. 7.2b, the Monodromy matrix of the period-1 orbit can be expressed as:

$$M(T,0) = \Phi(T, t_{\Sigma}) \times S \times \Phi(t_{\Sigma}, 0) \tag{7.6}$$

where $M(T,0)$ is the STM from $t=0$ to $t=T$ (the Monodromy matrix), $\Phi(t_B, t_A)$ is the STM from $t = t_A$ to $t = t_B$, and $\boldsymbol{S}$ is the STM across the switching manifold (the Saltation matrix). Since the vector fields in an SCDC drive are nonlinear, the STM along each of the two vector fields are obtained by solving a matrix differential equation instead of the simple exponential matrix found in piecewise linear systems.

Thus, Φ (t_{Σ}, 0) and Φ (T, t_{Σ}) are evaluated as follows:

$$\frac{d\Phi(t_\Sigma,0)}{dt} = J_1(t)\Phi(t_\Sigma,0);\Phi(0,0) = I_{n\times n} \tag{7.7}$$

where the initial condition Φ(0,0) is an identity matrix of order 2, and J_1(t) is the Jacobian matrix of the first vector field (f_1(X(t)) which is to be evaluated along the orbit from t=0 to t= t_Σ.

$$J_1 = \frac{\partial f_1(X)}{\partial X} = \begin{bmatrix} \frac{-B}{J} & \frac{2K_T x_2}{J} \\ \frac{-K_E x_2}{L} & \frac{(-R - K_E x_1}{L} \end{bmatrix} \tag{7.8}$$

Similarly, Φ(T, t_Σ) is to be evaluated by solving the matrix differential equation:

$$\frac{d\Phi(T,t_\Sigma)}{dt} = J_2(t)\Phi(T,t_\Sigma); \tag{7.9}$$

where J_2(t) is the Jacobian matrix of the second vector field and is to be evaluated along the orbit from t= t_Σ to t=T.

$$J_2 = \frac{\partial f_2(X)}{\partial X} = J_1 \tag{7.10}$$

To complete the derivation of the Monodromy matrix, the Saltation matrix or the STM at the switching instant (t_Σ) needs to be computed. This is expressed as:

$$\mathbf{S} = \begin{bmatrix} 1 & 0 \\ 0 & 1 \end{bmatrix} + \frac{(\mathbf{f}_{\mathbf{ON}} - \mathbf{f}_{\mathbf{OFF}})\mathbf{n}^T}{\mathbf{n}^T\,\mathbf{f}_{\mathbf{OFF}} + \left.\frac{\partial h(\mathbf{X}(t))}{\partial t}\right|_{t=t_\Sigma}} \tag{7.11}$$

where :

$$\mathbf{f}_{\mathbf{ON}} = \mathbf{f}_{\mathbf{on}}(\mathbf{X}(t_\Sigma)) = \begin{bmatrix} \frac{\left(K_t\, x_2{}^2(t_\Sigma) - T_L - Bx_1(t_\Sigma)\right)}{J} \\ \frac{-x_2(t_\Sigma)R - K_e x_2(t_\Sigma)x_1(t_\Sigma) + V_{in}}{L} \end{bmatrix} \tag{7.12}$$

$$\mathbf{f_{OFF}} = \mathbf{f_{off}}(\mathbf{X}(t_\Sigma)) = \begin{bmatrix} \dfrac{\left(K_t\, x_2^{\,2}(t_\Sigma) - T_L - Bx_1(t_\Sigma)\right)}{J} \\ \dfrac{-x_2(t_\Sigma)R - K_e x_2(t_\Sigma)x_1(t_\Sigma)}{L} \end{bmatrix} \tag{7.13}$$

Since the switching between the different subsystems occurs when $V_{\mathrm{con}}(t)=V_{\mathrm{ramp}}(t)$, the switching hypersurface ($h(\mathbf{X}(t))$) is expressed as:

$$h(\mathbf{X}(t)) = V_{con}(t) - V_{ramp}(t) = (x_1(t) - \omega_{ref}) - \frac{1}{g}\left((V_L + (V_U - V_L))\frac{t}{T} \right) = 0 \tag{7.14}$$

The partial derivative of $h(\mathbf{X}(t)$ with respect to time and the normal vector are expressed as:

$$\frac{\partial h(\mathbf{X}(t))}{\partial t} = \frac{-(V_U - V_L)}{T \times g} \tag{7.15}$$

$$\mathbf{n} = \nabla h(\mathbf{X}(t), t) = \begin{bmatrix} \dfrac{\partial h(\mathbf{X}(t))}{\partial x_1} \\ \dfrac{\partial h(\mathbf{X}(t))}{\partial x_2} \end{bmatrix} = \begin{bmatrix} 1 \\ 0 \end{bmatrix} \tag{7.16}$$

The transpose of the normal to the hypersurface $(\mathbf{n}^T)$ is expressed as [1 0].

$$(\mathbf{f_{ON}} - \mathbf{f_{OFF}}) \times \mathbf{n}^T = \begin{bmatrix} 0 & 0 \\ \dfrac{V_{in}}{L} & 0 \end{bmatrix} \tag{7. 17}$$

$$\mathbf{n}^T \times \mathbf{f_{OFF}} = [1 \ \ \mathbf{0}] \times \begin{bmatrix} \dfrac{\left(K_t\, x_2^{\,2}(t_\Sigma) - T_L - Bx_1(t_\Sigma)\right)}{J} \\ \dfrac{-x_2(t_\Sigma)R - K_e x_2(t_\Sigma)x_1(t_\Sigma)}{L} \end{bmatrix} = \frac{\left(K_t\, x_2^{\,2}(t_\Sigma) - T_L - Bx_1(t_\Sigma)\right)}{J} \tag{7. 18}$$

Consequently, the Saltation matrix is given by:

$$\mathbf{S} = \begin{bmatrix} 1 & 0 \\ \dfrac{\dfrac{V_{in}}{L}}{\dfrac{\left(K_t\, x_2{}^2(t_\Sigma) - T_L - Bx_1(t_\Sigma)\right)}{J} - \dfrac{V_U - V_L}{g \times T}} & 1 \end{bmatrix} \tag{7. 19}$$

The computed Monodromy matrix and Floquet multipliers for various values of the bifurcation parameter (g) are shown in Table 7.1. From the Table, it could be seen that the nominal period-1 orbit loses stability at g=4.6 as one of the Floquet multipliers leaves the unit circle at this parameter value. This is in agreement with the bifurcation diagram of the system (Fig. 7.5).

Table 7. 1 Computed Monodromy matrix and Floquet multipliers

Gain(g)	**Monodromy Matrix**	**Floquet Multipliers**
1.2	$\begin{bmatrix} -0.0834 & 0.9726 \\ -0.2982 & -0.0297 \end{bmatrix}$	−0.0566 ±0.5379j
2	$\begin{bmatrix} -0.5507 & 0.4739 \\ -0.4255 & -0.1669 \end{bmatrix}$	−0.3588 ±0.4060*j*
3	$\begin{bmatrix} -0.9177 & 0.0198 \\ -0.5417 & -0.3045 \end{bmatrix}$	−0.8997 -0.3225
4.6	$\begin{bmatrix} -1.4691 & -0.5158 \\ -0.6756 & -0.4377 \end{bmatrix}$	−1.7373 −0.1695

7.5 Control of the Period Doubling Bifurcation in a Series Connected DC Drive

In Chapter 6, the various techniques for bifurcation and chaos control in electrical drives based on Saltation matrix manipulation were discussed. In this chapter, the first approach (injection of low amplitude sinusoidal signal in the switching hypersurface) will be adopted. The main idea is to locate the unstable periodic orbit (UPO) and then stabilise it by injecting a low amplitude sinusoidal signal in the switching hypersurface $h(\mathbf{X}(t),t)$. This can be achieved by replacing the reference speed (ω_{ref}) with ω_{ref} ($1+a\sin\omega t$), where the control parameter '*a*' is usually very small, and $\omega=2\pi/T$. As a result, the switching hypersurface $h(\mathbf{X}(t),t)$ and its partial derivative with respect to time $\frac{\partial h(\mathbf{X}(t),t)}{\partial t}$ will be expressed as:

$$h(\mathbf{X}(t)) = \left(x_1(t) - \omega_{ref}(1 + a\sin(\omega t)\right) - \frac{1}{g}\left(V_L + (V_U - V_L)\frac{t}{T}\right) = 0 \tag{7.20}$$

$$\left.\frac{\partial h(\mathbf{X}(t)}{\partial t}\right|_{t=t_\Sigma} = -\omega_{ref} \times a \times \omega \times \cos(\omega \times t_\Sigma) - \frac{\left(V_U - V_L\right)}{T \times g} \tag{7.21}$$

Consequently, the Saltation matrix will be a function of the control parameter '*a*', and will be expressed as:

$$\mathbf{S} = \begin{bmatrix} 1 & 0 \\ \dfrac{\dfrac{V_{in}}{L}}{\dfrac{\left(K_t\, x_2{}^2(t_\Sigma) - T_L - Bx_1(t_\Sigma)\right)}{J} - \omega_{ref} \times a \times \omega \times \cos(\omega \times t_\Sigma) - \dfrac{\left(V_U - V_L\right)}{T \times g}} & 1 \end{bmatrix} \tag{7.22}$$

By appropriate selection of the control parameter "*a*", the Saltation matrix and thus the Monodromy matrix can be adjusted with little influence on the PWM duty cycle. To test the response of the proposed controller, a step change of the proportional gain from g=1.2 to g=5 was introduced. The system response without the proposed controller is shown in Fig. 7.6, while the system response with the proposed controller is shown in Fig. 7.7.

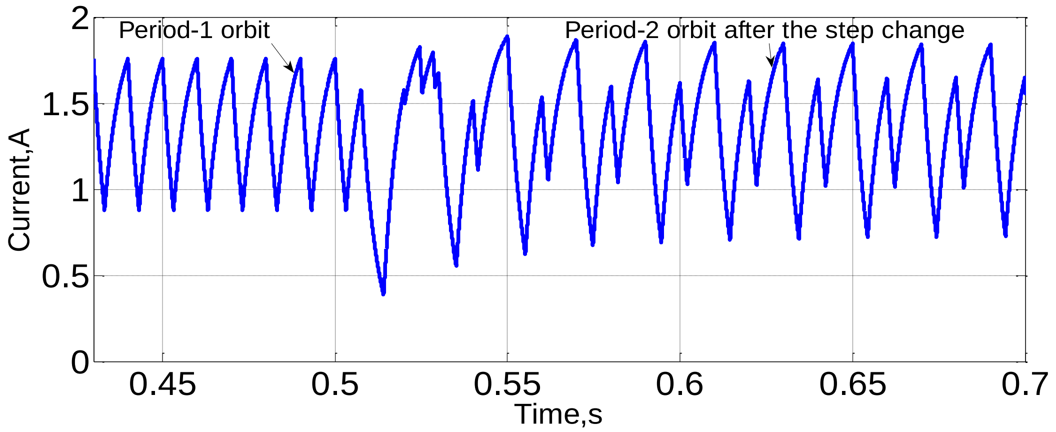

Fig. 7. 6 Step change from g=1.2 to g=5 (without the proposed controller).

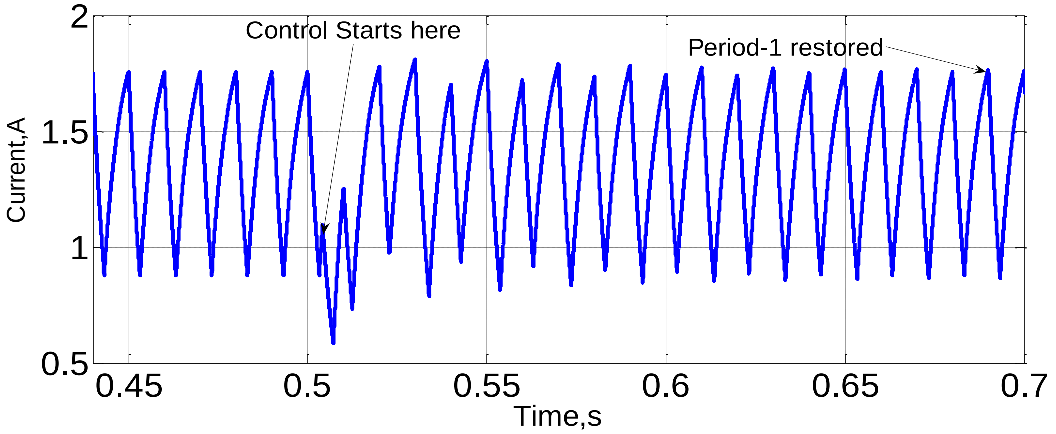

Fig. 7.7 Step change from g=1.2 to g=5 (with the bifurcation controller).

7.6 Summary

In this chapter, the fast-scale bifurcation in SCDC drive is analysed and controlled using the Monodromy matrix approach. Unlike piecewise linear systems such as PMDC drives and DC-DC converters where the STM is computed using simple exponential matrix, the STM in an SCDC drive is computed by solving MDEs, hence the complexity of the analysis. By manipulation of the Saltation matrix component of the Monodromy matrix, the period doubling bifurcation was controlled thus extending the system parameter range for nominal period-1 operation.

CHAPTER 8

ANALYSIS AND CONTROL OF NONLINEAR PHENOMENA IN FULL-BRIDGE CONVERTER DC DRIVE

8.1 Introduction.

In Chapter 4, the nonlinear phenomena in a DC chopper-fed PMDC employing the proportional and proportional integral controller were investigated. In this appendix, the nonlinear analysis is extended to a PMDC employing a full-bridge converter. Unlike the DC chopper-fed PMDC drive, the full-bridge converter drive can achieve four quadrant operations (forward motoring, forward braking, reverse motoring and reverse braking) and will be more suitable for traction applications [91]. Nonlinear bifurcation and chaotic phenomena in full-bridge converter PMDC drive were first reported in [58], but analytical validation of this phenomena is absent from the literature.

In this project, the fast-scale bifurcation phenomena in a full-bridge converter PMDC drive will be analyzed using the Monodromy matrix approach. Also, by manipulation of the Saltation matrix component of the Monodromy matrix, the onset of the drive’s fast-scale bifurcation is controlled thus extending the system parameter range for nominal period-1 operation. Apart from the fast scale bifurcation, the co-existence of period-1 and period-3 attractors at the same system parameter range was observed in this system and efforts to isolate the basins of attraction of the two attracting sets revealed the occurrence of fractal phenomena. Using the Monodromy matrix approach it was established that the co-existing period-3 attractor is born via a saddle node bifurcation.

This chapter is structured as follows. In section 8.2, a brief overview of a full-bridge converter PMDC drive is given, while the dynamic behavior of the system is discussed in section 8.3. The analysis of the fast-scale bifurcation is carried out in section 8.4, and control of the fast-scale bifurcation via Saltation matrix manipulation is discussed in section 8.5. In section 8.6, the co-existence of period-1 and period-3 attracting sets will be discussed. Section 8.7 is the summary of the chapter.

8.2 System Overview

The DC chopper fed PMDC drive can be operated only in the first quadrant of the speed-torque plane. In order to achieve four quadrant operation as some applications demand, a full-bridge converter DC drive (Fig. 8.1) must be employed. The system consists of the PMDC drive, a full-bridge converter circuit, and the control electronics.

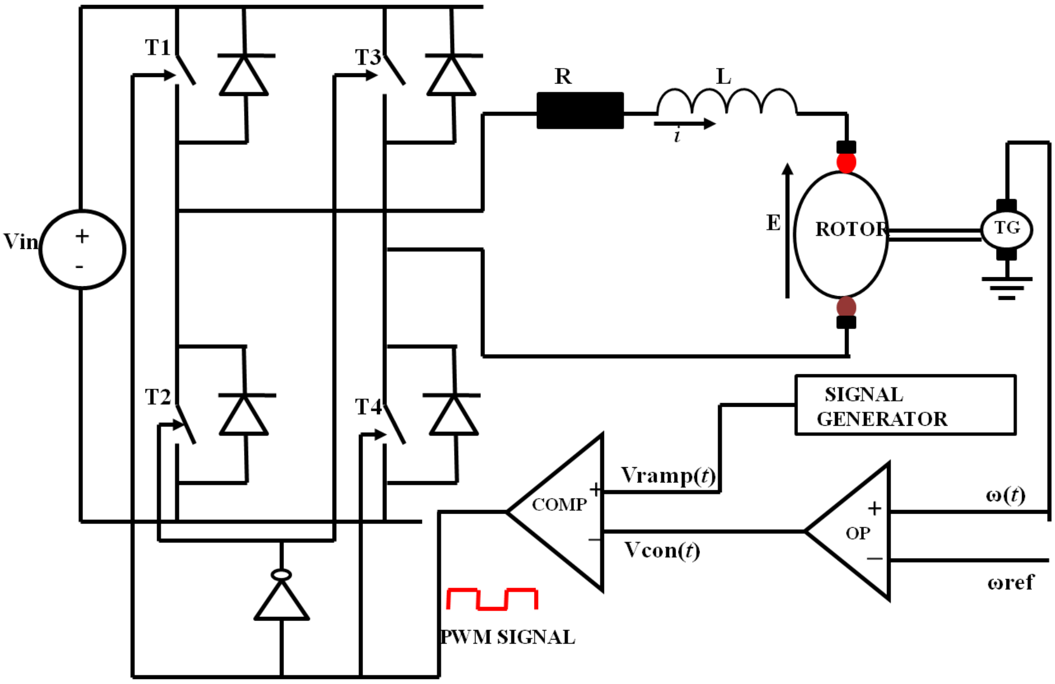

Fig. 8. 1 Full bridge converter PMDC Drive

The full-bridge converter consists of four power electronic switches (T1, T2, T3, and T4) and four freewheeling diodes. When using the bipolar PWM scheme, the two devices on each leg of the power converter act in a cyclic and complementary manner. For instance if T1 and T4 are switched ON, T2 and T3 are to be switched OFF and vice-versa.

Usually a control voltage $V_{\text{con}}(t)$ is compared with a sawtooth signal $V_{\text{ramp}}(t)$ to produce the PWM output which controls the switches. If the PWM output is high ($V_{\text{con}}(t)$ less than $V_{\text{ramp}}(t)$), T1 and T4 will be switched ON, while T2 and T3 will be switched OFF. But if the PWM output is low ($V_{\text{con}}(t)$ greater than $V_{\text{ramp}}(t)$), T2 and T3 will be switched ON, while T1 and T4 will be switched OFF. As a result, the system will alternate between two topological states that will be referred to as state 1 and state 2.

In state 1, $+V_{\text{in}}$ is applied at the armature terminals, while in state 2, $-V_{\text{in}}$ is applied to decrease the speed. As a result, the system behaviour is described by a differential equation with a discontinuous right hand side as shown:

$$\frac{d\mathbf{X}(t)}{dt} = \begin{cases} \mathbf{f}_-(\mathbf{X}(t)), & V_{con}(t) > V_{ramp}(t) \\ \mathbf{f}_+(\mathbf{X}(t)), & V_{con}(t) < V_{ramp}(t) \end{cases} \tag{8.1}$$

where $\mathbf{X}(t) = \begin{bmatrix} x_1(t) \\ x_2(t) \end{bmatrix} = \begin{bmatrix} \omega(t) \\ i(t) \end{bmatrix}$ is the state vector.

$\mathbf{f}_-(\mathbf{X}(t),t)$ and $\mathbf{f}_+(\mathbf{X}(t),t)$ are the vector fields before and after the switching instant, while $V_{con}(t) = g \times (\omega(t) - \omega_{ref}) = g \times (x_1(t) - \omega_{ref})$, and $V_{ramp}(t) = V_L + (V_U - V_L)\frac{t}{T} \bmod 1$.

$$\mathbf{f}_-(\mathbf{X}(t),t) = \mathbf{A}\mathbf{X}(t) + V_- = \begin{bmatrix} \dfrac{K_t x_2 - B x_1 - T_L}{J} \\ \dfrac{-R x_2 - K_e x_1 - V_{in}}{L} \end{bmatrix} \tag{8.2}$$

$$\mathbf{f}_+(\mathbf{X}(t),t) = \mathbf{A}\mathbf{X}(t) + V_+ = \begin{bmatrix} \dfrac{K_t x_2 - B x_1 - T_L}{J} \\ \dfrac{-R x_2 - K_e x_1 + V_{in}}{L} \end{bmatrix} \tag{8.3}$$

$$\mathbf{A} = \begin{bmatrix} \dfrac{-B}{J} & \dfrac{K_t}{J} \\ \dfrac{-K_e}{L} & \dfrac{-R}{L} \end{bmatrix},\ V_+ = \begin{bmatrix} \dfrac{-T_L}{J} \\ \dfrac{V_{in}}{L} \end{bmatrix} \text{ and } V_- = \begin{bmatrix} \dfrac{-T_L}{J} \\ \dfrac{-V_{in}}{L} \end{bmatrix}$$

8.3 Dynamic Behaviour of a Full-Bridge Converter PMDC Drive

The nominal steady state behaviour of the full-bridge converter PMDC drive is a period-1 orbit (Fig. 8.2). However, as some system parameter such as the supply voltage is varied, the desired period-1 orbit loses stability and a new orbit whose period is double the period of the original orbit emerges [58] (Fig. 8.3). Further variation of the system parameter leads to several period-doubling bifurcation cascades and chaos. The bifurcation diagram of the system as the supply voltage is varied is shown in Fig. 8.4. The fixed parameters of the system are: K_e=0.1356Vs/rad, K_t=0.1324NM/A,

R=2.8Ω, L=53.7mH, T_L=0.38NM, g=1.2, B=0.000275Nm.rad.sec, T=10msec, J=5.57×10^{-4}N.m.rad.sec^2, V_L=0, V_U=8V, ω_{ref}=100rad/sec .

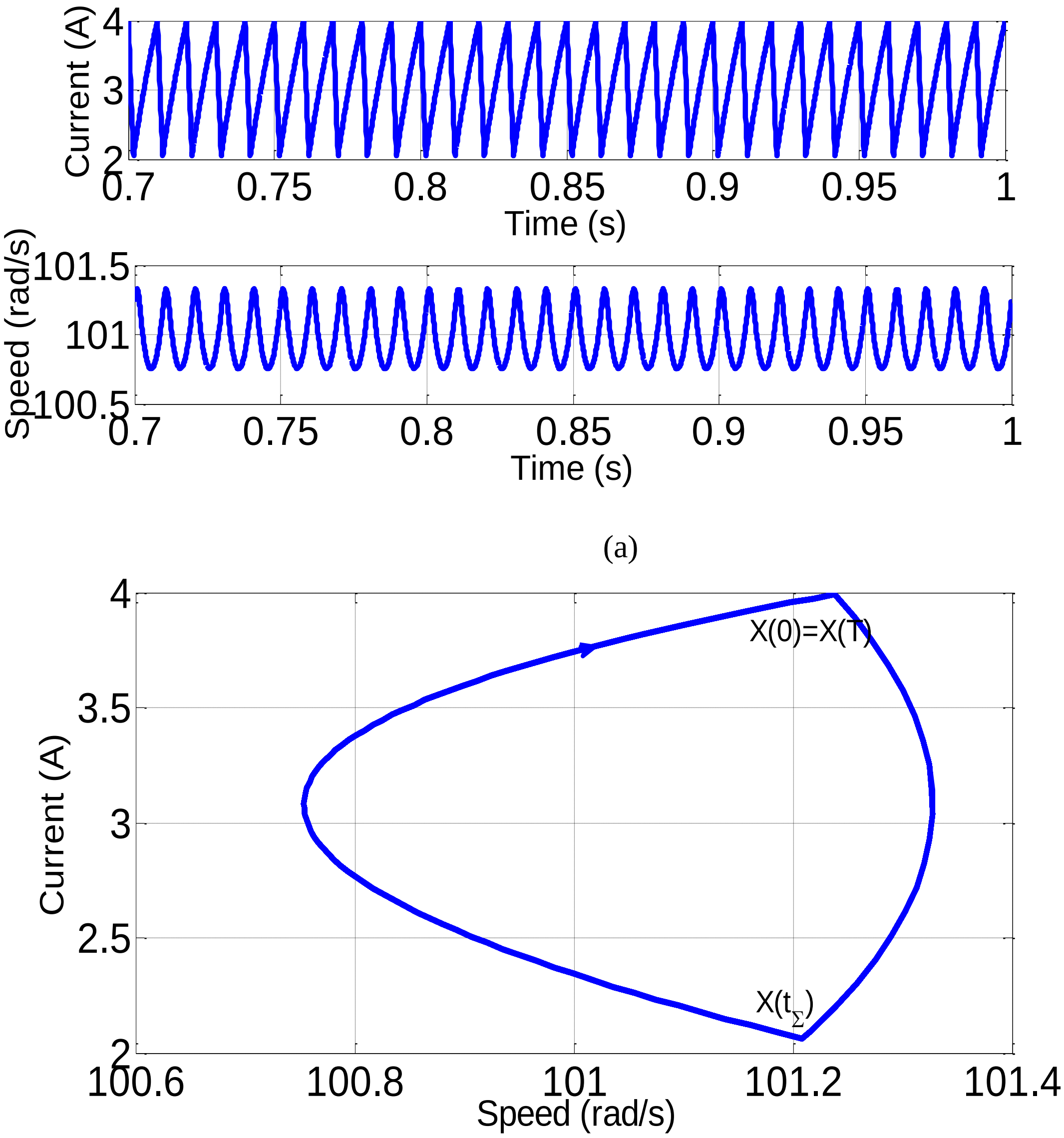

(a)

(b)

Fig. 8. 2 Period-1 behaviour at V_{in}=35V (a) current and speed response (b) phase portrait.

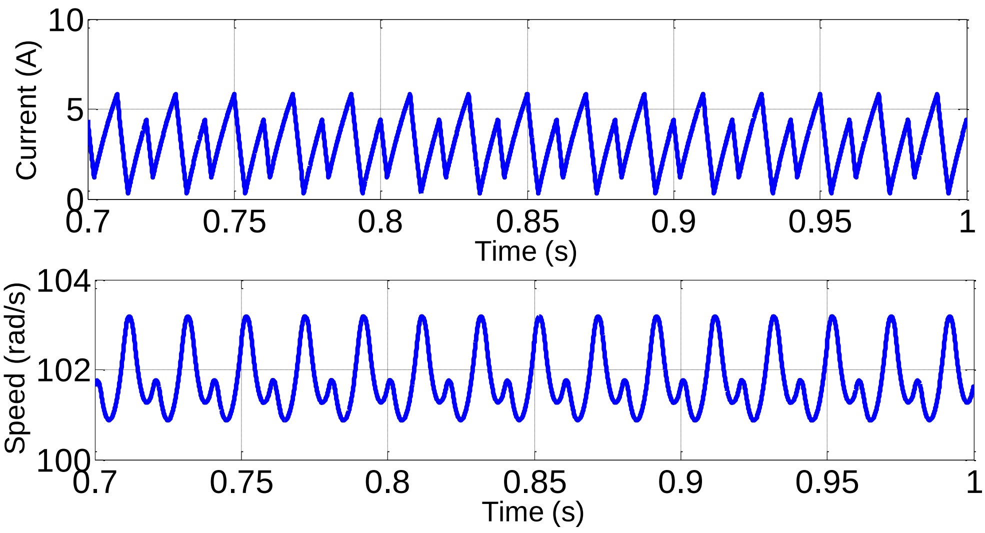

(a)

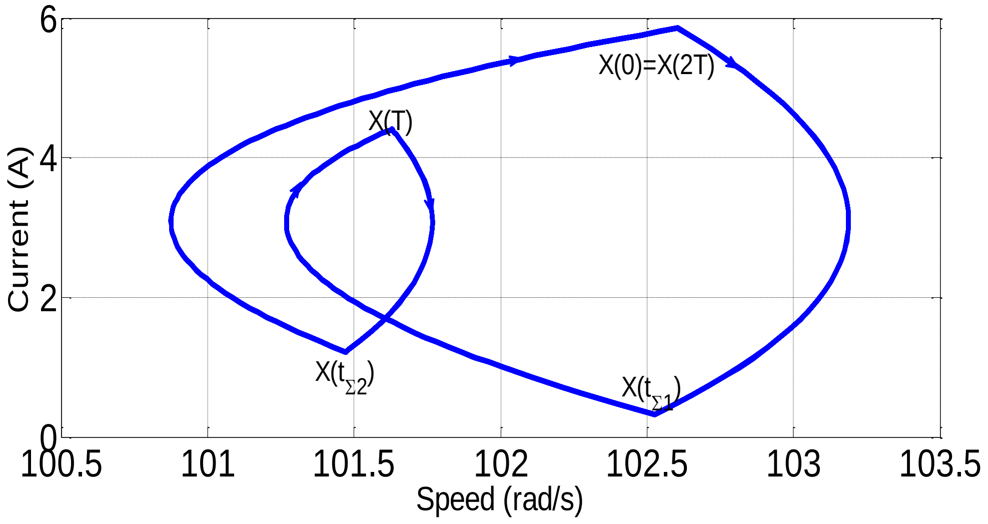

(b)

Fig. 8. 3 Period-2 trajectory at V_{in}=56V (a) current and speed response (b) phase portrait.

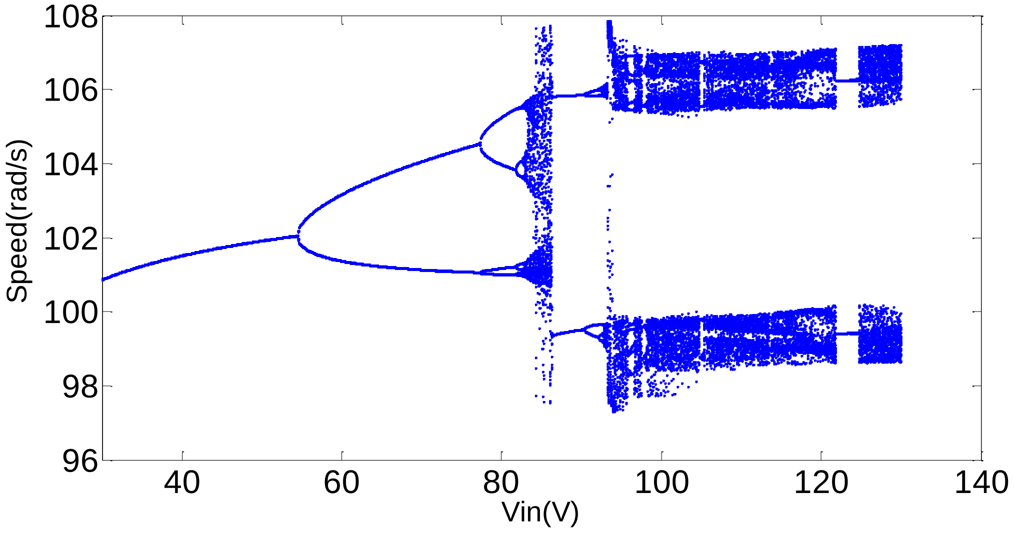

(a)

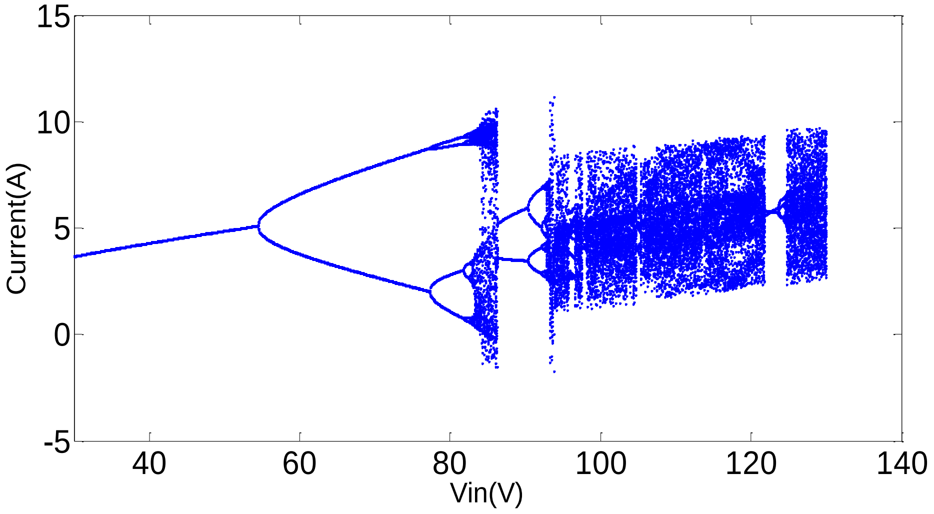

(b)

Fig. 8. 4 Bifurcation diagrams of the system (a) speed against supply voltage (b) current against supply voltage.

8.4 Analysis of the Fast-scale Bifurcation in a Full Bridge Converter PMDC Drive

To determine analytically the system parameter value at which the fast-scale bifurcation occurs we need to perform the stability analysis of the nominal period-1 orbit of the system (Fig. 8.2b). By employing the Monodromy matrix approach, we need to obtain the STM round the nominal orbit and evaluate its eigenvalues. The nominal orbit is stable if the absolute values of the Floquet multipliers is within the unit circle and unstable otherwise. From Fig. 8.2b, the Monodromy matrix can be expressed as:

$$\mathbf{M}(T,0)=\Phi(T,t_\Sigma)\times\mathbf{S}\times\Phi(t_\Sigma,0) \tag{8.4}$$

where $\Phi(t_B,t_A)$ is the STM from $t=t_A$ to $t=t_B$, t_Σ is the switching instant and is a function of the PWM duty ratio ($t_\Sigma=d'T=(1-d)T$), and $(\mathbf{S})$ is the state transition matrix across the switching manifold (also known as the Saltation matrix). Since the vector fields are linear, the STM $(\Phi(t_B,t_A))$ can be expressed as an exponential matrix $\Phi(t_B,t_A)=e^{A(t_B-t_A)}$.

According to [23, 66], the Saltation matrix can be expressed as:

$$\mathbf{S}=\mathbf{I}+\frac{(\mathbf{f}_+-\mathbf{f}_-)\mathbf{n}^T}{\mathbf{n}^T\,\mathbf{f}_-+\left(\partial h(\mathbf{X}(t),t_\Sigma)/\partial t\right)} \tag{8.5}$$

where h defines the location of the switching hypersurface, $\mathbf{n}$ is the normal vector to the hypersurface h, $\mathbf{f}_-$ stands for $\lim_{t\uparrow t_\Sigma}\mathbf{f}_-(\mathbf{X}(t),t)$, $\mathbf{f}_+$ stands for $\lim_{t\downarrow t_\Sigma}\mathbf{f}_+(\mathbf{X}(t),t)$ and $\mathbf{I}$ is an identity matrix of the same order as that of the system. For the period-1 limit cycle ($t\in[0,T]$), the switching between the two vector fields occurs when $V_{con}(t)=V_{ramp}(t)$ and the switching hypersurface h could be expressed as:

$$h(X(t),t)=x_1(t)-\omega_{ref}-\frac{V_L+(V_U-V_L)t/T}{g}=0 \tag{8.6}$$

The normal to the hypersurface and its partial derivative with respect to time $\left(\partial h(\mathbf{X}(t),t_\Sigma)/\partial t\right)$ are expressed as:

$$\mathbf{n}=\nabla h(X(t),t)=\begin{bmatrix}\dfrac{\partial h(X(t),t)}{\partial x_1}\\[2mm]\dfrac{\partial h(X(t),t)}{\partial x_2}\end{bmatrix}=\begin{bmatrix}1\\0\end{bmatrix} \tag{8.7}$$

$$\frac{\partial h(X(t),t)}{\partial t}=\frac{-(V_U-V_L)}{T\times g} \tag{8.8}$$

$$\mathbf{f}_-=\mathbf{A}\mathbf{X}(t_\Sigma)+V_-=\begin{bmatrix}\dfrac{k_t x_2(t_\Sigma)-Bx_1(t_\Sigma)-T_L}{J}\\[2mm]\dfrac{-Rx_2(t_\Sigma)-k_e x_1(t_\Sigma)-V_{in}}{L}\end{bmatrix} \tag{8.9}$$

$$\mathbf{f}_{+} = \mathbf{A}\mathbf{X}(t_\Sigma) + V_{+} = \begin{bmatrix} \dfrac{k_t x_2(t_\Sigma) - Bx_1(t_\Sigma) - T_L}{J} \\ \dfrac{-Rx_2(t_\Sigma) - k_e x_1(t_\Sigma) + V_{in}}{L} \end{bmatrix} \tag{8.10}$$

$$\mathbf{n}^T \times \mathbf{f}_{-} = \left(\frac{k_t x_2(t_\Sigma) - Bx_1(t_\Sigma) - T_L}{J} \right) \tag{8.11}$$

$$(\mathbf{f}_{+} - \mathbf{f}_{-}) \times \mathbf{n}^T = \begin{bmatrix} 0 & 0 \\ \dfrac{2V_{in}}{L} & 0 \end{bmatrix} \tag{8.12}$$

Consequently, the Saltation matrix for the full-bridge converter PMDC drive for ($t \in [0,T]$) will be expressed as:

$$\mathbf{S} = \begin{bmatrix} 1 & 0 \\ \dfrac{\dfrac{2V_{in}}{L}}{\dfrac{k_t x_2(t_\Sigma) - Bx_1(t_\Sigma) - T_L}{J} - \dfrac{(V_U - V_L)}{g \times T}} & 1 \end{bmatrix} \tag{8.13}$$

where the switching instant $(t_\Sigma = d'T)$ and the state vector at the switching instant $(\mathbf{X}(t_\Sigma)$ are the only unknowns, and could be obtained from the limit cycle diagram (Fig.8.2b) as follows:

$$\mathbf{X}(T) = \mathbf{X}(0) = e^{\mathbf{A}(T-t_\Sigma)}\mathbf{X}(t_\Sigma) + \int_{t_\Sigma}^{T} e^{\mathbf{A}(T-\tau)} V_{+} d\tau \tag{8.14}$$

$$\mathbf{X}(t_\Sigma) = e^{\mathbf{A}(t_\Sigma)}\mathbf{X}(0) + \int_{0}^{t_\Sigma} e^{\mathbf{A}(t_\Sigma-\tau)} V_{-} d\tau \tag{8.15}$$

By substituting the expression for $\mathbf{X}(t_\Sigma)$ into (8.14), the initial state $\mathbf{X}(0)$ can be expressed as:

$$\mathbf{X}(0) = (\mathbf{I} - e^{\mathbf{A}T})^{-1} \times (e^{\mathbf{A}(T-t_\Sigma)} \int_{0}^{t_\Sigma} e^{\mathbf{A}(t_\Sigma-\tau)} V_{-} d\tau + \int_{t_\Sigma}^{T} e^{\mathbf{A}(T-\tau)} V_{+} d\tau) \tag{8.16}$$

Equation (8.16) expresses the initial state **X**(0) in terms of the switching instant $(t_\Sigma = d'T)$. To obtain the value of the state vector at the switching instant, X(t_Σ), the values of **X**(0) and t_Σ must be known. To obtain the duty ratio d' and thus the switching instant t_Σ , we make use of the hypersurface expression (8.6) and the expression for the switching instant (8.15) giving the equation:

$$x_1(t_\Sigma) = [1\ \mathbf{0}]\times\left(e^{\mathbf{A}(t_\Sigma)}\mathbf{X}(0)+\int_0^{t_\Sigma} e^{\mathbf{A}(t_\Sigma-\tau)}V\_d\tau\right) = \omega_{ref} + \frac{V_L+(V_U-V_L)\times t_\Sigma/T}{g} \tag{8.17}$$

$$[1\quad 0]\times\left(e^{\mathbf{A}d'T}\mathbf{X}(0)+\int_0^{d'T} e^{\mathbf{A}(d'T-\tau)}V\_d\tau\right)-\omega_{ref}-\frac{(V_L+(V_U-V_L)d')}{g}=0 \tag{8.18}$$

By substituting the expression for **X**(0) in (8.16) into (8.18), equation (8.18) can be solved numerically for the duty ratio using the Newton-Raphson method. Once the duty ratio (d') is computed, the switching instant $(t_\Sigma = d'T)$, initial state **X**(0), and the state vector at the switching instant $\mathbf{X}(t_\Sigma)$ will be evaluated. The Saltation matrix(**S**) will then be evaluated by substituting the value of $\mathbf{X}(t_\Sigma)$ into the equation (8.13).

Consequently, the Monodromy matrix $\mathbf{M}(T,0) = e^{\mathbf{A}(T-t_\Sigma)}\times\mathbf{S}\times e^{\mathbf{A}t_\Sigma}$ could then be evaluated. The computed Saltation matrix, Monodromy matrix and Floquet multipliers as the supply voltage (V_{in}) is being varied are shown in Table 8.1, and the eigenvalue loci are shown in Fig. 8.5. Both the tabulated result and the eigenvalue loci indicate that the period-1 orbit loses stability at V_{in}=55V as one of the Floquet multipliers moved out of the unit circle at that parameter value. This is in full agreement with the bifurcation diagram of the system shown in Fig. 8.4.

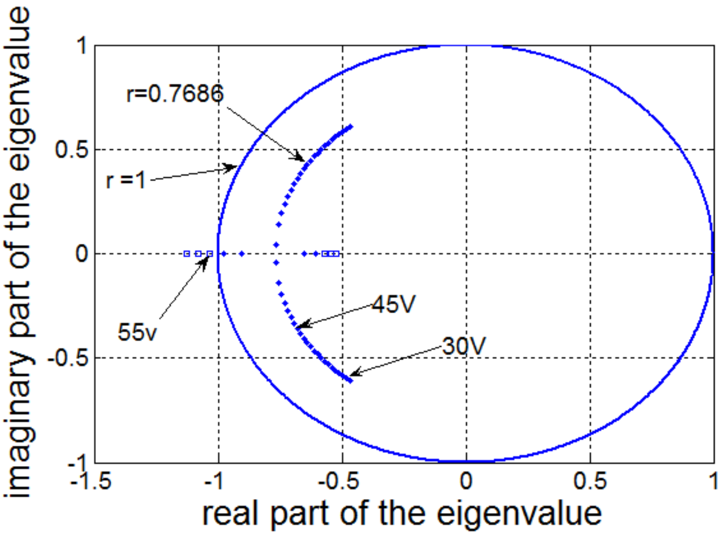

Fig. 8.5 Eigenvalue loci for $V_{in} \in [30V,55V]$.

Table 8. 1 Monodromy matrix and Floquet multipliers for $V_{in} \in [35V,55V]$.

V_{in}	**Saltation Matrix**	**Monodromy Matrix**	**Floquet Multipliers**
35 V	$\begin{bmatrix} 1 & 0 \\ -1.4345 & 1 \end{bmatrix}$	$\begin{bmatrix} 0.3934 & 0.9041 \\ -1.2953 & -1.4748 \end{bmatrix}$	-0.5407 $\pm 0.5463j$
45 V	$\begin{bmatrix} 1 & 0 \\ -1.5863 & 1 \end{bmatrix}$	$\begin{bmatrix} 0.0990 & 0.5317 \\ -1.3825 & -1.4580 \end{bmatrix}$	-0.6795 $\pm 0.3592j$
50 V	$\begin{bmatrix} 1 & 0 \\ -1.6557 & 1 \end{bmatrix}$	$\begin{bmatrix} -0.0229 & 0.3911 \\ -1.4249 & -1.4632 \end{bmatrix}$	-0.7430 $\pm 0.1966j$
55 V	$\begin{bmatrix} 1 & 0 \\ -1.7208 & 1 \end{bmatrix}$	$\begin{bmatrix} -0.1324 & 0.2701 \\ -1.4654 & -1.4726 \end{bmatrix}$	-0.5717 -1.0333

8.5 Control of the Fast-scale Bifurcation in a Full Bridge Converter PMDC Drive

The purpose of a fast-scale bifurcation controller is to extend the system parameter range for desirable period-1 operation. As was discussed in Chapter 6, three different techniques based on Saltation matrix manipulation could be explored. In this chapter, the Saltation matrix manipulation based on the introduction of a low amplitude sinusoidal signal will be adopted. This can be achieved by changing the value of the reference speed (ω_{ref}) to $\omega_{ref}(1+a\sin\omega t)$, where $\omega=2\pi/T$ and 'a' is the control parameter. Since the value of 'a' is usually very small, the change in (ω_{ref}) will has little effect in the control signal $(V_{con}(t) = g \times (\omega(t) - \omega_{ref}))$.

Consequently, the switching instant $(t_\Sigma = d'T)$ and the duty ratio will be relatively unchanged. But, very small values of 'a' will have a substantial effect on both the Saltation matrix and the Monodromy matrix. This can be illustrated by taking the time derivative of the switching hypersurface $h(\mathrm{X}(t),t)$. By replacing ω_{ref} in equation (8.6) with $\omega_{ref}(1+a\sin(\omega t))$ the hypersurface equation and its time derivative will be expressed as:

$$h(X(t),t) = x_1(t) - \omega_{ref} - \omega_{ref} a \sin(\omega t) - \frac{(V_L + (V_U - V_L)t}{g \times T} = 0 \tag{8.19}$$

$$\left.\frac{\partial h(X(t),t)}{\partial t}\right|_{t=t_\Sigma=d'T} = -a\omega\omega_{ref}\cos(\omega d'T) - \frac{(V_U - V_L)}{g \times T} \tag{8.20}$$

The Saltation matrix will thus be expressed as:

$$\mathbf{S} = \begin{bmatrix} 1 & 0 \\ \dfrac{\dfrac{2V_{in}}{L}}{\dfrac{k_t x_2(t_\Sigma) - Bx_1(t_\Sigma) - T_L}{J} - a\omega\omega_{ref}\cos(\omega d'T) - \dfrac{(V_U - V_L)}{g \times T}} & 1 \end{bmatrix} \tag{8.21}$$

From equation (8.21), the Saltation matrix and hence the Monodromy matrix is a function of the control parameter 'a'. To design a controller for the fast-scale bifurcation, we need to determine the values of 'a' capable of placing the Floquet multipliers (eigenvalues of the Monodromy matrix) within the unit circle. This can be achieved by solving the nonlinear transcendental equation (8.22), where 0.7686 is the radius of the stable eigenvalues (Fig. 8.5).

$$|eig(\mathbf{M}(T,0))| - 0.7686 = 0 \tag{8.22}$$

where the Monodromy matrix $\mathbf{M}(T,0)$ is a function of the control parameter 'a'. By solving equation (8.22) for different values of the supply voltage, a polynomial equation that expresses the control parameter ‘*a*’ as a function of the supply voltage was obtained using Matlab Polyfit function. Based on the polynomial equation, a look table (Fig. 8.6) that could be used to determine the required value of the control parameter as the supply voltage is varied, was created.

$$a(V_{in}) = -2.74\times10^{-6}V_{in}^3 + 4.96\times10^{-4}V_{in}^2 - 3.01\times10^{-2}V_{in} + 6.11\times10^{-1} \qquad (8.23)$$

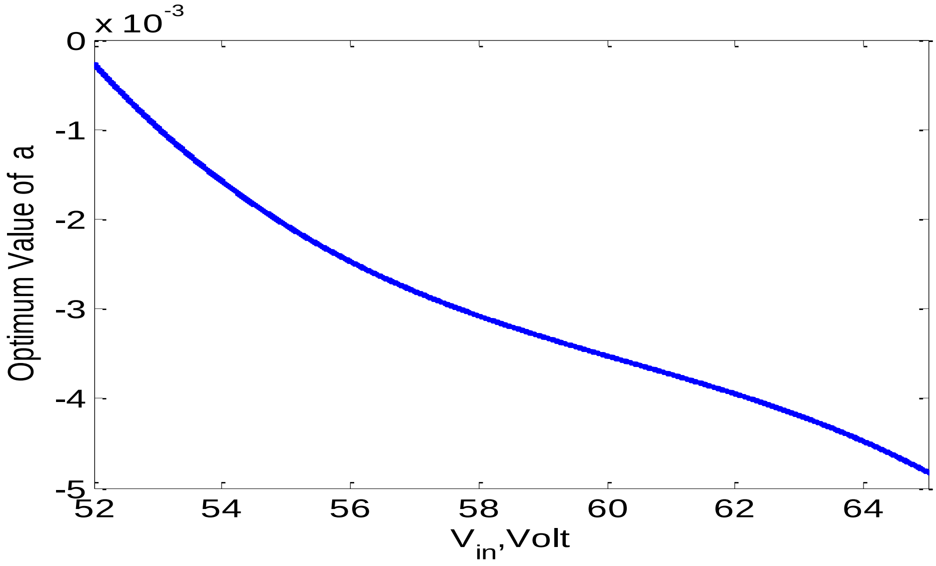

Fig. 8. 6 Computed value of the control parameter as the Supply voltage is varied.

To test the response of the bifurcation controller, a step change in supply voltage from V_{in}=50V to 57V was performed. The system response to the step change without the bifurcation controller is shown in Fig.8.7, while the system response with the bifurcation controller is at Fig. 8.8. Without the bifurcation controller, the step change resulted in period-2 steady-state subharmonics. But the bifurcation controller was able to restore the nominal period-1 operation within a very short time interval.

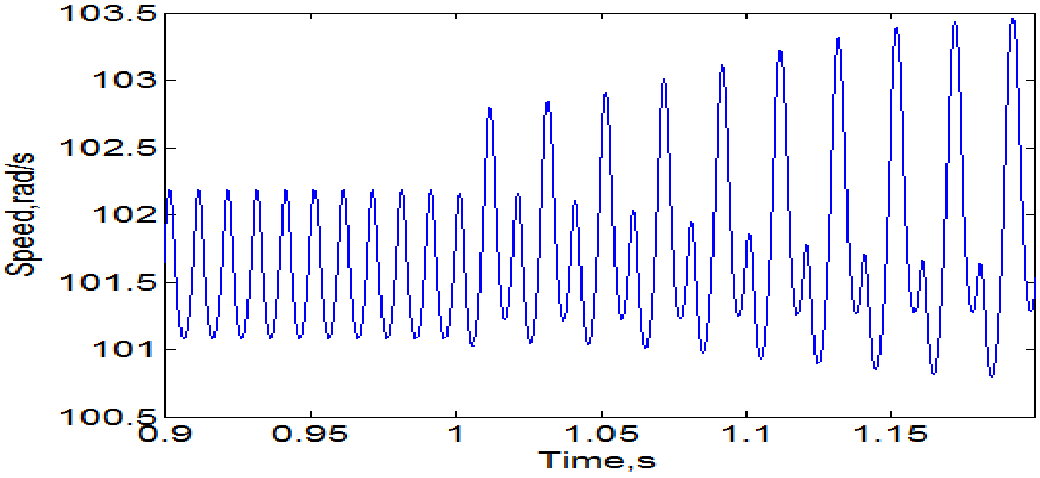

Fig. 8.7 Step response without the bifurcation controller

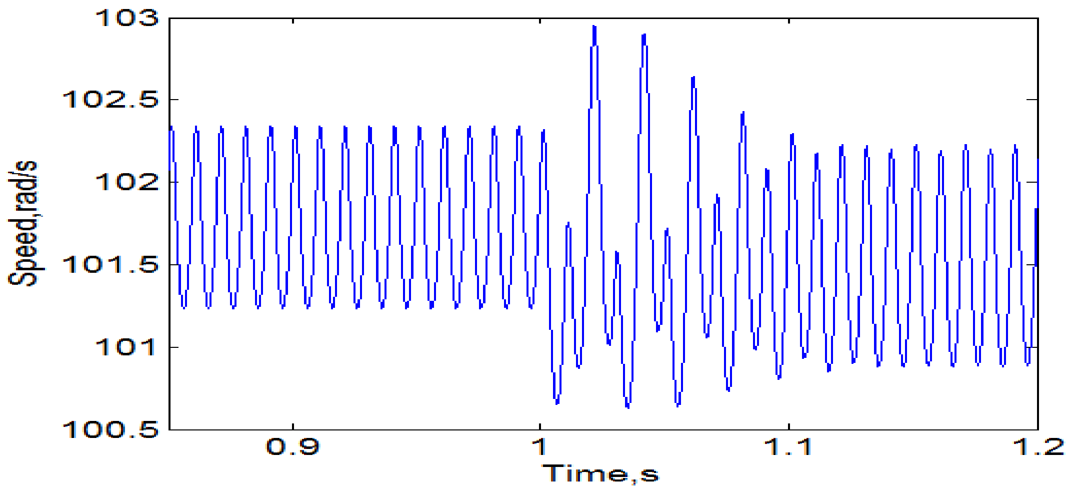

Fig. 8.8 Step response with the bifurcation controller.

8.6 Co-existing Attractors and Fractal Basin Boundaries in a Full Bridge Converter DC Drive

If the control signal $V_{\text{con}}(t)$ was changed to $V_{con}(t) = g \times (\omega_{ref} - \omega(t))$ instead of $g \times (\omega(t) - \omega_{ref})$ as described above, the system will still undergo the conventional period doubling route to chaos, but co-existence of period-1 and period-3 attractors at some system parameter values was also observed. The analysis of this phenomenon using the Monodromy matrix approach revealed that the period-3 attractor was born via a saddle node bifurcation at some critical value of the supply voltage.

8.6.1 System Dynamic Behaviour with the Change in Control Signal

As a result of the change in the control signal, the system behavior could be described by:

$$\frac{d\mathbf{X}(t)}{dt} = \begin{cases} \mathbf{f}_{-}(\mathbf{X}(t)), & V_{con}(t) < V_{ramp}(t) \\ \mathbf{f}_{+}(\mathbf{X}(t)), & V_{con}(t) > V_{ramp}(t) \end{cases} \tag{8.24}$$

where $\mathbf{f}_{-}(\mathbf{X}(t))$ and $\mathbf{f}_{+}(\mathbf{X}(t))$ have been previously defined in (8.2) and (8.3), respectively. As the supply voltage is varied from 30 V to 130V, the bifurcation diagram based on the new control signal is shown in Fig. 8.9.

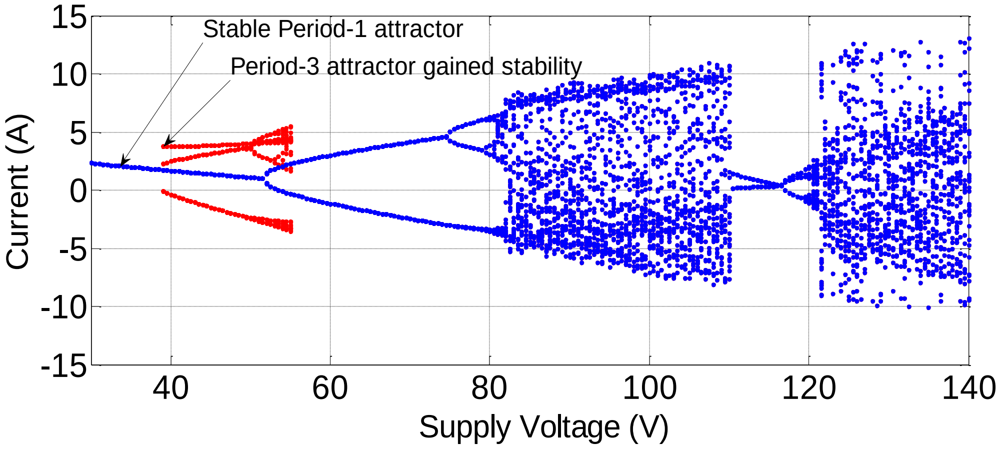

Fig. 8. 9 Bifurcation diagram of the system based on the new control signal.

From Fig. 8.9 it could be seen that for (30V < V_{in} < 38.516V) the only attracting set is the period-1 attractor, but at V_{in}=38.516V a period-3 orbit gains stability via a saddle node bifurcation and thus co-exists with the stable period-1 orbit. To confirm the occurrence of co-existing attractors in the region $V_{in} \in [38.516,50]$ the system was simulated at V_{in}=40V using two different sets of initial values, and the results are shown in Fig. 8.10 and Fig. 8.11. When the initial state is $\omega(0)=0$, $i(0)=0$, the trajectory converged on the period-1 attractor, but when the initial state is $\omega(0)$=3rad/sec, $i(0)$= 2A, the trajectory converged on the period-3 attractor.

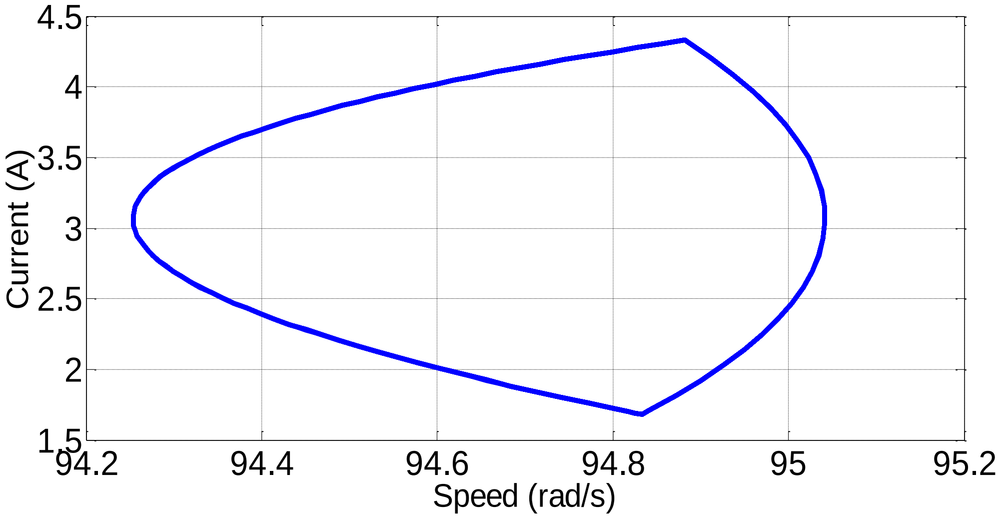

Fig. 8. 10 Period-1 attractor at V_{in}=40V, $i(0)=0$, $\omega(0)=0$.

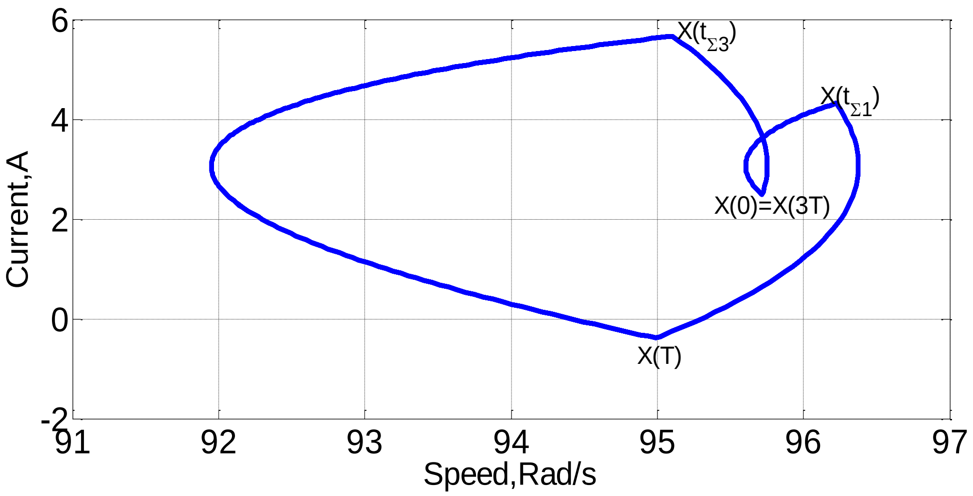

Fig. 8.11 Period-3 attractor at V_{in}=40V, $i(0)$=2A, $\omega(0)$=3Rad/s.

Further attempt to ascertain the basin of attraction of the two attracting sets revealed the occurrence of a riddled or fractal basin boundary (Fig. 8.12), thus making any future prediction of system behaviour practically impossible.

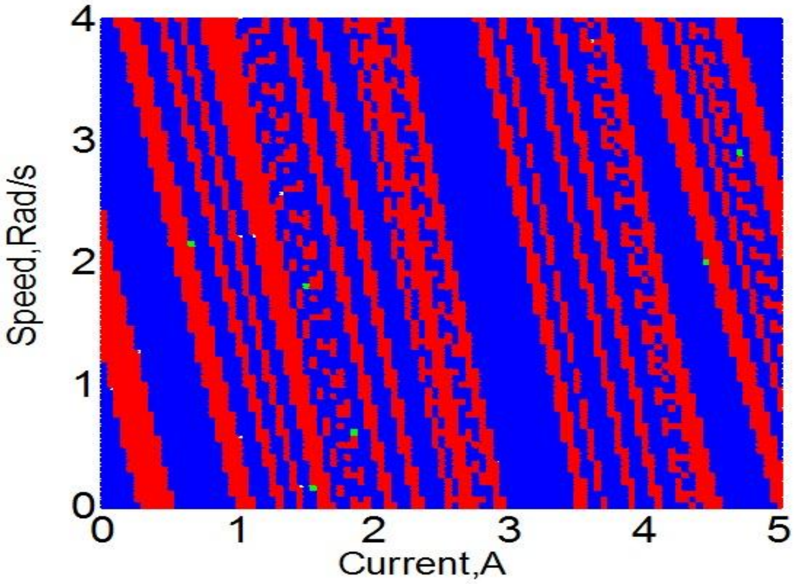

Fig. 8. 12 Basin of attraction of the co-existing period-1 and period-3 attractors.

In Fig. 8.12, initial points whose trajectories converged on the period-1 attractor are marked as blue, while initial points whose trajectories converged on the period-3 attractor are marked as red. It is thus obvious that the boundaries of the two attracting sets are difficult to isolate, hence the fractal phenomena.

8.6.2 Analysis of the Birth and Death of the Co-existing Period-3 Attractor Using the Monodromy Matrix Approach

To ascertain the system parameter values at which the co-existing period-3 attractor gains and loses stability, we need to perform the stability analysis of the period-3 orbit (Fig. 8.11). By employing the Monodromy matrix technique, we need to obtain the STM over the entire period-3 cycle ($t \in [0,3T]$) and evaluate its eigenvalues. From Fig.8.11, the Monodromy matrix can be expressed as:

$$\begin{aligned}\mathbf{M}(3T,0) &= \Phi(3T,t_{\Sigma 3})\times \mathbf{S}_3 \times \Phi(t_{\Sigma 3},T)\times \mathbf{S}_2 \times \Phi(T,t_{\Sigma 1})\times \mathbf{S}_1 \times \Phi(t_{\Sigma 1},0) \\ &= e^{A(3T-t_{\Sigma 3})}\times \mathbf{S}_3 \times e^{A(t_{\Sigma 3}-T)}\times \mathbf{S}_2 \times e^{A(T-t_{\Sigma 1})}\times \mathbf{S}_1 \times e^{A(t_{\Sigma 1})}\end{aligned} \tag{8.25}$$

where $\mathbf{S}_1$, $\mathbf{S}_2$, and $\mathbf{S}_3$ are the Saltation matrices at the three switching instants $t_{\Sigma 1}$, T, and $t_{\Sigma 3}$ respectively. The switching instants ($t_{\Sigma 1}$ and $t_{\Sigma 3}$) depend on the PWM duty ratio which varies around the limit cycle ($t_{\Sigma 1} = d_1 T$ and $t_{\Sigma 3} = 2T + d_3 T$). Hence, to evaluate the Monodromy matrix we need to evaluate the two duty ratios d_1 and d_3 as well as the three Saltation matrices. The Saltation matrix $\mathbf{S}_2$ is an identity matrix as the switching hypersurface is discontinuous at $t=T$, while S_1 and S_3 are computed following the same procedure described in section 4.2.6. The computed Saltation matrices, Monodromy matrix and Floquet multiplier as the supply voltage is varied are shown in Table 8.2. From the tabuled results, it could be seen that the period-3 orbit suddenly gained stability at V_{in}=38.516V via a saddle node bifurcation and thereafter co-existed with the period-1 attractor. At V_{in}=49.8V, the period-3 orbit lost stability (as the absolute value of one of the Floquet multipliers falls outside the unit circle), which is in agreement with the bifurcation diagram shown in Fig. 8.9.

Table 8. 2 Computed Saltation matrices, Monodromy matrix and Floquet multipliers.

V_{in}	$\mathbf{S}_1$	$\mathbf{S}_3$	Monodromy Matrix	Floquet Multipliers
38.516	$\begin{bmatrix} 1 & 0 \\ -1.6146 & 1 \end{bmatrix}$	$\begin{bmatrix} 1 & 0 \\ -1.1585 & 1 \end{bmatrix}$	$\begin{bmatrix} -1.1569 & -0.8936 \\ 3.2787 & 2.3542 \end{bmatrix}$	0.2085 0.9887
38.6	$\begin{bmatrix} 1 & 0 \\ -1.5951 & 1 \end{bmatrix}$	$\begin{bmatrix} 1 & 0 \\ -1.1593 & 1 \end{bmatrix}$	$\begin{bmatrix} -1.2167 & -0.8982 \\ 3.2784 & 2.2507 \end{bmatrix}$	0.2698 0.7641
39 V	$\begin{bmatrix} 1 & 0 \\ -1.5706 & 1 \end{bmatrix}$	$\begin{bmatrix} 1 & 0 \\ -1.1603 & 1 \end{bmatrix}$	$\begin{bmatrix} -1.2975 & -0.8832 \\ 3.2878 & 2.0793 \end{bmatrix}$	$0.3909 \pm 0.231j$
40 V	$\begin{bmatrix} 1 & 0 \\ -1.5475 & 1 \end{bmatrix}$	$\begin{bmatrix} 1 & 0 \\ -1.1606 & 1 \end{bmatrix}$	$\begin{bmatrix} -1.3874 & -0.8281 \\ 3.3152 & 1.8300 \end{bmatrix}$	$-0.2213 \pm 0.3965j$
45 V	$\begin{bmatrix} 1 & 0 \\ -1.5249 & 1 \end{bmatrix}$	$\begin{bmatrix} 1 & 0 \\ -1.1539 & 1 \end{bmatrix}$	$\begin{bmatrix} -1.5819 & -0.5413 \\ 3.4420 & 1.0475 \end{bmatrix}$	$-0.2672 \pm 0.3671j$
49.5 V	$\begin{bmatrix} 1 & 0 \\ -1.5305 & 1 \end{bmatrix}$	$\begin{bmatrix} 1 & 0 \\ -1.1456 & 1 \end{bmatrix}$	$\begin{bmatrix} -1.6938 & -0.3073 \\ 3.5407 & 0.5206 \end{bmatrix}$	–0.9580 –0.2152
49.8 V	$\begin{bmatrix} 1 & 0 \\ -1.5215 & 1 \end{bmatrix}$	$\begin{bmatrix} 1 & 0 \\ -1.1554 & 1 \end{bmatrix}$	$\begin{bmatrix} -1.7447 & -0.3106 \\ 3.5738 & 0.5180 \end{bmatrix}$	–1.0257 –0.2010

8.7 Summary

In this chapter, the nonlinear phenomena in Full bridge converter PMDC drive are analysed using the Monodromy matrix approach. Apart from the period doubling bifurcation cascades that were earlier reported, the system also exhibits co-existing attractors with riddled or fractal basin boundaries. The co-existence of stable period-1 and period-3 attracting sets and fractal basin boundaries in full-bridge converter PMDC drives will have some practical implications, especially when the drive is used in high precision applications such as in medical equipments or robotic arms. Under such circumstance, the much desired period-1 orbit may not be achieved with certainty as the system operators are unlikely to maintain absolute control over the initial state of the system.

CHAPTER 9

CONCLUSION AND SUGGESTIONS FOR FUTURE WORK

9.1 Conclusion

In this thesis, the nonlinear phenomena in some commonly used electrical drives (PMDC drives, SRM drives and SCDC drives) are analysed for the first time and controlled using the recently introduced Monodromy matrix approach. The desired invariant set in these drives is a period-1 orbit, but as some system parameter is varied the period-1 orbit loses stability and a period-nT orbit (in PMDC drives employing proportional control, SRM drives and SCDC drives) or a quasi-periodic orbit (in PI controlled PMDC drives) is born. The birth of a period-nT orbit from the period-1 orbit is known as a *fast-scale instability* or period doubling bifurcation, while the birth of a quasi-periodic orbit is known as a *slow-scale instability* or Neimark-Sacker bifurcation. Further variation of the system parameter leads to the birth of an aperiodic or chaotic attractor. The occurrence of co-existing attractors with fractal basin of attraction was also observed for the first time in both the DC chopper fed and full-bridge converter PMDC drive.

To ascertain analytically the system parameter value at which the fast-scale instability occurs, the Monodromy matrix based technique was employed. This method (which is based on Filippov’s method of differential inclusion) was found to be simpler and more straightforward to apply than the conventional Poincaré map technique, and this thesis represents the first application of the technique in the analysis and control of electrical drive systems. To perform the stability analysis of the nominal period-1 orbit using the Monodromy matrix technique the STM around the entire orbit (including the STM at the switching manifold known as the Saltation matrix) was obtained. The orbital stability depends on the eigenvalue of the Monodromy matrix (also referred to as Floquet multipliers). The period-1 orbit is stable if the absolute values of the Floquet multipliers are within the unit circle and unstable otherwise.

Also, to ascertain the system parameter value at which the slow-scale instability (Neimark-Sacker bifurcation) occurs, both the Monodromy matrix and state space average techniques were employed, and results from the two analytical techniques showed good agreement. A Neimark-Sacker bifurcation occurs when two of the eigenvalues of the Monodromy matrix leave the unit circle at the same time or when the eigenvalues of the state matrix of the average model suddenly crossed to the positive side of the complex eigenvalue plane. It should be noted that the state space averaging technique is suitable for analysing only slow scale instability, while the Monodromy matrix approach is suitable for analysing both slow scale and fast-scale instabilities. The occurrence of the Neimark-Sacker bifurcation in the PI controlled PMDC drive was further validated experimentally (for the first time) using a low cost digital signal controller (dsPIC30F3010). Numerical, analytical and experimental results showed good agreement.

Another advantage of the Monodromy matrix approach is the insight it gives in terms of the control of the fast-scale instability. By manipulation of the Saltation matrix component of the Monodromy matrix, the fast-scale instability can be controlled and the system parameter range for nominal period-1 operation extended. Three control techniques based on Saltation matrix manipulation were employed (detailed in chapter 6) and were found to be successful in controlling the onset of the fast-scale instability in the selected electrical drive systems. The goal of the controller is to push the Floquet multiplier back to the unit circle and this could be achieved by manipulating either the partial derivative of the switching hypersurface with respect to time $(\partial h(\mathbf{X}(t)/dt)$ or by manipulating the normal to the hypersurface $(\partial h(\mathbf{X}(t)/d\mathbf{X})$.

9.2 Suggestions for Future Work

In this thesis, the nonlinear phenomena in PMDC drives, SRM drives and SCDC drives were analysed and controlled using the Monodromy matrix approach. Future work in this area may include:

- Combining the Saltation matrix based control technique with artificial intelligence (AI) techniques such as artificial neural network (ANN) and fuzzy logic in developing an optimal controller for the nonlinear phenomena in electrical drives.
- Combining the Saltation matrix based control technique with sliding mode control scheme for a more robust control of electrical drive systems.

- The application of the Monodromy matrix technique in the stability analysis of brushless DC drives, permanent magnet synchronous drives, and full-bridge converter DC drives employing the unipolar PWM switching technique.
- The application of the Monodromy matrix technique in the stability analysis of complex systems with more than one interacting electrical drives such as robotic arms, unmanned aerial vehicles etc.

APPENDIX A

EXPERIMENTAL SET-UP

A.1 Introduction

The experiment set up used in this investigation consisted of a PMDC motor and electronic load unit, the power converter circuit and the control electronics. The shaft speed was measured using a 3 channel quadrature encoder (HEDS-5540). The power converter and the control electronics are mounted on a flexible dsPIC30F3010 inverter board originally built for a three-phase brushless DC motor drive (Fig.4.43). The board was slightly modified in this project to enable the use of the built-in quadrature encoder interface (QEI) peripheral in the dsPIC30F3010 digital signal controller (DSC). Only two of the three inverter legs (or four power MOSFETS) are used, thus forming an H-bridge. The speed control algorithm was implemented in C language using the Microchip MPLAB integrated development environment (IDE) and C30 compiler. The executable code was downloaded to the DSC using the Microchip ICD2 debugging device. The hardware set up is shown in Fig.A.1

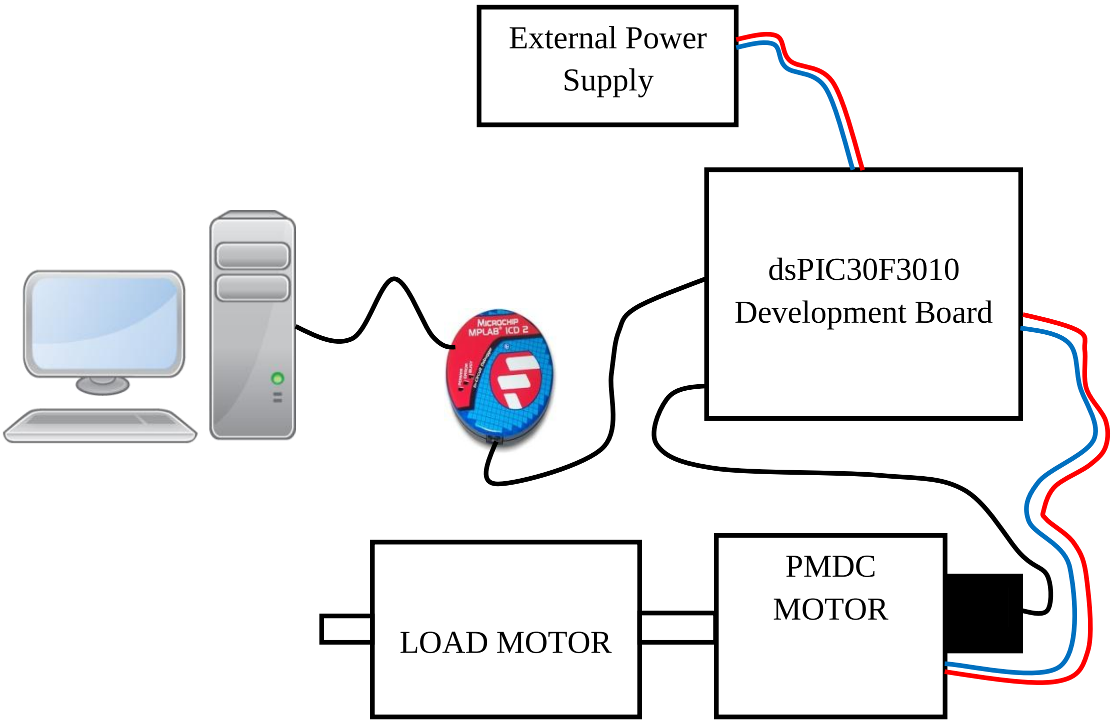

Fig. A.1 Hardware set up

A.2 Control and Power Circuits

The block diagram representation of the control and power circuits is shown in Fig. A.2. The key dsPIC30F3010 peripherals used in this project are the 10-bit analogue to digital conversion (ADC) unit, the QEI module, and the motor control PMW (MCPWM) module. Detail information on these peripherals could be found in the device data sheet. The reference speed (ω_{ref}) is provided by the potentiometer (whose output is connected to one of the ADC pins of the DSC) and the actual speed is measured by the quadrature encoder. The voltage pulses produced by the three channels of the encoder (phase A, phase B and Index) are processed using the built-in QEI peripheral to obtain the actual speed. The speed can be measured by counting the number of encoder pulses in a fixed time interval or by measuring the time it takes to obtain a fixed number of encoder pulses.

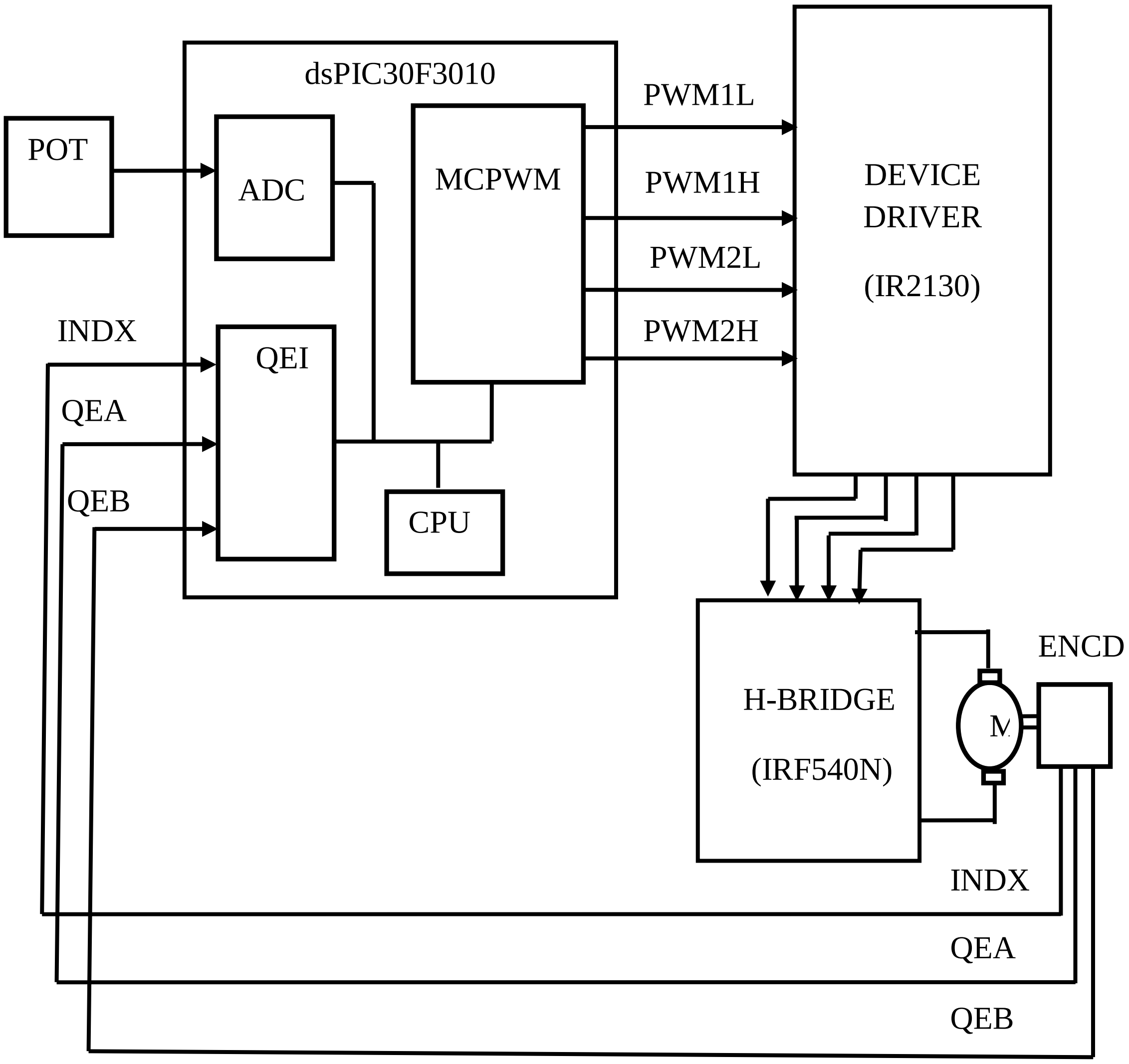

Fig. A. 2 Control and power Circuit

The speed error (the difference between the reference speed and the actual speed) is processed by the PI control algorithm to obtain the modulation index (control signal). The modulation index is then processed by the motor control PWM (MCPWM) peripheral of the DSC to obtain the four PWM outputs (PWM1L, PWM1H, PWM2L, and PWM2H) used to turn the power switches in the H-bridge ON and OFF. By varying the PWM duty cycle the average voltage applied at the armature terminals and the motor speed can be controlled. The power switch used in this project is 1RF540 N channel Power MOSFET, and the device driver is high speed power MOSFET/IGBT driver (IR2130) which has three independent high and low side output channels (H01,2,3 and L01,2,3). Fig. A.3 shows the status of the four power switches in the H-bridge during forward motoring operation.

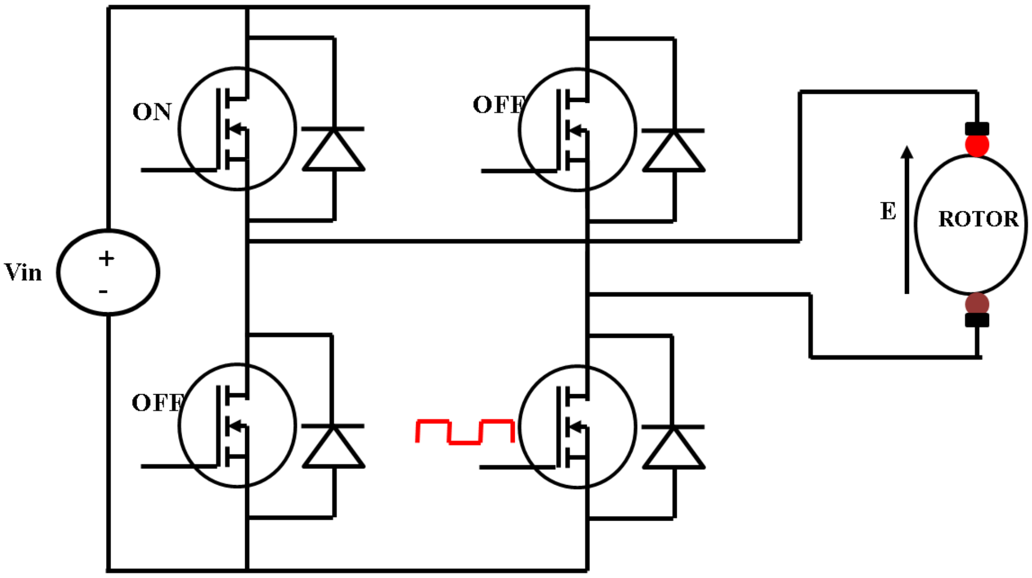

Fig. A.3 Forward motoring operation

A.3 Configuring the dsPIC30F30F3010 Peripherals in C Language

The configuration of the three key peripherals of the DsPIC30F3010 (QEI, MCPWM, and ADC) using C language will be discussed in this section. Three software routines: QEI_CONFIG (), MCPWM_CONFIG () and ADC_CONFIG () were created for this role.

A.3.1 QEI Configuration

Quadrature or optical encoders are commonly used for shaft speed and position measurements in closed loop digital implementations of electrical drives. Usually, three output channels (phase A, phase B and Index) provide information on the movement of the motor shaft including distance and direction. The QEI peripheral in dsPIC30F3010 is used for processing the signals from the quadrature encoder, thus relieving the burden from the CPU. The peripheral is composed of digital filters for conditioning the input signals, quadrature decoder logic for interpreting the phase A and phase B signals, and an up/down counter for accumulating the count. The four control registers that govern the operation of the QEI peripheral are:

- QEI Control Register (QEICON). This 16bit register allows the control of the QEI operation and status flag.
- Digital Filter Control Register (DFLTCON). This register allows the control of the digital input filter operation
- Position Count Register (POSCNT). This register allows writing or reading of the 16bit position counter.
- Maximum Count Register (MAXCNT). This register holds a value that will be compared with the pulse count in the POSCNT register. The CPU will be interrupted if the pulse count in POSCNT register matches the value stored in MAXCNT register.

```
/******************QEI peripheral configuration******************************
//The software routine implemented to configure the above registers is listed below. The
//quadrature encoder used is HEDS-5540 which has 3 output channels and 500 counts
//per revolution (CPR). The QEI peripheral is configured in ×4 operating mode thus
//increasing the encoder resolution to 2000 CPR.

************************************************************************/

void QEI_CONFIG(void)

{

QEICONbits.QEIM = 0;

QEICONbits.CNTERR = 0;

QEICONbits.QEISIDL = 0;

QEICONbits.SWPAB = 0;

QEICONbits.PCDOUT = 0;
```

```
QEICONbits.POSRES = 0;

DFLTCONbits.CEID = 1;

DFLTCONbits.QEOUT = 1;

DFLTCONbits.QECK = 7;

POSCNT = 0; // Reset position counter

MAXCNT=50;

QEICONbits.QEIM =7;

 IFS2bits.QEIIF=0;//QEI Interrupt flag reset.

return;

}
```

A.3.2 MCPWM Configuration

Speed control in modern electrical drives is achieved using PWM. In the past, PWM was implemented using special PWM chips or circuits, thus increasing the overall cost of the system. The MCPWM peripheral in dsPIC30F3010 is aimed at simplifying the task of producing PWM signals. The peripheral has 3 PWM generators and each PWM generator can produce two PWM outputs. Thus, the 3 PWM generators can produce 6 PWM outputs. Two output pins are provided for each PWM generator and the output pin pair can be configured for complementary or independent operation. Also the PWM output of any of the pins can be overridden manually using the OVDCON register of the MCPWM peripheral. The key control registers that need to be configured are:

- PWM time base control register (PTCON)
- PWM time base register (PTMR)
- PWM time base period register (PTPER)
- PWM control register 1 and 2 (PWMCON1 and PWMCON2)
- Dead time control registers 1 and 2 (DTCON1 and DTCON2)
- Fault A and B control registers (FLTACON and FLTBCON)
- PWM Duty cycle registers (PDC1, PDC2 and PDC3)

```
/*******************The MCPWM Peripheral Configuration*******************

 //The software routine implemented to configure the control registers is shown below.
//PWM_FREQ=20000hz
//FCY=30000000(30MIPS)
//Independent PWM mode is implemented.

**********************************************************************/

void MCPWM_CONFIG(void)

{

        PTCON = 0x8000; //Timebase On, runs in idle, no post or prescaler, free-running.

        PTPER = (FCY/PWM_FREQ)-1; //FCY and PWM_FREQ are constants.

        SEVTCMP = 0;

        PWMCON1 = 0x0FFF;

        PWMCON2 = 0x0004;

        FLTACON = 0x0000;

        OVDCON = 0;

        PDC1 = 0;

        PDC2 =0;

        PDC3 = 0;

        IFS2bits.PWMIF = 0;

        IFS2bits.FLTAIF =0;

        return;

}
```

A.3.3 ADC Configuration

The speed reference is obtained via the potentiometer connected to one of the DsPIC30F3010 analogue input pins. The analogue voltage from the potentiometer is converted to discrete value using the 10-bit ADC peripheral available in dsPIC30F3010. To use this peripheral, the following control registers were configured:

- A/D Control Register 1, 2 and 3(ADCON1, ADCON2 and ADCON3)
- A/D Input Channel Select Register (ADCHS)
- A/D Port Configuration Register (ADPCFG)
- A/D Input Scan Select Register (ADCSSL)

```
/************************The ADC Peripheral Configuration******************
//The software routine implemented to configure the control registers is listed below.
//Clearing of the ADCON1 samp bit ends sampling and starts conversion.

**********************************************************************/
Void ADC_CONFIG (void)

{

        ADPCFG = 0b1111111111111000;

        ADCHS = 2;

        ADCON1 = 0x030E;

        ADCON2 = 0x0200;

        ADCON3 = 0x007;

        ADCSSL = 0x003F;

        IFS0bits.ADIF = 0;

        ADCON1bits.ADON=1;

        return;

}
```

REFERENCES

[1] T. Wildi, *Electrical Machines, Drives, and Power Systems*, Fifth ed.: Prentice Hall, 2002.

[2] A. Hughes, *Electric Motors and Drives*, Third ed.: Newnes, 2006.

[3] M. A. El-Sharkawi, *Fundamentals of Electric Drives*: Brooks/Cole, 2000.

[4] S. Banerjee and G. Verghese, *Nonlinear Phenomena in Power Electronics: Bifurcation, Chaos, Control and Applications*: Wiley-IEEE Press, 2001.

[5] J. H. B. Deane and D. C. Hamill, "Instability, subharmonics, and chaos in power electronic systems," *Power Electronics, IEEE Transactions on*, vol. 5, pp. 260-268, 1990.

[6] D. C. Hamill, "Power electronics: a field rich in nonlinear dynamics," *Workshop on Nonlinear Dynamics of Electronic Systems*, pp. 164-179, 1995.

[7] K. T. Chau, J. H. Chen, C. C. Chan, J. K. H. Pong, and D. T. W. Chan, "Chaotic behavior in a simple DC drive," in *Power Electronics and Drive Systems, 1997. Proceedings., 1997 International Conference on*, 1997, pp. 473-479 vol.1.

[8] J. H. Chen, K. T. Chau, and C. C. Chan, "Analysis of chaos in current-mode-controlled DC drive systems," *Industrial Electronics, IEEE Transactions on*, vol. 47, pp. 67-76, 2000.

[9] S. H. Strogatz, *Nonlinear Dynamics and Chaos : With Applications to Physics, Biology, Chemistry, and Engineering* . New York , United States: Perseus Books Publishing, LLC, 1994.

[10] R. C. Hilborn, *Chaos and Nonlinear Dynamics : An Introduction for Scientist and Engineers*, 2nd Edition ed. New York: Oxford University Press inc, 2000.

[11] C. K. Tse, Y. M. Lai, and H. H. C. Iu, "Hopf bifurcation and chaos in a hysteretic current-controlled Cuk regulator," in *Power Electronics Specialists Conference, 1998. PESC 98 Record. 29th Annual IEEE*, 1998, pp. 1091-1097 vol.2.

[12] D. Dai, X. Ma, B. Zhang, and C. K. Tse, "Hopf bifurcation and chaos from torus breakdown in voltage-mode controlled DC drive systems," *Chaos, Solitons & Fractals*, vol. 41, pp. 1027-1033, 2009.

[13] A. El Aroudi, L. Benadero, E. Toribio, and G. Olivar, "Hopf bifurcation and chaos from torus breakdown in a PWM voltage-controlled DC-DC boost converter," *Circuits and Systems I: Fundamental Theory and Applications, IEEE Transactions on*, vol. 46, pp. 1374-1382, 1999.

[14] A. El Aroudi, E. Rodriguez, R. Leyva, and E. Alarcon, "A Design-Oriented Combined Approach for Bifurcation Prediction in Switched-Mode Power Converters," *Circuits and Systems II: Express Briefs, IEEE Transactions on*, vol. 57, pp. 218-222, 2010.

[15] D. Giaouris, S. Banerjee, O. Imrayed, K. Mandal, B. Zahawi, and V. Pickert, "Complex Interaction Between Tori and Onset of Three-Frequency Quasi-Periodicity in a Current Mode Controlled Boost Converter," *Circuits and Systems I: Regular Papers, IEEE Transactions on*, vol. 59, pp. 207-214.

[16] R. D. Middlebrook and S. C. uk, "A general unified approach to modeling switching-converter power stages," *IEEE Power Electronics Specialists Conf., Cleverand, OH*, pp. 18–34., 1976.

[17] P. T. Krein, J. Bentsman, R. M. Bass, and B. C. Lesieutre, "On the use of averaging for the analysis of power electronic systems," in *Power Electronics*

Specialists Conference, 1989. PESC '89 Record., 20th Annual IEEE, 1989, pp. 463-467 vol.1.

[18] C. K. Tse, *Complex Behaviour of Switching Power converter*: CRC Press, 2004.

[19] J. Mahdavi, A. Emaadi, M. D. Bellar, and M. Ehsani, "Analysis of power electronic converters using the generalized state-space averaging approach," *Circuits and Systems I: Fundamental Theory and Applications, IEEE Transactions on,* vol. 44, pp. 767-770, 1997.

[20] M. di Bernardo and F. Vasca, "Discrete-time maps for the analysis of bifurcations and chaos in DC/DC converters," *Circuits and Systems I: Fundamental Theory and Applications, IEEE Transactions on,* vol. 47, pp. 130-143, 2000.

[21] J. H. B. Deane and D. C. Hamill, "Chaotic behaviour in current-mode controlled DC-DC convertor," *Electronics Letters*, vol. 27, pp. 1172-1173, 1991.

[22] A. F. Filippov, *Differential Equations With Discontinuous Righthand Sides.* . Dordrecht, The Netherlands Kluwer, 1988.

[23] D. Giaouris, S. Banerjee, B. Zahawi, and V. Pickert, "Stability Analysis of the Continous Conduction Mode Buck Converter Via Filippov's Method," *IEEE Transactions on Circuits and Systems,* vol. 55, May 2008.

[24] A. Elbkosh, D. Giaouris, V. Pickert, B. Zahawi, and S. Banerjee, "Stability analysis and control of bifurcations of parallel connected DC/DC converters using the monodromy matrix," in *Circuits and Systems, 2008. ISCAS 2008. IEEE International Symposium on*, 2008, pp. 556-559.

[25] E. Ott, C. Grebogi, and J. A. Yorke, "Controlling chaos," *Physical Review Letters,* vol. 64, p. 1196, 1990.

[26] K. Chakrabarty and S. Banerjee, "Control of chaos in piecewise linear systems with switching nonlinearity," *Physics Letters A,* vol. 200, pp. 115-120, 1995.

[27] G. Poddar, K. Chakrabarty, and S. Banerjee, "Control of chaos in the boost converter," *Electronics Letters,* vol. 31, pp. 841-842, 1995.

[28] G. Poddar, K. Chakrabarty, and S. Banerjee, "Experimental control of chaotic behavior of buck converter," *Circuits and Systems I: Fundamental Theory and Applications, IEEE Transactions on,* vol. 42, pp. 502-504, 1995.

[29] J. Baillieul, R. Brockett, and R. Washburn, "Chaotic motion in nonlinear feedback systems," *IEEE Transactions on circuits and system,* vol. 27, pp. 990 - 997, 1980

[30] D. C. Hamill and D. J. Jeffries, "Subharmonics and chaos in a controlled switched-mode power converter," *Circuits and Systems, IEEE Transactions on,* vol. 35, pp. 1059-1061, 1988.

[31] J. H. B. Deane and D. C. Hamill, "Analysis, simulation and experimental study of chaos in the buck converter," in *Power Electronics Specialists Conference, 1990. PESC '90 Record., 21st Annual IEEE*, 1990, pp. 491-498.

[32] D. C. Hamill, J. H. B. Deane, and D. J. Jefferies, "Modeling of chaotic DC-DC converters by iterated nonlinear mappings," *IEEE Transactions on Power Electronics,* vol. 7, pp. 25-36, 1992.

[33] M. d. Bernardo, C. Budd, and A. Champneys, "Grazing, skipping and sliding: Analysis of the non-smooth dynamics of the DC/DC buck converter," *Nonlinearity,* 1998.

[34] C. K. Tse and M. Di Bernardo, "Complex behavior in switching power converters," *Proceedings of the IEEE,* vol. 90, pp. 768-781, 2002.

[35] H. Lihong, J. Meimei, D. Zhongwen, and W. Jianhua, "Chaos control for the Boost converter under current-mode control," in *Control and Decision Conference* (*CCDC*), *2010 Chinese,* pp. 3579-3583.

[36] S. Banerjee and K. Chakrabarty, "Nonlinear modeling and bifurcations in the boost converter," *Power Electronics, IEEE Transactions on,* vol. 13, pp. 252-260, 1998.

[37] H. Lihong, J. Meimei, and S. Guangyan, "Chaos control for the Buck-Boost converter under current-mode control," in *Advanced Computational Intelligence (IWACI), 2010 Third International Workshop on*, pp. 426-431.

[38] C. D. Xu, K. W. E. Cheng, H. Zhang, X. K. Ma, and K. Ding, "Study of Intermittent Bifurcations and Chaos in Buck-Boost Converters with Input regulators," in *Power Electronics Systems and Applications, 2006. ICPESA '06. 2nd International Conference on*, 2006, pp. 268-272.

[39] C. K. Tse and W. C. Y. Chan, "Instability and chaos in a current-mode controlled Cuk converter," in *Power Electronics Specialists Conference, 1995. PESC '95 Record., 26th Annual IEEE*, 1995, pp. 608-613 vol.1.

[40] C. K. Tse, Y. M. Lai, and H. H. C. Iu, "Hopf bifurcation and chaos in a free-running current-controlled Cuk switching regulator," *Circuits and Systems I: Fundamental Theory and Applications, IEEE Transactions on,* vol. 47, pp. 448-457, 2000.

[41] L. Ming, D. Dong, M. Xikui, and H. H. C. Iu, "Fast-scale period-doubling bifurcation in voltage-mode controlled full-bridge inverter," in *Circuits and Systems, 2008. ISCAS 2008. IEEE International Symposium on*, 2008, pp. 2829-2832.

[42] M. Li, D. Dai, and X. Ma, "Slow-Scale and Fast-Scale Instabilities in Voltage-Mode Controlled Full-Bridge Inverter," *Circuits, Systems, and Signal Processing,* vol. 27, pp. 811-831, 2008.

[43] Y. Kuroe and S. Hayashi, "Analysis of bifurcation in power electronic induction motor drive systems," in *Power Electronics Specialists Conference, 1989. PESC '89 Record., 20th Annual IEEE*, 1989, pp. 923-930 vol.2.

[44] I. Nagy, "Tolerance band based current control of induction machines highlighted with the theory of chaos," in *Power Electronics Congress, 1994. Technical Proceedings. CIEP '94., 3rd International*, 1994, pp. 155-160.

[45] N. Hemati, "Strange attractors in brushless DC motors," *Circuits and Systems I: Fundamental Theory and Applications, IEEE Transactions on,* vol. 41, pp. 40-45, 1994.

[46] K. T. Chau, J. H. Chen, C. C. Chan, and D. T. W. Chan, "Modeling of subharmonics and chaos in DC motor drives," in *Industrial Electronics, Control and Instrumentation, 1997. IECON 97. 23rd International Conference on*, 1997, pp. 523-528 vol.2.

[47] J. H. Chen, K. T. Chau, C. C. Chan, and Q. Jiang, "Subharmonics and Chaos in Switched Reluctance Motor Drives," *Power Engineering Review, IEEE,* vol. 22, pp. 57-57, 2002.

[48] Z. Suto, I. Nagy, and E. Masada, "Period adding route to chaos in a hysteresis current controlled AC drive," in *Advanced Motion Control, 2000. Proceedings. 6th International Workshop on*, 2000, pp. 299-304.

[49] L. Zhong, P. Jin Bae, J. Young Hoon, Z. Bo, and C. Guanrong, "Bifurcations and chaos in a permanent-magnet synchronous motor," *Circuits and Systems I: Fundamental Theory and Applications, IEEE Transactions on,* vol. 49, pp. 383-387, 2002.

[50] Y. Gao and K. T. Chau, "Hopf bifurcation and chaos in synchronous reluctance motor drives," *Energy Conversion, IEEE Transactions on,* vol. 19, pp. 296-302, 2004.

[51] K. Pyragas, "Continuous control of chaos by self-controlling feedback," *Physics Letters A*, vol. 170, pp. 421-428, 1992.

[52] K. Pyragas, "Control of Chaos via an Unstable Delayed Feedback Controller," *Physical Review Letters,* vol. 86, p. 2265, 2001.

[53] J. H. Chen, K. T. Chau, S. M. Siu, and C. C. Chan, "Experimental stabilization of chaos in a voltage-mode DC drive system," *Circuits and Systems I: Fundamental Theory and Applications, IEEE Transactions on,* vol. 47, pp. 1093-1095, 2000.

[54] T. Asakura, K. Yoneda, Y. Saito, and M. Shioya, "Chaos detection in velocity control of induction motor and its control by using neural network," in *Signal Processing Proceedings, 2000. WCCC-ICSP 2000. 5th International Conference on*, 2000, pp. 1633-1638 vol.3.

[55] R. Haipeng and L. Ding, "Nonlinear feedback control of chaos in permanent magnet synchronous motor," *Circuits and Systems II: Express Briefs, IEEE Transactions on,* vol. 53, pp. 45-50, 2006.

[56] W. Cheng, Y. Tong, and C. Li, "Chaos Control of Permanent Magnet Synchronous Motor via Sliding Mode Variable Structure Scheme," in *Intelligent Systems and Applications (ISA), 2011 3rd International Workshop on*, pp. 1-4.

[57] G. Xiaohui and H. Jin, "Chaos control of permanent magnet synchronous motor," in *Electrical Machines and Systems, 2005. ICEMS 2005. Proceedings of the Eighth International Conference on*, 2005, pp. 484-488 Vol. 1.

[58] T. Tang, M. Yang, H. Li, and D. Shen, "A New Discovery and Analysis on Chaos and Bifurcation in DC Motor Drive System with Full-bridge Converter," in *Industrial Electronics and Applications, 2006 1ST IEEE Conference* Singapore, 2006.

[59] A. Ralph and C. Shaw, *Dynamics--The geometry of behaviour*, 1982.

[60] J. R. Brannan and W. E. Boyce, *Differential Equations :An Introduction to Modern Methods and Applications.* Hoboken, NJ, United States: John Wiley&Sons,Inc, 2007.

[61] B. C. Kuo, *Automatic Control Systems*. New Jersey: Prentice-Hall,Inc, 1995.

[62] K. T. Alligood, T. D. Sauer, and J. A. Yorke, *Chaos, an introduction to dynamical systems*.

[63] F. Verhulst, *Nonlinear Differential Equations and Dynamical Systems*, Second ed.: Springer, 1996.

[64] D. C. Hamill, J. H. B. Deane, and D. J. Jefferies, "Modeling of chaotic DC-DC converters by iterated nonlinear mappings," *Power Electronics, IEEE Transactions on,* vol. 7, pp. 25-36, 1992.

[65] R. I. Leine and H. Nijmeijer, *Dynamics and Bifurcations of Non-Smooth Mechanical Systems.* New-York: Springer-Verlag, 2004.

[66] D. Giaouris, S. Maity, S. Banerjee, V. Pickert, and B. Zahawi, "Application of Filippov method for the analysis of subharmonic instability in dc\–dc converters " *Int. J. of Circuit Theory Applications*, vol. 37, pp. 899-919, 2009.

[67] J. R. Brannan and W. E. Boyce, "Differential equations--An introduction to modern methods and Applictaions."

[68] N. Hong, L. Chao, Z. Yajun, and S. Haiyi, "The bifurcation analysis and chaos anti-control of a differential-algebraic system," in *Bio-Inspired Computing: Theories and Applications (BIC-TA), 2010 IEEE Fifth International Conference on*, pp. 104-108.

[69] D. Borserio, H. Villanueva, and J. Falconer, "Chaotic analysis of fetal heart rate variability," in *Engineering in Medicine and Biology Society, 1994. Engineering*

Advances: New Opportunities for Biomedical Engineers. Proceedings of the 16th Annual International Conference of the IEEE, 1994, pp. 1258-1259 vol.2.

[70] U. Galvanetto, S. R. Bishop, and X. Daolin, "Adaptive control of chaotic stick-slip mechanical systems," in *Control of Oscillations and Chaos, 2000. Proceedings. 2000 2nd International Conference*, 2000, pp. 225-228 vol.2.

[71] S. Banerjee, "Coexisting attractors, chaotic saddles, and fractal basins in a power electronic circuit," *Circuits and Systems I: Fundamental Theory and Applications, IEEE Transactions on*, vol. 44, pp. 847-849, 1997.

[72] D. C. Hamill and J. H. B. Deane, "Modelling of chaotic dc-dc converters by iterative nonlinear mapping," *IEEE Trans. Power Electronics.*, vol. Vol.7, pp. 25-36, Jan. 1992.

[73] J. Chiasson, "Nonlinear Differential-Geometric Technique for Control of a Series DC Motor," *IEEE Transactions on Control Systems and Technology*, vol. 2, pp. 35-42, 1994.

[74] S. Mehta and J. Chiasson, "Nonlinear control of a series DC motor: theory and experiment," *Industrial Electronics, IEEE Transactions on*, vol. 45, pp. 134-141, 1998.

[75] F. Ismail, S. Wahsh, and A. Z. Mohamed, "High-performance prediction for variable-speed switched reluctance drives," in *Energy Conversion Engineering Conference, 1997. IECEC-97., Proceedings of the 32nd Intersociety*, 1997, pp. 348-352 vol.1.

[76] O. Cornea, D. Popovici, and A. Argeseanu, "A switched reluctance motor drive model using standard simulink library components," in *Optimization of Electrical and Electronic Equipment, 2008. OPTIM 2008. 11th International Conference on*, 2008, pp. 69-74.

[77] T. J. E. Miller, *Switched Reluctance Motors and Their Control*: Oxford University Press, 1993.

[78] F. Soares and P. J. C. Branco, "Simulation of a 6/4 Switched Reluctance Motor Based on Matlab/Simulink Environment," *IEEE Transactions on Aerospace and Electronic Systems*, vol. 37, 2001.

[79] X. Wang and J. K. Hale, "On monodromy matrix computation," *Computer Methods in Applied Mechanics and Engineering*, vol. 190, pp. 2263-2275, 2001.

[80] H. Vasquez and J. K. Parker, "A new simplified mathematical model for a switched reluctance motor in a variable speed pumping application," *Mechatronics*, vol. 14, pp. 1055-1068, 2004.

[81] H. Vasquez, J. Parker, and T. Haskew, "Control of a 6/4 switched reluctance motor in a variable speed pumping application," *Mechatronics*, vol. 15, pp. 1061-1071, 2005.

[82] Z. Suying and L. Hui, "Modeling and Simulation of Switched Reluctance Motor Double Closed Loop Control System," in *Intelligent Control and Automation, 2006. WCICA 2006. The Sixth World Congress on*, 2006, pp. 6151-6155.

[83] B. C. Mecrow, E. A. El-Kharashi, J. W. Finch, and A. G. Jack, "Preliminary Performance Evaluation of Switched Reluctance Motors with Segmental Rotors," *IEEE Transactions on Energy Conversion*, vol. 19, pp. 679-686, 2004.

[84] B. C. Mecrow, C. Weiner, and A. C. Clothier, "The Modeling of Switched Reluctance Machines With Magnetically Coupled Windings," *IEEE TRANSACTIONS ON INDUSTRY APPLICATIONS* vol. 37, 2001.

[85] M. di Bernardo, F. Garofalo, L. Glielmo, and F. Vasca, "Quasi-periodic behaviors in DC/DC converters," in *Power Electronics Specialists Conference, 1996. PESC '96 Record., 27th Annual IEEE*, 1996, pp. 1376-1381 vol.2.

[86] M. Debbat, A. El Aroudi, R. Giral, and L. Martinez-Salamero, "Hopf bifurcation in PWM controlled asymmetrical interleaved dual boost DC-DC converter," in *Industrial Technology, 2003 IEEE International Conference on*, 2003, pp. 860-865 Vol.2.

[87] J. H. Chen, K. T. Chau, C. C. Chan, and J. Quan, "Subharmonics and chaos in switched reluctance motor drives," *Energy conversion, ieee transactions on*, vol. 17, pp. 73-78, 2002.

[88] D. Giaouris, A. Elbkosh, S. Banerjee, B. Zahawi, and V. Pickert, "Control of switching circuits using complete-cycle solution matrices," in *Industrial Technology, 2006. ICIT 2006. IEEE International Conference on*, 2006, pp. 1960-1965.

[89] A. N. Natsheh, N. B. Janson, and J. G. Kettleborough, "Control of chaos in a DC-DC boost converter," in *Industrial Electronics, 2008. ISIE 2008. IEEE International Symposium on*, 2008, pp. 317-322.

[90] K. Chakrabarty, U. Kar, and S. Kundu, "Bifurcation behavior and Co-existing attractor of PWM controlled DC drives," in *India Conference (INDICON), 2011 Annual IEEE*, pp. 1-6.

[91] T. H. Abdelhamid, "Performance of Single-phase DC Drive System Controlled by Uniform P WM Full-Bridge DC-DC Converter," in *10th Meditwranean Electrotechnical Conference, MEleCon 2000*, 2000.